THE EFFECTS OF ATOMIC OXYGEN ON SILICON-CARBON SYSTEMS IN EXTREME ENVIRONMENTS

by

David Zuyu Chen

A dissertation submitted in partial fulfillment
of the requirements for the degree

of

Doctor of Philosophy

in

Chemistry

MONTANA STATE UNIVERSITY
Bozeman, Montana

April 2021

DEDICATION

To my family, especially to my parents, for convincing me that going back to school was a good idea. To all my friends, for constantly reminding me that the grass really is greener on the other side. And, to all my loved ones, for providing the emotional support to keep me going to the end.

ACKNOWLEDGEMENTS

I want to start by acknowledging my advisor, Professor Timothy Minton. It was a challenging but ultimately productive experience learning and working under him. I especially want to thank him for giving me the opportunity to switch fields into Physical Chemistry despite my background in Biology. This field has stimulated my interest in more ways than I had anticipated. I also want to acknowledge my committee members: Professor Rob Walker, Professor Nicolas Stadie, Professor Erik Grumstrup, and Professor Patrick Callis. Their classes have greatly broadened my understanding of this field. I also want to acknowledge the members of the Minton Lab Group. I want to thank Dr. Chenbiao Xu for his extensive training as well as assistance with the work presented herein. I want to thank Dr. Brody Bessire for introducing me to the fundamentals of lab work and for providing me an opportunity to learn LabVIEW. I want to thank Dr. Vanessa Murray for providing me additional training in the lab and to thank Dr. Eric Smoll for his many wise words of wisdom. And, of course, I want to thank Nicole Wolf for her efforts in keeping everything running.

Finally, I want to acknowledge both NASA Ames (Grant No. 80NSSC18M0065) and the Air Force Office of Scientific Research (Grant No. FA 9550-17-0057) for providing the opportunity to work on this research.

TABLE OF CONTENTS

TABLE OF CONTENTS CONTINUED

TABLE OF CONTENTS CONTINUED

LIST OF TABLES

Table Page

LIST OF FIGURES

LIST OF FIGURES CONTINUED

Figure Page

LIST OF FIGURES CONTINUED

Figure Page

LIST OF FIGURES CONTINUED

Figure Page

LIST OF FIGURES CONTINUED

Figure Page

LIST OF FIGURES CONTINUED

Figure Page

ABSTRACT

Vehicles traveling at hypersonic speeds require thermal protection systems (TPSs) that can withstand the extreme temperatures and reactive atomic oxygen species present in these environments. Ultra-high temperature ceramics are candidate TPSs, and many of them contain silicon carbide, allowing them to resist chemical attack by forming a protective oxide-containing layer, called passive oxidation. At very high temperatures, however, the layer will decompose, subjecting the material to ablation from reaction with O-atoms, called active oxidation, through a process called the passive-to-active oxidation transition (PAT). We have conducted molecular beam-surface scattering experiments to investigate the interactions of O-atoms with SiC at high temperatures, which revealed that with a lower fluence of O-atoms above the PAT, the SiC surface undergoes graphitization, while a sufficiently higher fluence of O-atoms promotes active oxidation. Analysis of the oxide layer decomposition revealed a decomposition process that initiated at the oxide-SiC interface. These insights will be useful for the development of more accurate predictive models, but they also aided understanding of the ablation of silicone-coated heat shields for atmospheric entry applications. For these applications, phenolic impregnated carbon ablator (PICA), a material composed of a carbon fiber network (FiberForm) and a resole phenolic resin stable against high heat convection and conduction, is used. Silicone is sprayed onto PICA to reduce dust, but the silicone can also form an oxide layer, which, like on SiC, will resist O-atom attack until it decomposes at very high temperatures, exposing the underlying material to reactive O-atoms. We conducted additional experiments in which a beam of atomic oxygen was directed at silicone-coated and uncoated samples of PICA as well as FiberForm, which revealed high nonreactive O-atom product scattering when the oxide layer was present, while with the decomposition of the oxide, product scattering resembled O-atom scattering from the underlying substrate. Additional studies probed the oxidation layer that is formed on pure silicone during O-atom bombardment, which revealed a three orders of magnitude reduction in erosion yield compared to that of Kapton H, a polyimide. This new data on PICA and FiberForm has been provided to NASA Ames for their development of an ablation model.

CHAPTER ONE

INTRODUCTION

1.1. Dissertation Theme

The work presented in this dissertation was an investigation into the molecular-level chemistry of thermal protection materials (TPSs) in the presence of atomic oxygen. These materials have applications for vehicles traveling at hypersonic velocities in extreme environments. The materials studied were silicon carbide, which has applications for ultra-high temperature ceramics; PICA and its substrate of FiberForm, which are ablative TPSs used for atmospheric entry applications; and silicones, which are used for protection in low-Earth orbit (LEO) but are also sprayed onto ablative TPSs like PICA. The studies described in this dissertation were performed using a unique high temperature atomic oxygen molecular beam-surface scattering apparatus that can provide high-resolution dynamics information of reactive and nonreactive species scattering from the silicon-based samples while the atomic oxygen beam is directed onto their surfaces. The remainder of this chapter will provide brief backgrounds and motivations for the materials and substrates used for the work presented in the subsequent chapters as well as provide necessary information on the technique of high temperature molecular beam-surface scattering and its data analysis.

1.2. Protective Materials

1.2.2 Ultra-High Temperature Ceramics for Hypersonic Applications

Vehicles traveling at hypersonic speeds in extreme environments require protection from both the extremely high temperatures[1] in these environments as well as reactive chemical species. Traveling at these velocities, these vehicles will experience aerodynamic heating that will raise temperatures to over 2000 °C.[2-3] To protect these vehicles and minimize their ablation, materials known as thermal protection systems (TPSs) are utilized. Ultra-high temperature ceramics (UHTCs) are a special class of TPSs that are being investigated as the TPS material for use on the leading edges of hypersonic vehicles traveling through the Earth's atmosphere.[4-6] As ceramics, these materials have a very high melting point and are designed to resist chemical attack from highly reactive species. Similar to the thermal protection system used on the Space Shuttle, these new materials are designed to be reusable,[7] but unlike the rapid-duration atmospheric entry conditions encountered by the Space Shuttle TPS, UHTCs are designed to allow vehicles to descend more gradually through the atmosphere, trading in a short, high-heat flux reentry for a longer duration, lower-heat flux descent.[8]

Despite these slower descent conditions, the longer duration flight also means that there is more time for reactive species to chemically attack the TPS, and because these conditions are hypersonic, with velocities surpassing 6 km s^{-1} (12 km s^{-1} when considering typical atmospheric entry), the vast majority of these reactive species are atomic oxygen. Because these velocities surpass the speed of sound, a shock wave forms in front of the vehicle within which diffusing gas molecules such as oxygen dissociate into monoatomic

species (**Fig. 1-1**). Counterintuitively, as the dissociated atomic oxygen passes through the boundary layer and approaches the surface of the vehicle's TPS, its velocity slows down to such an extent that its mean velocity will only approach 4 km s^{-1}, with translational energies around 1-2 eV.[9] Protection from these species have historically been provided by the incorporation of high-melting point materials such as silicon carbide.[10]

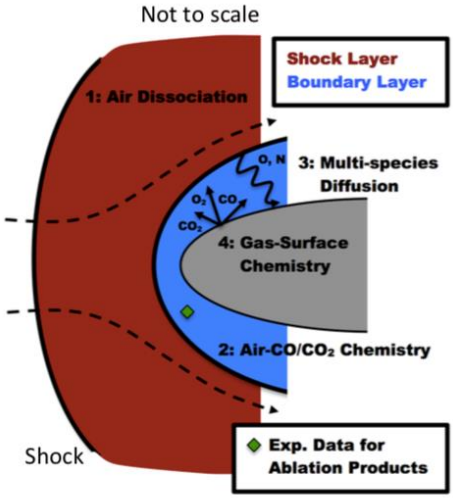

Fig. 1-1. Diagram of shock and boundary layer. Molecular species dissociate as they pass through the shock layer of a vehicle traveling in hypersonic conditions. Figure obtained from Thomas Schwartzentruber.

Silicon carbide (SiC) is a material incorporated into reusable TPSs, both in those of the former Space Shuttle[11] as well as UHTCs.[12-14] UHTCs in particular containing 20-30% by volume SiC have been found to provide maximum oxidation protection. SiC provides this protection through the formation of an oxide layer. In the presence of oxygen, SiC will react to form silicon dioxide,[15-16] as shown below:

$$2SiC(s) + 3O_2(g) \rightarrow 2SiO_2(s) + 2CO(g) \qquad \text{(Eq. 1-1)}$$

This process, called passive oxidation, confers protection to the underlying material by preventing oxygen from further penetrating through the oxide layer, in a manner analogous to how aluminum oxide prevents further oxidation of the underlying aluminum. However, above a certain temperature, this process of passive oxidation undergoes a transition.[15, 17-18] Instead of the formation of solid and passivating silicon dioxide, the process transitions into an "active" phase whereby volatile silicon monoxide is generated instead, as shown below:

$$SiC(s) + O_2(g) \rightarrow SiO(s) + CO(g) \qquad \text{(Eq. 1-2)}$$

This transition leads to the breakdown of the oxide layer protecting the material, leading to further erosion of the silicon carbide bulk as it is further exposed to oxygen and limiting the effectiveness and reusability of the material in extended flight times.

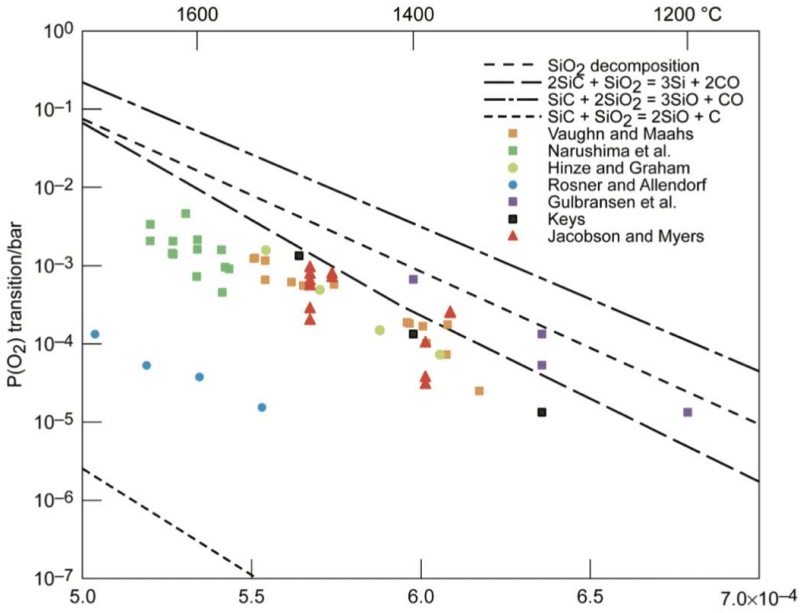

Fig. 1-2. Active-to-passive and passive-to-active oxidation transitions. Tabulated by Jacobsen et al. (2012).[9]

This passive-to-active oxidation transition (PAT) phenomenon has been studied extensively (**Fig. 1-2**) both in the aerospace context[1, 15, 19-20] as well as in regards to the manufacturing of semiconductors,[21] but the ablation mechanism remains poorly understood. In addition, while the PAT is well-understood with molecular oxygen, less is known about atomic oxygen oxidation. A number of studies on UHTC composite materials containing SiC have been conducted using high temperature atomic oxygen plasma facilities.[12, 22] However, the nature of the high-temperature heterogeneous plasma environments, containing considerable fractions of ionic and molecular oxygen in addition to atomic oxygen, meant that for these experiments, many chemical processes were coupled, making it difficult to resolve molecular-level processes. In addition, in many of these studies of carbon fiber/SiC candidates, temperature jumps were observed occurring around the passive-to-active oxidation transition temperature, the cause of which was relatively poorly understood (**Fig. 1-3**). A recent work on investigating the high-temperature oxidation of SiC used thermodynamic principles to model the ablation behavior, with reasonable concurrence with existing data in certain areas like passive-to-active oxidation transition conditions and surface temperatures.[23] However, limitations were observed in the development of finite-rate parameters, as reaction-specific rates could not be derived due to insufficient experimental data in the literature. Thus, it is important to understand the fundamental mechanisms of high-temperature atomic oxygen oxidation of silicon carbide in order to further develop accurate and predictive models. Atomic oxygen molecular beam-surface scattering experiments were thus conducted in order to investigate the molecular interactions of atomic oxygen with SiC, especially in the

temperature range spanning both passive and active oxidation regimes. These experiments are described in Chapter Two.

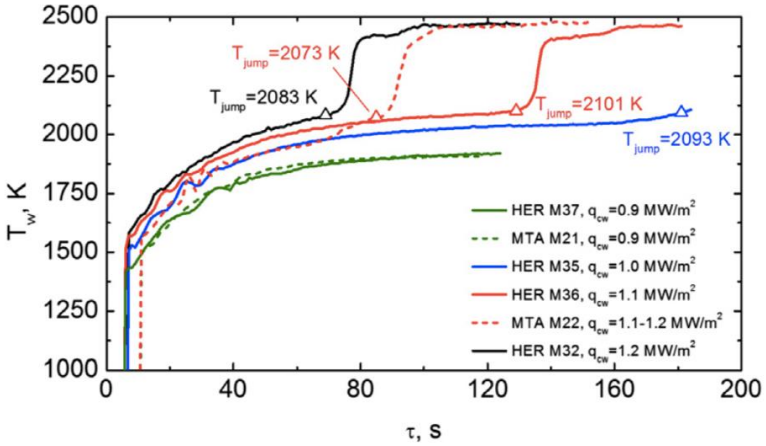

Fig. 1-3. Temperature jump phenomenon. Data observed by Panerai et al. (2014).[22]

1.2.3 Silicone Coatings

In low-Earth orbit (LEO), satellites orbiting the Earth do not experience the extreme heat vehicles traveling at hypersonic speed experience. However, these vehicles are still vulnerable to LEO environmental factors that can cause material degradation, such as UV radiation[24-26] and high energy reactive chemical species such as atomic oxygen.[27-29] Though the atmosphere is thin, unprotected exposure to solar radiation results in the photodissociation of molecules such as oxygen and nitrogen, creating an abundance of highly-reactive species, including ionic species and neutral monoatomic species. The apparent energy of LEO atomic oxygen is further increased due to the orbital velocity of the satellite. At a typical 7.8 km s^{-1} orbital velocity, LEO vehicles will impact incident "ram" atomic oxygen with energies of around 5 eV,[29] a translational energy actually higher than atomic oxygen species in hypersonic conditions. To provide protection from these

elements, silicones, with chemical compositions of chains of polymeric siloxane units, are utilized for their resistance to chemical and UV degradation.[30-32] Silicones are polymers typically consisting of polydimethylsiloxane (PDMS) chains or other siloxane constituents such as polydiphenylsiloxane chains (**Fig. 1-4**). Like silicon carbide, under exposure to atomic oxygen, the siloxane units will react to form passivating protective silicon-oxide layers.[28] Silicones have primarily been used as protective coatings applied to the outside of satellites traveling in low-earth orbit (LEO),[25, 28, 33] but they are also being investigated for use in high-temperature heat shield applications through pretreatment of the silicones with atomic oxygen exposure to form a silicon-oxide layer prior to use. Thus, using an atomic oxygen beam source, two dimethyl-, diphenylpolysiloxane silicones, CV-1144-0 and RTV-560, were exposed to a high fluence of atomic oxygen in order to investigate the silicon-oxide layer formed from pretreatment to atomic oxygen and assess their chemical and morphological changes to determine their efficacy for use in these applications. These experiments are described in Chapter Three.

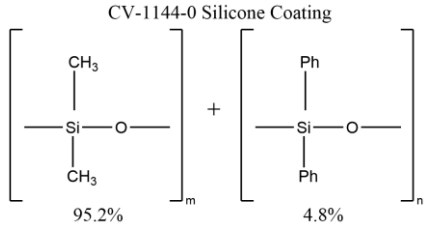

Fig. 1-4. Formula for CV-1144-0. CV-1144-0 is an example of a silicone coating used for LEO protective applications. This formula was obtained from Yan et al. (2001).[27]

1.2.4 Application of Silicones to FiberForm and PICA

Phenolic Impregnated Carbon Ablator, or PICA, is a carbon-carbon composite TPS material composed of a carbon fiber preform substrate filled with a resole phenolic resin

(**Fig. 1-5**).[34-36] This material is resistant to high heat convection and conduction, remaining stable at extremely high temperatures. The substrate, otherwise known as FiberForm from its brand name, is a highly porous material composed of a three-dimensional network of carbon fibers.[37] In addition, PICA is capable of dissipating heat through the pyrolysis of the phenolic resin filler. Like UHTCs, PICA is also vulnerable to reactive oxygen species in these environments. However, while UHTCs are being investigated for lower hypersonic velocity conditions, PICA was specifically designed for atmospheric entry applications, having been used on the Mars Science Laboratory,[38] Mars 2020,[39] and even being used by private companies such as SpaceX. With atmospheric entry velocities reaching 12 km s^{-1}, these materials are designed for high-heat flux, short duration entry into the atmosphere.

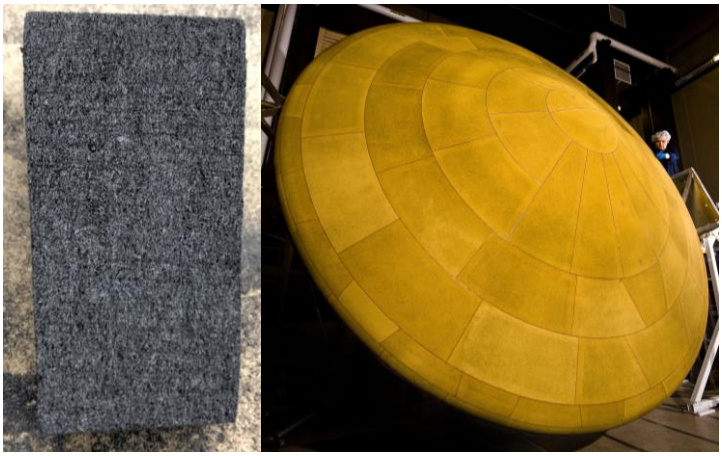

Fig. 1-5. FiberForm and PICA. (left) Slab of FiberForm. (right) PICA heat shield installed on the Mars Science Laboratory.[40]

Material response models designed to predict the oxidation of PICA have primarily relied on the material vitreous carbon (VC) as the model material representative of FiberForm. Known more generically as glassy carbon,[41] VC is an sp^2-hybridized disordered carbon material that approximates the disordered and porous carbon fiber

preform substrate in carbon-carbon composites. The most recent iterations of these models relied on atomic oxygen molecular beam-surface scattering studies of VC by Murray et al.[42-43] Using the inelastic and reactive scattering dynamics data gathered by Murray et al., Poovathingal et al. (2017),[44] Swaminathan-Gopalan et al. (2018),[45] and Prata et al. (2021)[46] all developed TPS oxidation models for use in hypersonic conditions. However, a more complete model of a specific TPS material such as PICA would require considering the atomic oxygen beam-surface scattering dynamics from actual FiberForm and PICA. Through further experimentation studying the atomic oxygen beam-surface scattering dynamics of all these materials could a more complete oxidation model be developed.

Recently Poovathingal et al. (2021)[47] conducted an atomic oxygen molecular beam-surface scattering study on FiberForm, which revealed similar temperature-dependent chemical behavior as that from VC.[42] In both studies, the flux of O-atom and CO products increased as temperature rose from 1000 K to 1800 K, and in both studies a hysteresis was observed in the O and CO temperature-dependent flux. These similarities meant that material response models involving the use of VC as a model material can still be relevant for FiberForm applications. For PICA, numerous oxidation studies have been conducted on C/C composite type materials.[48-49] In addition, PICA pyrolysis decomposition studies were performed by Bessire et al.[35-36] that were able to quantify how molar yields of decomposed products varied with the temperature heating rate, providing valuable experimental data for TPS ablation modelers. However, no atomic oxygen molecular beam-surface scattering study has ever been conducted on PICA.

Complicating matters, silicone coatings applied to PICA need to be considered as well. For the Mars Science Laboratory (MSL) mission as well as the Mars 2020 mission, CV-1144-0 silicone was applied to the PICA TPS as an anti-dust agent.[50] As mentioned in the previous section, pretreatment of the silicone to atomic oxygen will cause the formation of an oxide layer on the surface. From the in-flight data collected during the entry, descent, and landing of MSL, modelers at NASA had discovered gaps in the material response models they had used to predict the performance of the PICA TPS, finding discrepancies due to the exclusion of the silicone from their model. Thus, to better understand the oxidation mechanisms in these ablative materials, a comparative study using an atomic oxygen beam-surface scattering apparatus was conducted on four types of materials: FiberForm, silicone-coated FiberForm, PICA, and silicone-coated PICA. Building upon the knowledge gained in Chapter Two regarding the atomic oxygen beam-surface scattering from oxide-covered SiC as well as the passive-to-active oxidation transition, and the knowledge gained in Chapter Three regarding the oxidized silicone coatings, Chapter Four will thus delve into the differences in atomic oxygen oxidation between that of FiberForm, PICA, silicone-coated FiberForm, and silicone-coated PICA.

1.3 Primary Techniques and Data Analysis

1.3.1 Molecular Beam-Surface Scattering Apparatus

The primary investigative tool used for the research presented was a crossed molecular beams apparatus reconfigured for beam-surface scattering (**Fig. 1-6**).[51-53] The apparatus consisted of two differentially pumped vacuum chambers, with the main

chamber being where the beam-surface scattering took place and the secondary chamber being the source of the molecular beam. The main chamber contained the rotatable mass spectrometer detector, the sample mount, and it was evacuated with two large high vacuum pumps. While the molecular beam was running, the typical pressure in the main chamber hovered around 5 x 10^{-7} Torr. The O-atom beam itself operated as follows: first, high purity O_2 gas with a backing pressure around 550 psi was introduced into the source chamber via a pulsed valve and conical nozzle. Following a delay after the gas was introduced, a ~7 J $pulse^{-1}$ CO_2 TEA laser operating at 2 Hz and synchronized with the pulse valve fired through a ZnSe window onto a gold-plated concave mirror. The curvature of the mirror caused the beam to reflect and concentrate into the copper nozzle, exciting and breaking down the gas and creating a plasma greater than 20,000 K.[54] This plasma rapidly expanded to engulf the remaining gas, and upon cooling down after exiting the conical nozzle, it was composed mostly of atomic oxygen, $O(^3P)$,[55] with a small proportion of molecular oxygen, $O_2(^3\Sigma_g^-)$,[56] with typical operating energies of around 5 eV. The beam was then collimated, first through a skimmer separating the source chamber from the main chamber, followed by further collimation through an aperture. Samples that needed to be exposed to a large fluence of atomic oxygen were placed onto a sample mount within the source, as shown in **Fig. 1-6**.[57-58] For these exposure experiments, the rotatable mass spectrometer detector was held within the line of the beam in order to monitor its status.

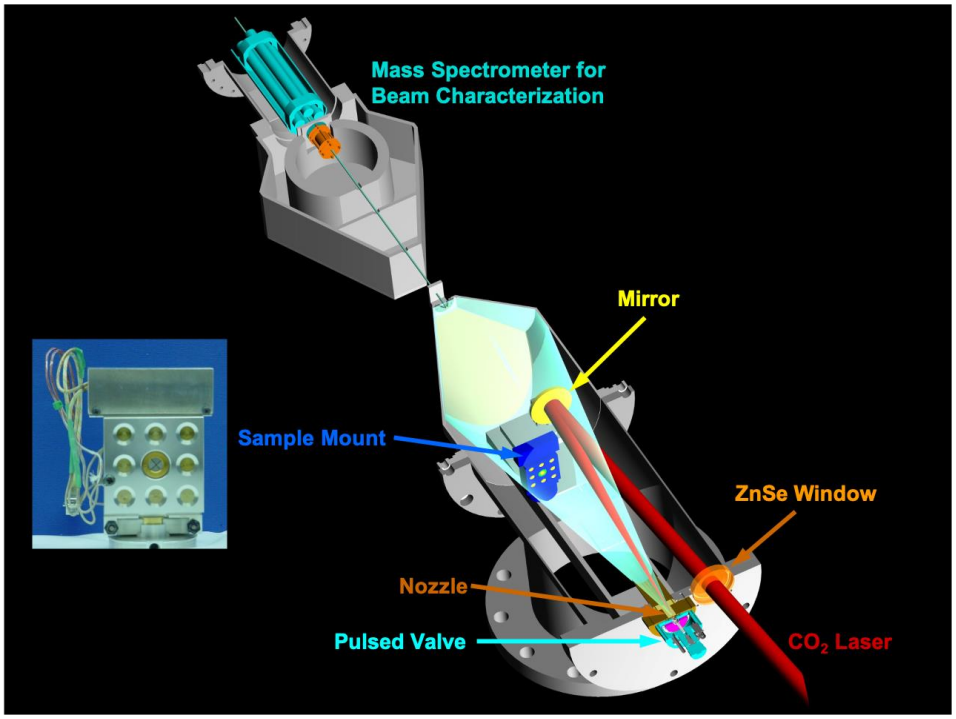

Fig. 1-6. Diagram of molecular beam gas-surface scattering apparatus configured for high fluence atomic oxygen exposure. Sample mount used for exposure shown in bottom left.[57]

The apparatus configured for beam-surface scattering experiments is shown in **Fig. 1-8**. A chopper wheel, synchronized to the laser detonation pulse, having three equally spaced 1.6 mm-thick slots and a rotation frequency of 300 Hz, was installed to allow for further velocity selection of the beam. A water-cooled electrically conductive copper mount with a ceramic spacer separating the anodic and cathodic regions was used as the high-temperature sample mount. Power for this sample mount was provided by a 20 V high current power supply. For all the beam-surface scattering experiments presented in this dissertation the sample mount was rotated such that the incident beam impinged at an angle 45° to the normal of the apparent surface of the sample (θ_i). Detection of scattered products was accomplished by rotating the mass spectrometer detector within the plane defined by the incident molecular beam axis and the sample's surface normal (**Fig. 1-7**). The mass

spectrometer detector itself consisted of an electron impact ionizer[59] with an electron energy of 160 eV, a quadrupole mass filter, and a Daly-type ion counter,[60] and the entire detector was triply differentially pumped with three ion pumps, along with an additional small pump that allowed for further reduction of residual gases within the region.

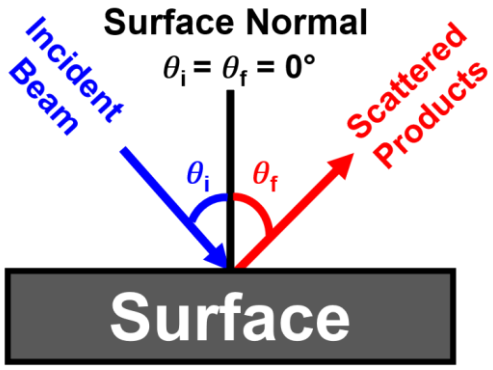

Fig. 1-7. Diagram demonstrating scattering of molecular beam from a target surface.

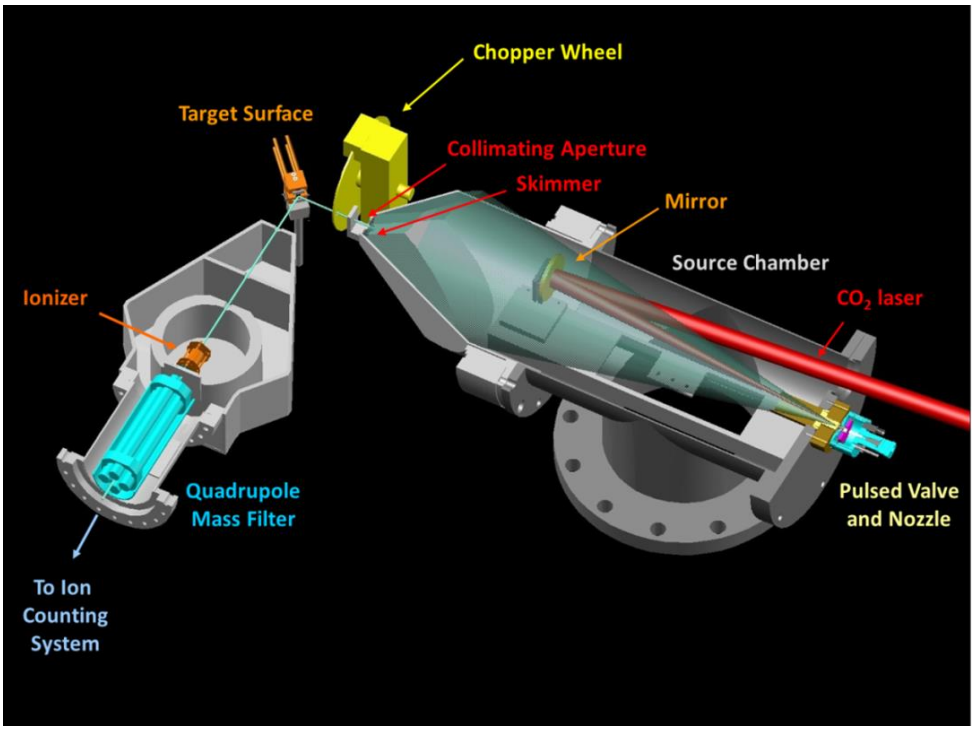

Fig. 1-8. Diagram of molecular beam gas-surface scattering apparatus configured for high temperature surface scattering.[42]

The Daly detector counted pulses as ions impacted the detector, and the signal was then recorded by a multichannel scaler that yielded a signal proportional to the scattered product number density as a function of flight time, *N(t)*, from the surface to the ionizer, a distance of 34.4 cm. These so-called time-of-flight (TOF) distributions were used to derive translational energy distributions of the scattered products with a density-to-flux conversion that assumes a monoenergetic incident beam.[52, 61] Using these translational energy distributions, average energies were determined which were then integrated to obtain the total relative flux of scattered species from the sample surface at a particular scattering angle, θ_f. These relative fluxes were then plotted while temperature was held steady as a function of θ_f, thus obtaining flux angular distributions, and vice versa, obtaining temperature-dependent fluxes at a specific θ_f. The surface temperature of the sample was measured using a pyrometer with a disappearing carbon filament.[47]

1.3.2 Sample Pyrolysis and Decomposition

The molecular beam-surface scattering apparatus was also reconfigured to monitor decomposition products from pyrolyzing samples by recording full mass spectra as a function of temperature.[35] By setting the quadrupole mass filter to scan a range of *m/z* ratios over a set period of time instead of holding at a single *m/z* ratio, mass spectra up to *m/z* = 110 amu was collected. Using a custom LabVIEW program designed to interface with the power supply, current was run through the sample in constant increments per interval of time, allowing for a correspondingly linear temperature increase every time interval. In this configuration, while the sample mount was still held at θ_i = 45°, the mass spectrometer detector was rotated so that θ_f was as close to the sample's surface normal as possible,

which was important as desorption from a planar surface is at its greatest at the surface normal.

1.3.3 Fitting Analysis of Time-of-Flight Distributions

The individual TOF distributions of scattered products can be further separated based on two scattering mechanisms as shown in **Fig. 1-9**: inelastic, or impulsive scattering (IS), and thermal desorption (TD).[61-62] Signal observed leaving the surface through IS channels represent atoms and molecules that undergo only a few collisions with the surface and transfer very little energy before exiting the surface at a time scale too small for equilibrium to be established. Within an individual TOF distribution, IS signal is observed as a narrow peak at very short flight times. Plotting the IS flux (**Fig. 1-10(a)**) as a function of the θ_f yields an angular distribution from which morphological information about the sample surface such as roughness can be obtained, as **Fig. 1-11** shows. In contrast, signal observed leaving the surface through TD channels represent atoms and molecules that establish thermal equilibrium with the surface before desorption. This signal is observed as a broad Maxwell-Boltzmann distribution of translational energies given by the temperature of the sample surface. Plotting the TD flux as a function of the θ_f yields an angular distribution that typically follows a $\cos^x(\theta_f)$ distribution, as shown in **Fig. 1-10(b)**. This process of separating the different channels of desorption often proceeds through first fitting the TD signal with a Maxwell-Boltzmann distribution. IS is then calculated from the difference between the total flux and the TD flux above translational energies of 2RT (2*gas constant*temperature).

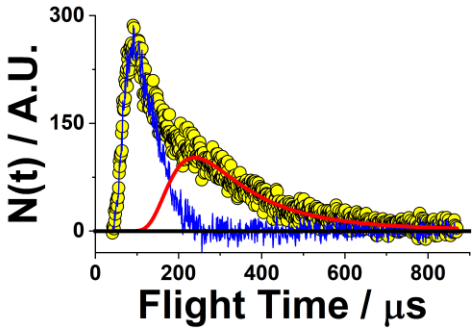

Fig. 1-9. Representative time-of-flight distribution with IS and TD channels separated. Yellow circles represent total signal. Red line represents TD channel fit with a Maxwell-Boltzmann distribution at a particular temperature. Blue represents IS channel.

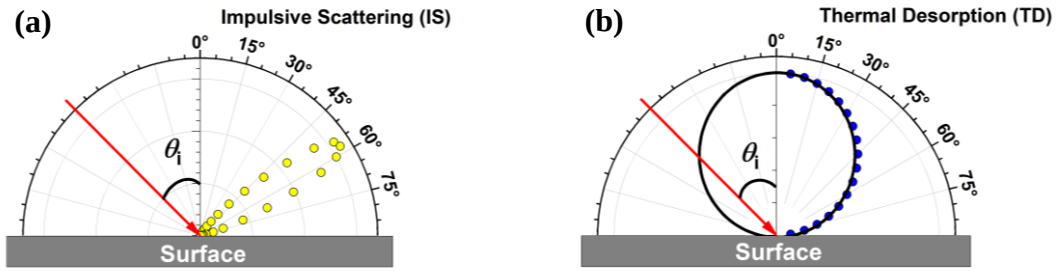

Fig. 1-10. Representative flux angular distributions for IS and TD. (a) Representative flux angular distribution reflecting IS channel flux from a range of θ_f. (b) Representative flux angular distribution reflecting TD channel flux from a range of θ_f.

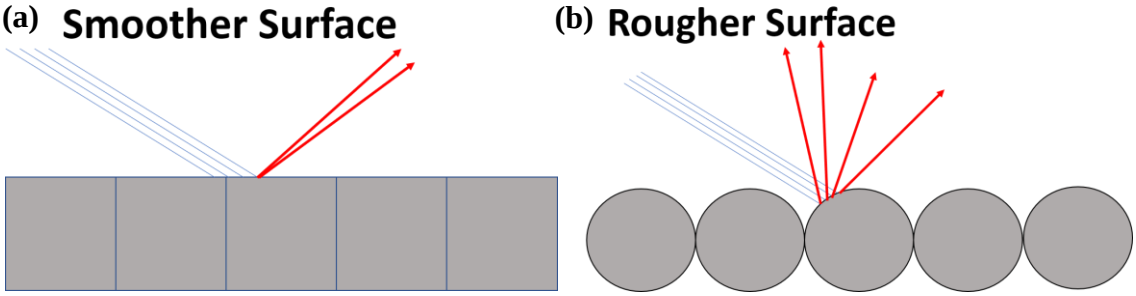

Fig. 1-11. Representative surfaces that produce different angular distributions. **(a)** Representation of a surface that will produce a very narrow IS angular distribution. **(b)** Representation of a surface that will produce a relatively broad IS angular distribution.

Scattering channels other than IS and TD were also considered. These channels are described in more detail in Chapters Two and Four, but briefly, these additional scattering channels were considered because a Maxwell-Boltzmann distribution did not fully fit many TOF distributions well for the experiments outlined in this research. One such scattering channel is referred to as TD_{fast}. TD_{fast} signal is represented in a TOF distribution by a thermal desorption signal that arrives at times shorter than those predicted by a Maxwell-Boltzmann distribution for a particular temperature, with average translational energies greater than 2RT. The presence of this signal indicates desorption over a barrier, and thus instead of a typical MB fit, a different fitting procedure, described by Michelsen and Auerbach (1991)[63] and applied by Murray et al. (2018)[64] in their TOF distributions, is utilized. While this fitting procedure is very versatile in fitting non-typical TD signals, one cannot necessarily assume that the theoretical basis for the fit is present within a system. Signal observed above 2RT could also be the result of IS signal derived from multiple bounces. Thus, the TD_{fast} fitting requires an additional theoretical basis to justify itself. Another scattering channel of importance is referred to as TD_{slow}. If some atoms or molecules continue to reside on a surface for some time after thermal equilibrium, some of the scattered signal will appear in the TOF distribution at times longer than that predicted by a MB distribution. This type of signal was observed in the TOF distribution from atomic oxygen scattering from both VC[42] and FiberForm.[47] There is not a single explanation for what causes these slower signals, with Murray et al. (2015)[42] speculating that the slow fit was due to the Boudouard reaction, and Poovathingal et al. (2021)[47] merely speculating the fits were due to distinct thermal processes. This type of signal can be fit using a convolution

of the MB distribution with an exponential first-order decay function, and this convoluted first-order decay fit has been observed to exist simultaneously with the normal TD fit represented by an MB distribution.

1.4. Organization of Following Chapters

Chapter Two describes the investigation of the high temperature atomic oxygen oxidation, as well as the decomposition, of oxide-covered silicon carbide. Chapter Three describes the investigation of the chemical and morphological changes of two representative silicone coatings, CV-1144-0 and RTV-560, as they were exposed to atomic oxygen at room temperature and 300°C, as well as the room temperature erosion yield of CV-1144-0. Chapter Four describes the investigation of how incorporation of silicon through the spraying of silicone coatings into both carbon fiber preform and the ablative TPS material Phenolic Impregnated Carbon Ablator (PICA) changed the oxidation dynamics and decomposition of these more complicated materials, and utilizes the insights gained from the beam-surface scattering dynamics and decomposition knowledge of Chapter Two and the silicone oxidation knowledge of Chapter Three. Finally, Chapter Five provides a summary and future directions for the work hereby presented.

1.5. References

1. Biamino, S.; Liedtke, V.; Badini, C.; Euchberger, G.; Huertas Olivares, I.; Pavese, M.; Fino, P., Multilayer SiC for thermal protection system of space vehicles: Manufacturing and testing under simulated re-entry conditions. *Journal of the European Ceramic Society* **2008**, *28*, 2791-2800.
2. Natali, M.; Kenny, J. M.; Torre, L., Science and technology of polymeric ablative materials for thermal protection systems and propulsion devices: A review. *Progress in Materials Science* **2016**, *84*, 192-275.
3. Opeka, M. M.; Talmy, I. G.; Zaykoski, J. A., Oxidation-based materials selection for 2000°C + hypersonic aerosurfaces: Theoretical considerations and historical experience. *Journal of Materials Science* **2004**, *39*, 5887-5904.
4. Steyer, T. E., Shaping the Future of Ceramics for Aerospace Applications. *International Journal of Applied Ceramic Technology* **2013**, *10*, 389-394.
5. Monti, R.; Pezzella, G.; Savino, R.; Paterna, D.; Esposito, A. In *Aerothermodynamic study of an advanced thermal protection system*, Hot Structures and Thermal Protection Systems for Space Vehicles, 2003; p 275.
6. Monti, R.; Fumo, M. D. S.; Savino, R., Thermal Shielding of a Reentry Vehicle by Ultra-High-Tempreature Ceramic Materials. *Journal of Thermophysics and Heat Transfer* **2006**, *20*, 500-506.
7. Hald, H., Operational limits for reusable space transportation systems due to physical boundaries of C/SiC materials. *Aerospace Science and Technology* **2003**, *7*, 551-559.
8. Monti, R.; Pezzella, G., Low Risk Re-entry Vehicles. In *12th AIAA International Space Planes and Hypersonic Systems and Technologies*, 2003.
9. Poovathingal, S.; Schwartzentruber, T. E.; Murray, V. J.; Minton, T. K., Molecular Simulation of Carbon Ablation Using Beam Experiments and Resolved Microstructure. *AIAA Journal* **2016**, *54*, 999-1010.
10. Gulbransen, E. A.; Jansson, S. A., The high-temperature oxidation, reduction, and volatilization reactions of silicon and silicon carbide. *Oxidation of Metals* **1972**, *4*, 181-201.
11. Burns, A., Structural evaluation of candidate space shuttle thermal protection systems. **1972**.
12. Marschall, J.; Pejaković, D. A.; Fahrenholtz, W. G.; Hilmas, G. E.; Panerai, F.; Chazot, O., Temperature Jump Phenomenon During Plasmatron Testing of ZrB2-SiC Ultrahigh-Temperature Ceramics. *Journal of Thermophysics and Heat Transfer* **2012**, *26*, 559-572.
13. Hu, P.; Gui, K.; Yang, Y.; Dong, S.; Zhang, X., Effect of SiC Content on the Ablation and Oxidation Behavior of ZrB2-Based Ultra High Temperature Ceramic Composites. *Materials (Basel)* **2013**, *6*, 1730-1744.
14. Johnson, S.; Gasch, M.; Stackpoole, M.; Lawson, J.; Gusman, M., Recent Developments in Ultra High Temperature Ceramics at NASA Ames. In *16th*

AIAA/DLR/DGLR International Space Planes and Hypersonic Systems and Technologies Conference, American Institute of Aeronautics and Astronautics: 2009.
15. Balat, M.; Flamant, G.; Male, G.; Pichelin, G., Active to passive transition in the oxidation of silicon carbide at high temperature and low pressure in molecular and atomic oxygen. *Journal of Materials Science* **1992**, *27*, 697-703.
16. Song, Y.; Dhar, S.; Feldman, L. C.; Chung, G.; Williams, J. R., Modified Deal Grove model for the thermal oxidation of silicon carbide. *Journal of Applied Physics* **2004**, *95*, 4953-4957.
17. Jacobson, N. S.; Myers, D. L.; Harder, B. J., Active oxidation of silicon carbide. *Materials at High Temperatures* **2012**, *29*, 193-198.
18. Jacobson, N.; Harder, B.; Myers, D., Oxidation Transitions for SiC Part I. Active-to-Passive Transitions. *J. Am. Ceram. Soc.* **2013**, *96*, 838-844.
19. Berton, B.; Bacos, M. P.; Demange, D.; Lahaye, J., High-temperature oxidation of silicon carbide in simulated atmospheric re-entry conditions. *Journal of Materials Science* **1992**, *27*, 3206-3210.
20. Deng, D.; Luo, X.; Chen, S.; Yu, J.; Ai, B., The active-to-passive oxidation transition mechanism and engineering prediction method of C/SiC composites. *Science China Technological Sciences* **2013**, *56*, 1403-1408.
21. Huang, H.; Chen, S.; Wee, A.; Chen, W., *Epitaxial growth of graphene on silicon carbide (SiC)*, 2014, p 3-26.
22. Panerai, F.; Helber, B.; Chazot, O.; Balat-Pichelin, M., Surface temperature jump beyond active oxidation of carbon/silicon carbide composites in extreme aerothermal conditions. *Carbon* **2014**, *71*, 102-119.
23. Chen, S. Y.; Boyd, I. D., Chemical equilibrium analysis of silicon carbide oxidation in oxygen and air. *Journal of the American Ceramic Society* **2019**, *102*, 4272-4284.
24. Finckenor, M.; Visentine, J.; Adam, S.; Zwiener, J.; Loebs, V. In *CONTAMINATION, UV RADIATION, AND ATOMIC OXYGEN EFFECTS ON ISS THERMAL CONTROL MATERIALS*, 41st Aerospace Sciences Meeting and Exhibit, 2003; p 1084.
25. de Groh, K. K.; McCollum, T. A., Low Earth orbit durability of protected silicone for refractive photovoltaic concentrator arrays. *Journal of Spacecraft and Rockets* **1995**, *32*, 103-109.
26. Haffke, J. E.; Woollam, J. A. In *Synergistic Degradation of CV-1144-O Due to Ultraviolet Radiation and Heat*, Dordrecht, Springer Netherlands: Dordrecht, 2003; pp 183-191.
27. Yan, L.; Gao, X.; Bungay, C.; Woollam, J. A., Study of surface chemical changes and erosion rates for CV-1144-0 silicone under electron cyclotron resonance oxygen plasma exposure. *Journal of Vacuum Science & Technology A* **2001**, *19*, 447-454.
28. Scialdone, J. J.; Clatterbuck, C. H.; Ayres-Treusdell, M.; Park, G.; Kolos, D., *Atomic Oxygen and Space Environment Effects on Aerospace Materials Flown with EOIM-III Experiment*, 1996.
29. Samwel, S. W., Low Earth Orbital Atomic Oxygen Erosion Effect on Spacecraft Materials. *Space Research Journal* **2014**, *7*, 1-13.

30. Dworak, D. P.; Banks, B. A.; Karniotis, C. A.; Soucek, M. D., Evaluation of Protective Silicone/Siloxane Coatings in Simulated Low-Earth-Orbit Environment. *Journal of Spacecraft and Rockets* **2006**, *43*, 393-401.
31. Qian, M.; Murray, V. J.; Wei, W.; Marshall, B. C.; Minton, T. K., Resistance of POSS Polyimide Blends to Hyperthermal Atomic Oxygen Attack. *ACS Applied Materials & Interfaces* **2016**, *8*, 33982-33992.
32. Minton, T. K., et al., Atomic Oxygen Effects on POSS Polyimides in Low Earth Orbit. *ACS Applied Materials & Interfaces* **2012**, *4*, 492-502.
33. De Groh, K. K.; Banks, B. A., Atomic Oxygen Erosion Data from the MISSE 2-8 Missions. **2019**.
34. Wong, H.-W.; Peck, J.; Assif, J.; Lachaud, J.; Mansour, N. N. In *Quantitative determination of species production from the pyrolysis of the Phenolic Impregnated Carbon Ablator (PICA)*, 53rd AIAA Aerospace Sciences Meeting, 2015; p 1447.
35. Bessire, B. K.; Lahankar, S. A.; Minton, T. K., Pyrolysis of Phenolic Impregnated Carbon Ablator (PICA). *ACS Applied Materials & Interfaces* **2015**, *7*, 1383-1395.
36. Bessire, B. K.; Minton, T. K., Decomposition of Phenolic Impregnated Carbon Ablator (PICA) as a Function of Temperature and Heating Rate. *ACS Applied Materials & Interfaces* **2017**, *9*, 21422-21437.
37. Panerai, F.; White, J. D.; Cochell, T. J.; Schroeder, O. M.; Mansour, N. N.; Wright, M. J.; Martin, A., Experimental measurements of the permeability of fibrous carbon at high-temperature. *International Journal of Heat and Mass Transfer* **2016**, *101*, 267-273.
38. Beck, R. A. S.; Driver, D. M.; Wright, M. J.; Hwang, H. H.; Edquist, K. T.; Sepka, S. A., Development of the Mars Science Laboratory Heatshield Thermal Protection System. *Journal of Spacecraft and Rockets* **2014**, *51*, 1139-1150.
39. Nelessen, A., et al. In *Mars 2020 Entry, Descent, and Landing System Overview*, 2019 IEEE Aerospace Conference, 2-9 March 2019; 2019; pp 1-20.
40. Roberts, G. J., The Heat is On. In *Building a Better Heat Shield for a Mars Mission*, Berkeley Lab, 2017.
41. Noda, T.; Inagaki, M.; Yamada, S., Glass-like carbons. *Journal of Non-Crystalline Solids* **1969**, *1*, 285-302.
42. Murray, V. J.; Marshall, B. C.; Woodburn, P. J.; Minton, T. K., Inelastic and Reactive Scattering Dynamics of Hyperthermal O and O2 on Hot Vitreous Carbon Surfaces. *The Journal of Physical Chemistry C* **2015**, *119*, 14780-14796.
43. Murray, V. J.; Recio, P.; Caracciolo, A.; Miossec, C.; Balucani, N.; Casavecchia, P.; Minton, T. K., Oxidation and nitridation of vitreous carbon at high temperatures. *Carbon* **2020**, *167*, 388-402.
44. Poovathingal, S.; Schwartzentruber, T. E.; Murray, V. J.; Minton, T. K.; Candler, G. V., Finite-Rate Oxidation Model for Carbon Surfaces from Molecular Beam Experiments. *AIAA Journal* **2017**, *55*, 1644-1658.
45. Swaminathan-Gopalan, K.; Borner, A.; Murray, V. J.; Poovathingal, S.; Minton, T. K.; Mansour, N. N.; Stephani, K. A., Development and validation of a finite-rate model for carbon oxidation by atomic oxygen. *Carbon* **2018**, *137*, 313-332.

46. Prata, K. S.; Minton, T.; Schwartzentruber, T. E., *Air-Carbon Ablation Model for Hypersonic Flight from Molecular Beam Data*, 2020.
47. Poovathingal, S. J.; Qian, M.; Murray, V. J.; Minton, T. K., Reactive and Inelastic Scattering Dynamics of Hyperthermal O and O2 from a Carbon Fiber Network. 2021.
48. Marshall, T. D.; Pawelko, R. J.; Anderl, R. A.; Smolik, G. R.; Merrill, B. J.; Moore, R. L.; Petti, D. A., Oxygen reactivity of a carbon fiber composite. *Fusion Engineering and Design* **2003**, *69*, 663-667.
49. McKee, D. W., Oxidation behavior of matrix-inhibited carbon/carbon composites. *Carbon* **1988**, *26*, 659-664.
50. Bessire, B. K.; Borner, A. P.; Meurisse, J. B.; Monk, J. D., Progress Towards Modeling the Mars Science Laboratory PICA-NuSil Heatshield. **2019**.
51. Lee, Y. T.; McDonald, J. D.; LeBreton, P. R.; Herschbach, D. R., Molecular Beam Reactive Scattering Apparatus with Electron Bombardment Detector. *Review of Scientific Instruments* **1969**, *40*, 1402-1408.
52. Zhang, J.; Garton, D. J.; Minton, T. K., Reactive and inelastic scattering dynamics of hyperthermal oxygen atoms on a saturated hydrocarbon surface. *The Journal of Chemical Physics* **2002**, *117*, 6239-6251.
53. Zhang, J.; Upadhyaya, H. P.; Brunsvold, A. L.; Minton, T. K., Hyperthermal Reactions of O and O2 with a Hydrocarbon Surface: Direct C−C Bond Breakage by O and H-Atom Abstraction by O2. *The Journal of Physical Chemistry B* **2006**, *110*, 12500-12511.
54. Garton, D. J.; Brunsvold, A. L.; Minton, T. K.; Troya, D.; Maiti, B.; Schatz, G. C., Experimental and Theoretical Investigations of the Inelastic and Reactive Scattering Dynamics of O(3P) + D2 *The Journal of Physical Chemistry A* **2006**, *110*, 1327-1341.
55. Garton, D. J.; Minton, T. K.; Maiti, B.; Troya, D.; Schatz, G. C., A crossed molecular beams study of the O(3P)+H2 reaction: Comparison of excitation function with accurate quantum reactive scattering calculations. **2003**, *118*, 1585-1588.
56. Troya, D.; Schatz, G. C.; Garton, D. J.; Brunsvold, A. L.; Minton, T. K., Crossed beams and theoretical studies of the O(3P)+CH4→H+OCH3 reaction excitation function. *The Journal of Chemical Physics* **2004**, *120*, 731-739.
57. Buczala, D. M.; Brunsvold, A. L.; Minton, T. K., Erosion of Kapton H® by Hyperthermal Atomic Oxygen. *Journal of Spacecraft and Rockets* **2006**, *43*, 421-425.
58. Wright, J. S.; Jones, A.; Farmer, B.; Rodman, D. L.; Minton, T. K., POSS-enhanced colorless organic/inorganic nanocomposite (CORIN®) for atomic oxygen resistance in low earth orbit. *CEAS Space Journal* **2021**.
59. Brink, G. O., Electron Bombardment Molecular Beam Detector. *Review of Scientific Instruments* **1966**, *37*, 857-860.
60. Daly, N. R., Scintillation Type Mass Spectrometer Ion Detector. *Review of Scientific Instruments* **1960**, *31*, 264-267.
61. Minton, T. K.; Giapis, K. P.; Moore, T., Inelastic Scattering Dynamics of Hyperthermal Fluorine Atoms on a Fluorinated Silicon Surface. *The Journal of Physical Chemistry A* **1997**, *101*, 6549-6555.

62. Hurst, J. E.; Becker, C. A.; Cowin, J. P.; Janda, K. C.; Wharton, L.; Auerbach, D. J., Observation of Direct Inelastic Scattering in the Presence of Trapping-Desorption Scattering: Xe on Pt(111). *Physical Review Letters* **1979**, *43*, 1175-1177.
63. Michelsen, H. A.; Auerbach, D. J., A critical examination of data on the dissociative adsorption and associative desorption of hydrogen at copper surfaces. *The Journal of Chemical Physics* **1991**, *94*, 7502-7520.
64. Murray, V. J.; Smoll, E. J.; Minton, T. K., Dynamics of Graphite Oxidation at High Temperature. *The Journal of Physical Chemistry C* **2018**, *122*, 6602-6617.

CHAPTER TWO

OXIDATION OF SILICON CARBIDE THROUGH THE PASSIVE-TO-ACTIVE TRANSITION

Contribution of Authors and Co-Authors

Manuscript in Chapter 2

Author: David Z. Chen

Contributions: Assisted in conducting and collecting experimental data using hyperthermal beam. Analyzed all scattering data. Wrote and edited the manuscript.

Author: Chenbiao Xu

Contributions: Conducted hyperthermal beam-surface scattering and collected data. Assisted in analyzing hyperthermal beam-surface scattering data.

Author: Vanessa J. Murray

Contributions: Assisted with XPS analysis on samples used for hyperthermal beam experiment. Conducted and collected experimental data using continuous supersonic beam. Assisted in analyzing continuous beam scattering data.

Author: Timothy K. Minton

Contributions: Assisted with analysis and editing of the manuscript for final submission.

Manuscript Information

David Z. Chen, Chenbiao Xu, Vanessa J. Murray, Timothy K. Minton

The Journal of Chemical Physics

Status of Manuscript:
_x__ Prepared for submission to a peer-reviewed journal
____ Officially submitted to a peer-reviewed journal
____ Accepted by a peer-reviewed journal
____ Published in a peer-reviewed journal

AIP Publishing

2.1. Introduction

Hypersonic vehicles traveling through the atmosphere can often reach velocities approaching 7.8 km s^{-1}. While traversing this environment, these high velocities combined with the air density can lead to aerodynamic heating where the skin friction caused by parasitic drag can raise the temperatures of these vehicles' surfaces up to over 2000 °C.[2-3] In these conditions, a shock layer forms in front of the vehicle that can dissociate incoming gas molecules into their highly reactive monoatomic species, notably oxygen and nitrogen.[65] After dissociating, these species then travel through the underlying boundary layer before colliding with the vehicle's surface at around 4 km s^{-1}.[9] Atomic oxygen (AO) species are particularly responsible for much of the degradation on the surface of the vehicle.

In order to protect vehicles traveling through these extreme environmental conditions, thermal protection systems (TPS), materials designed to thermally insulate the vehicle from these extreme temperatures, are used. A class of TPSs called Ultra-High Temperature Ceramics (UHTCs) are currently being investigated for these environments.[4] With very high melting points, the ability to resist chemical attack from reactive oxygen species, and designs for reusability, UHTCs are a promising new material for these applications. Key to these materials is the addition of silicon carbide (SiC) as a component of the composite.[66] Unlike a TPS material primarily composed of carbon, which will form volatile CO and CO_2 when in contact with oxygen,[9, 42] thus degrading the material, silicon carbide will instead form a protective oxide layer on its surface.[18] The formation of this oxide layer on SiC, called passive oxidation, provides effective protection for the

remainder of the material, preventing further degradation from oxygen attack (**Table 2-1(a)**).[67]

However, at the high temperatures experienced in hypersonic velocities, the oxidation of silicon carbide can undergo a transition from a passive to an active mode, a transition that will form volatile SiO rather than solid SiO_2 (**Table 2-1(b)**).[68] This passive-to-active oxidation transition (PAT) is a major concern for the design of SiC-containing reusable TPS materials, as this can result in erosion that will shorten the lifetime of these materials. Previous studies investigating the PAT found that this change occurred at temperatures ranging from 1500 K to 1700 K for molecular oxygen pressures in the 10^{-4} to 10^{-5} bar range.[17] Jacobson et al. (2012)[17] has proposed a number of reaction mechanisms processes that could occur during this transition (**Table 2-1(c-e)**).

Table 2-1. Table of important mechanisms for SiC. **(a)** and **(b)** represent passive and active oxidation, respectively.[18] **(c)**, **(d)**, and **(e)** are proposed mechanisms by Jacobson et al.[17] **(f)** represents the sublimation of silicon from bulk silicon carbide.[69-70]

(a)	$2SiC(s) + 3O_2(g) \rightarrow 2SiO_2(s) + 2CO(g)$
(b)	$SiC(s) + O_2(g) \rightarrow SiO(g) + CO(g)$
(c)	$SiC(s) + 2SiO_2(s) \rightarrow 3SiO(g) + CO(g)$
(d)	$SiC(s) + SiO_2(s) \rightarrow 2SiO(g) + C(s)$
(e)	$2SiC(s) + SiO_2(s) \rightarrow 3Si(l, s) + 2CO(g)$
(f)	$SiC(s) \rightarrow Si(g) + C(s)$

In the absence of oxygen and under vacuum conditions, when silicon carbide is heated up to very high temperatures in the 2000 K range, it will undergo a process first discovered by Edward Acheson[71] whereby the C-Si bond breaks and the silicon sublimes into monoatomic gaseous silicon, leaving behind graphitic carbon (**Table 2-1(f)**). This is a process well-known to semiconductor and graphene manufacturers.[69, 72-73] Under

conditions where the volatile silicon is allowed to leak out of the chamber, very high quality graphene can be formed on the surface.[69] This process of graphitization can be further controlled through the use of a silicon beam.[74] An oxide layer on the SiC surface can complicate the surface chemistry, however. A number of studies so far have been conducted on the decomposition of silica on the surface of a silicon wafer,[75-78] though fewer have so far investigated silica decomposition on the surface of SiC.[17, 79]

While the molecular oxygen oxidation of SiC through the PAT temperature is well-characterized and understood,[15, 17-18] fewer studies have been conducted using atomic oxygen. Some studies have been conducted on SiC/carbon fiber composites exposed in atomic oxygen plasma wind tunnels, however. These studies have consistently observed spontaneous temperature jumps during conditions of high heat flux and low pressure, dissociated flows.[22, 80-81] These studies found the temperature jump to occur above the PAT temperature, a phenomenon Panerai et al.[22] attributed to be related to the transition, while Luo et al.[81] attributed the jump they observed to the loss of the SiC component, leaving the underlying carbon fibers exposed. One theoretical thermodynamic study has already been produced investigating this jump, but there are still uncertainties in their investigations.[23] To further understand the molecular-level interactions between specifically atomic oxygen and silicon carbide, as well as to clarify this observed temperature jump, we have conducted an investigation using a well-characterized hyperthermal atomic oxygen molecular beam gas-surface scattering apparatus. While previous studies have used techniques such as O-atom plasma torches,[82] mass loss measurements,[22, 83] and *in-situ* temperature measurements[22, 81] to determine the processes present as the SiC passes

through the transition point during oxidation, the study presented here used mass spectrometry analysis in order to measure *in-situ* nonreactive and reactive product scattering using a well-characterized neutral atomic oxygen beam.

2.2. Materials and Methods

2.2.1. Hyperthermal Beam-Surface Scattering Experimental Design

The setup for the hyperthermal beam-surface scattering apparatus has been described in detail in a previous publication.[64] These experiments were conducted with the use of a crossed molecular beams apparatus reconfigured for beam-surface scattering.[51-53] A pulsed molecular beam composed of high translational energy O and O_2 was directed at an (α)6H-SiC wafer, conductively heated with a strip of resistively heated vitreous carbon (Grade 22 SPI-Glas obtained from Structure Probe, Inc.) of equal size placed behind the SiC strip away from the beam and detector, a technique utilized in a previous experiment,[64] at an incidence angle $\theta_i = 45°$ as measured from the surface normal. Products exiting the surface can be detected at a variety of final angles, θ_f, from the opposite side of the surface normal from the incident beam by a mass spectrometer detector that rotates within the plane defined by the incident molecular beam axis and the surface normal. The detector itself consists of an electron impact ionizer,[59] quadrupole mass filter, and a Daly type ion counter operated in pulse counting mode,[60] with the entire detector triply differentially pumped with ion pumps. A multichannel scaler recorded the electrical pulses produced by the Daly detector that were correlated with ion impacts, yielding a signal proportional to the number density of the scattered products as a function of the flight time from the surface to the

ionizer of the detector, N(t), which were 34.4 cm apart. Also known as time-of-flight (TOF) distributions, these number density distributions as a function of the flight time can be used to derive translational energy distributions, $P(E_T)$, of the scattered products with the use of a density-to-flux conversion that assumes a monoenergetic incident beam.[52, 61] The average energies of the scattered products are determined from the $P(E_T)$ distributions. The $P(E_T)$ distribution obtained for each TOF distribution was integrated to obtain the total relative flux of the scattered products at a particular θ_f. Flux angular distributions were obtained by plotting the flux of the scattered products as a function of θ_f.

A laser detonation source, described in detail previously,[54] was used to produce the molecular beam of high translational energy $O(^3P)$[55] and $O_2(^3\Sigma_g^-)$.[56] The TOF distributions, corresponding $P(E_T)$ distributions, and relative fluxes of O and O_2 in the incident beam were determined by lowering the sample out of the beam path and directing the beam into the detector. The molecular beam, operating at a frequency of 2 Hz, was velocity-filtered with a synchronized chopper wheel that had three equally spaced 1.6 mm-thick slots and a rotation frequency of 300 Hz. Prior to analysis, the dissociative ionization of O_2 was subtracted from the TOF distribution for O. The mean translational energy of O was 484 kJ mol^{-1} with an energy width (full width at half-maximum, fwhm) of 62.7 kJ mol^{-1}. The O_2 had a mean translational energy of 967 kJ mol^{-1} and a fwhm energy width of 99.1 kJ mol^{-1}. The mole fractions of O and O_2 in the beam were 97% and 3%, respectively (**Fig. 2-1**).

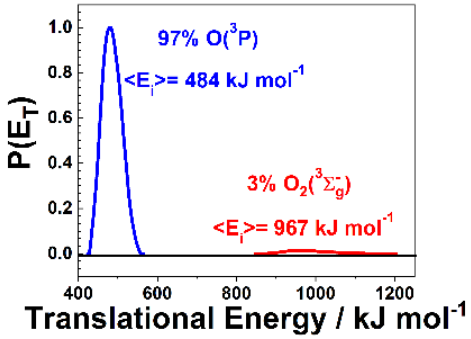

Fig. 2-1. Translational energy distributions of hyperthermal O-atom beam. The O curve has been normalized to 1.0, and the area of the O_2 curve reflects the relative mole fraction of O_2 in the beam compared to O.

2.2.2. Sample Preparation and Surface Analysis

6H-silicon carbide wafers were obtained from Precision Micro-Optics Inc. and diced into dimensions of 25 mm x 7 mm x 0.430 mm. The surface temperature of the SiC sample was measured using an optical pyrometer.[47] O-atom beam scattering was performed on both a pristine silicon carbide surface and a SiC surface pretreated with exposure to atomic oxygen. Since a more realistic SiC surface entering the atmosphere would have an oxide layer due to exposure to oxygen either in the air or in space, and because the PAT involves a change in the oxidation chemistry from production of SiO_2 to that of SiO,[17-18, 68] an oxide layer was grown on the SiC surface in order to better represent realistic conditions. Thus, several SiC wafers were pretreated with an atomic oxygen exposure of ~2 x 10^{20} O-atoms cm^{-2} fluence in the atomic oxygen source chamber using a technique previously deployed,[84] producing ~5 nm thick oxide layers (Eq. 2-1 below).

$$SiC(s) + 3O(g) \rightarrow SiO_2(s) + CO(g) \qquad \text{(Eq. 2-1)}$$

The surface chemistries of the pristine and pretreated silicon carbide wafers were verified using X-ray Photoelectron Spectroscopy (XPS), with results showing nearly no oxygen on

the pristine SiC and a large amount of oxygen on the oxidized sample, along with a shift in the Si2p XPS peaks to that of an SiO_2 environment (**Fig. 2-2**). Additional SiC wafers with 100 nm thick oxide layers were also acquired. These 100 nm thick oxide samples were acquired specifically to enhance the signal coming from the surface as it was heated up.

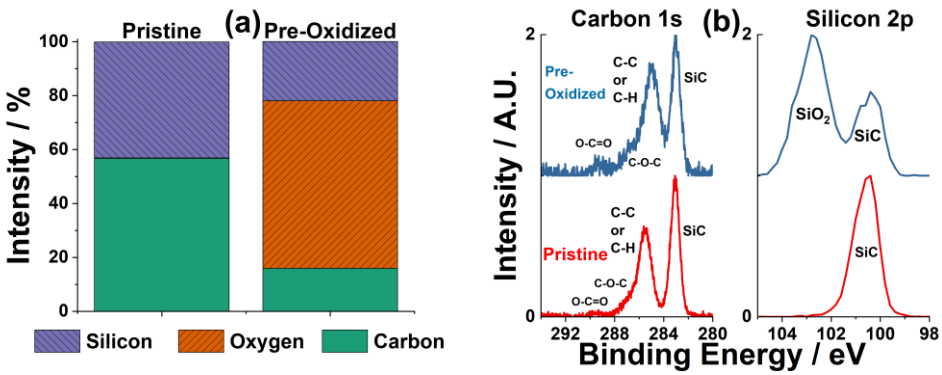

Fig. 2-2. XPS results of pristine and atomic oxygen pretreated SiC. **(a)** Percent chemical composition and **(b)** chemical bonding environments.

2.2.3. Temperature Dependence of Surface Reactivity with Hyperthermal Beam

The effect of surface temperature on the reactivity of the surface was investigated on SiC and oxidized SiC wafers over a range of temperatures for fixed incidence and final angles (θ_i = 45° and θ_f = 60°, 45°, 30°, and 10°). For both types of wafers, temperature was initially raised to 1123 K, incremented to 1273 K, and from there the surface temperature was increased in 100 K increments until a temperature of 1973 K was reached, after which temperature was decreased in 100 K steps to 1273 K, and then finally to 1123 K again. At each temperature, TOF distributions were collected for mass-to-charge ratios (*m/z*) of 16 (O^+), 32 (O_2^+), 28 (CO^+ or Si^+), and 44 (CO_2^+ or SiO^+) for 200, 200, 1000, and 500 beam pulses, respectively. TOF distributions for *m/z* = 28 and 44 were only collected at θ_f = 45° and 10°, while TOF distributions for *m/z* = 16 and 32 were collected for all four final angles.

m/z = 60 (SiO_2^+) was investigated but not observed in these scattering experiments. Only TOF distributions and fluxes at θ_f = 45° and 10° will be shown in this study. At each temperature, there was a hold time of roughly 40 minutes during which TOF distributions were collected at the various *m/z* ratios. Data were collected for one full cycle, from 1123 K to 1973 K, and from 1973 K to 1123 K, with the entire cycle covering around 18 hours. After the experiment, the SiC wafer was removed at ambient temperature and pressure and examined by XPS and Raman spectroscopy.

2.2.4. Dynamics Below and Above Passive-to-Active Oxidation Transition Temperature

The angle-dependent scattering dynamics of reactive and nonreactive products from oxidized SiC were studied in detail for surface temperatures directly below and above the passive-to-active oxidation transition temperature, at 1473 and 1973 K, and for fixed incident angle θ_i = 45°. TOF distributions were collected over the full range of accessible θ_f angles for *m/z* = 16 (O^+), 32 (O_2^+), 28 (CO^+), and 44 (CO_2^+). At 1473 K, θ_f was varied sequentially in 5° increments from 5° to 85°, and then from 85° to 5°, while at 1973 K, θ_f was varied in 2.5° increments from 5° to 85°, then from 85° to 5°. Analysis was conducted on the summed TOF distributions for each *m/z* at a given θ_f. For both *m/z* = 16 (O^+) and 32 (O_2^+), TOF distributions were collected for a total of 3400 pulses at 1473 K and 6800 pulses at 1973 K for each mass. For *m/z* = 28 and 44, TOF distributions were collected at 1973 K for a total of 17000 pulses and 8500 pulses, respectively. Prior to analysis, the summed TOF distributions for O was corrected for the dissociative ionization of O_2.

2.2.5. Oxide-layer Decomposition

To investigate how the oxide layer decomposes during the PAT without any O-atom exposure facilitating the process, another experiment was conducted with the beam-surface scattering apparatus without use of the O-atom beam. A special SiC wafer coated with a 100 nm silicon-oxide layer was installed onto the high-temperature sample mount with the rotatable mass spectrometer detector set to measure spectra at $\theta_f = 10°$ from the sample's surface normal. The mass spectrometer settings scanned a range of $m/z = 8$ to 65, with a dwell time of 10 ms for every $m/z = 0.1$ increment, and thus a rate of one full scan for every 5.7 s. Before the scan, several background scans of the main chamber were taken. The sample temperature was raised to 1573 K, and then raised at a rate of 0.56 K/s until reaching 1973 K, while mass spectra were collected every 5.7 s in this interval. Backgrounds were then subtracted from the mass spectra, and peak analysis was conducted using OriginPro 2019.

2.2.6. Beam-Surface Scattering with Continuous Supersonic AO Beam Source

Additional beam-surface scattering experiments were conducted using an RF-plasma source based supersonic continuous atomic oxygen beam apparatus located in Perugia, Italy. Modifications to this apparatus are described in Murray et al. (2020),[43] and this experiment was conducted under a nearly identical setup as that using the hyperthermal beam, with only one fixed incident and one fixed final angle ($\theta_i = 60°$; $\theta_f = 15°$). As with the pulsed beam, a wafer of vitreous carbon was placed behind the silicon carbide to heat it. Unlike the hyperthermal source described above, this continuous atomic oxygen beam source produces much higher O-atom flux with much lower supersonic velocities. This

higher flux allowed investigation into how differences in atomic oxygen flux affects the reactive scattering chemistry of silicon carbide. The mean translational energy of O was 38.5 kJ mol^{-1} with a full width at half-maximum (fwhm) of 31 kJ mol^{-1}. The O_2 had a mean translational energy of 65.3 kJ mol^{-1}, with a fwhm of 56.7 kJ mol^{-1}. The mole fraction of O to O_2 in the beam was 1:1 (**Fig. 2-3**).

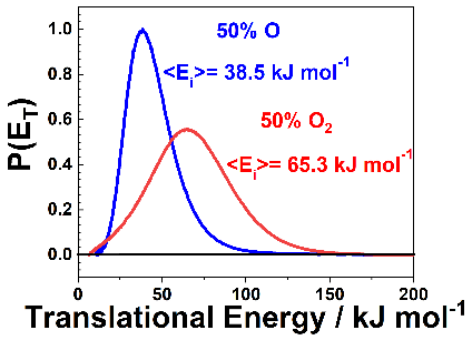

Fig. 2-3. Translational energy distributions of the supersonic O-atom beam. The O curve has been normalized to 1.0, and the area of the O_2 curve reflects the relative mole fraction of O_2 in the beam compared to O.

The effect of surface temperature on the reactivity of the surface using the continuous supersonic beam was investigated on a pristine SiC wafer over the temperature range 1073 K to 1773 K. The surface temperature of the SiC was initially raised to 1073 K, then increased in 100 K increments until a temperature of 1773 K was reached. TOF distributions were collected for mass-to-charge ratios (*m/z*) of 16 (O^+), 32 (O_2^+), 28 (CO^+ or Si^+), and 44 (CO_2^+ or SiO^+) with 50,000 shots passing through the chopper wheel for each temperature going up and down. Additional higher-resolution TOF distributions for *m/z* = 44, 45, and 46 were collected at 1773 K with 300,000 shots. *m/z* = 29, 30, and 60 were not investigated for this experiment. After the TOF distributions at 1773 K were

collected, the sample temperature was decreased, first to 1673 K, then to 1573 K, with TOF distributions from *m/z* = 16, 32, 28, and 44 again collected for both temperatures.

2.3. Results and Analysis

2.3.1. Beam-Surface Interaction Mechanisms and Their Scattering Signatures

Products were observed leaving the silicon carbide surface at *m/z* = 16, 32, 28, and 44, corresponding to either no net reaction in the case of 16 and 32 (O and O_2), or reaction and/or abstraction in the case of 28, 32, and 44 (CO and/or Si; O_2; CO_2 and/or SiO). The TOF distributions for all scattered products are considered in terms of two limiting cases: impulsive, or inelastic, scattering (IS), and thermal desorption (TD).[61-62] IS atoms or molecules undergo one or a few collisions with the surface and transfer little energy before exiting the surface on a time scale too short for thermal equilibrium to be established. Therefore, the IS products retain much of their initial kinetic energies and appear at short flight times in the TOF distributions. In contrast, TD atoms or molecules exchange a significant amount of energy with the surface through multiple collisions, physisorption, or even chemisorption, before coming into thermal equilibrium with the surface, followed by desorption. TD atoms or molecules have relatively low kinetic energies that are determined by the surface temperature, and they generally appear as a broad feature in a TOF distribution at longer flight times compared to IS products. If the desorption process has no barrier above the adsorption potential energy well, then the TD products typically have a Maxwell-Boltzmann (MB) distribution of translational energies given by the surface temperature. However, if such a barrier exists, then the low-energy products will be

suppressed, and the TD products will have a translational energy distribution that has a higher average energy than predicted by an MB distribution at the surface temperature.[85]

2.3.2. Temperature Dependence of Products of Hyperthermal O-atom Scattering

The effect of surface temperature on the fluxes of the scattered products from oxidized SiC and their TOF distributions are shown in **Fig. 2-4**, **Fig. 2-5**, and **Fig. 2-6**. For $\theta_f = 45°$ the $m/z = 16$ TOF distributions shown in **Fig. 2-5** are bimodal, with the first peak corresponding to IS and the second corresponding to TD. At 1673 K, a large reduction in $m/z = 16$ flux was observed, but returned to previous levels by 1873 K. A correspondingly large increase in O_2 flux was observed at 1673 K, remaining at elevated levels for the remainder of the experiment. As the $m/z = 16$ plot in **Fig. 2-5** shows, the second peak corresponding to increased TD signal did not appear until 1673 K and began to fade away as the temperature was reduced to 1123 K. For the reactive scattering products at $m/z = 28$ and 44 from $\theta_f = 45°$, very little flux was observed until 1673 K, at which point the $m/z = 28$ flux increased, maximizing at 1773 K before disappearing again as the sample was increased to 1973 K and lowered from there. The $m/z = 44$ flux reached a maximum at 1673 K. For $m/z = 28$ at 1773 K, an extremely long tail also appeared. As temperature was reduced to 1123 K, flux for both $m/z = 28$ and 44 rose again.

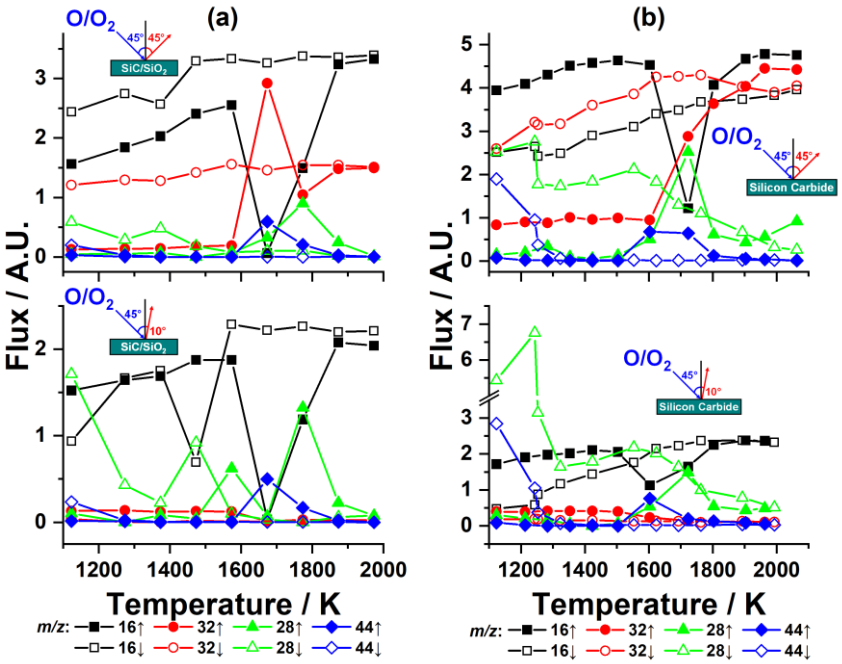

Fig. 2-4. Fluxes of scattered products as a function of temperature following bombardment of SiC/SiO_2 and pristine SiC with the hyperthermal O/O_2 beam at an angle of incidence, θ_i = 45°. **(a)** are fluxes from SiC/SiO_2. **(b)** are fluxes from pristine SiC. Hyperthermal O/O_2 beam described in **Fig. 2-1**. **(top)** θ_f = 45°. **(bottom)** θ_f = 10°.

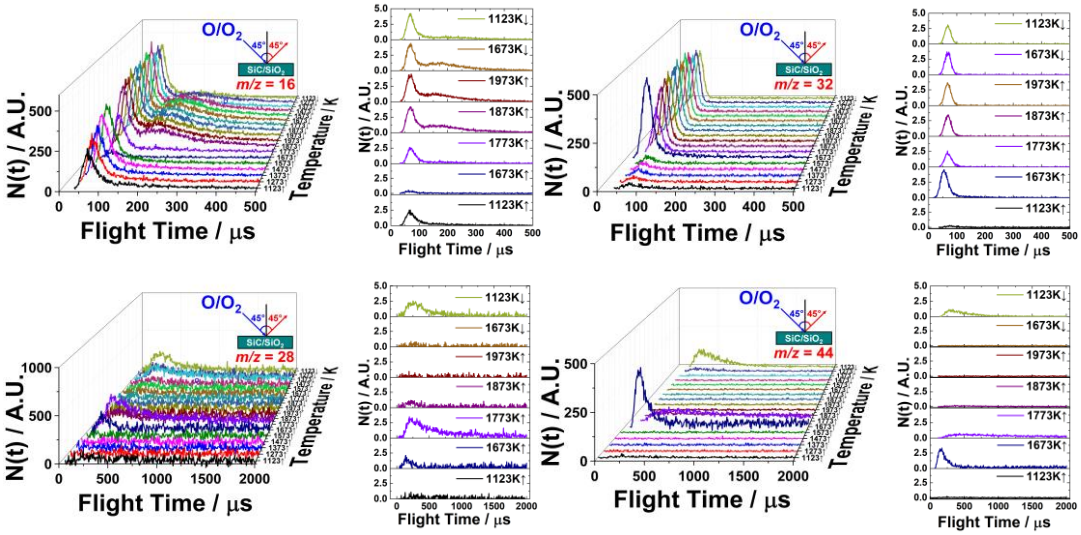

Fig. 2-5. TOF distributions, collected with surface temperatures from 1123 to 1973 K, for the four scattered products observed following bombardment of the SiC/SiO_2 surface with the hyperthermal O/O_2 beam described in **Fig. 2-1**, at an angle of incidence, θ_i = 45° and a final angle, θ_f = 45°. The up arrows represent the temperature increasing, while down arrows represent the temperature decreasing.

For θ_f = 10°, the *m/z* = 16 flux decreased at 1673 K as temperature increased (**Fig. 2-4(a, bottom)**), returning and remaining at elevated levels again as temperature reached 1873 K. These trends are similar to those observed for *m/z* = 16 flux from θ_f = 45°. However, *m/*z = 32 flux exhibited different trends from that at θ_f = 10°, with its flux decreasing nearly to zero once the temperature reached 1773 K and remaining low as the sample was decreased back down to 1123 K. Within the *m/z* = 16 TOF distribution from θ_f = 10° (**Fig. 2-6**), above 1673 K the main peak irreversibly shifted to a longer flight time, remaining at this position even as the temperature was decreased down to 1123 K. For *m/z* = 28 from θ_f = 10°, similar to trends from θ_f = 45°, there was again negligible flux until the temperature reached 1673 K, reaching a maximum at 1773 K before decreasing again. For *m/z* = 44, also like trends from θ_f = 45°, its flux reached a maximum at 1673 K and produced a long tail at 1773 K. As with the trends at θ_f = 45°, the flux of *m/z* = 28 and 44 increased again as the temperature was decreased to 1123 K. At 1473 K as temperature was decreased, there was also a large reduction in the O-atom flux along with a corresponding increase in the flux of *m/z* = 28, an anomalous results for which we do not have a ready explanation.

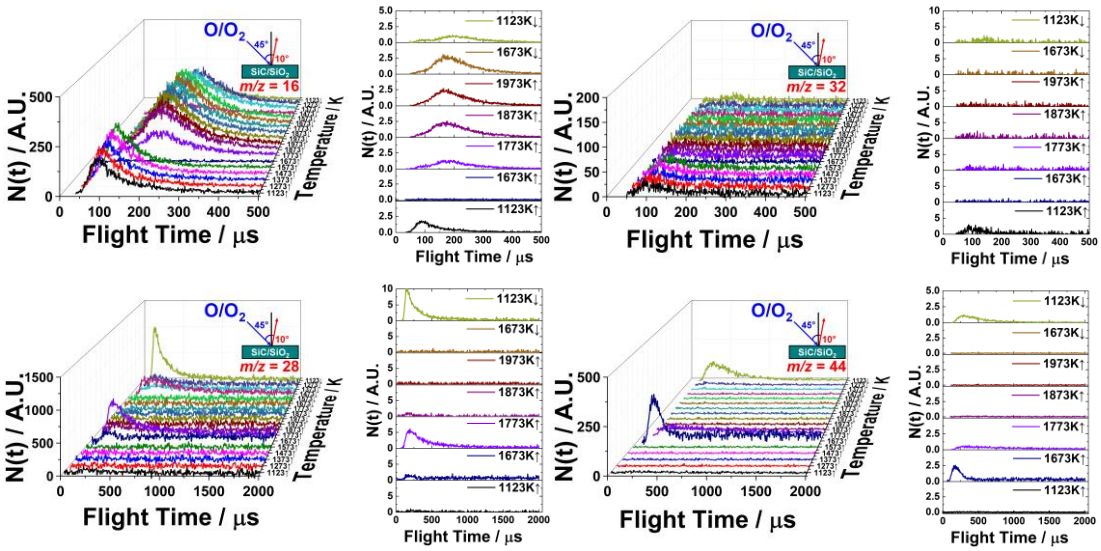

Fig. 2-6. TOF distributions, collected with surface temperatures from 1123 to 1973 K, for the four scattered products observed following bombardment of the SiC/SiO_2 surface with the hyperthermal O/O_2 beam described in **Fig. 2-1**, at an angle of incidence, $\theta_i = 45°$ and a final angle, $\theta_f = 10°$. The up arrows represent the temperature increasing, while the down arrows represent the temperature decreasing.

Qualitatively similar temperature trends were observed in the scattered product flux from pristine silicon carbide (**Fig. 2-4(b)**). The primary difference between the oxidized and pristine temperature-dependent fluxes was a much higher production of $m/z = 28$ products as temperature decreased from the pristine SiC. The drop in $m/z = 16$ and rise in $m/z = 28$ at 1473 K from $\theta_f = 10°$ as temperature decreased was not observed in the pristine SiC results, which further suggests this phenomenon was an anomalous occurrence. XPS analysis of the oxidized silicon carbide heated and exposed to O-atoms (**Fig. 2-7**) showed a large increase in surface carbon composition, along with very small amounts of residual silicon and oxygen remaining. The peaks in the XPS spectra of the wafer showed a shift to that of graphitic carbon, while the silicon 2p peak indicated some possible silicon

oxycarbide presence.[86-88] Raman analysis of the silicon carbide sample also confirmed the presence of graphitic carbon (**Fig. 2-8**).

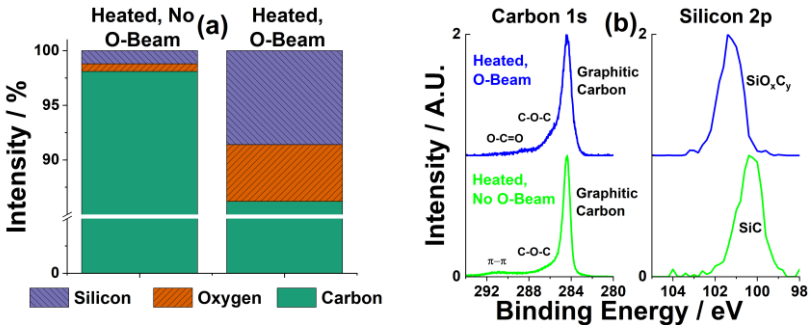

Fig. 2-7. XPS results of SiC heated above 1673 K with and without exposure to O-atom beam. **(a)** percent chemical composition. **(b)** chemical bonding environments.

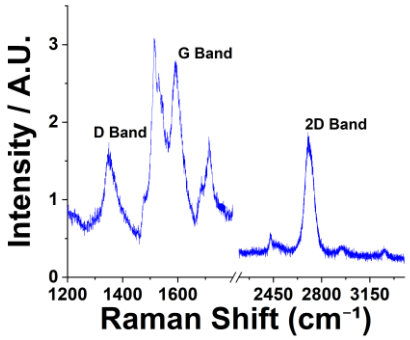

Fig. 2-8. Results from Raman analysis of silicon carbide that was heated during O-atom bombardment, showing characteristic peaks representative of graphitic carbon.

2.3.3. O and O_2 Scattering Dynamics at 1473 and 1973 K

Because reactive product formation was observed as temperature reached 1673 K, this temperature was thus used as the reference point for the PAT temperature. Flux angular distributions were collected below and above this temperature. At 1473 K, the m/z = 16 TOF distributions can be fitted with IS and TD curves at every θ_f, indicating that O-atoms exit the silicon carbide surface through both IS and TD channels. Representative TOF

distributions for O-atoms at surface temperatures of 1473 K and θ_f = 75°, 45°, and 15° are shown in **Fig. 2-9(a)**. The IS and TD components were separated by fitting the component at longer flight times with an MB distribution of flight times characterized by the surface temperature and subtracting the fit from the total signal intensity, which yielded the IS distribution. The O-atoms primarily exited the surface through the IS channel, with the fwhm and θ_{max} being 46.1° and 60°, respectively (**Fig. 2-9(c)**). The TD angular distributions showed characteristic $\cos^x(\theta)$ distributions typical of Maxwell-Boltzmann desorption from the surface, with the TD distribution fit to an x = 2.5 power and the TD maximum toward the surface normal (**Fig. 2-9(d)**). As for m/z = 32(O_2), its TOF distributions appeared to show only IS products exiting the surface (**Fig. 2-9(b)**), with the fwhm and θ_{max} being 40.9° and 65°, respectively (**Fig. 2-9(e)**). Integrating the total flux at all measured angles within the detector rotation plane, the flux ratio of O/O_2 was found to be 12.4.

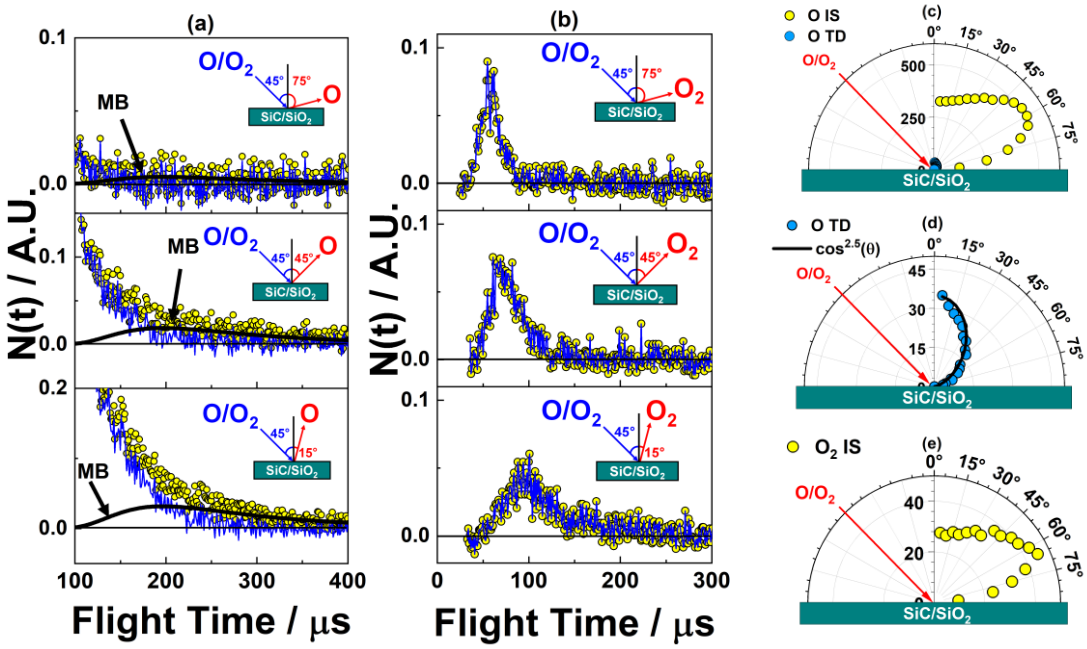

Fig. 2-9. Representative TOF distributions for O and O_2 species exiting the SiC/SiO_2 surface at θ_f = 15°, 45°, and 75°, following bombardment by the hyperthermal O/O_2 beam pulse at θ_i = 45° for a surface temperature of 1473 K, as well as flux angular distributions at a multitude of final angles. **(a, b)** For the TOF distributions total values for number density, nonthermal scattering (IS), and thermal desorption (TD) are represented by yellow, blue, and black colors, respectively. The thick black lines represent the fits of the thermal desorption (TD) components using an MB distribution. **(c)** represents the IS and TD angular distributions of O-atoms from SiC/SiO_2. **(d)** represents the TD angular distribution in **(c)** zoomed in. **(e)** represents the IS distribution of O_2 from SiC/SiO_2. No TD signal was fit from the O_2 TOF distribution.

At 1973 K, a significant narrowing of the IS scattering distribution was observed in both *m/z* = 16 (O) and *m/z* = 32 (O_2) species exiting the surface (**Fig. 2-10(c, d)**). The fwhm of the angular distributions are 22.4° and 19.1°, while θ_{max} are 55° and 57.5°, for O and O_2, respectively. Like at 1473 K, the O_2 TOF distributions at 1973 K do not indicate the presence of any TD scattered products (**Fig. 2-10(b)**). However, for O-atom desorption at 1973 K, the TD components are not fit well by a normal MB distribution. At all angles measured, the arrival times of the TD component are shorter than those predicted by a MB

distribution (black curved line, **Fig. 2-10(a)**). These desorption channels, referred to as TD_{fast}, have average translational energies greater than $2RT_s$. In order to properly fit these TOF distributions, a flux-weight fitting procedure described by Michelson and Auerbach (1991)[63] and utilized by Murray et al. (2018)[64] to fit O-atom scattering from highly-oriented pyrolytic graphite, was used. Using this fit, the new TD_{fast} angular distribution showed characteristic $\cos^x(\theta)$ distributions typical of Maxwell-Boltzmann desorption from the surface, where x = 2.2 here, and with the maximum pointed towards the surface normal (**Fig. 2-10(c)**). Integrating the total flux at all measured angles, the O/O_2 ratio was found to be 2.5, a significant reduction from the ratio at 1473 K, 12.4.

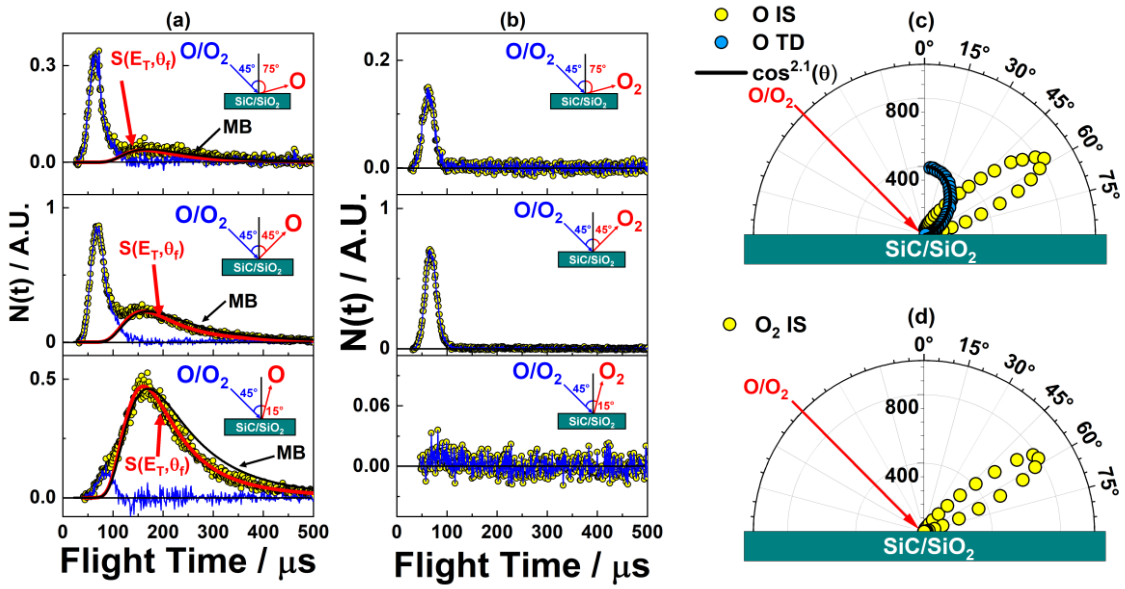

Fig. 2-10. Representative TOF distributions for O and O_2 species exiting the SiC/SiO_2 surface at θ_f = 15°, 45°, and 75°, following bombardment by the hyperthermal O/O_2 beam pulse at θ_i = 45° for a surface temperature of 1973 K, along with flux angular distributions at a multitude of final angles. **(a, b)** Total values for number density, nonthermal scattering (IS), and thermal desorption (TD) are represented by yellow, blue, and red colors, respectively. The red lines represent the fits of the thermal desorption (TD) components using $S(E_T,\theta_f)$. The thick black lines represent the corresponding Maxwell-Boltzmann distribution fits for each angle at 1973 K. **(c)** represents the IS and TD angular distributions of O-atoms from SiC/SiO_2. **(d)** represents the IS angular distribution of O_2 from SiC/SiO_2. No TD signal was fit from the O_2 TOF distribution.

2.3.4. Results of Scattering Products Using the Continuous Supersonic Beam

The effect of surface temperature on the measured flux of the scattered products from the continuous beam is shown in **Fig. 2-11**. As the temperature approached 1773 K, O and O_2 flux slightly decreased, and as temperature was reduced back down to 1573 K, flux rose again but remained low compared to the flux at 1573 K as temperature was increased. The reduction in flux of *m/z* = 16 and 32 are reflected in the temperature-dependent TOF distribution plots in **Fig. 2-12**. This reduction in flux was also accompanied by a shift in the main peaks of these *m/z* ratios' TOF distributions, with peaks for both *m/z*

= 16 and 32 shifting to a longer flight time (**Fig. 2-13(a, b)**). These shifts were also not irreversible, with the peaks shifting back to a shorter flight time as the temperature returns to 1573 K. *m/z* = 28 and 44 fluxes were relatively constant until reaching 1773 K, at which point their signal could be detected. As temperature was decreased to 1573 K, their flux remained elevated compared to their fluxes as temperature increased. Importantly, unlike with the low-flux pulsed beam experiment, products continued to be observed at these two mass-to-charge ratios, allowing for further analysis of their TOF distributions.

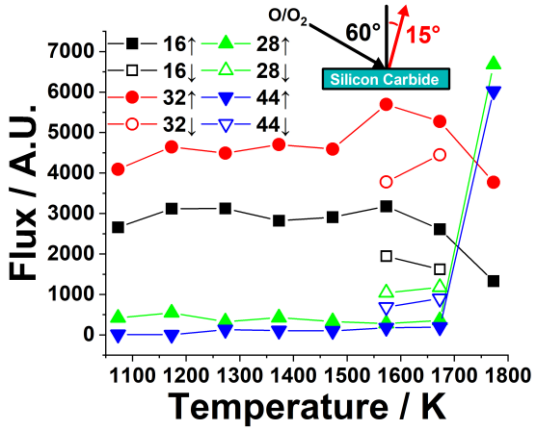

Fig. 2-11. Flux of scattered products as a function of temperature following bombardment of pristine silicon carbide with the supersonic O/O_2 beam at an angle of incidence, $\theta_i = 60°$, and a final angle, $\theta_f = 15°$. Beam described in **Fig. 2-3**.

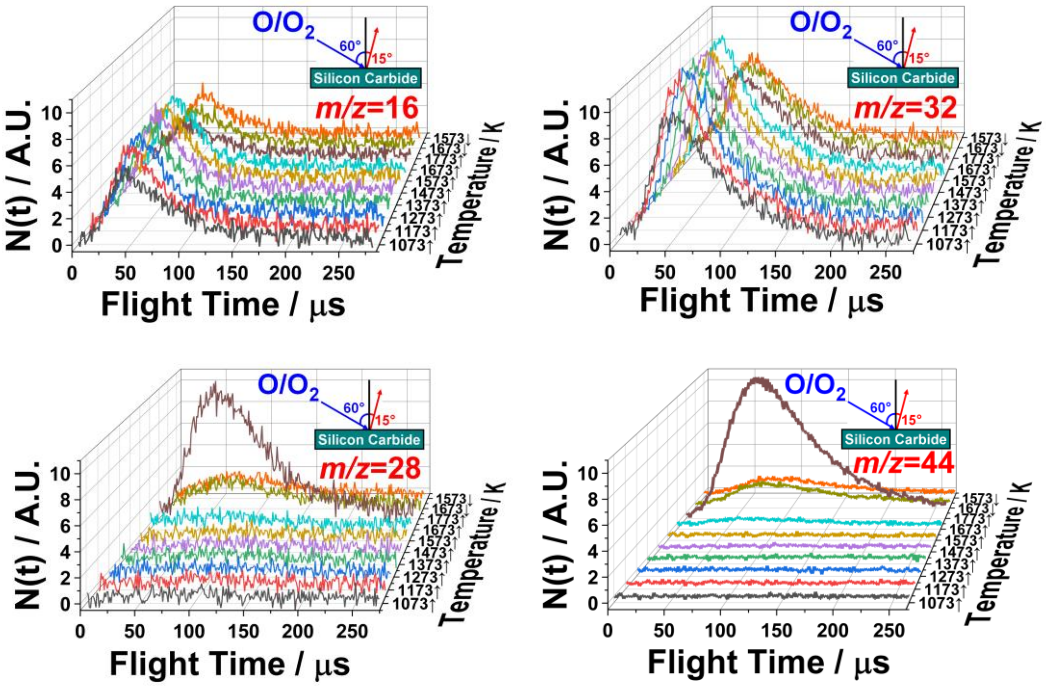

Fig. 2-12. TOF distributions, collected with surface temperatures from 1023 to 1773 K, for the four scattered products observed following bombardment of the silicon carbide surface with the supersonic O/O_2 beam at an angle of incidence, θ_i = 60° and a final angle, θ_f = 15°. Beam described in **Fig. 2-3**.

At 1773 K the temperature was held while products were observed at *m/z* = 16, 28, 32, and 44. Higher resolution TOF distributions were also collected for *m/z* = 44, 45, and 46. Representative TOF distributions for all these products are shown in **Fig. 2-13**. Because neither full angular distributions nor multiple incident angle scattering was conducted, the only attempted fit for these TOF distributions are their representative MB distributions. While a detailed fit was not attempted, the TOF distributions for O and O_2 do show a shift in the main peak from one consisting primarily of IS signal to one more resembling an MB distribution as the temperature approaches 1773 K (**Fig. 2-13(a, b)**). As stated above, these shifts were reversible, with the peaks returning to a fit resembling IS again as the

temperature was lowered back to 1573 K. The MB distribution fit the O-atom TOF distribution relatively well, but the O_2 TOF distribution was slightly shifted from where the MB distribution would be fit. As the TOF distributions collected at 1773 K demonstrate (**Fig. 2-13(c)**), near stoichiometrically equal production of *m/z* = 28 and 44 was observed, and the higher resolution TOF distributions (**Fig. 2-13(d)**) collected for *m/z* = 44, 45, and 46 showed product percentages very similar to the isotopic ratios of silicon. Further experiments with the continuous beam were not undertaken, but nevertheless, active oxidation was observed (Eq. 2-2 below).

$$SiC(s) + 2O(g) \rightarrow SiO(g) + CO(g) \qquad \text{(Eq. 2-2)}$$

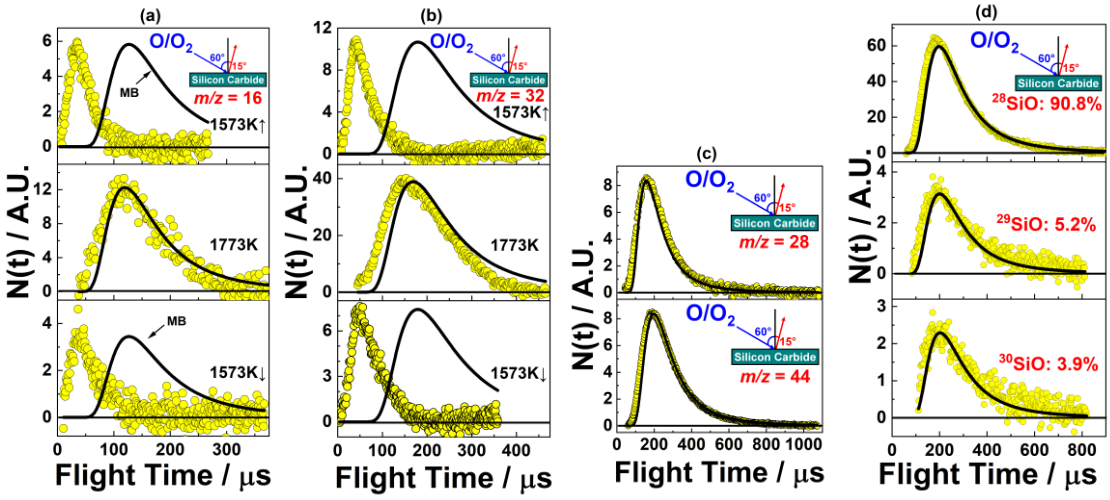

Fig. 2-13. Representative TOF distributions for products exiting the silicon carbide surface at θ_f = 15°, following bombardment by the supersonic O/O_2 beam at θ_i = 60°. Beam described in **Fig. 2-3**. Yellow points represent number density, and dashed black lines represent MB distributions characterized by the surface temperature. **(a)** and **(b)** represent shifts in the TOF distribution as the temperature was raised from 1573 K, held at 1773 K, then brought back down to 1573 K for *m/z* = 16 and 32, respectively. **(c)** represents the higher definition TOF distributions at *m/z* = 44, 45, and 46 at 1773 K. **(d)** represents the representative TOF distributions of *m/z* = 28 and 44 at 1773 K using the original parameters.

Atomic force microscopy analysis of the silicon carbide wafer after the experiment with the continuous O-atom beam show etching on the surface oriented along the path of the beam (**Fig. 2-14**).

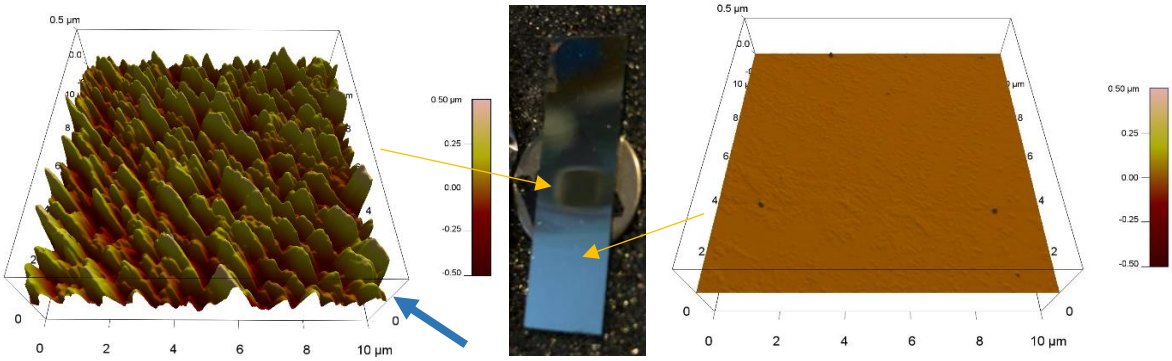

Fig. 2-14. 10 x 10 micrometer section of silicon carbide wafer (center) after exposure to heating and bombardment by continuous atomic oxygen beam. AFM of exposed area (left) and unexposed area (right). The orientation of the topographical features of the exposed SiC surface aligns with the direction of the beam, represented by thick blue arrow pointing from bottom right.

2.3.5. Decomposition of Silicon-Oxide Layer Without the Presence of the O-atom Beam

XPS analysis of the surface of the 5 nm oxide silicon carbide wafer thermally cycled up to 1973 K (**Fig. 2-7**) without *in-situ* O-atom exposure showed an even greater increase in the percentage of carbon on the surface compared to the sample that was continuously exposed to the O-atom beam while it was heated, with a nearly negligible amount of silicon and carbon detected. Just like the "Heated, O-atom" sample, the XPS peaks representing the surface chemistry shifted to an environment of that of graphitic carbon, with very little SiC remaining detectable on the surface. Mass spectral results from the decomposition of the 100 nm thick oxide silicon carbide are shown in **Fig. 2-15**. Overall integrated product intensity from the surface was at a maximum at 1873 K. As shown in **Fig. 2-16(b)**, the two main peaks from the mass spectrum collected at 1873 K were at *m/*z

= 44 and 28. For *m/z* = 44, 45, and 46, the integrated areas of these peaks closely correspond to the isotopic ratio of silicon (92.2%, 4.7%, and 3.1%, respectively). As temperature rose, the proportion of each individual species' integrated intensity divided by the sum of all the species' integrated intensities at each temperature point remained relatively steady, with no proportional increases or decreases of any of the species until the temperature passed 1950 K, at which point the proportional intensity of each species began diverging (**Fig. 2-17(b)**). Within this constant range, the average proportional intensities for *m/z* = 44, 45, and 46 were 93.5%, 3.9%, and 2.6%, respectively, suggesting that nearly all the *m/z* = 44 signal was SiO. For *m/z* = 28, 29, and 30, the proportion of each species integrated intensity divided by the sum of all the species' integrated intensities at each temperature point did not remain steady as the SiC temperature increased (**Fig. 2-17(d)**). The proportional intensity of *m/*z = 28 decreased from 1723 to 2023 K, while the proportional intensities of *m/z* = 29 and 30 continuously increased in this range. Though these percentages were not constant, the average proportional intensities over the entire temperature range for each species are very similar to the isotopic ratios of silicon (93.8%, 3.8%, and 2.4% for *m/z* = 28, 29, and 30, respectively). The gradual convergence of the intensities as temperature increased suggests the presence of another species present at *m/z* = 28, potentially CO. In addition to the species at *m/*z = 28 and 44, a couple of smaller peaks relevant to SiC could also be observed. A prominent peak at *m/z* = 60 appeared around 1450°C, then disappeared around 1690°C. This peak could represent molecular SiO_2, though as no peaks were detected at *m/z* = 61 or 62, it could not definitively be identified as such. An additional

peak at *m/z* = 52 was also observed that could correspond to SiC_2, as previously observed by Drowart and de Maria (1960).[70]

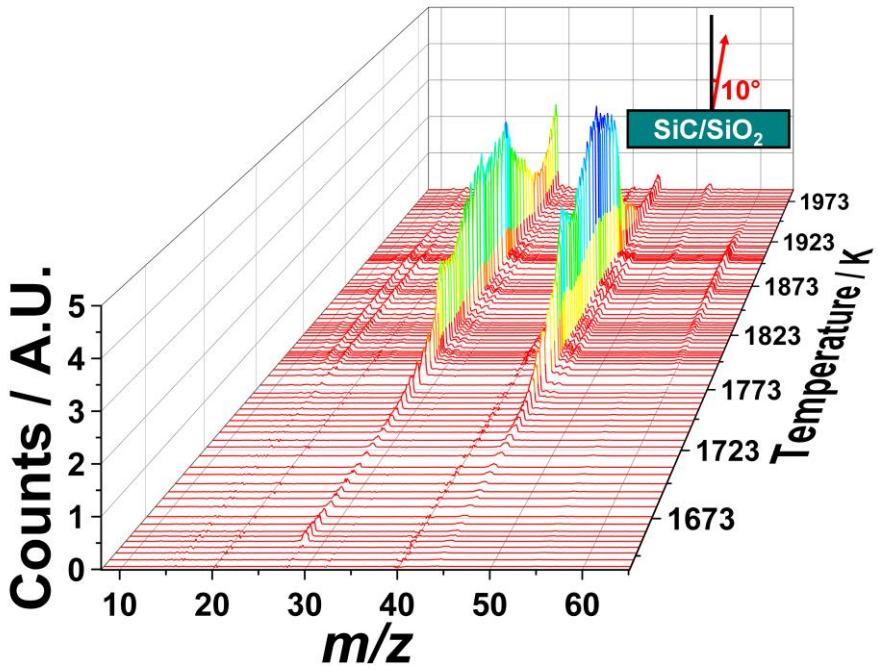

Fig. 2-15. Plot of mass spectra from decomposition of 100 nm-thick SiO_2-coated silicon carbide collected as a function of time as the current and temperature was raised.

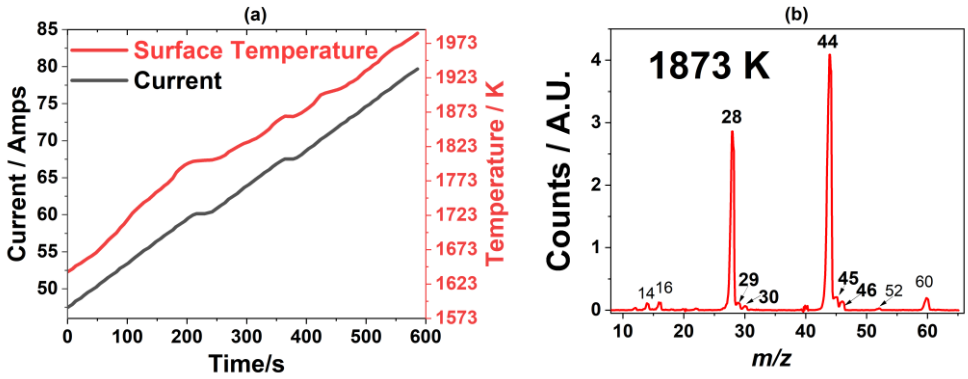

Fig. 2-16. (a) Current and temperature/time profile of the experiment. **(b)** Representative mass spectrum of products observed at 1873 K.

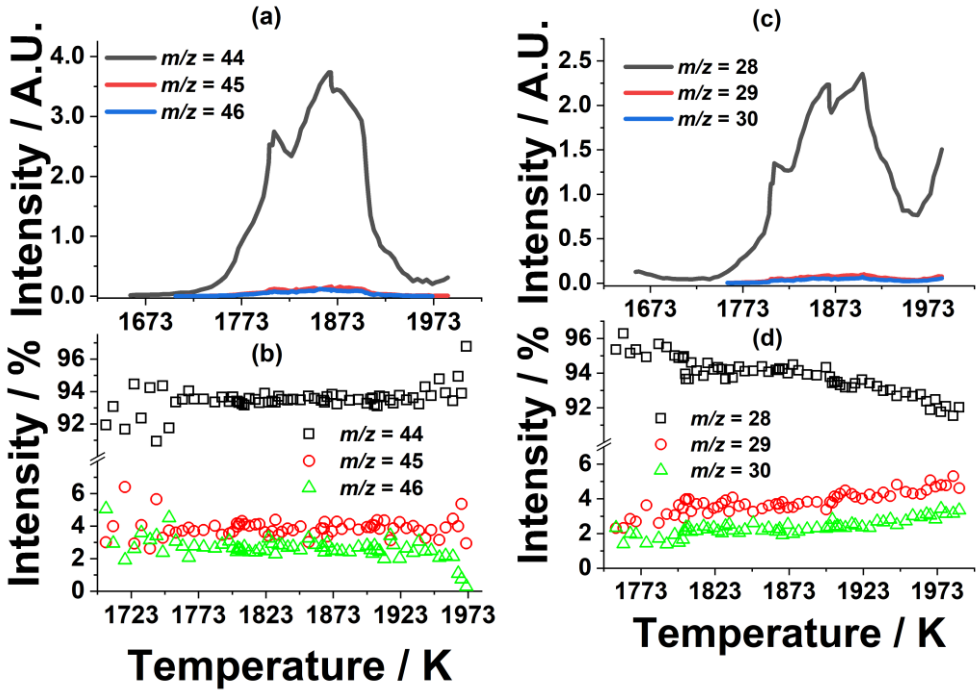

Fig. 2-17. Isotopic analysis of SiO_2 decomposition. **(a)** Change in integrated intensity of peaks observed at *m/z* = 44, 45, and 46. **(b)** Comparison of these three isotopes' abundance as a percentage of their overall intensity at each temperature. **(c)** Change in integrated intensity of peaks observed at *m/z* = 28, 29, and 30. **(d)** Comparison of these three isotopes' abundance as a percentage of their overall intensity at each temperature.

2.4. Discussion

Changes in the shape of the flux angular distributions of *m/z* = 16 and 32 from 1473 K to 1973 K were indicative of morphological changes on the surface of the SiC. In particular, the narrowing of both the *m/*z = 16 *m/*z = 32 angular distributions from oxidized SiC as the silicon carbide passed through the transition temperature was indicative of a significant reduction in the roughness of the surface of the wafer, which was shown to be graphitic carbon by both XPS analysis and Raman spectroscopy. The experiments conducted with heating the oxide-covered SiC wafers without the O-atom beam demonstrate that a graphitic layer forms in the absence of continued O-atom bombardment.

While formation of a graphitic layer on SiC through thermal decomposition is a known process,[72] the formation of a graphitic layer while the O-atom beam was present was still unexpected, as the process should have transitioned to active oxidation, with continuous production of CO and SiO as the O-atom beam scattered against the SiC wafer. Experiments from Drowart and de Maria (1960)[70] suggest a sublimation process at high temperatures under vacuum where the silicon with its higher vapor pressures sublimes away, leaving behind a graphitic layer. Simulations conducted by Newsome et al. (2012)[89] also suggest formation of a stable graphite layer when there is a lack of available oxygen species. This means that there was a competition between different reaction pathways based on the amount of O-atom flux reaching the surface, and we reasoned that increasing the O-atom flux would allow enough O-atoms to erode through the graphitic layer and continue reacting with the SiC underneath. The experiments with the continuous O-atom beam suggest this, with continuous production of *m/z* = 28 and 44 in near-equivalent proportions at 1773 K observed, and with *m/z* = 44 confirmed to be SiO based on the proportional intensities of *m/z* = 44, 45, and 46. There is the possibility that *m/z* = 28 could represent monoatomic silicon, but *m/z* = 29 and 30 were not investigated, and the equivalent *m/*z = 28 and 44 production precludes the presence of any other species. Between 1573 and 1773 K, the TOF distributions for *m/z* = 16 and 32 shifted from IS to TD channels. Additionally, TOF distributions for *m/z* = 28 and 44 at 1773 K all show desorption from TD channels. This suggests that the mechanism of active oxidation is a thermal process occurring at equilibrium on the surface. Further investigation will be needed, however, to determine the exact mechanism.

While XPS analysis of the pretreated oxidized SiC showed that most of the silicon was in the SiO_2 chemical environment, the actual composition from the bulk to the surface could be quite complicated, especially at the interface, where various silicon oxycarbide combinations of SiO_xC_y could exist.[90-91] The decomposition of the 100 nm oxide-covered SiC produced very high signal mass spectra that showed mostly production of SiO and monoatomic Si. However, no O_2 was detected and very little O was produced. The lack of both O and O_2 in the product distribution suggests that the decomposition of the oxide layer does not proceed at the surface, but rather takes place at the interface between the oxide and the bulk. This is a mechanism that Jacobson et al. (2012)[17] have hypothesized (**Table 2-1 (c-e)**). While there have not been many decomposition studies measuring products from oxide-covered SiC, far more extensive decomposition studies have been conducted on oxide-covered silicon. Unlike pure silica, which when decomposing in a chemically neutral environment produces O and O_2 in addition to SiO,[92] silica on silicon almost exclusively decomposes into SiO.[92] As described in previous studies,[75, 77] when Si/SiO_2 is thermally cycled, voids appear within the oxide layer that end up exposing the bulk silicon, allowing more of the oxide access to the underlying silicon. Raider et al. (1991)[93-94] found that carbon impurities found at the Si/SiO_2 interface catalyze the formation of these voids and hypothesized the follow mechanism: $2SiC(s) + SiO_2(s) \rightarrow 3Si(l, s) + 2CO(g)$ (**Table 2-1(e)**). **Fig. 2-17** suggests the presence of a small amount of CO at $m/z = 28$ that decreases as temperature increases, which lends credence to Raider's mechanism. This could also mean that oxide decomposition from SiC occurs far more quickly than from a comparable oxide on Si due to the presence of carbon. The small amount of molecular SiO_2 suggests

that the oxide layer was thick enough for some decomposition to proceed at the surface. This was still only a small fraction of all the species observed, and the far larger amount of monoatomic Si produced suggests that the SiC bulk was either preferentially evaporating Si, leaving behind a carbon layer while the gaseous Si reacts with the oxide layer (**Table 2-1(f)**), or it was undergoing a concerted reaction with SiO_2 (**Table 2-1(d)**). The process was likely a combination of both, as most of the reactivity was still occurring at the interface.

On the graphitized silicon carbide heated with concurrent bombardment by the hyperthermal beam, the flux of CO and CO_2 as temperature decreased show qualitative similarities with atomic oxygen scattering from highly-oriented pyrolytic graphite (HOPG),[64] with CO_2 flux increasing at lower temperatures and CO flux showing a maximum from 1100 to 1300 K. The thermal desorption of O-atoms in these conditions was representative of TD_{fast} channels showing desorption above a barrier. A similar phenomenon was also observed by Murray et al. (2018)[64] from their atomic oxygen scattering from HOPG. However, while we observe TD_{fast} O-atom products at all final angles for graphitized silicon carbide at 1973 K, in their experiment, TD_{fast} was only observed for O-atoms exiting at $\theta_f > 60°$. *m/z* = 28 production at 1973 K was also not observed at any angle in our pulsed O-atom beam experiment, contrary to the results observed by Murray et al. (2018), where they observed *m/z* = 28 flux at 1900 K. The IS angular distributions of the O and O_2 scattering at 1973 K are also both qualitatively and quantitatively nearly identical to that observed by Murray et al., especially in regards to their fwhm (O-atom = 22.2° for HOPG, 22.4° for $SiC_{graphite}$; O_2 fwhm = 19° for HOPG,

19.1° for $SiC_{graphite}$), while their θ_{max} only slightly differs (O-atom = 56.5° for HOPG, 55° for $SiC_{graphite}$; O_2 = 56.5° for HOPG, 57.5° for $SiC_{graphite}$). At the lower temperature of 1473 K, the IS angular distributions of both O and O_2 are qualitatively similar to that observed with O-atom scattering from SiO_2 on silicon as reported by Murray et al. (2017).[95] While their experiment used a more grazing angle of θ_i = 60° and a temperature of 673 K, as opposed to our angle of θ_i = 45° and temperature of 1473 K, the overall shape of their IS distribution was still similar to that of our experiment. Finally, the decrease and increase in scattered flux of O and O_2, respectively, from the oxidized SiC at 1673 K at a final angle of θ_f = 45° was possibly indicative of O-atom recombination. This phenomenon of O decrease and O_2 increase was not observed from the final angle of θ_f = 10°, and it was also not observed in the supersonic beam scattering results. In addition, while there was a large momentary drop in O flux from pristine SiC around 1723 K, there was no corresponding increase then decrease in the O_2 flux as the temperature increased. From the angular distributions, the O/O_2 ratio from 12.4 to 2.5 from 1473 to 1973 K shows a large relative decrease in the amount of O leaving the surface with a correspondingly large relative increase in O_2 that could also be indicative of O-atom recombination on the surface; however, O-atom recombination was not certain, as the change in surface structure may also be causing O-atoms to be scattering away from the detector's rotation plane.

Because the sample temperature was maintained at a specific temperature, the temperature jump was unable to be observed as in other studies. Both Luo et al. (2016)[81] and Marschall et al. (2012)[12] observed the temperature jump in their high-temperature plasma studies on SiC-carbon composites, and they both suggested that the cause of the

temperature jump was related to the erosion of the SiC component. Panerai et al. (2014)[22] suggested that the sublimation of the SiC component was also a contributor to the erosion. Regardless, all these studies made a connection between the eventual exposure of the carbon fiber preform in their composites to atomic oxygen and the temperature jump. Compared to what was observed in this study, this hypothesis does not match with the reactive oxidation trends from the graphitized SiC. Except for 1673 K and 1773 K, flux of $m/z = 28$ was very low or negligible at all remaining temperatures in the experiment after the PAT. Despite this incongruity, there is evidence for the hypothesis presented from the high-temperature plasma experiments. First, in the study of O-atom beam scattering from HOPG, Murray et al. (2018),[64] the product flux of CO, the only reactive product observed from HOPG above 1600 K, did not change appreciably with increasing temperature from 1700 K to 2300 K. This suggests that, in scattering O-atoms from the graphitized SiC, reactive product flux should not be expected to change with temperature increase. Second, and more importantly, it has been shown from O-atom molecular beam scattering of both vitreous carbon[42] and FiberForm[47] (a carbon fiber preform) that, unlike with O-atom scattering from graphite, reactive CO flux increases as temperature increases, though with vitreous carbon, the CO flux reached a peak at 1200 K, while with FiberForm, CO flux continued to increase as temperature reached 1823 K. This means that reactivity of the carbon fiber with atomic oxygen at very high temperatures is going to be very high. Thus, what may be occurring in the high-temperature plasma experiments is that at the point at which the surface heat balance reaches an equilibrium, both the decomposition of the silicon-oxide layer as well as the erosion of the remainder of the SiC component had begun.

Once the SiC component had completely eroded, only the carbon fiber component was left to be exposed to the atomic oxygen plasma. This naked exposure of the carbon fiber component caused the heat balance to change on the surface and allowed the temperature to increase until a new equilibrium temperature was reached. Thus, it was the exposure of the bare carbon fibers and its much higher reactivity that was likely reflected in the temperature jump observed by the groups mentioned previously. Finally, it is likely that, even with a different experimental setup from the one presented in this chapter, this temperature jump may not be able to be observed from a model material such as silicon carbide. In addition to the reasons mentioned above, this jump also could not be observed from exposure in a Plasmatron chamber of a bulk SiC ceramic to high energy atomic oxygen, as Luo et al. (2016)[81] observed. It appears that the presence of a particular morphological arrangement of carbon was what was needed to cause the temperature jump.

2.5. Conclusion

Both the atomic oxygen scattering dynamics from silicon carbide and its passive-to-active oxidation transition have been investigated. Pulsed beams containing high-velocity (7.4 km s^{-1}) atomic oxygen were directed onto 6H-silicon carbide wafers at high temperature, and products at m/z = 16 and 32 were observed. Near the PAT temperature, a change in the flux of scattered products was observed, with a momentary appearance of both m/z = 28 and 44. After heating oxide-covered SiC through the PAT temperature with and without the O-atom beam, XPS and Raman analysis revealed the surface primarily to consist of a graphitic layer. Surmising that increasing the flux of O-atoms would allow us

to promote active oxidation instead, we used a higher flux continuous O-atom beam and found stoichiometrically similar production of both *m/z* = 28, possibly corresponding to CO, and 44, confirmed to be SiO through isotopic analysis. Further investigations into the decomposition of a 100 nm oxide-covered silicon carbide wafer revealed production of *m/z* = 28 and 44, corresponding to monoatomic silicon as well as SiO, respectively, with additional peaks at *m/z* = 29, 30, 45, and 46, corresponding to the naturally occurring isotopes of silicon and silicon monoxide, respectively. These results suggest a competition between different reactive processes within the transition from passive oxidation to active oxidation of silicon carbide that is dependent on the flux of O-atoms reaching the surface of the silicon carbide. With enough atomic oxygen flux, active oxidation can initiate unimpeded. However, if the atomic oxygen flux is low enough, a layer of graphitic carbon forms, which is relatively unreactive to incident O-atoms. The temperature jump observed in studies of SiC/Carbon fiber composites was not observed in this experiment, which was attributed to the experimental design. However, we also surmised that a temperature jump was unlikely to be observed from just silicon carbide itself, with the temperature jump in the previous studies associated with the presence of carbon fibers in the composite TPS material. All this information could prove vital to the design of UHTCs in the future. In addition to the dynamics of scattered products from the surface being useful for model development, the insight regarding the temperature jump could be important in designing UHTCs to account for unexpected spikes in temperature and erosion.

2.6. References

2. Natali, M.; Kenny, J. M.; Torre, L., Science and technology of polymeric ablative materials for thermal protection systems and propulsion devices: A review. *Progress in Materials Science* **2016**, *84*, 192-275.
3. Opeka, M. M.; Talmy, I. G.; Zaykoski, J. A., Oxidation-based materials selection for 2000°C + hypersonic aerosurfaces: Theoretical considerations and historical experience. *Journal of Materials Science* **2004**, *39*, 5887-5904.
4. Steyer, T. E., Shaping the Future of Ceramics for Aerospace Applications. *International Journal of Applied Ceramic Technology* **2013**, *10*, 389-394.
9. Poovathingal, S.; Schwartzentruber, T. E.; Murray, V. J.; Minton, T. K., Molecular Simulation of Carbon Ablation Using Beam Experiments and Resolved Microstructure. *AIAA Journal* **2016**, *54*, 999-1010.
12. Marschall, J.; Pejaković, D. A.; Fahrenholtz, W. G.; Hilmas, G. E.; Panerai, F.; Chazot, O., Temperature Jump Phenomenon During Plasmatron Testing of ZrB2-SiC Ultrahigh-Temperature Ceramics. *Journal of Thermophysics and Heat Transfer* **2012**, *26*, 559-572.
15. Balat, M.; Flamant, G.; Male, G.; Pichelin, G., Active to passive transition in the oxidation of silicon carbide at high temperature and low pressure in molecular and atomic oxygen. *Journal of Materials Science* **1992**, *27*, 697-703.
17. Jacobson, N. S.; Myers, D. L.; Harder, B. J., Active oxidation of silicon carbide. *Materials at High Temperatures* **2012**, *29*, 193-198.
18. Jacobson, N.; Harder, B.; Myers, D., Oxidation Transitions for SiC Part I. Active-to-Passive Transitions. *J. Am. Ceram. Soc.* **2013**, *96*, 838-844.
22. Panerai, F.; Helber, B.; Chazot, O.; Balat-Pichelin, M., Surface temperature jump beyond active oxidation of carbon/silicon carbide composites in extreme aerothermal conditions. *Carbon* **2014**, *71*, 102-119.
23. Chen, S. Y.; Boyd, I. D., Chemical equilibrium analysis of silicon carbide oxidation in oxygen and air. *Journal of the American Ceramic Society* **2019**, *102*, 4272-4284.
42. Murray, V. J.; Marshall, B. C.; Woodburn, P. J.; Minton, T. K., Inelastic and Reactive Scattering Dynamics of Hyperthermal O and O2 on Hot Vitreous Carbon Surfaces. *The Journal of Physical Chemistry C* **2015**, *119*, 14780-14796.
43. Murray, V. J.; Recio, P.; Caracciolo, A.; Miossec, C.; Balucani, N.; Casavecchia, P.; Minton, T. K., Oxidation and nitridation of vitreous carbon at high temperatures. *Carbon* **2020**, *167*, 388-402.
47. Poovathingal, S. J.; Qian, M.; Murray, V. J.; Minton, T. K., Reactive and Inelastic Scattering Dynamics of Hyperthermal O and O2 from a Carbon Fiber Network. 2021.
51. Lee, Y. T.; McDonald, J. D.; LeBreton, P. R.; Herschbach, D. R., Molecular Beam Reactive Scattering Apparatus with Electron Bombardment Detector. *Review of Scientific Instruments* **1969**, *40*, 1402-1408.

52. Zhang, J.; Garton, D. J.; Minton, T. K., Reactive and inelastic scattering dynamics of hyperthermal oxygen atoms on a saturated hydrocarbon surface. *The Journal of Chemical Physics* **2002**, *117*, 6239-6251.
53. Zhang, J.; Upadhyaya, H. P.; Brunsvold, A. L.; Minton, T. K., Hyperthermal Reactions of O and O2 with a Hydrocarbon Surface: Direct C−C Bond Breakage by O and H-Atom Abstraction by O2. *The Journal of Physical Chemistry B* **2006**, *110*, 12500-12511.
54. Garton, D. J.; Brunsvold, A. L.; Minton, T. K.; Troya, D.; Maiti, B.; Schatz, G. C., Experimental and Theoretical Investigations of the Inelastic and Reactive Scattering Dynamics of O(3P) + D2 *The Journal of Physical Chemistry A* **2006**, *110*, 1327-1341.
55. Garton, D. J.; Minton, T. K.; Maiti, B.; Troya, D.; Schatz, G. C., A crossed molecular beams study of the O(3P)+H2 reaction: Comparison of excitation function with accurate quantum reactive scattering calculations. **2003**, *118*, 1585-1588.
56. Troya, D.; Schatz, G. C.; Garton, D. J.; Brunsvold, A. L.; Minton, T. K., Crossed beams and theoretical studies of the O(3P)+CH4→H+OCH3 reaction excitation function. *The Journal of Chemical Physics* **2004**, *120*, 731-739.
59. Brink, G. O., Electron Bombardment Molecular Beam Detector. *Review of Scientific Instruments* **1966**, *37*, 857-860.
60. Daly, N. R., Scintillation Type Mass Spectrometer Ion Detector. *Review of Scientific Instruments* **1960**, *31*, 264-267.
61. Minton, T. K.; Giapis, K. P.; Moore, T., Inelastic Scattering Dynamics of Hyperthermal Fluorine Atoms on a Fluorinated Silicon Surface. *The Journal of Physical Chemistry A* **1997**, *101*, 6549-6555.
62. Hurst, J. E.; Becker, C. A.; Cowin, J. P.; Janda, K. C.; Wharton, L.; Auerbach, D. J., Observation of Direct Inelastic Scattering in the Presence of Trapping-Desorption Scattering: Xe on Pt(111). *Physical Review Letters* **1979**, *43*, 1175-1177.
63. Michelsen, H. A.; Auerbach, D. J., A critical examination of data on the dissociative adsorption and associative desorption of hydrogen at copper surfaces. *The Journal of Chemical Physics* **1991**, *94*, 7502-7520.
64. Murray, V. J.; Smoll, E. J.; Minton, T. K., Dynamics of Graphite Oxidation at High Temperature. *The Journal of Physical Chemistry C* **2018**, *122*, 6602-6617.
65. Banks, B.; Miller, S.; de Groh, K., *Low Earth Orbital Atomic Oxygen Interactions With Materials*, 2004; Vol. 2.
66. Blum, Y. D.; Marschall, J.; Hui, D.; Young, S., Thick Protective UHTC Coatings for SiC-Based Structures: Process Establishment. *Journal of the American Ceramic Society* **2008**, *91*, 1453-1460.
67. Presser, V.; Nickel, K. G., Silica on Silicon Carbide. *Critical Reviews in Solid State and Materials Sciences* **2008**, *33*, 1-99.
68. Jacobson, N. S.; Myers, D. L. J. O. o. M., Active Oxidation of SiC. **2011**, *75*, 1-25.
69. de Heer, W. A.; Berger, C.; Ruan, M.; Sprinkle, M.; Li, X.; Hu, Y.; Zhang, B.; Hankinson, J.; Conrad, E., Large area and structured epitaxial graphene produced by confinement controlled sublimation of silicon carbide. *Proceedings of the National Academy of Sciences* **2011**, *108*, 16900-16905.

70. Drowart, J.; De Maria, G. In *Thermodynamic study of the binary system carbon-silicon using a mass spectrometer*, Proc. Conf. Silicon Carbide (1959, Boston), 1960; pp 16-23.
71. Guichelaar, P. J., Acheson process. In *Carbide, Nitride and Boride Materials Synthesis and Processing*, Springer: 1997; pp 115-129.
72. Mishra, N.; Boeckl, J.; Motta, N.; Iacopi, F., Graphene growth on silicon carbide: A review. *Phys. Status Solidi A* **2016**, *213*, 2277-2289.
73. Tromp, R. M.; Hannon, J. B., Thermodynamics and Kinetics of Graphene Growth on SiC(0001). *Physical Review Letters* **2009**, *102*, 106104.
74. Ciochoń, P.; Bodek, Ł.; Garb, M.; Zając, Ł.; Kołodziej, J. J., Si beam-assisted graphitization of SiC (0001). *Applied Physics A* **2018**, *124*, 727.
75. Enta, Y.; Nagai, T.; Yoshida, T.; Ujiie, N.; Nakazawa, H., Decomposition kinetics of silicon oxide layers on silicon substrates during annealing in vacuum. *Journal of Applied Physics* **2013**, *114*, 114104.
76. Gallet, J. J.; Silly, M. G.; Kazzi, M. E.; Bournel, F.; Sirotti, F.; Rochet, F., Chemical and kinetic insights into the Thermal Decomposition of an Oxide Layer on Si(111) from Millisecond Photoelectron Spectroscopy. *Scientific Reports* **2017**, *7*, 14257.
77. Liehr, M.; Lewis, J. E.; Rubloff, G. W., Kinetics of high‐temperature thermal decomposition of SiO2 on Si(100). *Journal of Vacuum Science & Technology A* **1987**, *5*, 1559-1562.
78. Tromp, R.; Rubloff, G.; Balk, P.; LeGoues, F.; Van Loenen, E., High-Temperature SiO2 Decomposition at the SiO2/Si Interface. *Physical Review Letters* **1985**, *55*, 2332.
79. Zhiqiang, F.; Chunhe, T.; Liang, T.; Jean-Charles, R., Oxidation of SiC and decomposition of SiO2 at low partial pressure of oxygen in He-O2 system. *Nuclear Engineering and Design* **2004**, *234*, 45-49.
80. Herdrich, G.; Fertig, M.; Löhle, S.; Pidan, S.; Auweter-Kurtz, M.; Laux, T., Oxidation Behavior of Siliconcarbide-Based Materials by Using New Probe Techniques. *Journal of Spacecraft and Rockets* **2005**, *42*, 817-824.
81. Luo, L.; Wang, Y.; Liu, L.; Duan, L.; Wang, G.; Lu, Y., Ablation behavior of C/SiC composites in plasma wind tunnel. *Carbon* **2016**, *103*, 73-83.
82. Wang, Y.; Chen, Z.; Yu, S., Ablation behavior and mechanism analysis of C/SiC composites. *Journal of Materials Research and Technology* **2016**, *5*, 170-182.
83. Sakraker, I.; Asma, C. O., Experimental investigation of passive/active oxidation behavior of SiC based ceramic thermal protection materials exposed to high enthalpy plasma. *Journal of the European Ceramic Society* **2013**, *33*, 351-359.
84. Tagawa, M.; Ema, T.; Kinoshita, H.; Ohmae, N.; Umeno, M.; Minton, T. K., Formation of Thin Oxide Films on Room-Temperature Silicon (100) by Exposure to a Neutral Beam of Hyperthermal Atomic and Molecular Oxygen. *Japanese Journal of Applied Physics* **1998**, *37*, L1455-L1457.
85. Harris, J., On vibrationally-assisted dissociation of H2 at metal surfaces. *Surface Science* **1989**, *221*, 335-345.
86. Hornetz, B.; Michel, H. J.; Halbritter, J., Oxidation and 6H‐SiC‐SiO2 interfaces. *Journal of Vacuum Science & Technology A* **1995**, *13*, 767-771.

87. Önneby, C.; Pantano, C. G., Silicon oxycarbide formation on SiC surfaces and at the SiC/SiO2 interface. *Journal of Vacuum Science & Technology A* **1997**, *15*, 1597-1602.
88. Hijikata, Y.; Yaguchi, H.; Yoshikawa, M.; Yoshida, S., Composition analysis of SiO2/SiC interfaces by electron spectroscopic measurements using slope-shaped oxide films. *Applied Surface Science* **2001**, *184*, 161-166.
89. Newsome, D. A.; Sengupta, D.; Foroutan, H.; Russo, M. F.; van Duin, A. C. T., Oxidation of Silicon Carbide by O2 and H2O: A ReaxFF Reactive Molecular Dynamics Study, Part I. *The Journal of Physical Chemistry C* **2012**, *116*, 16111-16121.
90. Zhu, Q.; Huang, L.; Li, W.; Li, S.; Wang, D., Chemical structure study of SiO2/4H-SiC (0001) interface transition region by angle-dependent x-ray photoelectron spectroscopy. *Applied Physics Letters* **2011**, *99*, 082102.
91. Soukiassian, P.; Amy, F., Silicon carbide surface oxidation and SiO2/SiC interface formation investigated by soft X-ray synchrotron radiation. *Journal of Electron Spectroscopy and Related Phenomena* **2005**, *144-147*, 783-788.
92. Brewer, L.; Edwards, R. K., The Stability of SiO Solid and Gas. *The Journal of Physical Chemistry* **1954**, *58*, 351-358.
93. Raider, S. I.; Herd, S. R.; Walkup, R. E., SiO2 film decomposition reaction initiated by carbon impurities located at a Si‐SiO2 interface. *Applied Physics Letters* **1991**, *59*, 2424-2426.
94. Raider, S. I., Carbon impurities at a Si-SiO2 interface. *Microelectronic Engineering* **1993**, *22*, 29-34.
95. Murray, V. J.; Pilinski, M. D.; Smoll, E. J.; Qian, M.; Minton, T. K.; Madzunkov, S. M.; Darrach, M. R., Gas–Surface Scattering Dynamics Applied to Concentration of Gases for Mass Spectrometry in Tenuous Atmospheres. *The Journal of Physical Chemistry C* **2017**, *121*, 7903-7922.

CHAPTER THREE

EFFECT OF ATOMIC OXYGEN ON CV-1144-0 AND RTV-560 SILICONES

Contributions of Authors and Co-Authors

Manuscript in Chapter 3

Author: David Z. Chen

Contributions: Cured and prepared all samples. Conducted exposure experiments and collected QCM data. Conducted XPS and SEM analyses on all samples. Wrote and edited the manuscript.

Author: Chenbiao Xu

Contributions: Assisted in conducting exposure experiments and collecting QCM data.

Author: Timothy K. Minton

Contributions: Assisted with analysis and editing of the manuscript for final submission.

Manuscript Information

David Z. Chen, Chenbiao Xu, Timothy K. Minton

Acta Astronautica

Status of Manuscript:
_x__ Prepared for submission to a peer-reviewed journal
____ Officially submitted to a peer-reviewed journal
____ Accepted by a peer-reviewed journal
____ Published in a peer-reviewed journal

Elsevier

3.1. Introduction

Satellites traveling within low-Earth orbit (LEO) need protection from environmental factors such as solar radiation,[24] ions,[96] and highly reactive neutral species such as atomic oxygen[24, 29] and atomic nitrogen.[97] Materials that can provide protection are selected that can withstand the conditions of LEO and resist erosion, especially from atomic oxygen (AO). One means of providing this protection is the incorporation of silicon into the material. As described in Chapter Two, composites containing either silicon or silicon carbide will form a passivating silicon-oxide layer in the presence of atomic and molecular oxygen below a particular temperature, providing further protection from incident oxygen species. There are multiple ways to incorporate silicon into composites, including CVD[98] and pyrolysis,[99] but one common method is to apply a silicon-containing coating, namely those of silicones. Silicone coatings, especially DC 93-500[100] and CV-1144-0,[27] as well as constituent components such as polydimethylsiloxanes (PDMSs)[101] and polydiphenylsiloxanes,[102] have been studied both on Earth and in space for how their optical and morphological properties change after AO exposure. These changes are especially important because these coatings are quite often applied to solar panels,[25] which require minimal optical obstruction to function properly. These studies have also found that, even with passivation, there is measurable erosion of the silicone materials,[28] with cracking also observed on their surfaces.[103-104]

In addition to LEO applications, silicone materials have also been utilized in high temperature applications such as atmospheric entry.[50] There are significant differences in environments between LEO and atmospheric entry, for unlike LEO, where the

temperatures can cycle between 15 °C and 45 °C,[28] temperatures in atmospheric entry can approach and exceed 2000 °C, which means that there is an expectation that the silicone layer, both oxidized and unoxidized, will break down. PDMS has been observed to begin decomposing within the 400-650 °C range.[105-106] Additionally, and counterintuitively, AO translational energies in LEO can range around 5 eV because of the orbital velocity of the vehicle, while energies in atmospheric entry can be around 0.2-0.5 eV once the AO reaches the surface of the material, due in large part to the incident oxygen passing through a shock layer during entry.[9] Silicones pretreated with exposure to AO are thus being investigated for study in these conditions of high temperatures and greater AO fluence.[107] To investigate how AO exposure actually affects silicones in both of these environments, two representative examples of silicones used in these conditions have been examined in this study: CV-1144-0 and RTV-560.

CV-1144-0 is a dimethyl-diphenyl polysiloxane that has been used as a protective coating to cover exposed surface areas of satellites.[108] A comprehensive AO erosion study was conducted for CV-1144-0 coated on different substrates during the EOIM-III experiment on the Space Shuttle (STS-46), which found erosion yields in the range of 10^{-25} to 10^{-24} g O-atom^{-1}.[28] In atmospheric entry applications, it is sprayed onto the heat shield, phenolic impregnated carbon ablator (PICA), acting as an anti-dust agent,[50] but also incidentally providing protection against atomic oxygen during atmospheric entry. This application has been used in Mars Science Laboratory as well as the recent Mars 2020 mission. No prior high-temperature decomposition experiments have been conducted on this material yet. RTV-560, in contrast, though also being a dimethyl-diphenyl

polysiloxane, is primarily used as a binding agent, helping to adhere components of the thermal protection system together.[109-111] RTV-560 has been less comprehensively studied compared to CV-1144-0. It has been speculated to be a source of silicone contamination on spacecraft, and as a contaminant its optical properties have been studied.[24, 112] Its AO erosion yield was reported be on the order of 10^{-25} cm^3 O-$atom^{-1}$ after exposure in low-Earth orbit.[101] Thermogravimetric analyses on RTV-560 in a helium atmosphere and in air up to 1500 K have also been previously conducted.[113] With these two materials and the use of our unique atomic oxygen molecular beam apparatus, we studied the chemical and morphological effects of atomic oxygen exposure on these two silicone materials and quantified their erosion yields.

3.2. Sample Materials and Exposure Methods

The silicones, CV-1144-0 and RTV-560, were manufactured by NuSil Technologies LLC and Momentive Performance Materials, respectively. The curing of the CV-1144-0 and RTV-560 samples was conducted under varying conditions, all of which produced similar cured samples, that will be outlined in the subsequent sections. The cured chemical structure of CV-1144-0 consists of 95.2% dimethyl units and 4.8% diphenyl units.[27] For RTV-560, its exact chemical composition was unknown, but it has been described as a methyl-phenyl siloxane compound,[114-115] and it contained a significant amount of iron(III) oxide filler. Before each atomic oxygen exposure, X-ray photoelectron spectroscopy (XPS) and scanning electron microscopy (SEM) analyses were conducted of

the cured surfaces of these materials (**Fig. 3-1** and **Fig. 3-3**, **Fig. 3-2** and **Fig. 3-4**, respectively).

The experiments were performed using an apparatus as described previously.[57] In summary, for all of the atomic oxygen pretreatments, the atomic oxygen beam was composed of on average 83-84% O-atoms (^3P)[55] with the remainder being molecular oxygen ($^3\Sigma_g^-$).[56] A small quantity of ions was also present. The beam itself was formed through the laser detonation of O_2 gas in a conical nozzle with a 7 J pulse^{-1} CO_2 TEA laser, and it was operated at a rate of 2 Hz. The average O-atom translational energies were maintained around 5.2 eV. The first set of experiments, encompassing exposures at 25 °C and 300 °C, used the sample mount that had been used previously[57] to expose the two samples to 100,000 beam pulses. For both the 25 °C and 300 °C exposure, a circular disc cut out from a sheet of Kapton was placed in the center slot in the middle row of the sample mount along with a wire mesh screen. The wire mesh blocked AO erosion on parts of the Kapton it covered, resulting in quantifiable areas of erosion in the openings in the mesh. Total AO fluence was then calculated based on the accepted Kapton erosion yield of 3 x 10^{-24} cm^3 O-atom^{-1},[57] and the erosion depth of the Kapton was measured using a Dektak^3 surface profiler. Total measured O-atom fluence at 25 °C was 2.36 x 10^{20} O-atoms cm^{-2} with full-width half-maximum of 1.2 eV for the beam itself. For the 300 °C exposure, total measured fluence was 1.9 x 10^{20} O-atoms cm^{-2}, with full-width half-maximum of 2.1 eV for the beam.

In addition to the erosion depth of Kapton, measurements of the erosion depth of the two silicones after exposure were also attempted, but unfortunately there was not

enough erosion to reproducibly measure depths with the surface profiler. Thus, for the second set of experiments a quartz crystal microbalance (QCM) was used. The QCM device, called the Quartz Crystal Microbalance Research System, was made by Maxtek, and used 5 MHz gold-coated crystals. A G3 Spin Coater from Specialty Coating Systems was used to spin coat the silicones CV-1144-0 and RTV-560 onto the crystals. The design of the QCM in particular used two crystal positions that allowed for AO exposure mass loss measurements from two samples per trial, while the water-cooling system allowed the maintenance of the sample temperature at 25 °C.[31-32] AO fluence measurements were thus conducted from placing a piece of the wire mesh screened Kapton in-between the two crystal positions. The average O-atom flux for each experiment was related to the corresponding mass loss rate to calculate an erosion yield based on mass loss per O-atom. Polyimide films spin coated onto QCM crystals were used as references to compare their respective erosion yields to those of the silicones. These polyimide films were prepared from a polyamic acid (Pyralin PI-5878G from HD MicroSystems)[32, 116] with the same chemical repeating unit as Kapton H. Unfortunately, because an RTV-560 film was unable to be adhered properly to the QCM crystal such that the instrument can record it, we did not measure mass loss for that silicone. In addition, because the QCM instrument was unable to function at elevated temperatures, there are no higher-temperature mass loss measurements to report.

3.3. Results and Discussion

3.3.1. Room-Temperature Exposure

For the initial exposure experiments, CV-1144-0 was prepared by diluting it 1:1 with VM&P brand naphtha, followed by room temperature curing on Kapton substrates for 7 days, after which 10 mm diameter discs were cut out. RTV-560 was prepared by mixing it with a few drops of dibutyltin dilaurate (DBT), then pouring the mixture into an aluminum disposable crimped-sided petri dish and curing at room temperature for one day, after which 10 mm diameter discs were cut out. The cured RTV-560 did not strongly adhere to the petri dish and had a rubbery texture, so we were able to cut out 10 mm diameter discs from its bulk and pull out the silicone rubber directly. The RTV-560 discs were then placed directly into the sample mount. As DBT was already present in the CV-1144-0 mix, there was no need to add additional DBT into that mixture. XPS (**Fig. 3-1**) analysis of the 25 °C exposure experiments showed a significant shift in both the chemical composition of the surfaces as well as their chemical environments. For CV-1144-0, there was an increase in the oxygen and silicon percentage on the surface, along with a proportional decrease in carbon coverage. XPS analysis of RTV-560 also showed a similar change, with proportional increases in oxygen and silicon, and proportional decreases in carbon. Carbon coverage on RTV-560 after O-atom exposure was still proportionally higher compared to CV-1144-0, which suggests that the carbon was less accessible to incoming O-atoms. Tin was observed after exposure, however, which was attributed to erosion of the RTV-560 exposing the underlying species. The lack of iron was surprising, as it constituted more than 33% of the uncured RTV-560 material. It is likely that the iron could be found deeper

within the material below 10 nm. However, the silicone was not sputtered to elucidate this. The chemical shifts observed in the Si2p, Si2s (not shown), and O1s XPS peaks suggested that for both materials nearly all the silicone coating accessible within 10 nm have become either SiO_2 or some variant of SiO_x. It is important to note, however, that there was still a sizable amount of carbon detectable by XPS. Some of this was likely just adventitious carbon, but some could have been remnants of the unoxidized silicone, which suggests that the surface was not completely covered with SiO_x.

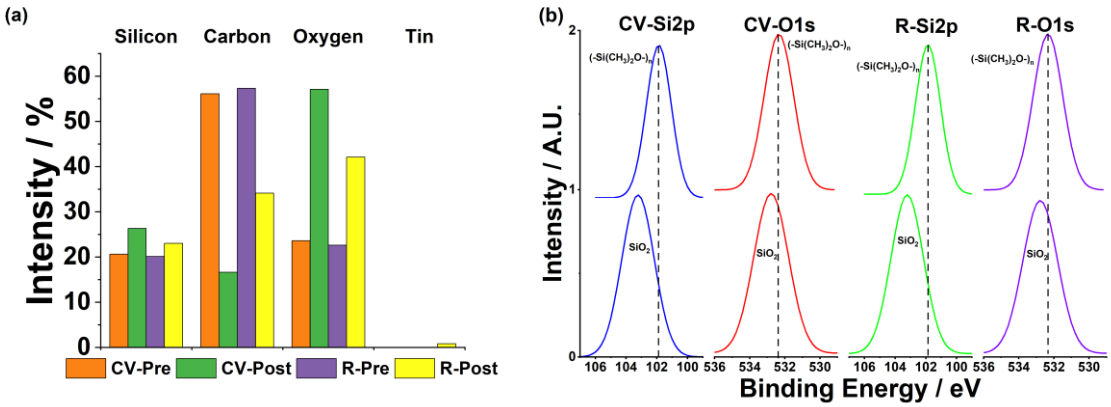

Fig. 3-1. XPS results for CV-1144-0 (CV) and RTV-560 (R) before and after O-atom exposure at 25 °C. **(a)** Atomic percentages and **(b)** XPS peaks. In **(b)** $(-Si(CH_3)_2O-)_n$ designates the chemical signature of polydimethylsiloxanes. Top row of **(b)** are XPS data collected before exposure, and bottom row are data collected after exposure. Dashed lines indicate positions of peak before exposure. XPS peaks for other elements not shown, as they do not show any shifts.

SEM (**Fig. 3-2**) analysis of the CV-1144-0 surface before and after atomic oxygen exposure also showed a significant change, with the surface becoming smoother, whereas before exposure it had a pockmarked structure likely resulting from bubbles forming during the curing process. In addition, cracks and valleys appeared on the surface after exposure. The widths of the observed cracks at this temperature ranged from ~0.5 to 1 μm. These

cracks formed because of the difference in density between the SiO_2 forming on the surface and the bulk silicone beneath, a well-known phenomenon for silicone coatings exposed to atomic oxygen.[117] As SiO_2 has a higher density (2.65 g cm^{-3})[118] compared to cured CV-1144-0 (1 g cm^{-3}),[119] the surface layer shrunk, causing crazing and cracking. On RTV-560, an intricate pattern formed on the surface after the initial curing that for the most part followed herringbone-like arrangements. Patterns like these, whether they are herringbone, zigzag, or labyrinthine,[120] can be observed on PDMS substrates modified with either metal thin films[104, 121-122] or plasma-induced silica coatings.[123] Interestingly, the RTV-560 surface did not exhibit the characteristics of a "hard" surface, as XPS analysis showed only the presence of polydimethylsiloxane instead of either silica or a metal. This was unusual, though not completely unexpected, as gels in general can form surface patterns under compressive pressure as they expand.[124] There is the possibility that the crimped edges in the aluminum dish that RTV-560 was cured in was a cause of these patterns. These patterns disappeared, however, after exposure, and left behind a smooth surface. Similar to what was observed on CV-1144-0, cracks also appeared on RTV-560 after exposure to O-atoms, though they were much smaller and occurred with lower frequency, and like its counterparts, the cracks forming on RTV-560 were likely a result of the density differences between the silicone and the silica being formed. The exact density of cured RTV-560 is unknown, but it likely has a density closer to that of SiO_2 compared to CV-1144-0, which would account for the lower frequency of cracks.

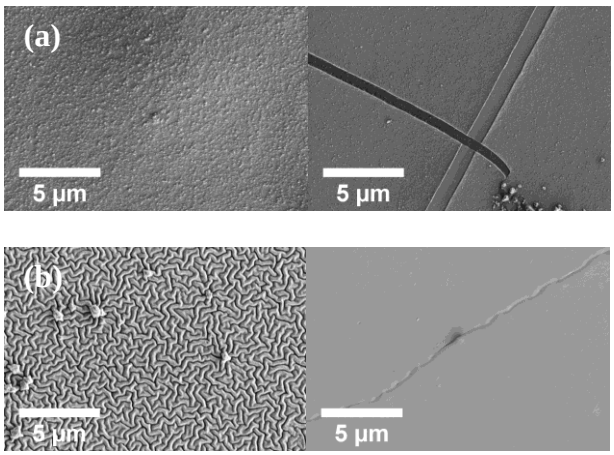

Fig. 3-2. SEM images of CV-1144-0 and RTV-560 before and after 25 °C exposure. (left) before, and (right) after O-atom exposure. **(a)** is CV-1144-0. **(b)** is RTV-560.

3.3.2. 300°C Exposure

Because Kapton degrades at higher temperatures, we decided to use silicon discs instead of Kapton as the substrate for the silicones for the 300 °C exposure. We obtained, from NASA Ames, CV-1144-0 diluted 1:1 with xylene and spin coated onto the silicon discs. We also spin coated and cured RTV-560 onto silicon discs in our own lab, though unlike CV-1144-0 these were undiluted. XPS (**Fig. 3-3**) analyses of the surfaces of both samples after O-atom exposure at 300 °C again showed proportional increases in silicon and oxygen coverage, along with proportional decreases in carbon coverage. XPS spectra also showed a shift in the peaks for silicon and oxygen for both materials into the SiO_2 binding energy region from polydimethylsiloxane. For CV-1144-0, one additional element revealed after exposure at this temperature was the presence of tin, which is found in the form of DBT as a component in the silicone mixture before curing. There was also a small amount of iron found after exposure that we believed to be the product of contamination (not shown). As the CV-1144-0 mixture should not contain any iron compounds like in

RTV-560, its source was likely environmental. XPS analysis of the RTV-560 correspondingly showed higher silicon and oxygen coverage along with proportionally lower carbon coverage. Like how RTV-560 exposed to AO at room temperature compared to CV-1144-0, RTV-560 exposed to AO at 300 °C appeared more resistant to oxidation compared to CV-1144-0. Tin was also revealed within the RTV-560 that corresponds to the DBT present.

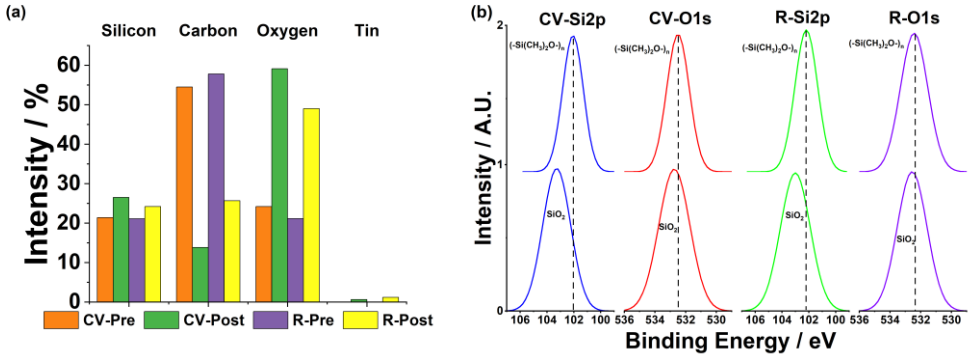

Fig. 3-3. XPS results for CV-1144-0 (CV) and RTV-560 (R) before and after O-atom exposure at 300 °C. **(a)** Atomic percentage and **(b)** XPS peaks. In **(b)**, $(-Si(CH_3)_2O-)_n$ designates the chemical signature of polydimethylsiloxane units. Top row of **(b)** are XPS peaks before exposure, and bottom row are after exposure. Dashed line indicates position of peak before exposure. XPS peaks for other elements not shown, as they do not show any shifts.

SEM (**Fig. 3-4**) analyses of the CV-1144-0 before exposure showed a much smoother surface compared to the solution-cast sample, likely indicating a lack of bubbles forming. After exposure, and similar to the CV-1144-0 exposure at 25 °C, there were significant cracks on the surface. The observed cracks appeared to be wider overall, with values ranging from 0.6 to 1.7 µm in width. The frequency of the cracking also appeared to be higher, with some of the cracking resembling tears within the coating (**Fig. 3-4(b)**). These cracks made sense considering the large differences in the coefficients of thermal

expansion (CTE) for a representative PDMS (volume CTE = 9.6 x 10^{-4} K^{-1} for Sylgard 184 from Dow Corning),[125] silicon dioxide (linear CTE = ~10^{-7} K^{-1}),[118] and silicon (linear CTE = ~10^{-6} K^{-1}).[126] The PDMS CTE is used as a substitute for CV-1144-0, as its CTE is unknown. Volumetric CTE can be approximated into linear CTE by dividing by 3 (PDMS linear CTE = ~3.2 x 10^{-4} K^{-1}). These incongruities can cause stresses between the layers that will lead to breakage. Because the AO exposure occurred at 300 °C, the cracks on the surface could form not only from the difference in density between the SiO_x formed and the underlying bulk CV-1144-0, but also because of the differences in the CTE between the substrate, the bulk silicone, and the silica film formed on top, with the bulk silicone growing and shrinking at a far greater magnitude compared to the other two layers. There may also be contributions from the possible thermal decomposition of the silicone at 300 °C causing the degradation. SEM analysis of the RTV-560 showed that the silicone cured on the silicon disc was far smoother before exposure compared to the silicone cured within the pan. Herringbone-like patterns appeared to emanate short distances from small pieces of dust incidentally found on the surface before disappearing on the rest of the surface. This observation led us to believe that outside pressures were what caused the patterns in the 25 °C sample, forming the patterns in a fashion similar to a mold. One other factor behind the lack of patterns could be the much thinner coating we originally cured on the silicon disc compared to that in the metal pan (~1 mm vs. ~1 cm). After exposure, more significant cracking and degradation was observed compared to the exposure at 25 °C, with crevices that resembled tearing within the bulk silicone. In addition, unlike the surface of RTV-560 after its 25 °C exposure, the surface of RTV-560 exposed at 300 °C was

otherwise not very smooth, with less regular wavy patterns observed on the surface structure of RTV-560 after exposure. As with CV-1144-0, the differences in the CTEs between the silicon substrate, the bulk silicone (linear CTE = 2.0 x 10^{-4} K^{-1}),[127] and the oxide layer have likely contributed to the cracking observed, with some of the cracking occurring while the material cooled down. The difference compared to CV-1144-0 could be because of the presence of ferric oxide in the bulk, though we cannot explain how that changes factors like the CTE. Finally, as with CV-1144-0, there were likely also contributions from the decomposition of RTV-560 that might be causing the surface degradation.

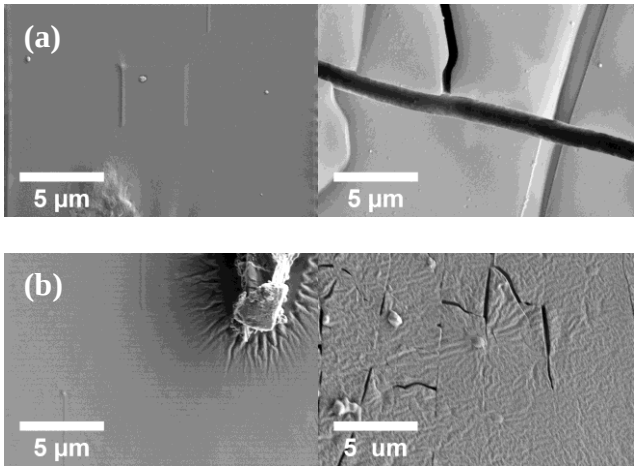

Fig. 3-4. SEM images of CV-1144-0 and RTV-560 before and after 300 °C exposure. (left) before and (right) after O-atom exposure. **(a)** is CV-1144-0. **(b)** is RTV-560.

3.3.3. QCM Erosion Yields

CV-1144-0 was diluted 1:1 with xylene and spin coated onto gold-coated QCM crystals, with which the erosion yield at 25 °C was then measured. Erosion yields for the Kapton-like polyimide spin coated onto the QCM crystals were also measured. Representative plots of mass loss per O-atom are shown (**Fig. 3-5(a)**). What was notable

about the CV-1144-0 erosion trends was that they all appeared to follow similar patterns whereby there was an initial gain in mass followed subsequently by a relatively linear rate of mass loss with respect to O-atom fluence. Because of the linear sections found in the plots, these sections were able to be fit with linear regressions in order to calculate an *in-situ* erosion yield. These numbers were converted to g O-atom^{-1} and are listed in the table below. The average erosion yield of the Pyralin polyimide samples was 3 x 10^{-24} g O-atom^{-1}, the same erosion yield as Kapton H.

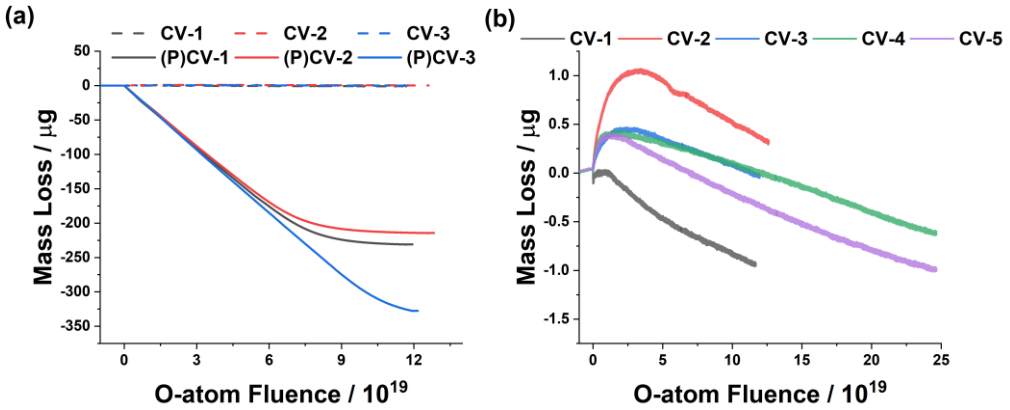

Fig. 3-5. QCM mass loss plots as a function of O-atom fluence. **(a)** Plots of CV-1144-0 and polyimide as a function of O-atom fluence from the QCM mass loss experiments conducted at 25 °C. (P) designates polyimide exposed at the same time with the respective CV-1144-0 in a particular experiment. **(b)** Same plots of CV-1144-0 as **(a)** but at a much smaller scale, with additional results from two higher-fluence mass loss experiments (CV-4 and CV-5) conducted for 2.5 x 10^{20} O-atoms cm^{-2}. Polyimide was not included for higher fluence exposures.

The erosion yields were variable, though they exist within a narrow range of 4.93 to 8.48 x 10^{-27} g O-atom^{-1}. Compared to CV-1144-0 exposures in LEO on EOIM-III,[28] this experiment's erosion yields were two to three orders of magnitude lower; yet, these LEO experiments were exposed to a fluence slightly lower than this experiment's maximum fluence (2.07 vs. 2.5 x 10^{20} O-atoms cm^{-2}, respectively). A study designed to replicate LEO

conditions using a plasma etcher in a simulated environment on Earth also produced a similar order of magnitude erosion yield as these EOIM-III samples.[128] The cause of these discrepancies is unclear. In regard to the results from plasma etcher experiment, one could cite a major factor being the presence of plasma, but it is unclear what the plasma density was during the EOIM-III experiments. Photodissociation has previously been identified as a cause of degradation, but its effects here are also unclear. It is also unlikely that outgassing would be a significant factor, for while the CV-1144-0 QCM trials were exposed within a run-time of 7-14 hours, the EOIM-III samples were exposed for only a slightly longer period of 58 hours.

Table 3-1. Erosion yields of CV-1144-0 with units of 10^{-27} g O-atom^{-1}, measured from linear sections of plots of mass loss over time. Numbers reflect different experiments (CV-1: CV-1144-0-1). Average reflects the mean erosion yield of all listed calculated yields.

Material	Erosion Yield
CV-1	8.48
CV-2	8.26
CV-3	5.35
CV-4	4.93
CV-5	6.10
Average	6.25

One other material the CV-1144-0 erosion yield can be compared to is that of DC 93-500, which has been exposed to atomic oxygen both in LEO (MISSE-8)[33, 129] and in a simulated environment on Earth (Townsend et al. (1996)).[128] Comparing the erosion yield from MISSE-8 to this experiment, DC 93-500 compares quite favorably to CV-1144-0, with a similar order of magnitude erosion yield. However, as with the EOIM-III experiments, there are complications to this comparison. First, unlike the experimental design of the QCM experiment, the MISSE-8 test had an order of magnitude higher atomic

oxygen fluence compared to the current study's highest fluence experiment (4.62 x 10^{21} O-atoms cm^{-2}). The MISSE-8 mission also operated in low-Earth orbit for 2 years. Thus, while one might assume that the recorded erosion yield of DC 93-500 was reflective of a constant rate of erosion, this was not necessarily the case. Above a certain AO fluence, there is the possibility that additional AO will not cause further mass loss as a result of the growing silicon-oxide layer preventing further oxidation. From our CV-1144-0 QCM experiment, we observed that even up to 2.5 x 10^{20} O-atoms cm^{-2} fluence the mass continues to slowly decrease in a linear fashion, whereas the DC 93-500 was exposed to a fluence ~18.5 times this amount. If erosion slowed down or even stopped at a certain point, this could affect the calculation of the erosion yield. As Yan et al. (2001)[27] observed with their studies on CV-1144-0, the rate of erosion of their sample decreased and nearly reached zero above a particular fluence. The atomic oxygen erosion of polyhedral oligomeric silsesquioxane (POSS) polyimides show a similar phenomenon, with mass loss rates trending downward over time.[32] These materials are relevant, as, similar to silicones, POSS will form a silicon-oxide layer after exposure to atomic oxygen. On the other hand, results from DC 93-500 eroded in a simulated atomic oxygen environment[30] using a plasma asher show an erosion yield three orders of magnitude higher than those of this study, with an AO fluence only ~3 times higher than its counterpart exposed in space. It is unclear why the ground-based exposure of DC 93-500 has such a high erosion yield, though the presence of plasma could be a factor.

Table 3-2. Erosion yields from literature. (top 3, Ground) Erosion yields of CV-1144-0 on various substrates from Townsend et al. (1996).[128] (top 3, LEO) Erosion yields of CV-1144-0 on various substrates from EOIM-III space exposure.[28] (bottom, ground) Erosion yield of DC 93-500 on ground from Dworak et al. (2006).[30] (bottom, LEO) Erosion yield of DC 93-500 from MISSE-8 space exposure.[129] Yields all measured from total mass loss divided by total O-atom fluence, with units in g O-atom^{-1}. DC 93-500 erosion yield calculated from density[129] = 1.08 g cm^{-3} and erosion yield = 3.81 x 10^{-27} cm^3 O-atom^{-1}.

Coating Substrate	Ground	LEO
Silver-coated Teflon	4.24 x 10^{-25}	9.8318 x 10^{-25}
Kapton-H	2.35 x 10^{-24}	2.6575 x 10^{-24}
Beta Cloth	2.79 x 10^{-25}	3.158 x 10^{-25}
DC 93-500	6.060 x 10^{-24}	4.12 x 10^{-27}

3.4. Conclusion

An atomic oxygen exposure study was conducted on the silicones CV-1144-0 and RTV-560, both to better characterize their oxidation properties and understand how they would perform in low-Earth orbit, as well as evaluate their performance at higher temperatures for the purposes of atmospheric entry. On both materials, extended exposure of O-atoms of 2.4 x 10^{20} O-atoms cm^{-2} at 25 °C led to much of the surface silicon and oxygen being composed of SiO_x along with residual carbon attributed to either adventitious carbon or silicon, while the surface overall became much smoother but with cracks appearing at certain points. The higher temperature exposure at 300 °C with 1.8 x 10^{20} O-atoms cm^{-2} fluence resulted in similar chemical changes as at 25 °C, but with far more significant cracking observed, along with more serious degradation observed on RTV-560. In addition, it was found that at 25 °C, for all of the trials, CV-1144-0 first gained, then steadily lost mass, with the average of the linear sections of the QCM plots being 6.25 x 10^{27} g O-atom^{-1}, a yield comparable to the average erosion yield of DC 93-500 exposed in

LEO, but far lower compared to plasma etching techniques using atomic oxygen as well as the CV-1144-0 average erosion yield observed from the EOIM-III LEO exposure. While the cracks are expected, more will need to be done to investigate these discrepancies in the results between this experiment and the other studies mentioned.

3.5. References

9. Poovathingal, S.; Schwartzentruber, T. E.; Murray, V. J.; Minton, T. K., Molecular Simulation of Carbon Ablation Using Beam Experiments and Resolved Microstructure. *AIAA Journal* **2016**, *54*, 999-1010.
24. Finckenor, M.; Visentine, J.; Adam, S.; Zwiener, J.; Loebs, V. In *CONTAMINATION, UV RADIATION, AND ATOMIC OXYGEN EFFECTS ON ISS THERMAL CONTROL MATERIALS*, 41st Aerospace Sciences Meeting and Exhibit, 2003; p 1084.
25. de Groh, K. K.; McCollum, T. A., Low Earth orbit durability of protected silicone for refractive photovoltaic concentrator arrays. *Journal of Spacecraft and Rockets* **1995**, *32*, 103-109.
27. Yan, L.; Gao, X.; Bungay, C.; Woollam, J. A., Study of surface chemical changes and erosion rates for CV-1144-0 silicone under electron cyclotron resonance oxygen plasma exposure. *Journal of Vacuum Science & Technology A* **2001**, *19*, 447-454.
28. Scialdone, J. J.; Clatterbuck, C. H.; Ayres-Treusdell, M.; Park, G.; Kolos, D., *Atomic Oxygen and Space Environment Effects on Aerospace Materials Flown with EOIM-III Experiment*, 1996.
29. Samwel, S. W., Low Earth Orbital Atomic Oxygen Erosion Effect on Spacecraft Materials. *Space Research Journal* **2014**, *7*, 1-13.
30. Dworak, D. P.; Banks, B. A.; Karniotis, C. A.; Soucek, M. D., Evaluation of Protective Silicone/Siloxane Coatings in Simulated Low-Earth-Orbit Environment. *Journal of Spacecraft and Rockets* **2006**, *43*, 393-401.
31. Qian, M.; Murray, V. J.; Wei, W.; Marshall, B. C.; Minton, T. K., Resistance of POSS Polyimide Blends to Hyperthermal Atomic Oxygen Attack. *ACS Applied Materials & Interfaces* **2016**, *8*, 33982-33992.
32. Minton, T. K., et al., Atomic Oxygen Effects on POSS Polyimides in Low Earth Orbit. *ACS Applied Materials & Interfaces* **2012**, *4*, 492-502.
33. De Groh, K. K.; Banks, B. A., Atomic Oxygen Erosion Data from the MISSE 2-8 Missions. **2019**.
50. Bessire, B. K.; Borner, A. P.; Meurisse, J. B.; Monk, J. D., Progress Towards Modeling the Mars Science Laboratory PICA-NuSil Heatshield. **2019**.
55. Garton, D. J.; Minton, T. K.; Maiti, B.; Troya, D.; Schatz, G. C., A crossed molecular beams study of the O(3P)+H2 reaction: Comparison of excitation function with accurate quantum reactive scattering calculations. **2003**, *118*, 1585-1588.
56. Troya, D.; Schatz, G. C.; Garton, D. J.; Brunsvold, A. L.; Minton, T. K., Crossed beams and theoretical studies of the O(3P)+CH4→H+OCH3 reaction excitation function. *The Journal of Chemical Physics* **2004**, *120*, 731-739.
57. Buczala, D. M.; Brunsvold, A. L.; Minton, T. K., Erosion of Kapton H® by Hyperthermal Atomic Oxygen. *Journal of Spacecraft and Rockets* **2006**, *43*, 421-425.
96. Murad, E., Spacecraft Interaction with Atmospheric Species in Low Earth Orbit. *Journal of Spacecraft and Rockets* **1996**, *33*, 131-136.

97. Flowers, O.; Stewart, D. A., *Catalytic surface effects on contaminated space shuttle tiles in a dissociated nitrogen stream*; National Aeronautics and Space Administration, Ames Research Center, 1985.
98. Magasinski, A.; Dixon, P.; Hertzberg, B.; Kvit, A.; Ayala, J.; Yushin, G., High-performance lithium-ion anodes using a hierarchical bottom-up approach. *Nature Materials* **2010**, *9*, 353-358.
99. Zhao, K.; Li, K.; Wang, Y., Rapid densification of C/SiC composite by incorporating SiC nanowires. *Composites Part B: Engineering* **2013**, *45*, 1583-1586.
100. Groh, K. K. d.; McCollum, T. A., Low Earth orbit durability of protected silicone for refractive photovoltaic concentrator arrays. *Journal of Spacecraft and Rockets* **1995**, *32*, 103-109.
101. Banks, B. A.; Rutledge, S. K.; Paulsen, P. E.; Steuber, T. J., Simulation of the low earth orbital atomic oxygen interaction with materials by means of an oxygen ion beam. *NASA Technical Memorandum* **1989**, *101971*.
102. Wang, H.; Minton, K. T.; Murray, J. V.; Dai, D.; Wu, B.; Yang, Y.; Che, L., Study on the Resistance of Thermal Control Coating of Phenyl Silicone Rubber to Hyperthermal Atomic Oxygen Attack. *Journal of Astronautics* **2017**, *38*, 662-668.
103. De Groh, K. K.; Dever, J. A.; Jaworske, D. A.; Miller, S. K.; Sechkar, E. A.; Panko, S. R., NASA Glenn research center's materials international space station experiments (MISSE 1-7). **2008**.
104. Shao, Y.; Brook, M. A., Structured metal films on silicone elastomers. *Journal of Materials Chemistry* **2010**, *20*, 8548-8556.
105. Grassie, N.; Macfarlane, I. G., The thermal degradation of polysiloxanes—I. Poly(dimethylsiloxane). *European Polymer Journal* **1978**, *14*, 875-884.
106. Camino, G.; Lomakin, S. M.; Lazzari, M., Polydimethylsiloxane thermal degradation Part 1. Kinetic aspects. *Polymer* **2001**, *42*, 2395-2402.
107. de Groh, H.; Miller, S.; Smith, I.; Daniels, C.; Steinetz, B. In *Adhesion of Silicone Elastomer Seals for NASA's Crew Exploration Vehicle*, 44th AIAA/ASME/SAE/ASEE Joint Propulsion Conference & Exhibit, 2008; p 4625.
108. Taylor, E. W. In *Overview of new and emerging radiation resistant materials for space environment applications*, 2011 Aerospace Conference, IEEE: 2011; pp 1-11.
109. Langston, S. L.; Lang, C. G.; Samareh, J. A. In *Parametric Study of an Ablative TPS and Hot Structure Heatshield for a Mars Entry Capsule Vehicle*, AIAA SPACE and Astronautics Forum and Exposition, 2017; p 5290.
110. Cooper, P.; Miserentino, R.; Sawyer, J.; Leatherwood, J. In *Assessment of the Shuttle Orbiter Thermal Protection System undensified tiles under mission dynamic loads*, 23rd Structures, Structural Dynamics and Materials Conference, 1982; p 790.
111. Schott, T.; Munk, M.; Herring, G.; Grinstead, J.; Prabhu, D. In *Fiber-based measurement of bow-shock spectra for reentry flight testing*, 48th AIAA Aerospace Sciences Meeting Including the New Horizons Forum and Aerospace Exposition, 2010; p 301.
112. Banks, B.; Rutledge, S.; Sechkar, E.; Stueber, T.; Snyder, A.; de Groh, K.; Haytas, C.; Brinker, D. In *Issues and effects of atomic oxygen interactions with silicone contamination on spacecraft in low earth orbit*, Materials in a Space Environment,

Proceedings of the 8 th International Symposium, and Protection of Materials and Structures from the LEO Space Environment, Proceedings of the 5 th International Conference. ICPMSE, 2000.
113. Milos, F. S.; Scott, C. D.; Papa, S. V. D., Arcjet Testing and Thermal Model Development for Multilayer Felt Reusable Surface Insulation. *Journal of Spacecraft and Rockets* **2014**, *51*, 397-411.
114. Liu, C. K.; Glassford, A. P. M., Kinetics data for diffusion of outgassing species from RTV 560 silicone rubber. *Journal of Vacuum Science and Technology* **1978**, *15*, 1761-1768.
115. Rao, N.; Xie, X.; Wielizcka, D.; Zhu, D.-M., Quartz crystal microbalance sample stage for in situ characterization of thickness and surface morphology of spin coated polymer films. *Review of Scientific Instruments* **2006**, *77*, 116111.
116. Cooper, R.; Upadhyaya, H. P.; Minton, T. K.; Berman, M. R.; Du, X.; George, S. M., Protection of polymer from atomic-oxygen erosion using Al2O3 atomic layer deposition coatings. *Thin Solid Films* **2008**, *516*, 4036-4039.
117. Packirisamy, S.; Schwam, D.; Litt, M. H., Atomic oxygen resistant coatings for low earth orbit space structures. *Journal of Materials Science* **1995**, *30*, 308-320.
118. El-Kareh, B.; Hutter, L. N., *Fundamentals of semiconductor processing technology*; Springer Science & Business Media, 2012.
119. NuSil CV-1144-0 DataSheet. NuSil Technology: 2014.
120. Vandeparre, H.; Damman, P., Wrinkling of Stimuloresponsive Surfaces: Mechanical Instability Coupled to Diffusion. *Physical Review Letters* **2008**, *101*, 124301.
121. Yu, S.; Ni, Y.; He, L.; Ye, Q.-L., Tunable Formation of Ordered Wrinkles in Metal Films with Controlled Thickness Gradients Deposited on Soft Elastic Substrates. *ACS Applied Materials & Interfaces* **2015**, *7*, 5160-5167.
122. Bowden, N.; Brittain, S.; Evans, A. G.; Hutchinson, J. W.; Whitesides, G. M., Spontaneous formation of ordered structures in thin films of metals supported on an elastomeric polymer. *Nature* **1998**, *393*, 146-149.
123. Chan, E. P.; Crosby, A. J., Spontaneous formation of stable aligned wrinkling patterns. *Soft Matter* **2006**, *2*, 324-328.
124. Tanaka, T.; Sun, S.-T.; Hirokawa, Y.; Katayama, S.; Kucera, J.; Hirose, Y.; Amiya, T., Mechanical instability of gels at the phase transition. *Nature* **1987**, *325*, 796-798.
125. Sylgard 184 Silicone Elastomer Data Sheet. Dow Corning: 1998.
126. Okada, Y.; Tokumaru, Y., Precise determination of lattice parameter and thermal expansion coefficient of silicon between 300 and 1500 K. *Journal of Applied Physics* **1984**, *56*, 314-320.
127. RTV560 Technical Data Sheet. Momentive Performance Materials: 2012.
128. Townsend, J. A.; Park, G. In *A comparison of atomic oxygen degradation in low earth orbit and in a plasma etcher*, NASA: 1996; pp 295-304.
129. De Groh, K. K.; Banks, B. A.; Asmar, O. C.; Yi, G. T.; Mitchell, G. G.; Guo, A.; Sechkar, E. A., Erosion Results of the MISSE 8 Polymers Experiment After 2 Years of Space Exposure on the International Space Station. **2017**.

CHAPTER FOUR

EFFECT OF SILICONE COATING ON ATOMIC OXYGEN REACTIVITY WITH FIBERFORM AND PHENOLIC IMPREGNATED CARBON ABLATOR

Contribution of Authors and Co-Authors

Manuscript in Chapter 4

Author: David Z. Chen

Contributions: Prepared all samples. Programmed heating program. Assisted in conducting and collecting scattering and decomposition experimental data. Conducted XPS and SEM analyses on all samples. Analyzed all scattering data. Assisted in writing and editing the manuscript.

Author: Chenbiao Xu

Contributions: Assisted in conducting and collecting scattering and decomposition experimental data. Provided important feedback for analysis.

Author: Timothy K. Minton

Contributions: Assisted with analysis and editing of the manuscript for final submission.

Manuscript Information

David Z. Chen, Chenbiao Xu, Timothy K. Minton

Journal of Spacecraft and Rockets

Status of Manuscript:
_x__ Prepared for submission to a peer-reviewed journal
____ Officially submitted to a peer-reviewed journal
____ Accepted by a peer-reviewed journal
____ Published in a peer-reviewed journal

AIP Publishing

4.1. Introduction

Ablative heat shields such as phenolic impregnated carbon ablator (PICA) and its variants PICA-X and PICA-D are used to protect spacecraft from the extreme heat of atmospheric entry through pyrolytic loss of mass.[34, 130] Composed of a carbon fiber preform substrate and a phenolic resin impregnated as the matrix, PICA and its variants are being used in current NASA missions such as Mars Science Laboratory,[34] Mars 2020,[39] the planned Dragonfly Mission,[130] as well as those of private industry such as SpaceX's Dragon capsule.[34] Accurate modeling of what happens to these materials in various atmospheric entry conditions requires a detailed understanding of how the resin decomposes thermally and how the charred material and the carbon fiber preform substrate reacts with atmospheric species, most importantly atomic oxygen.[50] The thermal decomposition of the resin has been the subject of numerous studies, including by our group,[35-36] and the oxidation of carbon at high temperatures has received increasing attention recently,[131-134] although less is known about the specific oxidation behavior of carbon fiber preform and char. The addition of a silicone anti-dust coating creates yet another variable that must be considered. Thus, we have conducted a study of silicone-coated and uncoated carbon fiber preform and PICA in order to gain a better understanding of how this coating affects the behavior of the underlying material. Knowing how to predict the material response of these heat shields is essential not only for protecting the safety of astronauts, but also for designing better heat shield materials for future development.

A number of previous studies have looked at the material response for different types of model systems. These have primarily involved mass-loss measurements of

different types of composites, including matrix-inhibited carbon/carbon composites,[48-49, 135] chars,[136-137] and C/SiC composites.[138-143] In contrast, our group has conducted molecular beam-surface scattering studies to probe the molecular-level details of the oxidation of vitreous carbon.[42] Vitreous, or glassy, carbon,[41] has an sp^2-configuration within a disordered carbon morphology that has been used as a model material for the base preform structure of an ablative heat shield. The molecular beam technique involving the use of a quadrupole mass spectrometer allowed us to quantify specific products leaving the surface as well as characterize their molecular beam-surface scattering dynamics. Using this technique, Murray et al.[42-43] was able to characterize vitreous carbon oxidation in highly specific detail, the data for which led to the development of three different oxidation material response models[44-46] and furthered our understanding of the mechanisms of heat shield oxidation. Our group also undertook O-atom beam scattering experiments with the actual carbon fiber preform substrate used in ablative heat shields, and the results showed remarkable similarities with that of vitreous carbon. As described in Poovathingal et al. (2021),[47] much of the behavior, such as the temperature-dependent flux of O and CO, as well as the angular distributions of scattered products, were similar to the dynamics described in Murray et al. (2015),[42] with the primary difference being that O-atom scattering on carbon fiber preform exhibits stronger characteristics of multiple-bounce scattering on the three-dimensional fiber network. Poovathingal et al.[47] investigated the long residence times of O and CO products that were clear in the data on carbon fiber preform and became noticeable in hindsight on the earlier experiments with vitreous carbon; these “slow” products are also important in the data that are presented herein.

In addition to vitreous carbon, we had studied the atomic oxygen oxidation of silicon carbide (SiC), another material of interest for certain heat shields and of relevance to the present study. SiC has received attention mainly for its potential as a coating or a matrix material within a carbon/SiC composite. Our study, as described in Chapter Two and using a similar molecular beam-surface scattering technique as was used with vitreous carbon,[42-43] focused on the O-atom interactions with an SiC wafer that already had an oxide layer on its surface. This study found the oxide layer to be stable up to a certain temperature, the passive-to-active oxidation transition temperature,[17-18] at which the decomposition of the oxide layer was rapid and irreversible and produced gaseous Si and SiO. When the incident O-atom flux was lower, a graphitic layer remained on the SiC surface above the passive-to-active transition and was relatively unreactive to O-atom attack. On the other hand, when the O-atom flux was higher, the graphitic layer did not form and the SiC surface was etched by bombarding O-atoms, leading to roughly equal fluxes of volatile SiO and CO products in the process. The formation and removal of a silicon-oxide layer is highly relevant to the present chapter which examines how a silicone coating affects the oxidation of the underlying material as it is heated under atomic oxygen attack.

The surface transformation of silicone by atomic oxygen has been investigated in previous studies with respect to its relevance to materials degradation in low-Earth orbit,[25, 28, 129] and we have conducted a companion study, described in Chapter Three, involving the specific silicones used for ablative heat shields that are relevant to the present study, CV-1144-0, a spray-on, anti-dust coating, and RTV-560, a binding agent. We exposed

these materials to extended atomic oxygen bombardment at room temperature and 300°C and examined the exposed surface by X-ray photoelectron spectroscopy (XPS) and scanning electron microscopy (SEM). We discovered that O-atom bombardment of both silicones transformed much of the surface layer to SiO_2, leaving behind far less of the original silicone chemical environment. SEM analysis also revealed cracks and fissures that were apparently formed during O-atom bombardment, with bigger cracks occurring at higher frequency observed after the higher temperature bombardment. Despite these, using a room-temperature quartz crystal microbalance, we still observed that high-fluence exposure of the CV-1144-0 to O-atoms resulted in negligible mass loss, especially compared to Pyralin, a Kapton-like PMDA-ODA polyimide.[32, 116]

In an effort to understand how a silicone coating might affect the performance of a carbon-phenolic heat shield in an oxidizing atmosphere, we have conducted a comparative study, described in this chapter, of the atomic oxygen beam-surface scattering dynamics on relevant model samples: pristine carbon fiber preform (also known as FiberForm), FiberForm with a coating of CV-1144-0, pristine PICA, and PICA with a coating of CV-1144-0. Coated PICA is most comparable to the actual heat shield material used on spacecraft designed for atmospheric entry.[50] Based on our previous studies, we expected that the addition of a silicone coating to FiberForm would both depress reactive product formation as well as dramatically increase O-atom scattering from the surface. We further expected that the inevitable decomposition of the oxide coating that was formed would return the temperature-dependent reactivity of the coated FiberForm back to that of uncoated FiberForm. We also aimed to examine the thermal decomposition products from

the materials as the sample was pyrolyzed. Our earlier studies of PICA pyrolysis were available to help in the interpretation of new data on silicone-coated PICA. On the other hand, no prior molecular beams studies have been conducted on any form of carbon-phenolic ablator, so the new experiments undertaken for the present study did not have a clear benchmark. Therefore, we found it helpful to compare the O-atom scattering dynamics on silicone-coated PICA with those on pristine PICA and silicone-coated FiberForm. One additional factor we wanted to study was whether our previous study on FiberForm was reflective of the way in which this material is actually used. In our prior study, FiberForm was first annealed up to 1800 K, followed by the temperature being reduced, before data collection began. FiberForm is known to contain impurities such as calcium,[144-145] which results in different reactivity with atomic oxygen before and after annealing. In addition, it is known that the presence of metal catalysts can promote the dissociation of O_2 into atomic oxygen, and thus promote its reactivity with adjacent carbon.[146] Furthermore, it is possible that pristine FiberForm is not completely pyrolyzed to carbon and a residual organic component might be removed upon annealing, also altering the reactivity of the fibers. Our study aims to shed light on all of these factors that might lead to uncertainties in relating the experimental results to material response in actual ablation environments.

4.2. Materials and Methods

4.2.1. Molecular Beam-Surface Scattering Apparatus

This study was conducted using a similar molecular beam-surface scattering technique as those involving the oxidation of vitreous carbon[42] and FiberForm.[47] The apparatus was a crossed molecular beams apparatus reconfigured for beam-surface scattering consisting of a primary chamber where the beam-surface scattering was conducted along with a differentially pumped secondary chamber that functioned as the source for the molecular beam. A pulsed molecular beam composed of hyperthermal O and O_2 was directed at the samples at an incident angle of $\theta_i = 45°$ as measured from the normal of the macroscopic surface (hereafter referred to as the "surface"). The primary chamber vacuum was maintained near ~5 x 10^{-7} Torr with a large cryogenic pump and a large turbomolecular pump while the beam was running, while that of the secondary chamber vacillated between ~1 to 7 x 10^{-4} Torr while the beam was pulsed. Detection of scattered products was accomplished with a rotatable mass spectrometer detector, which rotated in the plane defined by the incident molecular beam axis and the surface normal. The mass spectrometer consisted of an electron impact ionizer[59] with an electron energy of 160 eV, a quadrupole mass filter, and a Daly-type ion counter. The entire detector was triply differentially pumped with three ion pumps. The electron-impact ionizer was in the lowest-pressure region, which had an additional turbomolecular pump to assist the ion pump in further reduction of residual gases in the ionization region. The Daly detector's pulses, correlated with ion impacts, were recorded by a multichannel scaler that yielded a signal proportional to the scattered product number density as a function of flight time, *N(t)*, from

the surface to the ionizer, a distance of 34.4 cm. These time-of-flight (TOF) distributions were used to derive translational energy distributions of the scattered products with a density-to-flux conversion that assumed a monoenergetic incident beam.[53, 61] Average energies of the scattered products were determined from the translational energy distributions, which were then integrated to obtain the total relative flux of the scattered products at a particular final, or scattering, angle, θ_f. Flux angular distributions were thus obtained by plotting the flux of the scattered products as a function of θ_f.

A 2 Hz laser detonation source, described in a previous study,[54] was used to produce the molecular beam of hyperthermal $O(^3P)$[55] and $O_2(^3\Sigma_g^-)$.[56] The TOF distributions, corresponding translational energy distributions, and O/O_2 relative fluxes were determined by directing the beam straight into the detector. Further velocity selection of the beam was conducted using a chopper wheel, synchronized to the laser detonation pulse, that had three equally spaced 1.6 mm-thick slots and a rotation frequency of 300 Hz. During analysis of the data, the contribution of dissociative ionization of O_2 (to form O^+) was subtracted from the TOF distributions collected at a mass-to-charge ratio of 16 (O^+). The mean translational energies of the O and O_2 components of the beam had average energies of 487 and 948 kJ mol^{-1}, respectively, and the average mole fractions of O and O_2 were 91.2% and 88%, respectively. These conditions remained quite stable throughout the experiments. Plots detailing the specific translational energy distributions and mole fractions are shown in **Fig. A-1** below in the appendix.

4.2.2. Samples and Surface Analysis

Samples of both pristine and coated carbon fiber preform (branded as FiberForm), sourced from Fiber Materials Inc., were obtained from NASA Ames, with pristine FiberForm received in a large block, while coated FiberForm was received in 30 x 30 x 5 mm slabs. The coated samples had one box-coat of the anti-dust silicone CV-1144-0 on one side. Box coating is the process by which the coating is sprayed onto the sample. One box-coat typically represents an approximate coating thickness of 100-200 microns. The thickness presumably decreases deeper into the bulk of the fiber network, but it was unknown how deep the silicone penetration was. The silicone, from NuSil Technologies LLC, was composed of 95.2% polydimethylsiloxane chains and 4.8% polydiphenylsiloxane chains.[27] The coating was applied at NASA Ames and allowed to set at room temperature for seven days. To use these samples in our apparatus, we further cut the FiberForm into small units of 7 x 25 x 2 mm, preserving the silicone-coated sides on the FiberForm. In addition, samples of PICA were also prepared using a silicone-coated PICA block obtained from NASA Ames. The PICA block was coated on one side with 1.5 box-coats of CV-1144-0. From this block, we cut out 7 x 25 x 2 mm slabs from the coated side, as well as slabs opposite from the coated side to serve as samples of uncoated PICA. An initial oxide was prepared on the coated slabs by exposing the coated surfaces to a fluence of ~2.3 x 10^{20} O-atoms cm^{-2} using our atomic oxygen molecular beam source chamber with a technique described previously.[57] Before starting the experiments, SEM and XPS analyses were done on these samples, with complete XPS results shown in **Table 4-1**. In preparation for the experiments, the samples were mounted in our high-temperature

sample mount in the source chamber and heated resistively with an external power supply.[36, 42] Temperature was manually measured using a pyrometer with a disappearing carbon filament.[47]

Table 4-1. Chemical compositions of the macroscopic surfaces of the listed sample materials before and after annealing at 1800 K. "In-beam" refers to sample surface location where beam impinged. "Out-of-beam" refers to position away from beam spot. All other annealed samples had XPS taken at beam impingement spots.

		Carbon	Oxygen	Silicon	Calcium	Fluorine
(a)	**Pristine FiberForm**	96.3	3.4		0.8	
(b)	**Annealed FiberForm: In-beam**	98.8	1.2			
(c)	**Annealed FiberForm: Out-of-beam**	100				
(d)	**Coated FiberForm**	38.4	46.1	15.5		
(e)	**Annealed Coated FiberForm**	96.9	3.1			
(f)	**Uncoated PICA**	86.2	13.8			
(g)	**Annealed PICA**	96	2.6			1.4
(h)	**Coated PICA**	18.2	58.2	22.8	0.8	
(i)	**Annealed Coated PICA**	92.8	5.2	1.3	0.7	

4.2.3. Primary Experimental Procedure

Before conducting detailed experiments, we first examined the effect of annealing to 1800 K under high vacuum (~5 x 10^{-7} Torr) for 30 minutes on samples of uncoated and coated FiberForm. Afterwards, SEM analysis was conducted on the annealed samples (**Fig. 4-2**). For our primary O-atom beam-surface scattering experiments, on each of our samples we conducted the following procedures. First, we monitored the decomposition products from the FiberForm, PICA, coated FiberForm, and coated PICA samples with our mass spectrometer as they were heated, in high vacuum, from room temperature at a rate of 0.5°C s^{-1}, up to a high temperature, which was typically 1000 K. For coated FiberForm, we

conducted two experiments, one in which the initial high temperature was 1000 K and the second in which the initial high temperature was 1600 K. For convenience, we will refer to the coated FiberForm initially raised to 1000 K as coated FiberForm_A, and the coated FiberForm initially raised to 1600 K as coated FiberForm_B. During this initial temperature ramp, the detection (or final) angle of the detector was θ_f = 5° from the normal to the macroscopic sample plane facing toward the detector, which we will refer to as the sample "surface" while recognizing that the three-dimensional fiber network of the sample actually presents many microscopic surfaces, and mass spectra were collected with a scan range of *m/z* = 0.1 to 110 amu and a collection time for each mass spectrum of 11.01 s. A background mass spectrum was collected before the temperature ramp and subtracted from the mass spectra collected during heating for analysis. Integrated intensities for each peak were analyzed in OriginPro 2021. After reaching the initial high temperature (1000 K or 1600 K), each sample was held at this temperature for two hours before further experimentation commenced with the hyperthermal O/O_2 (described in 4.2.1).

The sample was then adjusted such that the incident O-atom beam was directed at the sample with an incident angle of θ_i = 45° with respect to the macroscopic surface normal, and TOF distributions were then collected with various final angles, θ_f, also with respect to the surface normal but on the opposite side of the normal from that of the incident beam. TOF distributions were collected for *m/z* = 16(O^+), 32(O_2^+), 28(CO^+, Si^+), and 44(CO_2^+, SiO^+) from θ_f = 5° to 85° in 5° intervals. These TOF distributions were collected in two rounds, first as θ_f increased from 5° to 85°, and then as θ_f decreased from 85° to 5°. This procedure was repeated such that two sets of TOF distributions for each *m/z* ratio were

collected at each θ_f, and these two sets were added together. Possible products at *m/z* = 17 and 60 were also investigated, but signals at these mass-to-charge ratios were weak or non-existent, so we did not attempt to analyze them. For FiberForm, TOF distributions were collected at each θ_f for a total of 17,000 pulses at all observed *m/z* ratios. For coated FiberForm_A, TOF distributions were collected for a total of 17,000 pulses for *m/*z = 16 and 32 and 34,000 pulses for *m/*z = 28 and 44. For the coated FiberForm_B, TOF distributions were collected for a total of 17,000 pulses for *m/*z = 16, 32, and 28, and 34,000 pulses for *m/*z = 44. For uncoated PICA, TOF distributions were collected for a total of 17,000 pulses for each and all *m/z* ratios. For the coated PICA, TOF distributions were collected for a total of 17,000 pulses for *m/z* = 16 and 32, and 34,000 for *m/z* = 28.

After TOF distributions were collected for all final angles at the initial high sample temperature, the detection angle was adjusted to $\theta_f = 45°$ (with θ_i remaining at 45°), and a study of the temperature dependence of volatile product evolution was conducted. For all samples, this temperature-dependent data began at 1000 K. Given that the relevant data had already been collected at 1000 K for all samples except coated FiberForm_B, the temperature of these samples was incremented to 1100 K. For FiberForm_B, the temperature was lowered from 1600 K to 1000 K. The temperature for all samples was raised in 100 K increments to 1800 K and then decreased in 100 K increments back to 1000 K. For each sample temperature, TOF distributions were collected at *m/z* = 16, 32, 28, and 44. For the uncoated FiberForm, coated FiberForm_A, and uncoated PICA, individual TOF distributions were collected for 500 beam pulses at each *m/z* ratio at each temperature. For the coated FiberForm_B, individual TOF distributions were collected for 500 beam pulses

at *m/z* = 16, 32, and 28, and for 1000 beam pulses for *m/z* = 44. For coated PICA, individual TOF distributions were collected for 500 beam pulses at *m/*z = 16 and 32 and for 1000 beam pulses at *m/*z = 28 and 44.

Finally, after the temperature-dependent data collection had been completed, TOF distributions were again collected over a range of final angles (θ_f = 5° to 75°), except the angle was incremented by 10° and data were collected for only one round of increasing angles. This second collection of angular distribution data at 1000 K was conducted for both coated FiberForm samples and both PICA samples, while different angular-dependent data was conducted with the uncoated FiberForm sample (*vide infra*). For coated FiberForm_A and coated PICA, TOF distributions were accumulated for a total of 4000 pulses for *m/z* = 16 and 32 and 8000 pulses for *m/z* = 28 and 44, while for coated FiberForm_B, TOF distributions were collected for a total of 4000 pulses for *m/z* = 16, 32, and 28, and 8000 pulses for *m/z* = 44. For uncoated PICA, TOF distributions were accumulated for a total of 8000 pulses for *m/z* = 16 and 4000 pulses for *m/z* = 32, 28, and 44. After the temperature-dependent data collection with the uncoated FiberForm sample had been completed and the sample was at a temperature of 1000 K, the temperature was raised again to 1600 K at which point TOF distributions were again collected with two rounds of increasing and decreasing final angles, over the angular range θ_f = 5° to 85°, in 5° increments. At this temperature, no signal at *m/z* = 44 was observed, so TOF distributions were only collected at *m/z* = 16, 32, and 28. For each *m/z* ratio, TOF distributions were collected for a total of 17,000 pulses. After the completion of all experiments with each sample, the sample temperature was returned to room temperature

while in high vacuum, and then the sample was removed to the atmosphere. XPS and SEM analyses were conducted on the exposed faces of each of the five samples. For the purposes of discussion here, angular distribution data collected at the initial high temperature will be labeled with an "up arrow" after the temperature (e.g., 1000 K↑), and angular distribution data collected at the same temperature after the collection of all the temperature-dependent data will be labeled with a "down arrow" after the temperature (e.g., 1000 K↓).

4.2.4. O_2 Reactivity and Effects of Annealing

To investigate whether pre-annealing to 1800 K affected the reactivity of the FiberForm, we conducted additional experiments with samples of uncoated FiberForm. We first collected temperature-dependent data, with $\theta_i = \theta_f = 45°$, as temperature was raised and lowered from 1000 K to 1800 K in 100 K increments in two rounds, while collecting TOF distributions for each temperature at m/z = 16, 32, 28, and 44, collected for 500, 500, 1000, and 500 pulses, respectively, of the hyperthermal O/O_2 beam. Differences in the TOF distributions collected as temperature increased compared to the TOF distributions as the temperature decreased provided insight into the changes in reactivity of the FiberForm induced by annealing at 1800 K. Next, we specifically investigated O_2 reactivity on FiberForm by collecting analogous temperature-dependent data from a pristine FiberForm sample. Instead of using the hyperthermal O/O_2 beam, we used the pulsed O_2 beam that exited the source without laser detonation, in which case the chopper wheel passed a portion of the thermal O_2 beam similar to what it passed with residual thermal O_2 in the beam pulse with laser detonation. We incremented the sample temperature from 1000 K

up to 1800 K while collecting TOF distributions for each temperature at *m/z* = 16, 32, 28, and 44, with the same collection times used with the laser-detonation source. After reaching 1800 K, data collection continued as the sample temperature was dropped immediately to 1400 K.

4.3. Results and Analysis

4.3.1. Decomposition of FiberForm, PICA, Coated FiberForm, and Coated PICA

Decomposition products from raising the temperature to 1000 K could be observed for all four sample types (**Fig. A-2** to **Fig. A-5**). Uncoated FiberForm released few gas-phase products (**Fig. A-2**), with products having dominant mass-to-charge ratios at *m/z* = 1, 2, 18, and 44 being released in significant quantities. Higher-mass products were observed in the vicinity of 400 K, but their signals were very small. The pyrolysis of coated FiberForm_A released many more products, especially above 600 K (**Fig. A-3**). The major product released had a dominant mass-to-charge ratio at *m/z* = 73. Smaller peaks were also observed. The settings on the mass spectrometer were optimized for the detection of weak signals from molecular beam scattering, so saturation was observed in the strong signals from pyrolysis gases. Saturation was also observed in the pyrolysis gas signals from both of the PICA samples (**Fig. A-4** and **Fig. A-5**). Nevertheless, it was clear that significant decomposition begins below 400 K and the release rate of PICA-exclusive pyrolysis products slowed down around 950 K.[35-36] Despite the saturation in the signals, it could be observed that the primary differences in product release between coated and uncoated PICA were in the *m/z* ratios for the silicone decomposition. There was a significant increase

in products at *m/z* = 73($SiOCH_2CH_3^+$) from the coated PICA pyrolysis, as well as residual products observed above 800 K for *m/z* = 15(CH_3^+), 16(CH_4^+, O^+), 74($SiOCH_3CH_3^+$), and 75($SiOHCH_3CH_3^+$). Considerable release of low-mass products with *m/z* near 1 were also observed from all five decomposition trials. The mass spectrometer was not optimized for resolution of such low-mass products, however, and based on the observed pyrolysis behavior and the similarity with an earlier detailed study of PICA pyrolysis in our laboratory,[35] we assign this peak to H_2. Because of the lower quality of the low-mass data with the mass spectrometer settings used, we have not further analyzed the signal in that region.

Decomposition products were also observed from the pyrolysis of coated FiberForm_B (**Fig. A-6(a)**) that reached 1600 K. Compared to the decomposition of FiberForm_A, there appeared to be a lower intensity of pyrolysis products from FiberForm_B. A closer examination of the mass spectra above 1000 K showed the intensities of products for *m/z* = 15, 16, 59, 73, 74, and 75 continuing to slowly decrease as temperature climbed to 1600 K (**Fig. 4-1(a)**). For other species, around 1200 K, their signals began to rise again, with *m/z* = 28 and 44 specifically peaking above 1400 K before decreasing again (**Fig. 4-1(b)**). For *m/z* = 39, its signal disappeared around 1400 K while the signal of *m/z* = 40 began to increase around that temperature. In order to identify the signals for *m/z* = 28 and 44, we measured the intensities of *m/z* = 44, 45, and 46 as well as *m/z* = 28, 29, and 30, and calculated their percent compositions out of the total intensities of each group at each temperature point from 1200 to 1600 K. These percent compositions were then compared to the natural isotopic abundances of silicon (92.2:4.7:3.1 for *m/z* =

28:29:30) to determine how much of the signal at either *m/z* = 28 or 44 consists of Si or SiO. As **Fig. 4-1(c)** shows, the curves reflecting their isotopic percentages appear to converge and level out between 1300 K to 1400 K. Within this level region, the ratios of *m/z* = 44:45:46 on average were 92.6:4.9:2.5, while above 1450 K the curves appeared to diverge, with *m/z* = 44 increasing and both *m/z* = 45 and 46 decreasing. Compared to the natural isotopic abundance of silicon, these values are very similar, suggesting that nearly all the *m/z* = 44 signal within the 1300 to 1400 K region was SiO, while outside the region CO_2 might constitute a larger proportion. As for *m/z* = 28, 29, and 30 (**Fig. 4-1(d)**), the curves for each species appeared to be linear, with divergence up to 1470 K, at which point *m/z* = 29 and 30 could not be detected anymore. At 1200 K, where the proportions of *m/z* = 29 and 30 are at their highest, the ratios of *m/z* = 28:29:30 are 98.7:0.8:0.4, which suggests that most of the *m/z* = 28 signal was CO rather than silicon. Isotopic percentages were also calculated for *m/z* = 73, 74, and 75 (**Fig. A-6**), but these values do not show any discernible pattern.

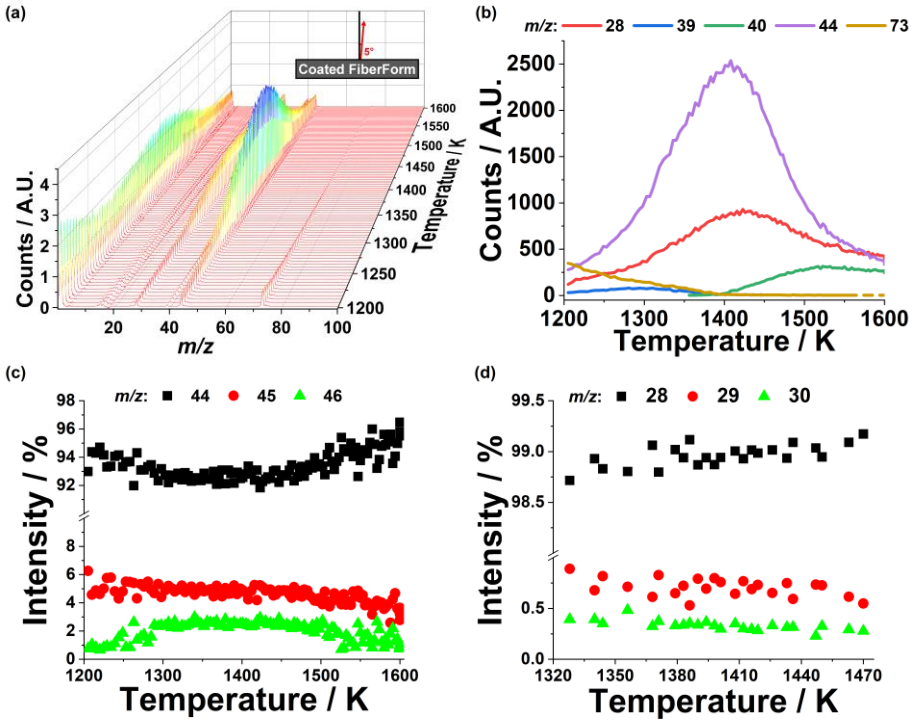

Fig. 4-1. Results from mass spectra from products released from coated FiberForm as it was heated from 1200 K to 1600 K, with a detector viewing angle of θ_f = 5° with respect to the normal of the macroscopic surface. **(a)** Mass spectra as a function of sample temperature. **(b)** Integrated intensities of peaks corresponding to specific m/z ratios as a function of sample temperature. **(c)** Intensities of signals detected at *m/z* = 44, 45, and 46 represented as percentages of the total signal at these three *m/z* ratios, as a function of sample temperature. **(d)** Intensities of signals detected at *m/z* = 28, 29, and 30 represented as percentages of the total signal at these three *m/z* ratios, as a function of sample temperature.

Additional samples of FiberForm and coated FiberForm pyrolyzed and annealed up to 1800 K for 30 minutes before being returned to room temperature showed noticeable changes from their pristine counterparts. SEM images of the annealed samples are shown in **Fig. 4-2(b, d)** and **Fig. A-7**. The general fiber orientations for both coated and uncoated FiberForm appeared to be random. In the FiberForm study from Poovathingal et al. (2021),[47] they were able to identify the orientation of the FiberForm surface, but no discernible orientation could be ascertained from SEM images of the samples in this study.

At lower resolution, no obvious differences could be discerned between coated and uncoated FiberForm. At a higher resolution, damage on the individual fibers could be observed, with pits of ~100 nm diameter forming on both sample types. Far more extensive damage was observed on the coated FiberForm, with large tears and fractures forming on the individual fibers. Compared to the pristine uncoated FiberForm, samples showed significant surface changes after annealing.

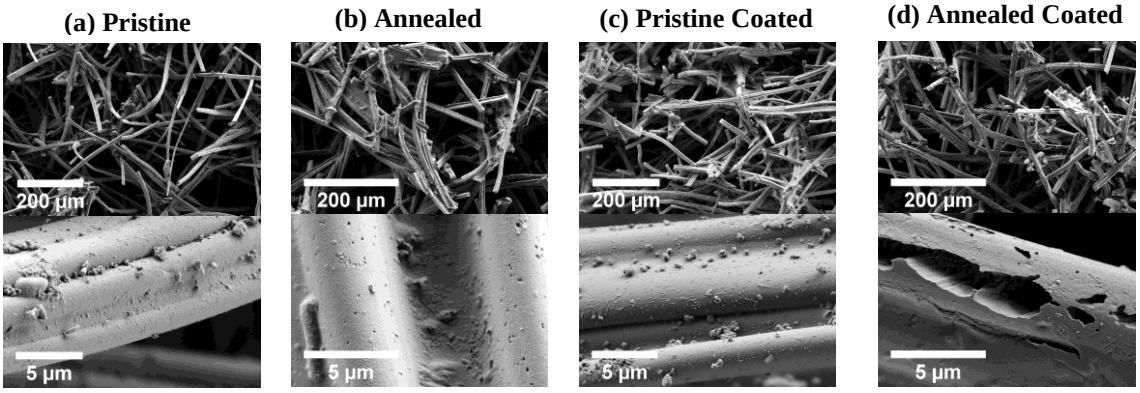

Fig. 4-2. SEM images, taken at two magnifications, of **(a, b)** uncoated and **(c, d)** coated FiberForm before and after annealing at 1800 K for 30 minutes.

4.3.2. Gas-Surface Scattering and Fitting Analysis

Products could be observed leaving the sample surface from *m/z* = 16, 32, 28, and 44, corresponding either to no net reaction in the cases of O and O_2 (*m/z* = 16 and 32), or reaction in the cases of CO and CO_2 (*m/z* = 28 and 44, respectively). The TOF distributions of scattered products are typically described in terms of two limiting mechanisms: impulsive scattering (IS) and thermal desorption (TD). IS species undergo one or a few collisions with the surface and transfer very little energy before exiting the surface on a time scale too short for equilibrium to be established. In a TOF distribution, IS products appear at short flight times. TD products, in contrast, establish thermal equilibrium with

the surface before desorption. TD products typically exit a surface with a Maxwell-Boltzmann (MB) distribution of translational energies given by the surface temperature. In addition to the TD mechanism, we observed a third thermal desorption signal from most of the TOF distributions for *m/*z = 16, 28, and 44, which we designated as TD_{slow}. The TD_{slow} mechanism was previously observed in studies on vitreous carbon and FiberForm by Murray et al. (2015)[42] and Poovathingal et al. (2021),[42] respectively. This corresponds to the remaining signal at longer flight times in the TOF distribution that could not be represented by either IS or TD. This remaining signal can be roughly fit using a 1^{st}-order exponential decay function of varying lifetimes convoluted with a Maxwell-Boltzmann fit for the different TOF distributions. IS flux is quantified by calculating the remainder after the TD and TD_{slow} flux is subtracted from the overall flux. **Fig. 4-3** shows representative fits for different TOF distributions. In a plot of the flux of TD products at different final angles, θ_f, from the normal, the angular distribution was fit to a cosine distribution $\cos^x(\theta)$, with x being a real positive value. A flux angular distribution of TD_{slow} products has no expected functional shape, and we did not attempt to find a fit for these distributions. On the TOF distributions for all species except for *m/z* = 32, the IS, TD, and TD_{slow} mechanisms could all be fit. For the TOF distributions of *m/z* = 32, only the IS and TD mechanisms can be fit. For the TOF distributions for *m/z* = 28 and 44, however, IS signal tended to be negligible, so we have excluded them from our flux figures. Backgrounds for each TOF distribution were also quantified. Before the TOF distribution can be analyzed, the raw signal must be corrected to subtract background and to shift the flight times such that time 0 reflects the moment the product leaves the surface of the material. Thus, from

the raw TOF distribution, we quantified the background by summing the intensity of the first 300 μs of the distribution before time 0. This measurement thus reflected the ambient background intensity of a particular species within the vacuum chamber (**Fig. 4-3(d)**).

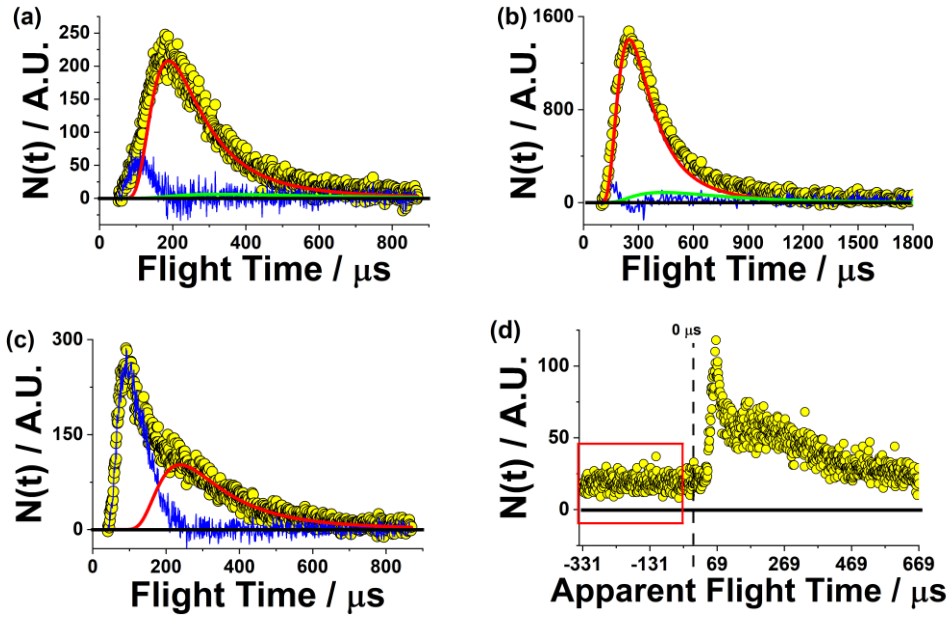

Fig. 4-3. Example fitting procedures for TOF distributions. **(a)** O at θ_f = 5° at 1600 K from coated FiberForm; **(b)** CO at θ_f = 5° at 1600 K from uncoated FiberForm; and **(c)** O at θ_f = 5° at 1000 K from coated FiberForm. Yellow circles represent total signal with background subtracted. Red lines represent MB distributions at each TOF distribution's respective temperature. Green lines represent 1st-order decay fits convoluted with MB distributions (TD_{slow}). Blue lines represent signal remaining after red and green lines are subtracted from the total signal and include IS signal in the lower time region. No TD_{slow} fit was needed for **(c)**. **(d)** represents an example TOF distribution collected that has not been corrected for either background or for time 0. The red outline marks the flight times on the distribution from which the species' ambient background intensity was calculated. The dotted line represents time 0, the moment at which the product leaves the sample surface.

4.3.3. Temperature-Dependent Flux and Angular Distributions of Uncoated FiberForm

Product TOF distributions from uncoated FiberForm as a function of temperature for O and CO, and O_2 and CO_2, are shown in **Fig. 4-4** and **Fig. A-8**, respectively. The shapes of the TOF distributions do not exhibit any significant changes or shifts within the temperature-dependent data. The total fluxes for each species, as shown in **Fig. 4-4(a)**, have all been corrected for the mass-dependent detection sensitivity of our mass spectrometer. Their background intensities at each temperature are shown in **Fig. A-9**. The fluxes for O and CO from 1100 K increased monotonically with temperature, and a clear hysteresis for both species was observed in the flux depending on whether temperature was increasing or decreasing, with O flux being higher at each temperature point as temperature decreased, and CO flux generally being lower as temperature decreased. Within the O flux, this almost monotonic behavior appeared to be contributed solely from the TD flux (**Fig. 4-4(b)**), as the IS flux stayed relatively constant throughout the experiment. There was a reversal around 1300 K and 1400 K where the CO flux at temperature points increasing in temperature was lower than the flux at the equivalent temperature points decreasing in temperature. In examining the TD and TD_{slow} components of the CO flux (**Fig. 4-4(c)**), this reversal was mostly reflected in the TD flux from 1300 to 1500 K. There was a maximum in the TD_{slow} flux at 1400 K both as temperature increased and as temperature decreased. However, because the TD_{slow} hysteresis was less pronounced compared to that of TD, this maximum did not change the shape of the overall CO flux. For O_2, its flux was relatively constant in comparison to the O and CO flux, and this lack of change was reflected as well when considering its IS and TD fluxes individually (**Fig. A-8**), while for CO_2, it only had

appreciable flux at 1000 K and 1100 K, remaining negligible above 1100 K. The background intensities of all the species were relatively constant (**Fig. A-9**). For the backgrounds of both O and O_2, their intensities decreased as temperature increased. For CO, its background intensity increased at 1200 K as temperature increased, peaking at 1400 K before returning to a baseline at 1700 K. As temperature decreased to 1000 K, the CO background intensity remained relatively constant. Finally, for CO_2, its background was only elevated at 1000 K as temperature increased and remained relatively constant for the remainder of the experiment.

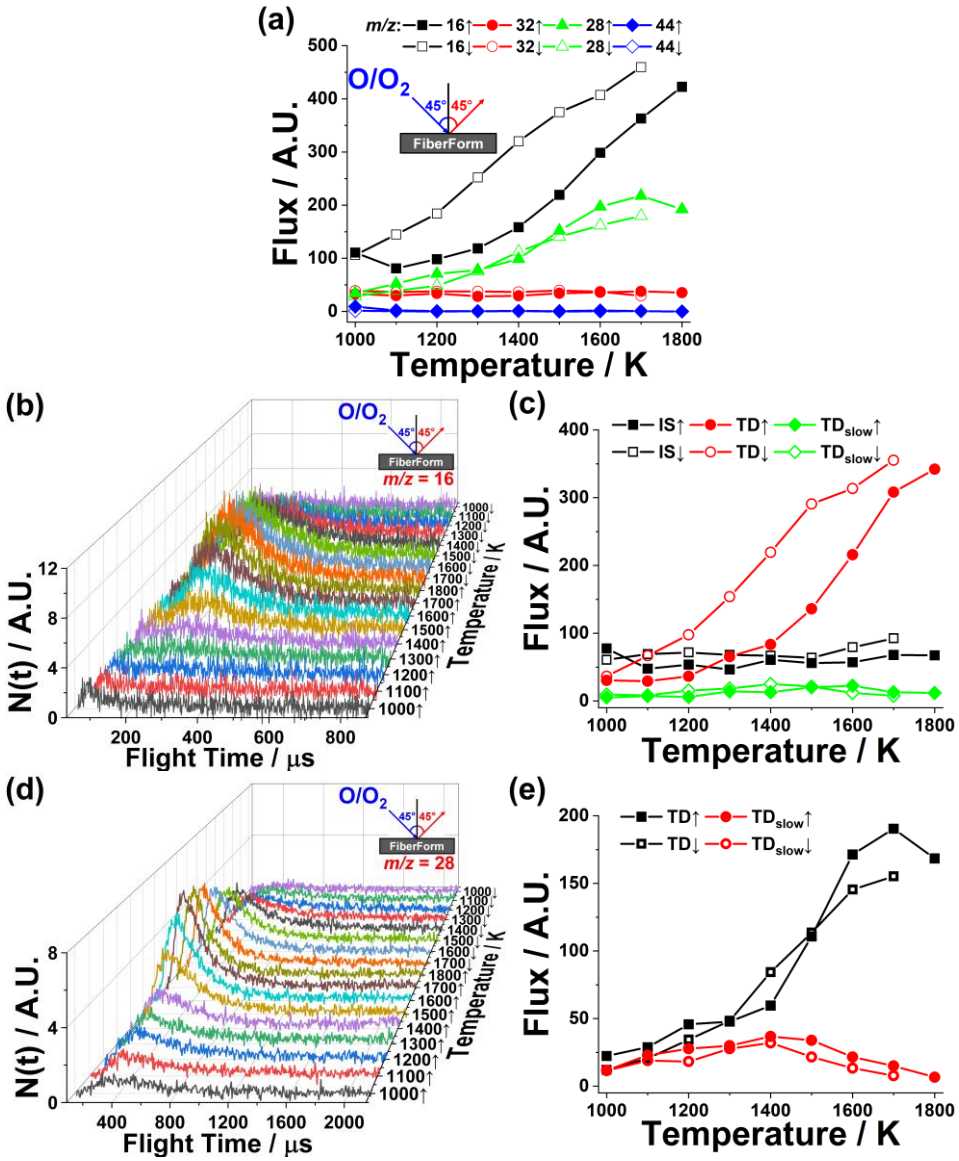

Fig. 4-4. Fluxes and TOF product distributions and fluxes from uncoated FiberForm. **(a)** Flux as a function of temperature from 1000 K to 1800 K for *m/z* = 16, 32, 28, and 44 products from coated FiberForm_A. TOF distributions as a function of temperature increasing up to 1800 K, then decreasing to 1000 K, for **(b)** O and **(d)** CO. Fluxes separated into their IS (O only), TD, and TD_{slow} components shown in **(c)** and **(e)** for O and CO, respectively. Arrows indicate whether temperature had been increasing or decreasing when temperature was reached.

Flux angular distributions collected at 1000 K and 1600 K are shown in **Fig. 4-5**. At 1000 K, signal could be detected at *m/z* = 16, 32, 28, and 44, corresponding to O, O_2, CO, and CO_2. For O, the flux was separated into IS, TD, and TD_{slow} components. The O TD cosine distribution was fit with an $x = 1.5$ power. The O IS flux was much larger than the O TD flux and its distribution resembled a lobular shape. The O TD_{slow} flux constituted less than half the flux of the O TD flux. For O_2, its flux was separated into IS and TD components, with the TD distribution fit with an $x = 0.8$ power. The O_2 IS distribution is roughly equivalent in shape to that of O_2 TD, with similar fluxes as well. For both CO and CO_2, the fluxes were separated into TD and TD_{slow}. The CO TD distribution was fit to an $x = 1.8$ power, and the CO_2 TD distribution was fit to an $x = 1.6$ power. The CO TD_{slow} flux constituted on average less than half that of its TD flux, while the CO_2 TD_{slow} flux was less than ¼ that of its TD flux. At 1600 K, there was sufficient product flux to collect angular distributions for O, O_2, and CO, but not CO_2, as shown in **Fig. 4-5**. For O, the flux was separated into IS, TD, and TD_{slow} components, with the TD distribution fit to an $x = 1.6$ power. Its IS flux was almost 1/5 that of TD, and its angular distribution had a broad shape. The TD_{slow} flux was much smaller, constituting about ¼ that of the IS flux. For O_2, its TD distribution was fit to an $x = 0.8$ power. Its IS flux was only slightly smaller than that of the TD flux. For CO, the flux was separated into TD and TD_{slow} components, with the TD distribution fit to an $x = 1.2$ power. The TD_{slow} flux was small, constituting around 1/7 that of the TD flux.

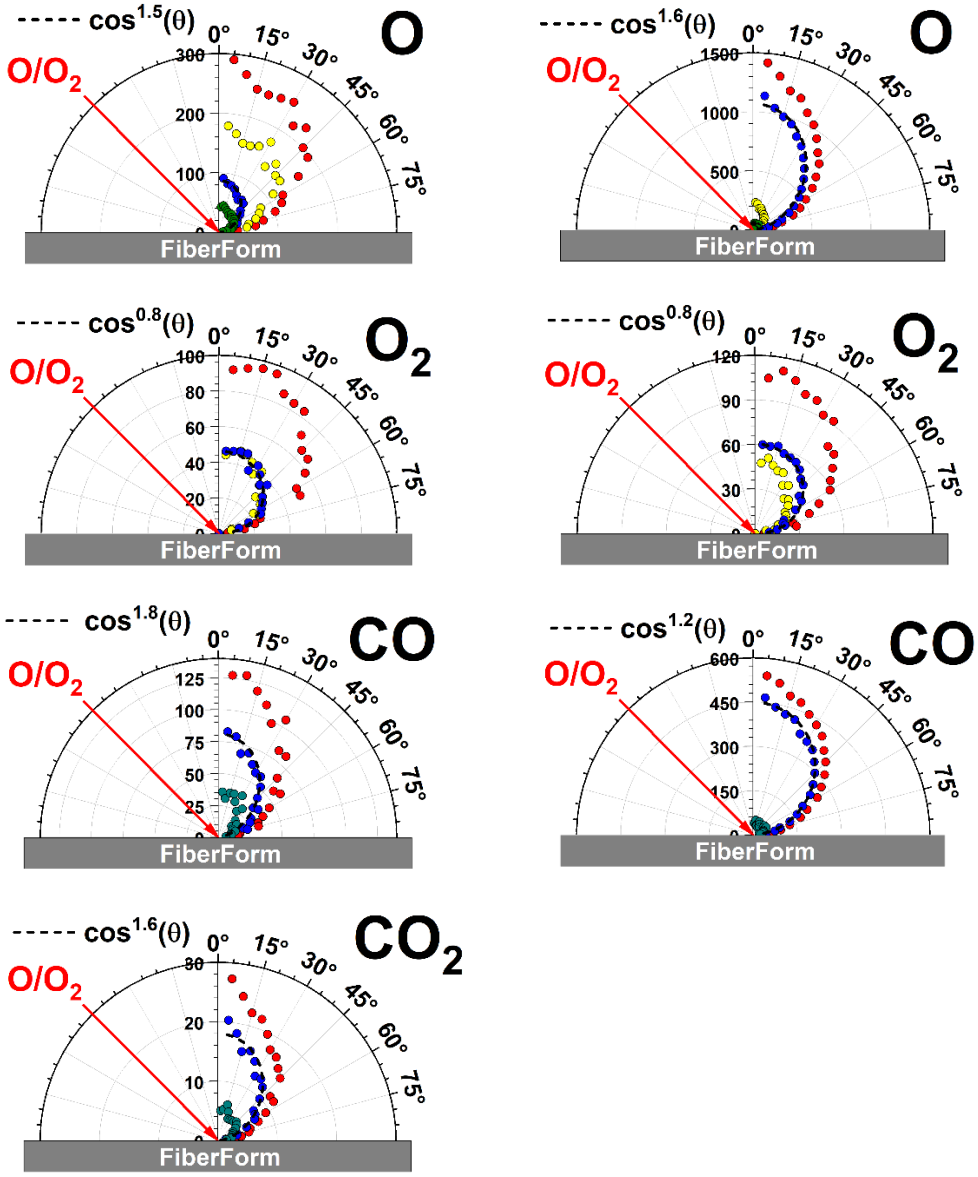

Fig. 4-5. Flux angular distributions of O, O_2, CO, and CO_2 (1000 K only) products from uncoated FiberForm at 1000 K (left) and 1600 K (right). Red points represent total flux for a particular product. Yellow points (O and O_2 only) represent IS flux. Blue points represent TD flux. Green points (O, CO, and CO_2 only) represent TD_{slow} flux. Dashed lines represent approximate cosine fits for each product's TD distribution.

SEM images of the surface after scattering at the higher resolution revealed pits forming on the individual fibers (**Fig. A-10**). This pitting phenomenon was present both in the area where the O-atom beam impacted as well as in areas outside of the beam impact area. The pitting also strongly resembled that of uncoated FiberForm annealed without the O-atom beam (**Fig. 4-2(b)**). In addition, XPS analysis of the impact spot (**Table 4-1(b)**) revealed nearly complete carbon coverage along with a minute fraction of oxygen. XPS of the out-of-beam area revealed only the presence of carbon, with no other elements detected (**Table 4-1(c)**). Unlike what was observed on pristine uncoated FiberForm (**Table 4-1(a)**), in both the in-beam and out-of-beam areas of uncoated FiberForm, calcium was not detected.

4.3.4. O_2 Reactivity of Uncoated FiberForm

CO TOF distributions collected from O-atom scattering of uncoated FiberForm subjected to two rounds of heating from 1000 K to 1800 K displayed subtle but distinct reactive peaks around 3 ms in the TOF distributions at 1300 K and 1400 K as temperature was increased during the first round of heating, as shown in **Fig. 4-6(a)**. This peak disappeared as the sample first reached 1500 K and did not appear again either while temperature was decreasing from 1800 K, or anytime during the second round of heating. The hysteresis of the CO flux also changed after the sample was heated in the first round, with no inversion of the flux around 1300 K between the temperature points as temperature increased and the temperature points as temperature decreased. Other *m/z* ratios measured revealed no significant difference in reactivity between pristine FiberForm and annealed FiberForm. CO TOF distributions collected from O_2-beam scattering of pristine uncoated

FiberForm are shown in **Fig. 4-6(c)**. As with O-atom beam scattering from pristine uncoated FiberForm, 3 ms peaks were again observed on the TOF distributions at 1300 K and 1400 K. The peak similarly disappeared as temperature reached 1500 K, and after the sample temperature reached 1800 K, the peak did not reappear when temperature was immediately reduced to 1400 K (**Fig. A-11(c)**). Taken together, these results with the O_2-beam suggest that the 3 ms peak observed was caused by O_2.

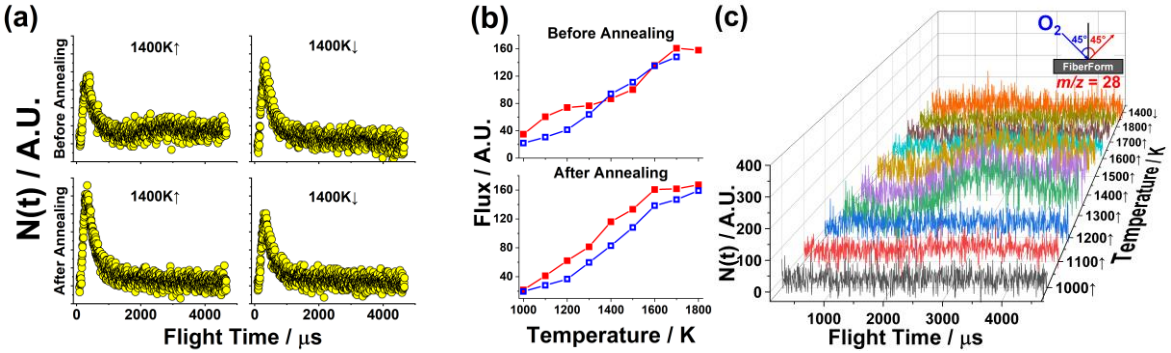

Fig. 4-6. Results from O_2 reactivity experiment. **(a)** Individual TOF distributions for CO from uncoated FiberForm hit with hyperthermal O/O_2 beam at 1400 K, with background unsubtracted and TOF plotted out to 5,000 μs. Top represents first round of annealing, while bottom represents second round of annealing. Arrows indicate whether temperature had been increasing or decreasing when temperature was reached. **(b)** Plots represent CO flux before and after annealing. Solid points are representative of temperature increasing. Hollow points are representative of temperature decreasing; **(c)** TOF distributions for CO of uncoated FiberForm scattered with O_2 up to 1800 K, then down to 1400 K, with background subtracted.

4.3.5. Temperature-Dependent Flux and Angular Distributions of Coated FiberForm_A

Product TOF distributions from coated FiberForm_A as a function of temperature for O and CO, and O_2 and products detected at m/z = 44, are shown in **Fig. 4-7** and **Fig. A-12**, respectively. The total fluxes, as shown in **Fig. 4-7(a)**, had all been corrected for the mass-dependent detection sensitivity of our mass spectrometer. Unlike those of uncoated FiberForm, the shapes of the TOF distributions, especially for O, exhibited significant

changes within the temperature-dependent data. Up to 1400 K, most of the O flux exited the sample surface through the IS channel, with TD flux constituting less than half that of the IS flux up until 1500 K. As the temperature reached 1500 K, the IS signal reduced significantly, and once 1600 K was reached, all the increase in flux came through the TD channel. As temperature was decreased from 1800 K, total O flux also monotonically decreased, resembling the O flux of uncoated FiberForm. A correlative phenomenon was observed with CO, as very little CO flux was observed until 1500 K, at which point the flux increased. This lower-temperature suppression of the CO flux was observed from both the TD and TD_{slow} channels. As the temperature decreased after reaching 1800 K, the flux also monotonically decreased, with the TD and TD_{slow} fluxes as temperature decreased resembling that of uncoated FiberForm as well. For the flux for O_2 (**Fig. A-12(b)**), it also remained relatively constant throughout the entire experiment compared to those of O and CO. There was a slightly more pronounced hysteresis in the TD flux of O compared to that of uncoated FiberForm. For products from *m/z* = 44, very little CO_2 flux was observed at 1000 and 1100 K, remaining negligible until higher temperatures were reached. As temperature approached 1600 K while temperature was increasing, a small but significant increase in flux was observed that was likely that of SiO rather than CO_2. As temperature decreased, the *m/*z = 44 flux resembled the flux of CO_2 leaving the surface of uncoated FiberForm. The backgrounds of *m/z* = 16, 28, and 44 (**Fig. A-13**) were reflective of the continuing changes as temperature increased, with the background intensities increasing at 1200 K, peaking at 1300 K, and then gradually decreasing as temperature reached 1800 K.

There was also a minor increase in the background intensity of m/z = 44 at 1600 K. The O_2 background intensity remained relatively constant throughout the experiment.

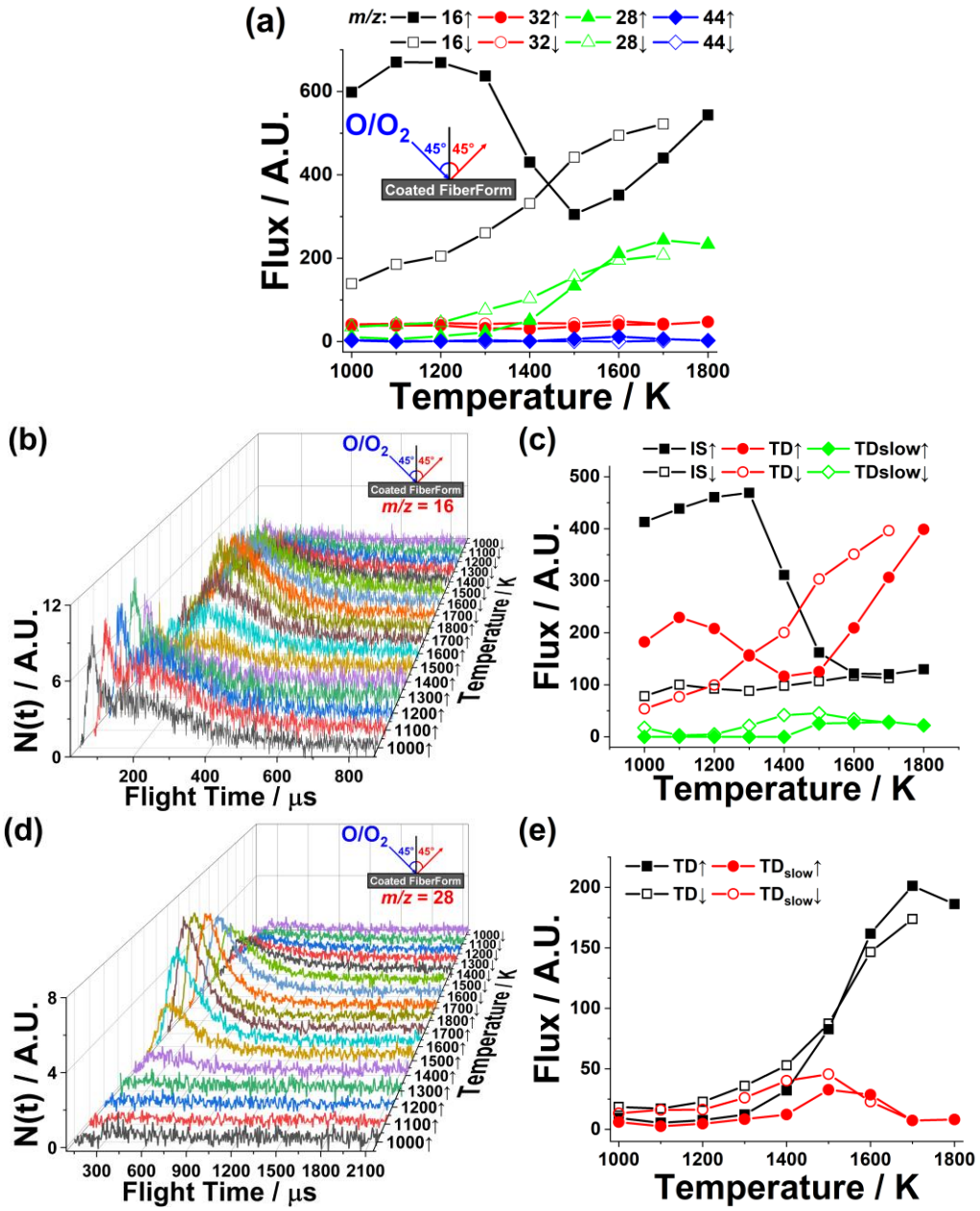

Fig. 4-7. Fluxes and TOF product distributions from coated FiberForm_A. **(a)** Flux as a function of temperature from 1000 K to 1800 K for *m/z* = 16, 32, 28, and 44 products from coated FiberForm_A. TOF distributions as a function of temperature increasing up to 1800 K, then decreasing to 1000 K, for **(b)** O and **(d)** CO. Fluxes separated into their IS, TD, and TD_{slow} components shown in **(c)** and **(e)** for O and CO, respectively. Arrows indicate signal at temperature point collected when temperature was either increasing or decreasing.

Flux angular distributions from the coated FiberForm_A collected at 1000 K↑ are shown in **Fig. 4-8**. Signal could be detected for O, O_2, CO, and CO_2. For O, the flux was only separated into IS and TD components, with no TD_{slow} component detected. The TD cosine distribution was fit with an $x = 1$ power. The IS flux was much larger than that of TD and its distribution had a relatively broad shape. For O_2, its flux was separated into IS and TD components. The TD distribution has an $x = 1.4$ power, and the IS distribution was roughly equivalent in shape compared to that of TD, while its flux was slightly greater. For CO, the flux was separated into TD and TD_{slow} components. The TD distribution was fit with an $x = 1.3$ power, with TD_{slow} flux around half that of TD. Finally, for CO_2, the flux was separated into TD and TD_{slow} components, with the TD distribution fit with an $x = 1.3$ power and TD_{slow} flux being less than half that of TD. Angular distributions collected at 1000 K↓ for O, O_2, CO, and CO_2 are also shown in **Fig. 4-8**. For O, the flux was separated into IS, TD, and TD_{slow} components. The TD distribution was fit with an $x = 2.5$ power, with TD_{slow} flux around 1/5 that of TD. The IS angular distribution has a lobular shape like that of uncoated FiberForm at 1000 K, with a flux slightly greater than that of TD. For O_2, flux was only separated into IS and TD components. The TD distribution was fit with an $x = 1.2$ power, while the IS flux, its distribution also resembling a lobular shape, was half that of the TD flux. For CO, the flux was separated into TD and TD_{slow}, with the TD distribution fit with an $x = 1.4$ power and TD_{slow} flux being less than half that of TD. For $m/z = 44$, the flux was also separated into TD and TD_{slow}, with the TD distribution fit with an $x = 1.3$ power and TD_{slow} flux being around 1/6 that of the TD flux.

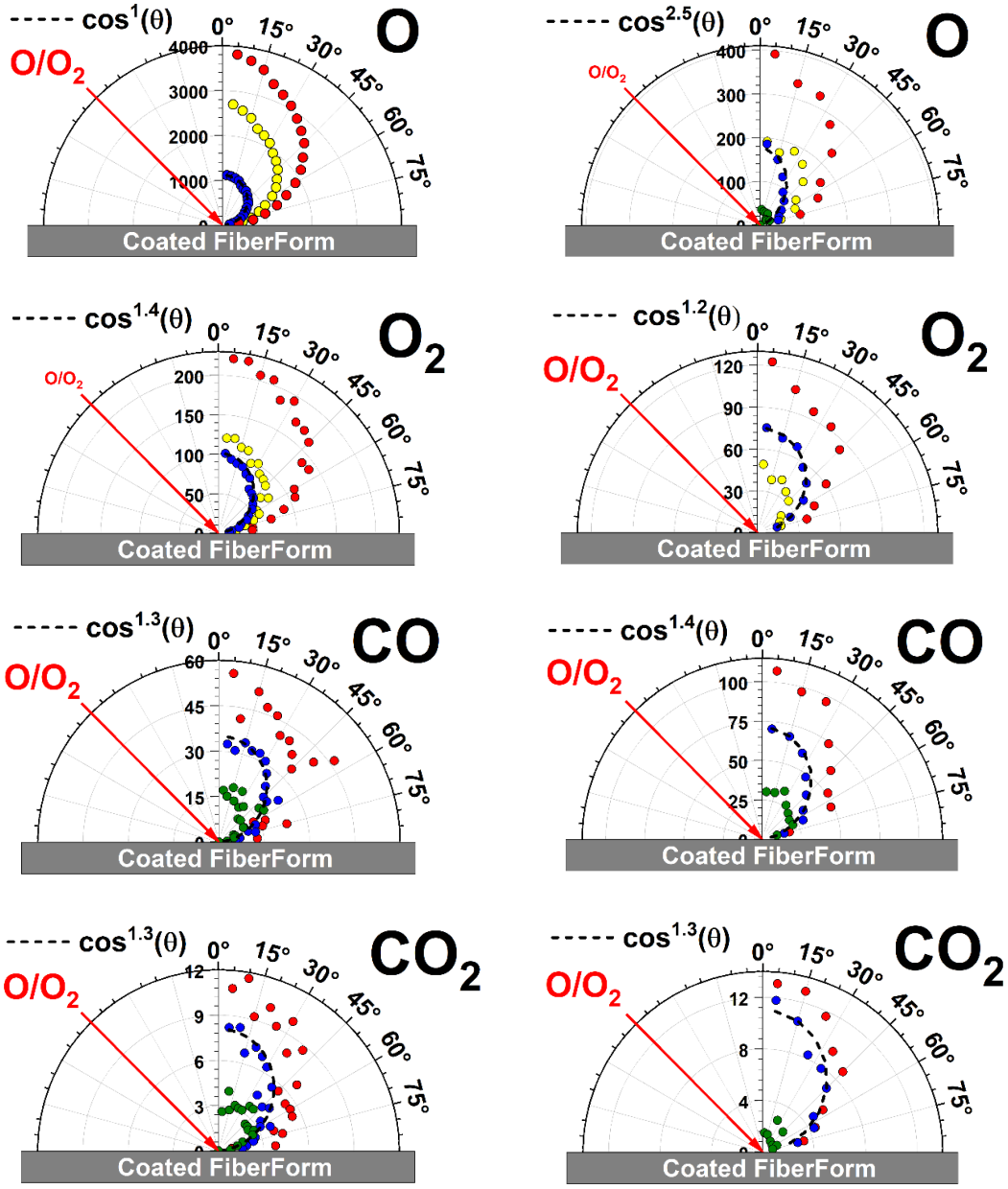

Fig. 4-8. Flux angular distributions of O, O_2, CO, and CO_2 products from coated FiberForm_A at 1000 K↑ (left) and 1000 K↓ (right), with arrows representing whether temperature had been increasing or decreasing before angular distributions were collected. Red points represent total flux for a particular product. Yellow points (O and O_2 only) represent IS flux. Blue points represent TD flux. Green points (O, CO, and CO_2 only) represent TD_{slow} flux. Dashed lines represent approximate cosine fits for each product's TD distribution.

4.3.6. Temperature-Dependent Flux and Angular Distributions of Coated FiberForm_B

Product TOF distributions from coated FiberForm_B as a function of temperature for O and CO, and O_2 and products observed at *m/*z = 44, are shown in **Fig. 4-9** and **Fig. A-14**. The fluxes (**Fig. 4-9(a)**) had all been corrected for the mass-dependent detection sensitivity of our mass spectrometer. Like that of uncoated FiberForm, the shapes of the TOF distributions remained consistent for all species within the temperature-dependent data. For O (**Fig. 4-9(b)**), IS flux remained relatively constant while TD flux increased monotonically. TD_{slow} flux also started increasing around 1300 K. In contrast to that of uncoated FiberForm, the TD_{slow} flux from FiberForm_B was proportionally higher compared to the IS flux. For CO, as compared to that of uncoated FiberForm, its flux from FiberForm_B did not exhibit a reversal in the hysteresis around 1400 K. Instead, the flux behavior was more similar to that of annealed FiberForm (**Fig. 4-6(b)**). The TD and TD_{slow} fluxes were also like those of uncoated FiberForm, with the fluxes diverging at 1600 K as TD flux continued to increase with temperature while TD_{slow} flux decreased. In addition, the fluxes of TD and TD_{slow} were much closer to each other than those in uncoated FiberForm. A hysteresis was also observed in the fluxes of both O and CO, with higher flux observed for O and lower flux observed for CO, respectively, as temperature decreased. For the flux of O_2, as with the other FiberForm experiments, it remained relatively constant throughout the entire experiment compared to those of O and CO, and this was reflected in the flux of both IS and TD (**Fig. A-14**). For the products observed at *m/z* = 44, its flux behavior was similar to that of *m/*z = 4 4 flux from coated FiberForm_A, with products observed at lower temperatures while temperature was increasing and

decreasing, and product only observed at higher temperatures while temperature was increasing. The backgrounds of the four signals from coated FiberForm_B (**Fig. A-15**) were similar to those from uncoated FiberForm, with O and O_2 background decreasing as temperature increased. Small increases in *m/z* = 28 and 44 background intensities at 1700 K were observed, corresponding to CO and Si, and CO_2 and SiO, respectively.

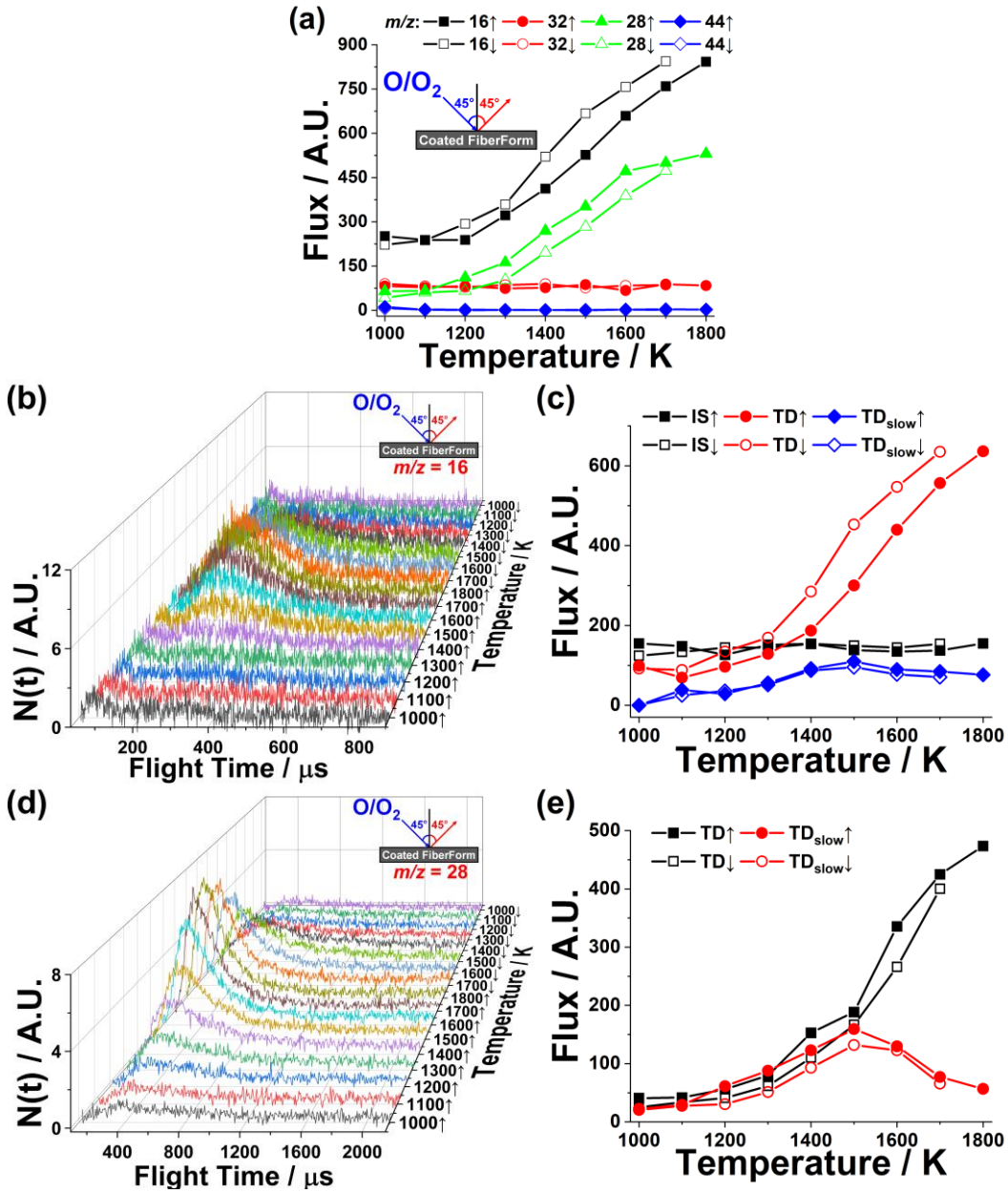

Fig. 4-9. Fluxes and TOF product distributions from coated FiberForm_B. **(a)** Flux as a function of temperature from 1000 K to 1800 K for *m/z* = 16, 32, 28, and 44 products from coated FiberForm_B. TOF distributions as a function of temperature increasing up to 1800 K, then decreasing to 1000 K, for **(b)** O and **(d)** CO. Fluxes separated into their IS (O only), TD, and TD_{slow} components shown in **(c)** and **(e)** for O and CO, respectively. Arrows indicate signal at temperature point collected when temperature was either increasing or decreasing.

Flux angular distributions for coated FiberForm_B collected at 1600 K are shown in **Fig. 4-10**. Signal could be detected at *m/z* = 16, 32, 28, and 44, corresponding to O, O_2, CO, and SiO. Because it is known, based on the experiment with uncoated FiberForm as well as the previous study with FiberForm,[47] that CO_2 is not produced above 1200 K from FiberForm, we assumed that *m/*z = 44 corresponds to SiO. For O, its flux was separated into IS, TD, and TD_{slow} components, with the TD cosine distribution fit with an $x = 2.2$ power. The IS flux was much smaller and followed a lobular distribution, while the TD_{slow} flux was around half that of IS. For O_2, the TD distribution was fit with an $x = 0.8$ power, while the IS flux was roughly equivalent in shape and slightly lower in flux compared to that of the TD flux. For CO, the flux was separated into TD and TD_{slow}, with the TD distribution fit with an $x = 1.1$ power and TD_{slow} flux being around 1/3 that of TD. Finally, for SiO, the flux was separated into TD and TD_{slow}, with the TD distribution fit with an $x = 1.9$ power. Both TD and TD_{slow} angular distributions were much noisier than the other angular distributions so far mentioned. Flux angular distributions collected at 1000 K for O, O_2, CO, and CO_2 are also shown in **Fig. 4-10**. For O, the flux was separated into IS, TD, and TD_{slow} components, with the TD distribution fit with an $x = 1.6$ power and TD_{slow} flux being less than half that of TD. The IS distribution resembled a lobular shape like that of O IS from uncoated FiberForm at 1000 K, with a flux slightly greater than that of its TD flux. For O_2, the TD distribution was fit with an $x = 0.9$ power, while the IS flux, also resembling a lobular shape, was much smaller than the O_2 TD flux. For CO, the flux was separated into TD and TD_{slow} channels, with the TD distribution fit with an $x = 1.1$ power, and the TD_{slow} flux being around 2/3 that of TD. Finally, for CO_2, the flux was also

separated into TD and TD_{slow}, with the TD distribution fit with $x = 1$ power and TD_{slow} flux being less than half that of TD.

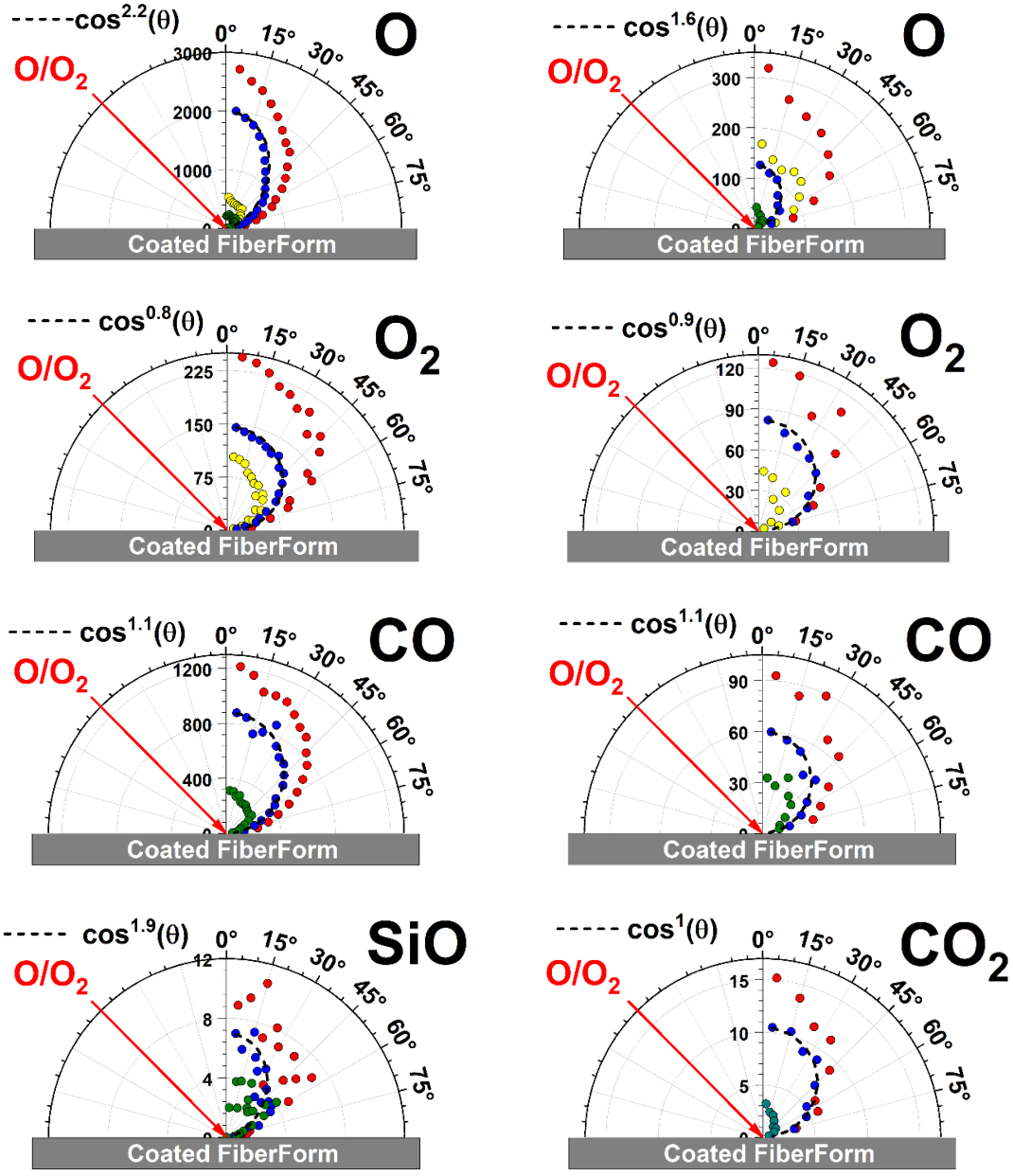

Fig. 4-10. Flux angular distributions of O, O_2, CO, SiO (1600 K only), and CO_2 (1000 K only) products from coated FiberForm_B at 1600 K (left) and 1000 K (right). Red points represent total flux for a particular product. Yellow points (O and O_2 only) represent IS flux. Blue points represent TD flux. Green points (O, CO, SiO, and CO_2 only) represent TD_{slow} flux. Dashed lines represent approximate cosine fits for each product's TD distribution.

SEM images of the coated FiberForm_B surface after O-atom scattering at higher resolution revealed significant damage on the individual fibers (**Fig. A-16**) compared to non-annealed coated FiberForm. In addition to the pitting, which was also present on annealed uncoated FiberForm (**Fig. 4-2(b)**), there was significant fracturing on the fibers, both in the area of O-atom beam impact as well as in areas outside of the impact. The pitting also appeared to be bigger than that of uncoated FiberForm. XPS analysis of the impact spot (**Table 4-1(e)**) revealed nearly complete carbon coverage (96.9%) along with a small fraction of oxygen coverage (3.1%), but no calcium was detected. In comparing the SEM images of the fiber surfaces between the coated FiberForm_A and coated FiberForm_B, no discernible differences could be seen. The damage observed on coated FiberForm after heating with O-beam scattering (**Fig. A-16**) was very similar to the damage observed on coated FiberForm after heating without the O-atom beam (**Fig. 4-2(d)**). In addition, like that from uncoated FiberForm, on coated FiberForm_A there was a small peak at 3 ms in the CO TOF distributions at 1500 K and 1600 K that disappeared as temperature increased.

4.3.7. Temperature-Dependent Flux and Angular Distributions of PICA

Product TOF distributions from uncoated PICA as a function of temperature for O and CO, and O_2 and CO_2, are shown in **Fig. 4-11** and **Fig. A-17**, respectively. The flux, as shown in **Fig. 4-11(a)**, had all been corrected for the mass-dependent detection sensitivity of our mass spectrometer. As with the uncoated FiberForm experiments, the shapes of the TOF distributions remained consistent for all species within the temperature-dependent data. Unlike the temperature-dependent fluxes of species leaving the surface of uncoated

FiberForm, products from uncoated PICA exhibited less obvious trends in flux as temperature was increased to 1800 K and decreased to 1000 K. For the flux of O (**Fig. 4-11(b)**), IS flux remained relatively constant as temperature increased, but as temperature decreased, the IS flux increased around 1300 K, with around double the flux at 1100 K and 1200 K as temperature decreased compared to 1100 K and 1200 K as temperature increased. TD flux increased more slowly with increasing temperature compared to uncoated FiberForm, though its trends were still similar to those from uncoated FiberForm. For CO, similar to that of the uncoated FiberForm flux (**Fig. 4-4(a)**), there was an inversion in the hysteresis around 1400 and 1500 K, with flux as temperature increased lower than the flux as temperature decreased. The TD and TD_{slow} flux of CO had near equal contributions from both channels, and from 1400 to 1600 K, TD_{slow} flux was higher than that of TD. Like the other samples already mentioned, the TD_{slow} flux decreased at higher temperatures, but decreasing at 1800 K instead of 1600 K from all the FiberForm experiments. For O_2, its flux (**Fig. A-17**) remained relatively constant throughout the experiment, though in examining its TD and TD_{slow} channels, as temperature increased its TD flux decreased until passing 1500 K. For CO_2, as with uncoated FiberForm, it had higher flux at lower temperatures, though its flux lingered up to 1400 K, while in uncoated FiberForm its CO_2 flux was negligible above 1100 K. The background intensities for the four species from PICA are shown in **Fig. A-18**. For O and O_2, their intensities decreased as temperature increased. For CO, its background intensity was elevated from 1100 to 1800 K as temperature increased, but its background intensity remained low and relatively constant as its temperature decreased. Finally, for CO_2, from 1000 K its background

intensity was slightly elevated, but as temperature increased to 1200 K its background intensity returned to a lower level and remained relatively constant for the remainder of the experiment.

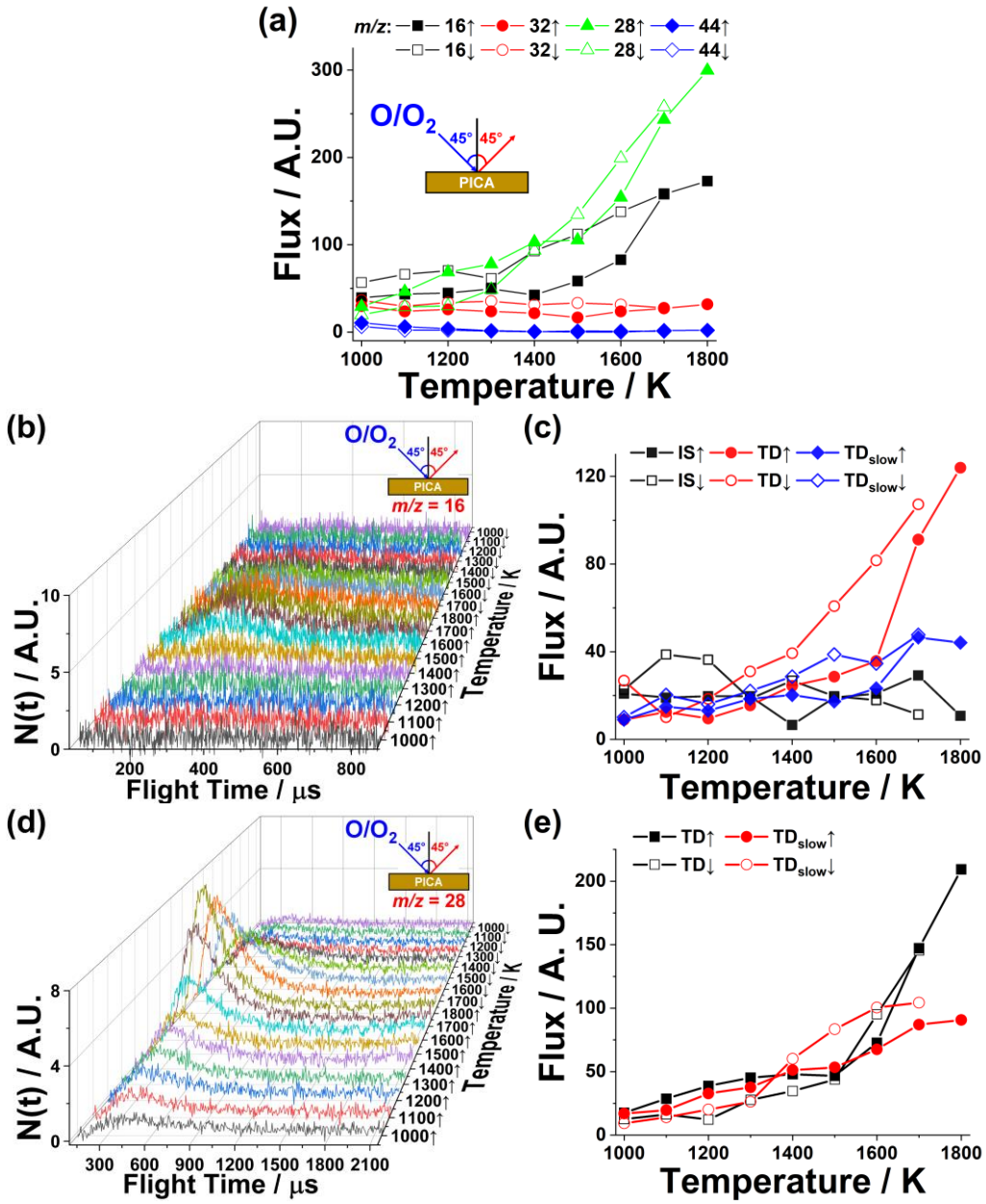

Fig. 4-11. Fluxes and TOF product distributions from uncoated PICA. **(a)** Flux as a function of temperature from 1000 K to 1800 K for *m/z* = 16, 32, 28, and 44 products from uncoated PICA. TOF distributions as a function of temperature increasing up to 1800 K, then decreasing to 1000 K, for **(b)** O and **(d)** CO. Fluxes separated into their IS (O only), TD, and TD_{slow} components shown in **(c)** and **(e)** for O and CO, respectively. Arrows indicate signal at temperature point collected when temperature was either increasing or decreasing.

Flux angular distributions for the uncoated PICA collected at 1000 K↑ are shown in **Fig. 4-12**. Signal could be detected at *m/z* = 16, 32, 28, and 44. Signal from *m/z* = 17 was also briefly observed when the detector angle of the mass spectrometer was set at θ_f = 5°, but this signal disappeared after around 20 minutes. For O, its flux was separated into IS, TD, and TD_{slow} components, with the TD cosine distribution fit with an x = 0.7 power, and the TD_{slow} flux was slightly lower than that of TD. The IS flux was like that of TD_{slow} and did not have a discernible shape. For all the O channels the flux angular distributions were relatively noisy. For O_2, the TD distribution was fit with an x = 1.5 power. The IS flux was much lower compared to that of the TD, and it had no discernible shape. For CO, the flux was separated into TD and TD_{slow} channels, with the TD distribution fit with an x = 1.3 power and the TD_{slow} flux being around 2/3 that of TD. The CO TD_{slow} distribution appeared to follow a cosine distribution. Finally, for CO_2, the flux was separated into TD and TD_{slow} channels, with the TD distribution fit with an x = 1.1 power and TD_{slow} flux being about 3/4 that of TD. The CO_2 TD_{slow} distribution appeared to follow a cosine distribution. Angular distributions collected at 1000 K↓ for O, O_2, CO, and CO_2, are also shown in **Fig. 4-12**. For O, the flux was separated into IS, TD, and TD_{slow} components, with the TD distribution fit with an x = 1.1 power and TD_{slow} flux being almost the same as that of TD. The shape of the IS flux angular distribution was relatively broad, with a flux like that of TD. For O_2, the TD distribution was fit with an x = 1.4 power, while the IS flux, with a distribution also resembling a lobular shape, was much smaller than the TD flux. For CO, the flux was separated into TD and TD_{slow} channels, with the TD distribution fit with an x = 1 power and TD_{slow} flux being around 3/4 that of TD. Finally, for CO_2, the

flux was separated into TD and TD_{slow}, with the TD distribution fit with an $x = 1.7$ power and TD_{slow} flux being around 1/3 that of TD.

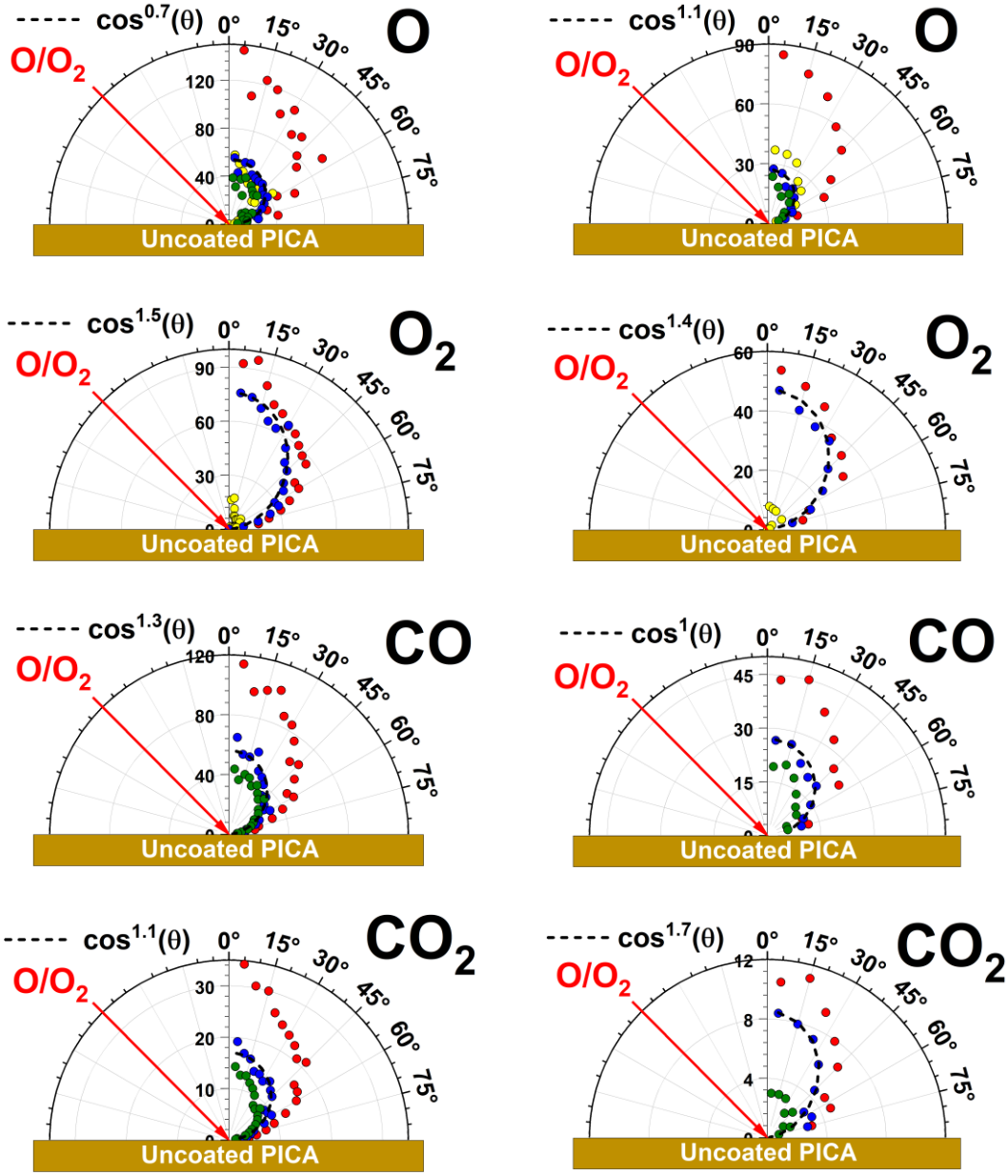

Fig. 4-12. Flux angular distributions of O, O_2, CO, and CO_2 products from uncoated PICA at 1000 K↑ (left) and 1000 K↓ (right), with arrows representing whether temperature had been increasing or decreasing before angular distributions were collected. Red points represent total flux for a particular product. Yellow points (O and O_2 only) represent IS flux. Blue points represent TD flux. Green points (O, CO, and CO_2 only) represent TD_{slow} flux. Dashed lines represent approximate cosine fits for each product's TD distribution.

The higher-resolution SEM images of the uncoated PICA surface after annealing and scattering showed small pits forming on the individual fibers (**Fig. 4-13(b)**). These pits were present both in the area where the O-atom beam impacted as well as in areas outside of the impact spot (**Fig. A-19**) in a manner similar to that of annealed uncoated FiberForm (**Fig. 4-2(b)**). The char surrounding the fibers showed slightly increased porosity compared to fresh uncoated PICA. XPS (**Table 4-1(g)**) of the impact spot showed nearly complete carbon coverage along with a small fraction of oxygen. There was also a small fraction of fluorine present that was not detected in pristine uncoated PICA. A 3 ms peak was observed in the TOF distribution of CO, like that observed from coated FiberForm_A and uncoated FiberForm. This signal appeared at 1300 K↑, and it was still present at 1300 K↓, though it disappeared at 1200 K↓.

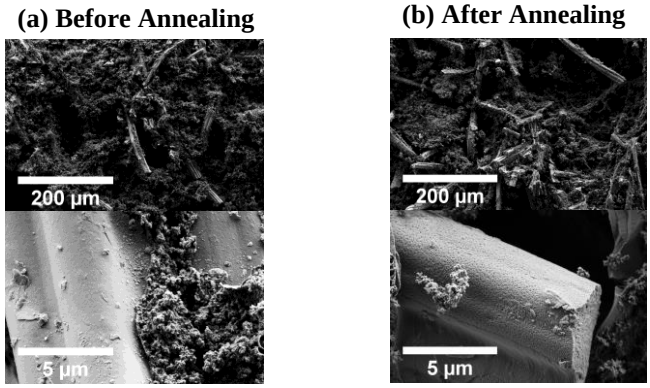

Fig. 4-13. SEM images, taken at two magnifications, of uncoated PICA **(a)** before and **(b)** after experiments with hyperthermal O/O_2 beam.

4.3.8. Temperature-Dependent Flux and Angular Distributions of Coated PICA

Product TOF distributions from coated PICA as a function of temperature for O and CO, and O_2 and products observed from m/z = 44, are shown in **Fig. 4-14** and **Fig. A-20**, respectively. The flux, as shown in **Fig. 4-14(a)**, had been corrected for the mass-

dependent detection sensitivity of our mass spectrometer. Like those on the coated FiberForm_A experiments, the shapes of the TOF distributions, especially for O, exhibited similar changes within the temperature-dependent data. As temperature increased from 1000 K to 1400 K, there was very high and relatively constant O-atom flux leaving the coated PICA surface, and as temperature reached 1500 K, there was nearly equal flux from both IS and TD channels (**Fig. 4-14(b)**). Upon reaching 1600 K, the behavior of the IS and TD signals changed, with IS flux decreasing and TD flux increasing. The total O-atom flux reflected this change, reaching a minimum as temperature reached 1600 K and increasing again as temperature increased to 1800 K. As temperature decreased from 1800 K, total flux monotonically decreased, resembling a trend already exhibited from all the other samples. A correlative phenomenon was observed with CO flux, where total flux was nearly negligible from 1000-1200 K, but as temperature increased to 1300 K, total flux increased, driven by increasing TD flux. Like that of coated FiberForm_A, the CO flux began increasing as temperature reached 1500 K. Similar to that of uncoated PICA, there was also a divergence in the TD and TD_{slow} flux at that point, with TD_{slow} flux increasing more slowly than that of TD as temperature was increased to 1800 K. As temperature decreased from 1800 K, the change in flux qualitatively resembled the change in flux observed from the FiberForm samples as their temperatures decreased. As temperature was decreased to 1500 K, TD and TD_{slow} flux were nearly equivalent, likely reflecting its PICA nature. The total flux for O_2 remained relatively constant (**Fig. A-20(b)**) throughout the whole experiment, reflecting trends observed from every other sample. Its IS and TD fluxes reflect this as well, though similar to uncoated PICA, there was a small decrease in the TD

flux as temperature increased from 1400 to 1600 K. For *m/z* = 44 flux (**Fig. A-20(d)**), there were more significant changes compared to those of the other experiments. Like trends observed from coated FiberForm_A, flux from 1000 to 1400 K as temperature increased was negligible. As temperature reached 1500 K, there were larger and more significant increases in flux compared to all the other samples. Like CO flux from uncoated PICA, the fluxes of both TD and TD_{slow} maintained similar magnitudes until temperature reached 1700 K. Because this sample had a silicone coating, we assumed that *m/z* = 44 signal at higher temperatures was SiO. No CO_2 was detected while the temperature increased from 1000 K, but CO_2 was detected at lower temperatures as temperature decreased to 1000 K. The backgrounds (**Fig. A-21**) were also reflective of the changes observed. As temperature increased, the background intensities of *m/z* = 16, 28, and 44 began rising at 1100 K, 1100 K, and 1200 K, respectively, and their intensities peaked at 1400 K, 1400 K, and 1300 K, respectively. For *m/z* = 16 and 44, corresponding to O, and SiO and CO_2, respectively, their background intensities reached a minimum at 1800 K, and as temperature decreased, their intensities remained relatively constant. However, the intensities of *m/z* = 28, corresponding to CO and possibly Si, reached a minimum at 1600 K before increasing again at 1700 K, and a minimum was not reached again until temperature was decreased to 1600 K, remaining relatively constant as temperature decreased to 1000 K. As with all the other samples, the *m/z* = 32 background intensities, corresponding to O_2, decreased with temperature.

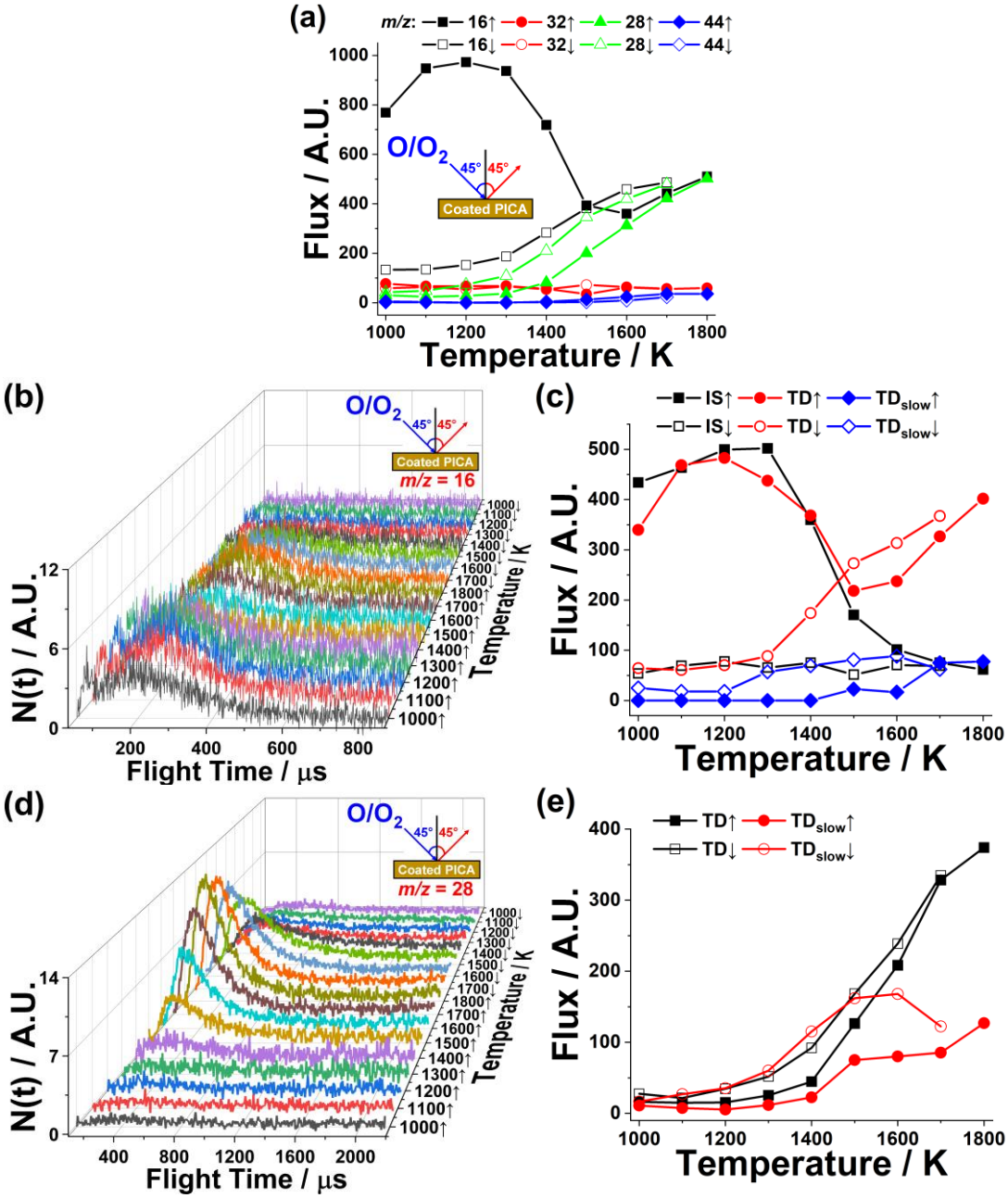

Fig. 4-14. Fluxes and TOF product distributions from coated PICA. **(a)** Flux as a function of temperature from 1000 K to 1800 K for *m/z* = 16, 32, 28, and 44 products from coated PICA. TOF distributions as a function of temperature increasing up to 1800 K, then decreasing to 1000 K, for **(b)** O and **(d)** CO. Fluxes separated into their IS (O only), TD, and TD_{slow} components shown in **(c)** and **(e)** for O and CO, respectively. Arrows indicate signal at temperature point collected when temperature was either increasing or decreasing.

Flux angular distributions for the coated PICA collected at 1000 K↑ are shown in **Fig. 4-15**. At 1000 K↑, sufficient product flux could only be detected for *m/z* = 16, 32, and 28, corresponding to O, O_2, and CO, but not for *m/z* = 44. For O, the flux was only separated into IS and TD components. The TD cosine distribution was fit with an $x = 1.1$ power. The IS flux was slightly larger than that of the TD flux and has a broad angular distribution. For *m/z* = 32, its TD distribution was fit with an $x = 1$ power, and the IS flux was around 2/3 that of TD, with flux directed more towards the surface normal. For CO, the flux was separated into TD and TD_{slow}, with the TD distribution fit with an $x = 1.2$ power and TD_{slow} flux being around 1/3 that of TD. The TD_{slow} angular distribution was also relatively noisy. Flux angular distributions collected at 1000 K↓ at *m/z* = 16, 32, 28, and 44, corresponding to O, O_2, CO, and CO_2, are also shown in **Fig. 4-15**. For O, the flux was separated into IS, TD, and TD_{slow} components. The TD distribution was fit with an $x = 1.3$ power, with TD_{slow} flux being less than half that of TD. The IS distribution resembles a lobular shape with a flux larger than that of TD. For O_2, the TD distribution was fit with an $x = 1.5$ power, while the IS flux was much smaller than the TD flux and oriented towards the surface normal. For CO, its flux was separated into TD and TD_{slow}, with the TD distribution fit with an $x = 1.3$ power and TD_{slow} flux being around 2/3 that of TD. For CO_2, the flux was separated into TD and TD_{slow}, with the TD distribution fit with an $x = 1.8$ power and TD_{slow} flux being less than half that of TD.

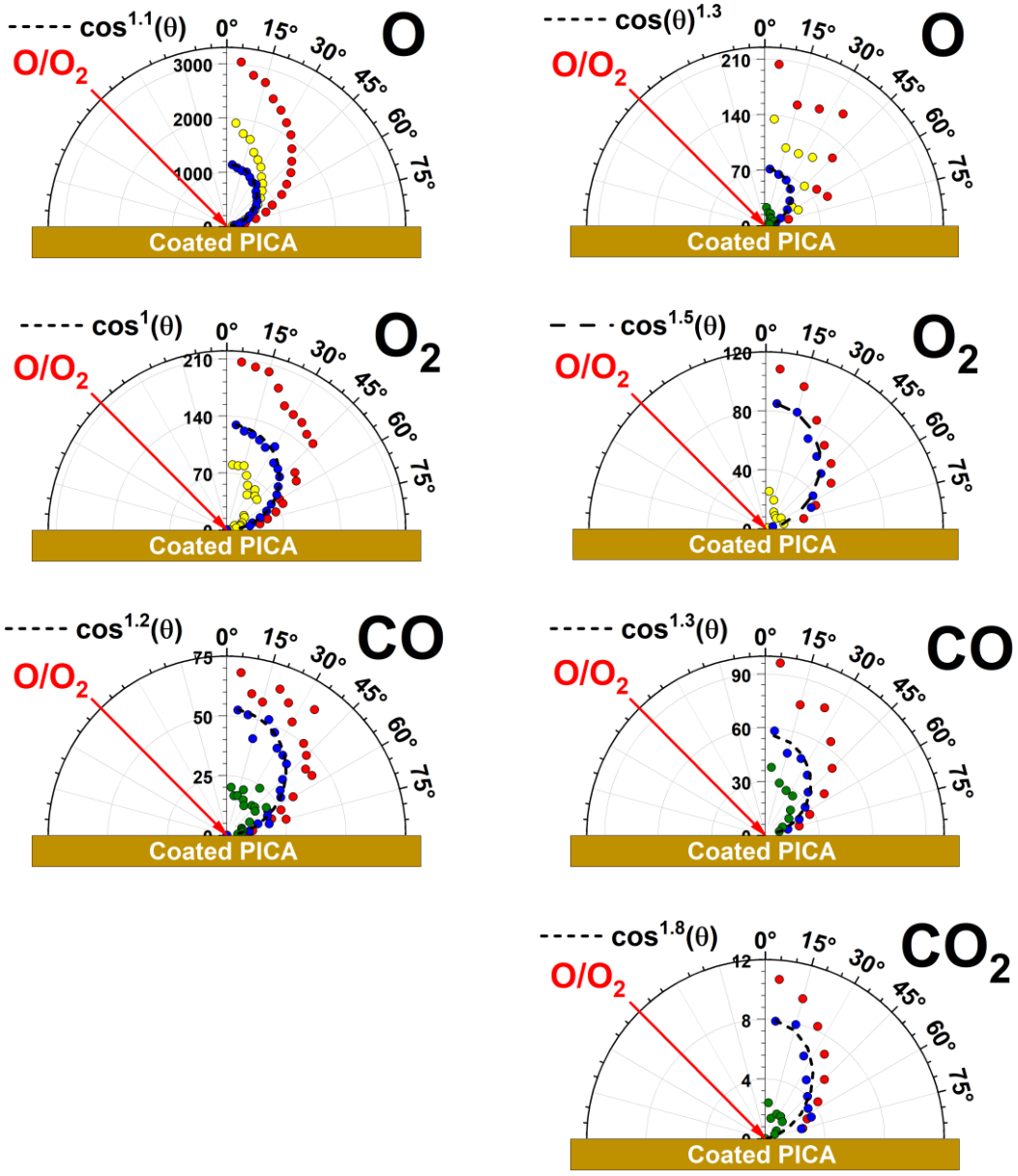

Fig. 4-15. Flux angular distributions of O, O_2, CO, and CO_2 (1000 K↓ only) products from coated PICA at 1000 K↑ (left) and 1000 K↓ (right), with arrows representing whether temperature had been increasing or decreasing before angular distributions were collected. Red points represent total flux for a particular product. Yellow points (O and O_2 only) represent IS flux. Blue points represent TD flux. Green points (O, CO, and CO_2 only) represent TD_{slow} flux. Dashed lines represent approximate cosine fits for each product's TD distribution.

SEM images of the coated PICA surface at high resolution after scattering showed major pitting and fractures forming on the individual fibers (**Fig. 4-16(b)**). These fractures were present both in the area where the O-atom beam impacted as well as in areas outside of the impact spot (**Fig. A-22**). Compared to the state of annealed coated FiberForm, the fiber damage on the coated PICA appeared to be even more extensive. The char surrounding the fibers appeared to be slightly more porous after annealing compared to pristine coated PICA, with more pronounced porosity compared to uncoated PICA. XPS of the impact spot (**Table 4-1(i)**) showed major carbon coverage (92.8%) as well as a small fraction of oxygen (5.2%), silicon (1.3%), and calcium (0.7%). Compared to pristine coated PICA (**Table 4-1(h)**), the fraction of oxygen and silicon decreased significantly, but the fraction of calcium had remained relatively unchanged. One factor related to this may be the presence of 3 ms peaks found within the TOF distributions of CO, like those observed from PICA, coated FiberForm_A, and uncoated FiberForm. This peak appeared as temperature increased to 1600 K and did not disappear until temperature decreased to 1200 K. The presence of this peak may be a sign of lingering impurities in the sample. Unlike the other samples, on coated PICA the 3 ms signal is also present in the SiO TOF distributions, from 1700 K↑ to 1600 K↓.

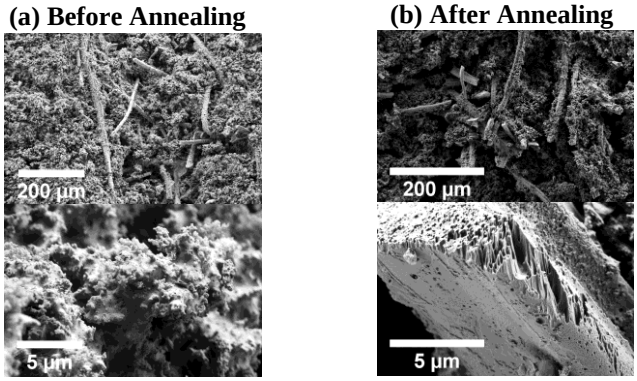

Fig. 4-16. SEM images, taken at two magnifications, of coated PICA **(a)** before and **(b)** after experiments with hyperthermal O/O_2 beam.

4.4. Discussion

We have observed that there were two primary factors affecting the differences in temperature-dependent reactivity and angular distributions of scattered product flux between the various samples and their experimental conditions. The first was the addition of CV-1144-0 silicone coating onto the uncoated FiberForm (pretreated with exposure to atomic oxygen). The second was the impregnation of phenolic resin into the fiber structure to form a carbon/carbon composite. In this section, we discuss how these two factors interact in different ways to explain the differences in behavior between the samples. One additional minor factor will be the effect of residual impurities within the FiberForm structure and how O_2 affects the overall oxidation behavior, which is also discussed.

4.4.1. Annealing and Decomposition without the Beam

The parameters of our experiment meant that we could not easily adjust for the saturation of the signal we observed for the decomposition of the materials as they were ramped to 1000 K or 1600 K. The saturation also means that we cannot accurately quantify

the pyrolyzed species leaving the sample nor can we necessarily identify the products coming off. Nevertheless, the spectra did still provide useful insights into what was contained within the samples and how the coatings affect the decomposition. For uncoated FiberForm, we learned that the pristine sample was not fully carbonized. At the lower temperatures, the presence of several higher mass species was likely indicative of various hydrocarbons adsorbed onto the surface, which was to be expected. However, at higher temperatures, species continued to desorb, with CO_2 and CO (corresponding to m/z = 44 and 28) being released in the 700 to 800 K range, as well as the CO product intensity rising once 1000 K was reached. On coated FiberForm, while the persistent saturation of m/z = 73 meant that we could not quantify its flux profile, the overwhelming prevalence of m/z = 73 meant that the silicone coating was likely not completely oxidized. While the XPS of coated FiberForm showed the Si2p peak within the SiO_2 binding energy, if the silicone were completely oxidized, it would be impossible for SiO_2 to produce signal at m/z = 73. A quick search of the NIST database[147] and other literature[148] indicated that m/z = 73 could fragment from any number of disiloxane or disilane compounds. There also appeared to be variation in the coating application between the two different coated FiberForm samples. While we took care to prepare slabs and oxidize them in as consistent a means as possible, it was very likely that the process of box coat application has inherent uncertainties in how evenly it was sprayed. Regardless, the decomposition of coated FiberForm with mass spectra measured up to 1600 K provided far more useful data at high temperatures, especially from 1200 to 1600 K. In this range, there was no saturation in the signal, which allowed us to properly quantify the amount of product at every important peak in this range.

From this high-temperature data, we found that this was the range in which SiO in particular left the surface. As discussed in Chapter Two, when oxidized SiC was annealed above 1600 K, SiO product was directly associated with the breakdown of the oxide layer. Though the oxide decomposition from FiberForm occurred several hundred kelvins lower than from SiC, the oxide persisted above 1000 K even when the underlying silicone has pyrolyzed away. The presence of this oxidized silicone coating had a major effect even in the absence of the O-atom beam: after coated FiberForm was annealed at 1800 K for 30 minutes the surface of the coated FiberForm (**Fig. 4-2(d)**) showed far more damage on its surface compared to the uncoated FiberForm (**Fig. 4-2(b)**). This showed that, like with the decomposition of the oxide from SiC, most of the decomposition likely occurred at the interface between the oxidized silicone and the surfaces of the individual carbon fibers. Similar changes were observed between the uncoated FiberForm and coated FiberForm experiments with the O-atom beam present. This suggests that, at least within the parameters of our experiment, the coating had a far more significant effect on the fibers compared to the O-atom beam itself. While a much higher O-atom flux could have a more noticeable impact on the fibers, SEM was unable to reveal any erosion solely because of the O-atom beam.

The decomposition of PICA was far more complicated compared to FiberForm. Additionally, because of the overwhelming saturation of so many peaks, there was no way to properly quantify the decomposition at most of the *m/z* ratios within the temperature range we surveyed. The data did provide some insights, however. Between the coated PICA (**Fig. A-5**) and the uncoated PICA(**Fig. A-4**), the only difference in product release

appeared to be the large addition of *m/z* = 73 in the coated PICA. Additionally, there did not appear to be any other change in the onset of any of the other peaks, limitations granted. This suggests that the silicone coating did not affect the pyrolysis chemistry of the PICA bulk in any significant way. This makes sense when one considers the model by which PICA pyrolyzes, in which many of the pyrolysis products originate from deeper within the PICA bulk.

4.4.2. Atomic Oxygen Oxidation of FiberForm

On uncoated FiberForm, the monotonic increases in the flux of O and CO as temperature rose to 1800 K followed similar trends as the flux increases seen in previous studies of O-atom scattering from the surfaces of both FiberForm and vitreous carbon. The CO flux increase could be attributed to increased carbon reactivity at high temperatures. As with the other studies, hysteresis was again present between the flux as temperature increased and the flux as temperature decreased. Intuitively, one might imagine that changes in the O and CO flux ought to be inverse to each other; for example, if CO flux increased and O flux decreased with an increase in temperature, one could surmise that the reactivity of FiberForm increases with temperature, consuming more O as more CO was produced. Instead, what was observed was that both O and CO flux concurrently increase with temperature, and while we could deduce that CO reactivity increased with temperature, we do not have a satisfactory explanation for why O flux also increased. Speculation from Murray et al. (2020)[43] surmised that surface-adsorbed O-atoms may migrate out of the scattering detection area faster at lower temperature than at higher temperature, in that at higher temperatures a higher fraction of adsorbed O-atoms will leave

the surface instead of remaining to migrate. One other possibility they raised was that more O-atoms are absorbed into the bulk of the material at lower temperatures than at higher temperatures, meaning that the higher O-atom flux at higher temperatures was an apparent effect from the release of absorbed O-atoms from the bulk. A final possibility raised in the original vitreous carbon study from Murray et al. (2015)[42] was speculation that the porosity of their vitreous carbon sample increases with temperature, thus allowing more collisions at the surface and possibly enhancing O-atom trapping. We do not have a way to verify this with our internal techniques, though there has been a recent study that has used transmission electron microscopy to study a glassy carbon surface *in situ* as their samples were slowly ramped up to 1200°C,[149] which means that this possibility could potentially be investigated in the future. As for the other species, the O_2 flux appeared to have very little discernible temperature dependencies with the heated FiberForm, remaining relatively constant compared to O and CO flux. This was similar to that observed from Poovathingal et al. (2021),[47] but dissimilar to both vitreous carbon studies from Murray et al.,[42-43] who found a slight increase in O_2 flux with temperature increase. Its backgrounds also decreased with increasing temperature. We do not have a ready explanation for either of these phenomena. Meanwhile, CO_2, similar to these previous O-atom beam-scattering studies on carbon, was only produced at lower temperatures, with its flux disappearing above 1100 K and its background remaining relatively constant throughout the experiment.

4.4.3. Impurities and O_2 Reactivity

The discovery of the reactivity of the FiberForm with O_2 was unexpected. While the flux of CO from the uncoated FiberForm still followed the general monotonic trend

observed in the previous FiberForm study, there were subtle differences in the trends that we found, which we attribute to annealing the FiberForm. From 1300 to 1500 K, there was a significant inversion in the flux as temperature increased compared to the flux when temperature decreased, where the flux as temperature increased was lower than the flux as temperature decreased. In the previous study on FiberForm,[47] CO flux as temperature increased was always lower than the flux as temperature decreased. Our investigation not only found that inversion disappeared after annealing the sample at 1800 K, we also found anomalous peaks at 3 ms in the CO TOF distributions at 1300 K and 1400 K that disappeared after annealing. Increasing CO products as the temperature of O_2-adsorbed carbons approached 1300 K has been observed in a number of prior studies.[150-151] Previous studies that have looked at O_2 scattering from graphite[131] and graphene[133] have shown etching at high surface temperatures of 1375 K localized within defect sites on the material. However, these studies did not look at the role of possible impurities in catalyzing the surface's reactivity, and all have focused on the use of relatively clean carbon samples. Instead, what we found was that scattering O_2 on the surface of a FiberForm filled with impurities, especially calcium, was the likely cause of both the inversion in the flux patterns as well as the appearance of the 3 ms peak. FiberForm oxidation studies from Panerai et al. (2013)[145] and Lachaud et al. (2011)[144] found calcium carbonate deposits left over after their high temperature oxidation experiments. The fact that their experiments only reached 1300 K may be why they were still able to detect impurities, whereas our FiberForm samples were annealed to 1800 K and revealed that the annealed surface was nearly all covered in carbon with a small fraction of oxygen. This phenomenon was not only observed

on the uncoated FiberForm, however. 3 ms peaks are also found from scattering on coated FiberForm (raised to 1000 K), PICA, as well as coated PICA. Not only might these impurities cause the 3 ms peak, they may also affect the flux as well, especially for CO. At the critical temperatures from 1300 to 1500 K, they may be the cause of a small decrease in CO production from pristine uncoated FiberForm as compared to temperature-dependent CO flux from an annealed sample of FiberForm. This decrease was not so obvious on either coated FiberForm or coated PICA, but on uncoated PICA, this might be the proximal cause of the slight plateauing in flux of CO from 1400 to 1500 K. These impurities may also be the cause of the 3 ms peak from the coated PICA SiO TOF distribution above 1500 K. One may wonder whether the 3 ms signal in these SiO TOF distributions might be because of the O_2 fraction in the beam, or whether the 3 ms peak was "inherent" to scattering from SiO_2. There is evidence for the former hypothesis, as the SiO TOF distribution from coated FiberForm, a material that we have observed to lose all its impurities after annealing, at this temperature does not show as distinctive peaks at 3 ms as coated PICA does. In addition, in the experiments described in Chapter Two, there was no distinct 3 ms peak observed in the m/z = 44 TOF distributions for those temperatures in which a TOF distribution was collected, which was evidence that there was not an "inherent" 3 ms peak found for SiO products. While this type of reactivity has not been directly observed before, we can still speculate on its general mechanism. In general, unlike O, which is highly reactive and reacts directly with its target, molecular oxygen must first dissociate before it is available to participate in a reaction.[152] As Chen and Yang (1998) describe,[152] this dissociated atomic oxygen can form an epoxide group with the surface carbons, helping to

weaken the C—C and promoting the desorption of carbon oxide species like carbon monoxide. This higher barrier resulting from dissociative chemisorption because of O_2 having to first dissociate may be the reason behind the comparatively slow desorption of O_2-induced CO formation. In addition, there has been a study from Schrader (1978)[153] that found calcium to catalytically increase the chemisorption rate of oxygen onto gold. This catalytic effect may be why we are able to observe the CO desorption, while on non-catalytically enhanced carbon, the CO desorption may be slower and occurring on a longer time scale. The reduction in the "normal" CO flux, however, is far from clear. There is certainly the possibility that calcium may have been interacting with the incident atomic oxygen, though the nature of the interaction is something we cannot speculate on. Because of the limitations of XPS, we cannot definitively determine the chemical nature of the calcium, whether it was in the form of $CaCO_3$, CaC_2, CaO, etc., though considering that $CaCO_3$ has been found previously and that it has the relatively lowest vapor pressure of those listed, it was more than likely in the carbonate form.

4.4.4. Atomic Oxygen Oxidation of Uncoated PICA

Product flux from O-atom scattering from PICA showed overall much reduced relative flux of O and CO in relation to O_2 when compared to relative flux from uncoated FiberForm, as well as more complicated behavior. This was not what we necessarily expected, as we assumed that the PICA was mostly charred once the temperature reached 1000 K, so we assumed that the behavior would be mostly like uncoated FiberForm. The CO background intensity (**Fig. A-18**) was contrary to this assumption, with overall elevated CO background signal all the way up to 1800 K. This suggests that that elevated

background could be because of residual phenolic resin continuing to char. Bessire et al. (2018)[36] discovered continued production of CO up to 1200°C and hypothesized that much of the CO production comes from the decomposition of oxygen-containing phenyl groups. The flux as temperature increased also provided clues, with the O-atom flux as temperature increased being relatively lower compared to O-atom flux from uncoated FiberForm, indicative of increased O-atom adsorption or absorption into the charring material, and quite possibly into the remains of the charred phenolic resin. A recent study from He et al. (2019)[154] investigated the atomic oxygen oxidation mechanisms of epoxy resins used in low-Earth orbit and found abstraction of hydrogen to form volatile –OH groups as well as formation of these same hydroxyl groups onto the epoxy polymers. Both of these mechanisms of either abstraction of a proton or the addition of O to phenylic species have been previously determined from the atomic oxygen attack on benzene.[155] For us, the transient observation of m/z = 17 product at the beginning of the uncoated PICA scattering experiment was evidence for possible O-atom abstraction of hydrogen from these lingering polycyclic aromatic hydrocarbons species still present during our experiment. Therefore, we believe that the relatively low O-atom flux up until 1500 K could be because of the residual aromatic hydrocarbons absorbing and reacting with the incident O-atoms. The overall higher CO flux in comparison to O-atom flux as the temperature increased was likely related. As the SEM images show, there was noticeably greater erosion within the charred phenolic resin after the experiment compared to pristine uncoated PICA (**Fig. 4-13**), with more of the carbon fibers being exposed, and this erosion was likely related to the higher CO production. This increase in char erosion was also observed in previous

oxidation and pyrolysis studies of PICA-like materials.[156] This phenomenon of the matrix eroding more quickly than the reinforcing carbon fibers is commonly assumed when developing oxidation models involving carbon/carbon fiber composites.[132, 157] As temperature decreased from 1800 K, the CO flux decreased monotonically, and the O-atom flux followed similar behavior except at 1200 K, increasing slightly before decreasing again at 1100 K, which suggests that the PICA's behavior more closely follows that of uncoated FiberForm after being annealed to 1800 K. This makes sense, because as the char eroded, the sample behavior was going to more resemble that of its carbon fiber substrate. In addition, as with uncoated FiberForm, there are pits found on the carbon fibers of charred PICA, while pristine PICA does not have any of these pits. Similar to what was observed on annealed uncoated FiberForm, it is likely that these pits are due primarily to the annealing to 1800 K, but as we did not examine any charred PICA without O-atom exposure, we cannot say how much the O-atoms also played a role. We also cannot compare the erosion of the char with and without O-atom exposure. One other factor that we must consider regarding the similarities and differences in behavior between PICA and FiberForm is the possible role of impurities. XPS of pristine PICA only showed carbon and oxygen on the surface, but annealed PICA also showed the presence of fluorine. While seemingly anomalous, this could just reflect the dominance of the presence of uncharred phenolic resin accessible by the XPS instrument. This could be why we observe fluorine in the annealed PICA that was not present in the pristine material, with the phenolic resin matrix mostly covering up any resident impurities in the material. One thing we could do in the future is pre-pyrolyze PICA to only 1000 K and then examining its XPS to reveal

more of its embedded impurities. Another possibility would be to pre-char the PICA up to 1800 K, then use the atomic oxygen beam-surface scattering apparatus to collect temperature-dependent data similar to what was done with all the samples mentioned in this chapter.

4.4.5. Effects of Oxidized Silicone Coating

The addition of silicone caused the temperature-dependent product flux from O-atom scattering of both silicone-coated FiberForm and silicone-coated PICA to show remarkable similarities, with greatly increased O flux from 1000 to 1500 K, along with a corresponding suppression of CO flux within this temperature range. This greater flux of O-atoms from the surface was because of the passivating effect of the oxide coating on the FiberForm fibers. Instead of adsorbing onto and reacting with the fiber surfaces, a large fraction of incident O-atoms scatters from the oxide layer through both IS and TD channels. Results from Chapter Two and from Murray et al. (2017)[95] show the vast majority of O-atom flux from SiO_2 leaving through IS channels. In contrast, on our coated FiberForm, the TD O flux was higher compared to that in those previous studies, constituting ~30% on average of the total O-atom flux at each temperature, while the TD O flux on coated PICA was even greater, constituting almost half of the total O-atom flux. Because we are the first to use this specific technique with coated FiberForm and coated PICA, we cannot rely on past oxidation studies with silicon-containing C/C composites to elucidate why the TD signal was so high. However, since CO flux was very low in this temperature range, we can reasonably assume that the fibers to which the O-atom beam has access are mostly coated with the silicone and thoroughly oxidized such that very little carbon was exposed

to the O-atom beam. Thus, we attributed this higher TD scattering compared to oxidized SiC to the fibrous and porous structure of the surface. Increased porosity means multiple bounces of the O-atoms between the fibers of FiberForm, driving a larger proportion of the incident atoms into thermal equilibrium, which means a higher proportion of TD scattering, especially compared to scattering from a flat, crystalline layer of SiO_2. Despite the porosity, however, there was no long-flight time component observed in the O-atom TOF distribution from coated FiberForm. This could be because of the additive effects from a lower adsorption affinity O-atoms have towards SiO_2 compared to carbon, along with the similar porosities both coated and uncoated FiberForm have. Around 1500 K this pattern breaks down, and upon reaching 1600 K, the O and CO flux reverts to a trend resembling that of scattering from uncoated FiberForm. It is known from Chapter Two that for oxide-covered SiC under high vacuum (~5 x 10^{-7} torr), the oxide layer began to break down around 1673 K. While this experiment suggests a breakdown beginning around 300 K lower compared to the wafer oxide, we could still see clearly from the species' backgrounds that the breakdown of the SiO_2 was the proximal cause of the change in reactivity for both O and CO. Starting at 1200 K, species with *m/z* = 16, 28, and 44 all increased significantly, with *m/z* = 28 and 44 likely corresponding partly to Si and SiO, respectively. The mass spectra from the pyrolysis of coated FiberForm from 1200 to 1600 K corroborated this data, showing a significant contribution from SiO in this range as well as a much smaller contribution from Si. This breakdown was most evident when examining the SEM for both coated FiberForm and coated PICA after the experiments. In fact, much of the erosion observed from these samples appeared to be because of the decomposition of the silicone

layer eroding much of the underlying carbon away with it, whether that was from the carbon fibers or from the char in regard to coated PICA. It was difficult to tell from **Fig. 4-16** if there was more char erosion in uncoated PICA compared to coated PICA, and in addition we did not conduct an experiment to anneal and examine the surface of coated PICA without O-atom exposure. The differences in the fluxes of O and CO from coated PICA (**Fig. 4-13(b)**) and coated FiberForm (**Fig. 4-7**, **Fig. 4-9**) as temperature decreased from 1800 K could be explained as follows. As coated PICA contains the charred matrix, the incident O-atom beam will preferentially react with the charred carbon, forming CO, whereas in coated FiberForm, only the carbon fibers were remaining, reducing the amount of reactive scattering. This could be why the fluxes of O and CO from coated PICA were closer to each other compared to the fluxes of O and CO from coated FiberForm_A and coated FiberForm_B. The CO background intensity at 1800 K for coated PICA, however, suggests that, especially compared to uncoated PICA, there was still a significant amount of residual aromatic hydrocarbons even at that temperature. A reason for this lingering presence could be explained when examining the XPS of coated PICA after the experiment, which found residual silicon on the surface as well as a small fraction of calcium. Analogous to uncoated PICA, the presence of the phenolic resin, even in its charred form, appeared to provide a shielding effect that prevented further loss of impurities through decomposition. One other reason for the lack of complete carbonization could also be that the PICA was coated with 1.5 box coats of CV-1144-0 instead of just 1 box coat. Having a coating of 150-300 μm instead of 100-200 μm may mean more energy was needed to decompose the silicone completely. We also did not find any fluorine in coated PICA,

while in uncoated PICA there was a clear peak for it. Again, further studies will need to be done with coated PICA, like uncoated PICA, to be able to address these discrepancies.

4.4.6. Angular Distribution Differences between Coated and Uncoated FiberForm

In comparing the O and O_2 flux angular distributions between FiberForm and coated FiberForm at 1000 K↑, the angular distributions from coated FiberForm were broader in shape and of much higher intensity compared to those of uncoated FiberForm. These differences were representative of the presence of oxide on the fibers. A significant difference in the power of the cosine distribution fit for the TD distributions between uncoated FiberForm at 1000 K and post-annealed coated FiberForm_A at 1000 K was observed (1.5 and 2.5, respectively). We cannot definitively ascertain the precise morphological reasons why this change occurred, but in general, there was likely a change in the overall orientation of the fibers in the local region in which the beam impinged. As described in Poovathingal et al. (2021),[47] thermal desorption from a planar surface ought to follow a $\cos^1(\theta_f)$ distribution. Deviations from this unit power are likely because of the many individual carbon fibers at the apparent surface of the FiberForm, with the fiber surfaces not necessarily parallel to the apparent surface of the FiberForm. Thus, the orientation distribution of the fibers may have changed as the silicone coating decomposed from the FiberForm, causing the change in the cosine powers. For the CO and CO_2 flux angular distributions, the similar shapes in comparing the distributions of coated and uncoated FiberForm suggest that their oxidation was representative of the "core" uncoated FiberForm, with the primary effect of the oxide layer being reduced flux, the overall intensity of reactive products from coated FiberForm being around half that of uncoated

FiberForm. Similar to our conclusion from the temperature dependence of coated FiberForm, we could not presume that the carbon fibers were completely coated, and there were likely defects within the oxide layer where the underlying carbon was exposed. The desorption channels, as with the temperature surveys, showed that, except for O_2, all the species had some slow signal that can be fit to a TD_{slow} function. It is unclear why O_2 does not desorb through a TD_{slow} channel. For O-atom angular distributions at 1000 K from all the samples except for O-atom distributions from non-annealed coated FiberForm, the presence of TD_{slow} flux was likely an innate characteristic of oxidation from FiberForm, having been observed from both FiberForm and vitreous carbon.[47] As for the lack of TD_{slow} O signal detected from nonannealed coated FiberForm_A, this did not necessarily mean there was zero slow signal for this species. After all, both CO and CO_2 were still detected with TD_{slow} signals. Instead, because of the overwhelmingly higher flux of O scattering from the oxide coating compared to all the other species, any TD_{slow} signal may have just ended up being drowned out.

At 1600 K, the similarities in the angular distributions between uncoated FiberForm and coated FiberForm suggest a very similar surface structure between the two samples. The main difference, other than the overall higher flux on coated FiberForm, was the presence of a very small m/z = 44 signal on coated FiberForm as opposed to uncoated FiberForm, where there was no detectable signal. As CO_2 production had repeatedly been observed to disappear above 1200 K on carbon, it was highly unlikely that the detected signal was CO_2. Instead, it was likely that residual silicon still left behind on the surface was the actual cause of the signal. We did not confirm this using the naturally occurring

isotopic ratio of silicon, though, as we did not check *m/z* = 45 or 46. For O, there was a noticeable difference in the cosine power of coated FiberForm_B, compared both to itself at 1000 K (2.2 vs 1.6) as well as to its uncoated counterpart at 1600 K (also 2.2 vs 1.6). As previously stated, this change was likely due to the local fibers' orientation distribution changing. It is unclear, however, why the cosine power from FiberForm_B at 1000 K was different from that of FiberForm_A at 1000 K↓ (1.6 vs 2.5).

4.4.7. Angular Distribution Differences between Coated and Uncoated PICA

Because this was the first O-atom beam-surface scattering study of PICA, we do not have readily available comparisons for our angular distributions. Regardless, we can say that, similar to the FiberForm samples, O_2 flux could be fully fit with only Maxwell-Boltzmann distributions, while all the other species show significant TD_{slow} flux. In fact, the TD_{slow} flux was a much higher proportion of the flux from the uncoated PICA compared to FiberForm, nearly composing an equivalent amount to the TD flux. Overall flux for both PICA samples was much lower compared to the three FiberForm samples, and combined with the much lower IS flux in both O and O_2, this suggests that far more of the O beam was being adsorbed and possibly even absorbed into the PICA system. Even on coated PICA, there was a much higher proportion of TD to IS flux of both O and O_2 species, which was more evidence of higher adsorption on the surface. Previous studies of carbon/carbon composite oxidation have all observed preferential oxidation of the carbon matrix as opposed to the carbon fiber FiberForm base.[158] This suggests that much of the reactive oxidation forming CO and CO_2 was occurring on the matrix instead of the fibers themselves. Interestingly, no *m/z* = 44 flux was observed from the coated PICA at 1000 K

before annealing. This could be because of the higher box-coat application of silicone used for coated PICA compared to coated FiberForm that ensured more complete coverage of the surface, though we are still unsure. We can make more direct comparisons between the post-annealed coated PICA at 1000 K and post-annealed coated FiberForm at 1000 K, and these comparisons showed remarkable similarities in both shape and overall flux, especially when this was juxtaposed with post-annealed uncoated PICA at 1000 K vs uncoated FiberForm at 1000 K. This might be related to the greater effect from the damage caused by the decomposing silicone on both the fibers and the matrix. It is difficult to draw concrete conclusions from this, however, and more studies will need to be done to elucidate the meanings behind the differences in behavior observed, including additional angular distributions at 1600 K.

4.5. Conclusion

In this study, we have conducted a comparative study on how the presence of CV-1144-0 silicone coating and phenolic resin matrix affects the atomic oxygen reactivity of FiberForm-based heat shields. The introduction of CV-1144-0 silicone coating onto the fibers of both FiberForm and PICA caused similar effects on both materials, with greatly reduced, yet not completely suppressed, reactive scattering, along with an enormous increase in nonreactive O-atom scattering, reflective of the protective and passivating effect of the silicon-oxide coating on the sample surface. This protection, however, only remains up until the passive-to-active oxidation transition, when the oxide coating began to decompose and the oxidation started to resemble that of its uncoated form, whether

FiberForm or PICA. The addition of the phenolic resin matrix into the FiberForm to form PICA resulted in far more complicated O-atom beam-surface scattering, where even the changes in flux of products leaving the surface as temperature decreased were dissimilar to that of FiberForm, whether coated or uncoated, though the pattern of coated PICA oxidation as temperature decreased was more similar to that of uncoated FiberForm than that of uncoated PICA. In addition, we have discovered that the presence of impurities may cause minor changes in the reactivity of the samples. When pristine uncoated FiberForm contains impurities such as calcium, its atomic oxygen reactivity will show slight differences compared to atomic oxygen oxidation of FiberForm that had been previously annealed. This difference was revealed in the slightly reduced flux of CO from 1300 to 1500 K from uncoated FiberForm as well as the presence of a 3 ms peak in the CO TOF distribution, a peak position that was also observed in CO and SiO TOF distributions from uncoated and coated PICA. We have observed this peak to appear with only an O_2 beam scattering against the impurity-filled sample, suggesting that O_2, even at such a low proportion of our O-atom beam, has a more significant effect on reactivity than we anticipated. Furthermore, we have discovered that, whether because the phenolic resin matrix contains more impurities, and/or because the matrix prevents the carbon fiber impurities from escaping the surface, the PICA, both coated and uncoated, still retains detectable fractions of impurities and trace amounts of silicon on coated PICA, even after oxidizing at 1800 K. Overall, we were able to characterize the dynamics of atomic oxygen molecular beam-surface scattering from samples of FiberForm, PICA, and their silicone-coated equivalents. This new data will be used by NASA to develop improved oxygen

ablation models. Further investigations, however, will still need to be conducted in order understand the atomic oxygen oxidation of these materials further. In particular, studies will need to be conducted on the charred PICA material.

4.6. References

17. Jacobson, N. S.; Myers, D. L.; Harder, B. J., Active oxidation of silicon carbide. *Materials at High Temperatures* **2012**, *29*, 193-198.
18. Jacobson, N.; Harder, B.; Myers, D., Oxidation Transitions for SiC Part I. Active-to-Passive Transitions. *J. Am. Ceram. Soc.* **2013**, *96*, 838-844.
25. de Groh, K. K.; McCollum, T. A., Low Earth orbit durability of protected silicone for refractive photovoltaic concentrator arrays. *Journal of Spacecraft and Rockets* **1995**, *32*, 103-109.
27. Yan, L.; Gao, X.; Bungay, C.; Woollam, J. A., Study of surface chemical changes and erosion rates for CV-1144-0 silicone under electron cyclotron resonance oxygen plasma exposure. *Journal of Vacuum Science & Technology A* **2001**, *19*, 447-454.
28. Scialdone, J. J.; Clatterbuck, C. H.; Ayres-Treusdell, M.; Park, G.; Kolos, D., *Atomic Oxygen and Space Environment Effects on Aerospace Materials Flown with EOIM-III Experiment*, 1996.
32. Minton, T. K., et al., Atomic Oxygen Effects on POSS Polyimides in Low Earth Orbit. *ACS Applied Materials & Interfaces* **2012**, *4*, 492-502.
34. Wong, H.-W.; Peck, J.; Assif, J.; Lachaud, J.; Mansour, N. N. In *Quantitative determination of species production from the pyrolysis of the Phenolic Impregnated Carbon Ablator (PICA)*, 53rd AIAA Aerospace Sciences Meeting, 2015; p 1447.
35. Bessire, B. K.; Lahankar, S. A.; Minton, T. K., Pyrolysis of Phenolic Impregnated Carbon Ablator (PICA). *ACS Applied Materials & Interfaces* **2015**, *7*, 1383-1395.
36. Bessire, B. K.; Minton, T. K., Decomposition of Phenolic Impregnated Carbon Ablator (PICA) as a Function of Temperature and Heating Rate. *ACS Applied Materials & Interfaces* **2017**, *9*, 21422-21437.
39. Nelessen, A., et al. In *Mars 2020 Entry, Descent, and Landing System Overview*, 2019 IEEE Aerospace Conference, 2-9 March 2019; 2019; pp 1-20.
41. Noda, T.; Inagaki, M.; Yamada, S., Glass-like carbons. *Journal of Non-Crystalline Solids* **1969**, *1*, 285-302.
42. Murray, V. J.; Marshall, B. C.; Woodburn, P. J.; Minton, T. K., Inelastic and Reactive Scattering Dynamics of Hyperthermal O and O2 on Hot Vitreous Carbon Surfaces. *The Journal of Physical Chemistry C* **2015**, *119*, 14780-14796.
43. Murray, V. J.; Recio, P.; Caracciolo, A.; Miossec, C.; Balucani, N.; Casavecchia, P.; Minton, T. K., Oxidation and nitridation of vitreous carbon at high temperatures. *Carbon* **2020**, *167*, 388-402.
44. Poovathingal, S.; Schwartzentruber, T. E.; Murray, V. J.; Minton, T. K.; Candler, G. V., Finite-Rate Oxidation Model for Carbon Surfaces from Molecular Beam Experiments. *AIAA Journal* **2017**, *55*, 1644-1658.
45. Swaminathan-Gopalan, K.; Borner, A.; Murray, V. J.; Poovathingal, S.; Minton, T. K.; Mansour, N. N.; Stephani, K. A., Development and validation of a finite-rate model for carbon oxidation by atomic oxygen. *Carbon* **2018**, *137*, 313-332.
46. Prata, K. S.; Minton, T.; Schwartzentruber, T. E., *Air-Carbon Ablation Model for Hypersonic Flight from Molecular Beam Data*, 2020.

47. Poovathingal, S. J.; Qian, M.; Murray, V. J.; Minton, T. K., Reactive and Inelastic Scattering Dynamics of Hyperthermal O and O2 from a Carbon Fiber Network. 2021.
48. Marshall, T. D.; Pawelko, R. J.; Anderl, R. A.; Smolik, G. R.; Merrill, B. J.; Moore, R. L.; Petti, D. A., Oxygen reactivity of a carbon fiber composite. *Fusion Engineering and Design* **2003**, *69*, 663-667.
49. McKee, D. W., Oxidation behavior of matrix-inhibited carbon/carbon composites. *Carbon* **1988**, *26*, 659-664.
50. Bessire, B. K.; Borner, A. P.; Meurisse, J. B.; Monk, J. D., Progress Towards Modeling the Mars Science Laboratory PICA-NuSil Heatshield. **2019**.
53. Zhang, J.; Upadhyaya, H. P.; Brunsvold, A. L.; Minton, T. K., Hyperthermal Reactions of O and O2 with a Hydrocarbon Surface: Direct C−C Bond Breakage by O and H-Atom Abstraction by O2. *The Journal of Physical Chemistry B* **2006**, *110*, 12500-12511.
54. Garton, D. J.; Brunsvold, A. L.; Minton, T. K.; Troya, D.; Maiti, B.; Schatz, G. C., Experimental and Theoretical Investigations of the Inelastic and Reactive Scattering Dynamics of O(3P) + D2 *The Journal of Physical Chemistry A* **2006**, *110*, 1327-1341.
55. Garton, D. J.; Minton, T. K.; Maiti, B.; Troya, D.; Schatz, G. C., A crossed molecular beams study of the O(3P)+H2 reaction: Comparison of excitation function with accurate quantum reactive scattering calculations. **2003**, *118*, 1585-1588.
56. Troya, D.; Schatz, G. C.; Garton, D. J.; Brunsvold, A. L.; Minton, T. K., Crossed beams and theoretical studies of the O(3P)+CH4→H+OCH3 reaction excitation function. *The Journal of Chemical Physics* **2004**, *120*, 731-739.
57. Buczala, D. M.; Brunsvold, A. L.; Minton, T. K., Erosion of Kapton H® by Hyperthermal Atomic Oxygen. *Journal of Spacecraft and Rockets* **2006**, *43*, 421-425.
59. Brink, G. O., Electron Bombardment Molecular Beam Detector. *Review of Scientific Instruments* **1966**, *37*, 857-860.
61. Minton, T. K.; Giapis, K. P.; Moore, T., Inelastic Scattering Dynamics of Hyperthermal Fluorine Atoms on a Fluorinated Silicon Surface. *The Journal of Physical Chemistry A* **1997**, *101*, 6549-6555.
95. Murray, V. J.; Pilinski, M. D.; Smoll, E. J.; Qian, M.; Minton, T. K.; Madzunkov, S. M.; Darrach, M. R., Gas–Surface Scattering Dynamics Applied to Concentration of Gases for Mass Spectrometry in Tenuous Atmospheres. *The Journal of Physical Chemistry C* **2017**, *121*, 7903-7922.
116. Cooper, R.; Upadhyaya, H. P.; Minton, T. K.; Berman, M. R.; Du, X.; George, S. M., Protection of polymer from atomic-oxygen erosion using Al2O3 atomic layer deposition coatings. *Thin Solid Films* **2008**, *516*, 4036-4039.
129. De Groh, K. K.; Banks, B. A.; Asmar, O. C.; Yi, G. T.; Mitchell, G. G.; Guo, A.; Sechkar, E. A., Erosion Results of the MISSE 8 Polymers Experiment After 2 Years of Space Exposure on the International Space Station. **2017**.
130. Fahy, W. P.; Chang, A.; Wu, H.; Koo, J. H., Recent Developments of Ablative Thermal Protection Systems for Atmospheric Entry. In *AIAA Scitech 2021 Forum*, 2021.
131. Edel, R.; Grabnic, T.; Wiggins, B.; Sibener, S. J., Atomically-Resolved Oxidative Erosion and Ablation of Basal Plane HOPG Graphite Using Supersonic Beams of O2

with Scanning Tunneling Microscopy Visualization. *The Journal of Physical Chemistry C* **2018**, *122*, 14706-14713.
132. Ferguson, J. C.; Panerai, F.; Lachaud, J.; Mansour, N. N., Theoretical study on the micro-scale oxidation of resin-infused carbon ablators. *Carbon* **2017**, *121*, 552-562.
133. Hariharan, S.; Majumder, M.; Edel, R.; Grabnic, T.; Sibener, S. J.; Hase, W. L., Exploratory Direct Dynamics Simulations of 3O2 Reaction with Graphene at High Temperatures. *The Journal of Physical Chemistry C* **2018**, *122*, 29368-29379.
134. Panerai, F.; Mansour, N. N.; Lachaud, J.; Martin, A., Numerical and experimental study of carbon fiber oxidation. In *52nd Aerospace Sciences Meeting*, 2014.
135. Tzeng, S.-S.; Chr, Y.-G., Evolution of microstructure and properties of phenolic resin-based carbon/carbon composites during pyrolysis. *Materials Chemistry and Physics* **2002**, *73*, 162-169.
136. Andreoli, S.; Eser, S., Relating reactivity to structure in cokes and carbon materials: Temperature-programmed oxidation and microscopy techniques. *Carbon* **2020**, *168*, 362-371.
137. Levendis, Y. A.; Flagan, R. C.; Gavalas, G. R., Oxidation kinetics of monodisperse spherical carbonaceous particles of variable properties. *Combustion and Flame* **1989**, *76*, 221-241.
138. Halbig, M. C.; McGuffin-Cawley, J. D.; Eckel, A. J.; Brewer, D. N., Oxidation Kinetics and Stress Effects for the Oxidation of Continuous Carbon Fibers within a Microcracked C/SiC Ceramic Matrix Composite. *Journal of the American Ceramic Society* **2008**, *91*, 519-526.
139. Hatta, H.; Aoki, T.; Kogo, Y.; Yarii, T., High-temperature oxidation behavior of SiC-coated carbon fiber-reinforced carbon matrix composites. *Composites Part A: Applied Science and Manufacturing* **1999**, *30*, 515-520.
140. Lamouroux, F.; Bertrand, S.; Pailler, R.; Naslain, R.; Cataldi, M., Oxidation-resistant carbon-fiber-reinforced ceramic-matrix composites. *Composites Science and Technology* **1999**, *59*, 1073-1085.
141. Lamouroux, F.; Camus, G.; Thébault, J., Kinetics and Mechanisms of Oxidation of 2D Woven C/SiC Composites: I, Experimental Approach. *Journal of the American Ceramic Society* **1994**, *77*, 2049-2057.
142. Liu, W.; Wei, Y.; Deng, J., Carbon-fiber-reinforced C-SiC binary matrix composites. *Carbon* **1995**, *33*, 441-447.
143. Murthy, T. S. R. C.; Reeman, L.; Zou, J.; Venkatachalam, V.; Baker, B.; Wang, M.; Binner, J., Role of rare earth oxide particles on the oxidation behaviour of silicon carbide coated 2.5D carbon fibre preforms. *Open Ceramics* **2020**, *2*, 100018.
144. Lachaud, J.; Mansour, N.; Ceballos, A.; Pejakovic, D.; Zhang, L.; Marschall, J., Validation of a volume-averaged fiber-scale model for the oxidation of a carbon-fiber preform. In *42nd AIAA Thermophysics Conference*, 2011.
145. Panerai, F.; Martin, A.; Mansour, N. N.; Sepka, S.; Lachaud, J., Flow-tube Oxidation Experiments on the Carbon Preform of PICA. In *44th AIAA Thermophysics Conference*, 2013.

146. Montemore, M. M.; van Spronsen, M. A.; Madix, R. J.; Friend, C. M., O2 Activation by Metal Surfaces: Implications for Bonding and Reactivity on Heterogeneous Catalysts. *Chemical Reviews* **2018**, *118*, 2816-2862.
147. Wallace, W. E., Mass Spectra. In *NIST Chemistry WebBook, NIST Standard Reference Database Number 69, Eds. P.J. Linstrom and W.G. Mallard*, National Institute of Standards and Technology, Gaithersburg MD, 20899.
148. Moldoveanu, S. C., Poly(siloxanes) and Other Silicon Containing Polymers. In *Analytical Pyrolysis of Synthetic Organic Polymers*, Elsevier: Amsterdam, 2005; Vol. 25, pp 657-666.
149. Sharma, S.; Shyam Kumar, C. N.; Korvink, J. G.; Kübel, C., Evolution of Glassy Carbon Microstructure: In Situ Transmission Electron Microscopy of the Pyrolysis Process. *Scientific Reports* **2018**, *8*, 16282.
150. Marchon, B.; Carrazza, J.; Heinemann, H.; Somorjai, G. A., TPD and XPS studies of O2, CO2, and H2O adsorption on clean polycrystalline graphite. *Carbon* **1988**, *26*, 507-514.
151. Laine, N. R.; Vastola, F. J.; Walker, P. L., THE IMPORTANCE OF ACTIVE SURFACE AREA IN THE CARBON-OXYGEN REACTION1,2. *The Journal of Physical Chemistry* **1963**, *67*, 2030-2034.
152. Chen, N.; Yang, R. T., Ab Initio Molecular Orbital Study of the Unified Mechanism and Pathways for Gas−Carbon Reactions. *The Journal of Physical Chemistry A* **1998**, *102*, 6348-6356.
153. E. Schrader, M., Chemisorption of oxygen to gold: AES study of catalytic effect of calcium. *Surface Science* **1978**, *78*, L227-L232.
154. He, Y.; Suliga, A.; Brinkmeyer, A.; Schenk, M.; Hamerton, I., Atomic oxygen degradation mechanisms of epoxy composites for space applications. *Polymer Degradation and Stability* **2019**, *166*, 108-120.
155. Boocock, G.; Cvetanović, R. J., REACTION OF OXYGEN ATOMS WITH BENZENE. *Canadian Journal of Chemistry* **1961**, *39*, 2436-2443.
156. Hong, C.; Han, J.; Zhang, X.; David, H.; Li, W.; Chen, Y.; Du, S., Novel phenolic impregnated 3-D Fine-woven pierced carbon fabric composites: Microstructure and ablation behavior. *Composites Part B: Engineering* **2012**, *43*, 2389-2394.
157. Lachaud, J.; Cozmuta, I.; Mansour, N. N., Multiscale Approach to Ablation Modeling of Phenolic Impregnated Carbon Ablators. *Journal of Spacecraft and Rockets* **2010**, *47*, 910-921.
158. Raether, F.; Meinhardt, J.; Kienzle, A., Oxidation behaviour of carbon short fibre reinforced C/SiC composites. *Journal of the European Ceramic Society* **2007**, *27*, 1217-1221.

CHAPTER FIVE

CONCLUSION AND FUTURE WORK

The primary purpose behind the experiments outlined in this dissertation was to use an atomic oxygen beam-surface scattering apparatus to study the molecular-level interactions of atomic oxygen with silicon-carbon system. Using this beam, 1) the fundamental beam-surface scattering dynamics from oxide-covered silicon carbide and the mechanisms in the transition from passive-to-active oxidation were studied, 2) the resilience of the oxide layers formed from atomic oxygen bombardment of films of silicone coatings was quantified, and 3) the knowledge and insights from these first two studies were utilized to examine how the atomic oxygen beam-surface scattering dynamics from the TPS material PICA changed with and without an oxidized silicone coating, as well as to examine how the passive-to-active oxidation transition further affected these dynamics.

To start out, a hyperthermal pulsed atomic oxygen beam was directed at an oxide-covered silicon carbide wafer as temperature was increased. After the sample passed through the passive-to-active oxidation transition temperature, no active oxidation took place, with the surface discovered afterwards to consist almost entirely of graphitic carbon. Further trials involving a higher fluence O-atom beam were able to initiate active oxidation (**Fig. 5-1**). Thermal decomposition studies on the oxidized silicon carbide showed rapid production of primarily SiO and volatile Si desorbing from the sample, suggesting most of the breakdown occurring at the oxide-SiC interface instead of at the surface between the oxide and the surrounding vacuum. In addition, though a temperature jump observed in

previous plasma oxidation studies on SiC/carbon fiber composites was not observed in this experiment, we hypothesized that the jump originated from erosion of the SiC layer and exposure to the carbon fiber substrate in the previous experiments. Atomic oxygen exposure of the silicones revealed that much of the silicone surface transformed into silicon dioxide, but the films still gradually lost mass under continued exposure to atomic oxygen, which indicated that the O-atoms might still be able to penetrate through the oxide layer. With this information, it was hypothesized that coating TPS materials with silicones followed by pretreatment with atomic oxygen will create an oxidized silicon layer on the TPSs that will allow the TPSs to resist atomic oxygen erosion. In addition, it was predicted that below the passive-to-active oxidation transition temperature and compared to uncoated TPSs, nonreactive scattering would increase, while reactive scattering will be minimal, which was corroborated by the results. In addition, after the coated materials passed through the passive-to-active oxidation transition temperature, thus losing their silicon-oxide coatings, it was expected that the scattering dynamics would follow that of the uncoated TPS materials. This was mostly corroborated as well by the results. With this knowledge gained, it is expected that more accurate material response oxidation models can be developed to better predict how silicon carbide-based and silicone-coated TPS materials will experience hypersonic and atmospheric entry conditions, with NASA Ames currently in the process of developing a model based on this data.

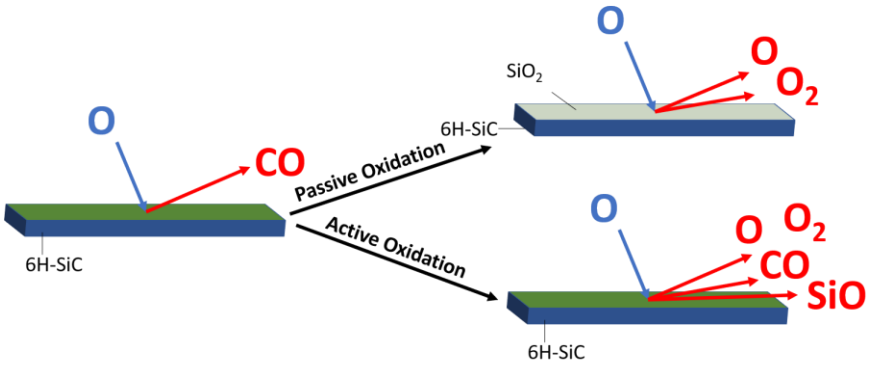

Fig. 5-1. Diagram of passive and active oxidation on silicon carbide. Formation of passivating oxide layer from atomic oxygen bombardment prevents further reactive oxidation with substrate. Under active oxidation regime, reactive oxidation proceeds with formation of SiO and CO.

5.1. Future Work

5.1.1. Silicon Carbide

Despite the progress in elucidating dynamics information from the scattering of atomic oxygen from silicon carbide, more work needs to be done to further answer questions related to this research. In particular, there are still questions related to active oxidation of silicon carbide. While atomic oxygen beam-surface scattering data was collected using a lower-flux pulsed atomic oxygen molecular beam, this particular beam was unable to initiate active oxidation, as above the passive-to-active oxidation transition temperature, the oxide layer decomposed while much of the surface silicon evaporated, leaving behind only a carbon graphitic layer. Active oxidation was achieved however, with use of a higher-flux continuous atomic oxygen molecular beam. Future use of the continuous O-atom beam can be applied towards further studying the O-atom beam-surface scattering dynamics from SiC within the active oxidation regime. Additional experiments

can also be conducted using UHTC composites instead of the model material silicon carbide.

5.1.2. Silicone Coatings

While steady-state atomic oxygen exposure studies were performed on the silicones CV-1144-0 and RTV-560 at 25°C and 300°C, so far only the atomic oxygen erosion yield of CV-1144-0 at 25°C could be successfully measured. Thus, future work on silicone coatings would involve measuring the erosion rate of RTV-560 at 25°C, as well as the erosion rates of both silicone coatings at more elevated temperatures. These types of experiments would be very useful for low-earth orbit applications. However, when silicones are applied to TPS materials, it is unrealistic to expect the material's temperature to remain constant. Therefore, a far more complicated experiment will involve measuring the mass loss rate with a QCM crystal as the silicone is heated and concurrently exposed to atomic oxygen. This, however, will be difficult, requiring significant programming to ensure that the change in temperature does not adversely affect the measurements of the QCM crystal. Studies of other silicones, such as DC 93-500, will also be important to see how the atomic oxygen used in this study compares to that of other facilities.

5.1.3. Silicone-Coated FiberForm and PICA

An extensive atomic oxygen beam-surface scattering study was completed for FiberForm, coated FiberForm, PICA, and coated PICA, with significant but expected differences observed in the beam-surface scattering dynamics between the coated and uncoated materials. Several questions remain, however. First, it was discovered that the

presence of calcium impurities within the FiberForm base material had small but noticeable effects on the reactive formation of CO. Especially around 1300 and 1400 K, O_2 was discovered to be the cause of CO formation at long flight times in the CO TOF distributions. In addition, calcium impurities could not be detected from the uncoated PICA, either virgin or annealed, nor from coated FiberForm, yet the presence of CO formation at long flight times could also be observed from these materials. While the focus of the study was not on how different metal impurities could affect oxidation, it would be useful to further study the influence of O_2 on these impurity-containing materials. Second, further oxidation studies will need to be conducted for uncoated PICA, and carbon-carbon composites in general. Unlike FiberForm, which can be compared to studies of the model material vitreous carbon, no atomic oxygen beam-surface scattering study has so far been conducted on either PICA or carbon-carbon composites until this research. Thus, it is difficult to interpret both the beam-surface scattering data as well as the temperature-dependent flux, as there is a lack of literature with which to compare the data. As it was discovered in this research, charred and annealed PICA still exhibit noticeable differences in the beam-surface scattering dynamics compared to that of annealed FiberForm. The temperature-dependent flux of PICA as temperature decreased from 1800 K to 1000 K also showed differences with that of FiberForm that could not easily be explained. Elucidating these differences was further limited by the lack of higher temperature 1600 K angular distributions from both PICA and coated PICA. Overall, the study of PICA, and carbon-carbon composites in general, is still in a primary stage. Thus, further atomic oxygen studies will be important both for furthering the understanding of the atomic oxygen

oxidation of more complex carbon-carbon composites, but also for giving modelers better insights into designing their simulations.

REFERENCES CITED

REFERENCES CITED

1. Biamino, S.; Liedtke, V.; Badini, C.; Euchberger, G.; Huertas Olivares, I.; Pavese, M.; Fino, P., Multilayer SiC for thermal protection system of space vehicles: Manufacturing and testing under simulated re-entry conditions. *Journal of the European Ceramic Society* **2008**, *28*, 2791-2800.
2. Natali, M.; Kenny, J. M.; Torre, L., Science and technology of polymeric ablative materials for thermal protection systems and propulsion devices: A review. *Progress in Materials Science* **2016**, *84*, 192-275.
3. Opeka, M. M.; Talmy, I. G.; Zaykoski, J. A., Oxidation-based materials selection for 2000°C + hypersonic aerosurfaces: Theoretical considerations and historical experience. *Journal of Materials Science* **2004**, *39*, 5887-5904.
4. Steyer, T. E., Shaping the Future of Ceramics for Aerospace Applications. *International Journal of Applied Ceramic Technology* **2013**, *10*, 389-394.
5. Monti, R.; Pezzella, G.; Savino, R.; Paterna, D.; Esposito, A. In *Aerothermodynamic study of an advanced thermal protection system*, Hot Structures and Thermal Protection Systems for Space Vehicles, 2003; p 275.
6. Monti, R.; Fumo, M. D. S.; Savino, R., Thermal Shielding of a Reentry Vehicle by Ultra-High-Tempreature Ceramic Materials. *Journal of Thermophysics and Heat Transfer* **2006**, *20*, 500-506.
7. Hald, H., Operational limits for reusable space transportation systems due to physical boundaries of C/SiC materials. *Aerospace Science and Technology* **2003**, *7*, 551-559.
8. Monti, R.; Pezzella, G., Low Risk Re-entry Vehicles. In *12th AIAA International Space Planes and Hypersonic Systems and Technologies*, 2003.
9. Poovathingal, S.; Schwartzentruber, T. E.; Murray, V. J.; Minton, T. K., Molecular Simulation of Carbon Ablation Using Beam Experiments and Resolved Microstructure. *AIAA Journal* **2016**, *54*, 999-1010.
10. Gulbransen, E. A.; Jansson, S. A., The high-temperature oxidation, reduction, and volatilization reactions of silicon and silicon carbide. *Oxidation of Metals* **1972**, *4*, 181-201.
11. Burns, A., Structural evaluation of candidate space shuttle thermal protection systems. **1972**.
12. Marschall, J.; Pejaković, D. A.; Fahrenholtz, W. G.; Hilmas, G. E.; Panerai, F.; Chazot, O., Temperature Jump Phenomenon During Plasmatron Testing of ZrB2-SiC Ultrahigh-Temperature Ceramics. *Journal of Thermophysics and Heat Transfer* **2012**, *26*, 559-572.
13. Hu, P.; Gui, K.; Yang, Y.; Dong, S.; Zhang, X., Effect of SiC Content on the Ablation and Oxidation Behavior of ZrB2-Based Ultra High Temperature Ceramic Composites. *Materials (Basel)* **2013**, *6*, 1730-1744.
14. Johnson, S.; Gasch, M.; Stackpoole, M.; Lawson, J.; Gusman, M., Recent Developments in Ultra High Temperature Ceramics at NASA Ames. In *16th*

AIAA/DLR/DGLR International Space Planes and Hypersonic Systems and Technologies Conference, American Institute of Aeronautics and Astronautics: 2009.
15. Balat, M.; Flamant, G.; Male, G.; Pichelin, G., Active to passive transition in the oxidation of silicon carbide at high temperature and low pressure in molecular and atomic oxygen. *Journal of Materials Science* **1992**, *27*, 697-703.
16. Song, Y.; Dhar, S.; Feldman, L. C.; Chung, G.; Williams, J. R., Modified Deal Grove model for the thermal oxidation of silicon carbide. *Journal of Applied Physics* **2004**, *95*, 4953-4957.
17. Jacobson, N. S.; Myers, D. L.; Harder, B. J., Active oxidation of silicon carbide. *Materials at High Temperatures* **2012**, *29*, 193-198.
18. Jacobson, N.; Harder, B.; Myers, D., Oxidation Transitions for SiC Part I. Active-to-Passive Transitions. *J. Am. Ceram. Soc.* **2013**, *96*, 838-844.
19. Berton, B.; Bacos, M. P.; Demange, D.; Lahaye, J., High-temperature oxidation of silicon carbide in simulated atmospheric re-entry conditions. *Journal of Materials Science* **1992**, *27*, 3206-3210.
20. Deng, D.; Luo, X.; Chen, S.; Yu, J.; Ai, B., The active-to-passive oxidation transition mechanism and engineering prediction method of C/SiC composites. *Science China Technological Sciences* **2013**, *56*, 1403-1408.
21. Huang, H.; Chen, S.; Wee, A.; Chen, W., *Epitaxial growth of graphene on silicon carbide (SiC)*, 2014, p 3-26.
22. Panerai, F.; Helber, B.; Chazot, O.; Balat-Pichelin, M., Surface temperature jump beyond active oxidation of carbon/silicon carbide composites in extreme aerothermal conditions. *Carbon* **2014**, *71*, 102-119.
23. Chen, S. Y.; Boyd, I. D., Chemical equilibrium analysis of silicon carbide oxidation in oxygen and air. *Journal of the American Ceramic Society* **2019**, *102*, 4272-4284.
24. Finckenor, M.; Visentine, J.; Adam, S.; Zwiener, J.; Loebs, V. In *CONTAMINATION, UV RADIATION, AND ATOMIC OXYGEN EFFECTS ON ISS THERMAL CONTROL MATERIALS*, 41st Aerospace Sciences Meeting and Exhibit, 2003; p 1084.
25. de Groh, K. K.; McCollum, T. A., Low Earth orbit durability of protected silicone for refractive photovoltaic concentrator arrays. *Journal of Spacecraft and Rockets* **1995**, *32*, 103-109.
26. Haffke, J. E.; Woollam, J. A. In *Synergistic Degradation of CV-1144-O Due to Ultraviolet Radiation and Heat*, Dordrecht, Springer Netherlands: Dordrecht, 2003; pp 183-191.
27. Yan, L.; Gao, X.; Bungay, C.; Woollam, J. A., Study of surface chemical changes and erosion rates for CV-1144-0 silicone under electron cyclotron resonance oxygen plasma exposure. *Journal of Vacuum Science & Technology A* **2001**, *19*, 447-454.
28. Scialdone, J. J.; Clatterbuck, C. H.; Ayres-Treusdell, M.; Park, G.; Kolos, D., *Atomic Oxygen and Space Environment Effects on Aerospace Materials Flown with EOIM-III Experiment*, 1996.
29. Samwel, S. W., Low Earth Orbital Atomic Oxygen Erosion Effect on Spacecraft Materials. *Space Research Journal* **2014**, *7*, 1-13.

30. Dworak, D. P.; Banks, B. A.; Karniotis, C. A.; Soucek, M. D., Evaluation of Protective Silicone/Siloxane Coatings in Simulated Low-Earth-Orbit Environment. *Journal of Spacecraft and Rockets* **2006**, *43*, 393-401.
31. Qian, M.; Murray, V. J.; Wei, W.; Marshall, B. C.; Minton, T. K., Resistance of POSS Polyimide Blends to Hyperthermal Atomic Oxygen Attack. *ACS Applied Materials & Interfaces* **2016**, *8*, 33982-33992.
32. Minton, T. K., et al., Atomic Oxygen Effects on POSS Polyimides in Low Earth Orbit. *ACS Applied Materials & Interfaces* **2012**, *4*, 492-502.
33. De Groh, K. K.; Banks, B. A., Atomic Oxygen Erosion Data from the MISSE 2-8 Missions. **2019**.
34. Wong, H.-W.; Peck, J.; Assif, J.; Lachaud, J.; Mansour, N. N. In *Quantitative determination of species production from the pyrolysis of the Phenolic Impregnated Carbon Ablator (PICA)*, 53rd AIAA Aerospace Sciences Meeting, 2015; p 1447.
35. Bessire, B. K.; Lahankar, S. A.; Minton, T. K., Pyrolysis of Phenolic Impregnated Carbon Ablator (PICA). *ACS Applied Materials & Interfaces* **2015**, *7*, 1383-1395.
36. Bessire, B. K.; Minton, T. K., Decomposition of Phenolic Impregnated Carbon Ablator (PICA) as a Function of Temperature and Heating Rate. *ACS Applied Materials & Interfaces* **2017**, *9*, 21422-21437.
37. Panerai, F.; White, J. D.; Cochell, T. J.; Schroeder, O. M.; Mansour, N. N.; Wright, M. J.; Martin, A., Experimental measurements of the permeability of fibrous carbon at high-temperature. *International Journal of Heat and Mass Transfer* **2016**, *101*, 267-273.
38. Beck, R. A. S.; Driver, D. M.; Wright, M. J.; Hwang, H. H.; Edquist, K. T.; Sepka, S. A., Development of the Mars Science Laboratory Heatshield Thermal Protection System. *Journal of Spacecraft and Rockets* **2014**, *51*, 1139-1150.
39. Nelessen, A., et al. In *Mars 2020 Entry, Descent, and Landing System Overview*, 2019 IEEE Aerospace Conference, 2-9 March 2019; 2019; pp 1-20.
40. Roberts, G. J., The Heat is On. In *Building a Better Heat Shield for a Mars Mission*, Berkeley Lab, 2017.
41. Noda, T.; Inagaki, M.; Yamada, S., Glass-like carbons. *Journal of Non-Crystalline Solids* **1969**, *1*, 285-302.
42. Murray, V. J.; Marshall, B. C.; Woodburn, P. J.; Minton, T. K., Inelastic and Reactive Scattering Dynamics of Hyperthermal O and O2 on Hot Vitreous Carbon Surfaces. *The Journal of Physical Chemistry C* **2015**, *119*, 14780-14796.
43. Murray, V. J.; Recio, P.; Caracciolo, A.; Miossec, C.; Balucani, N.; Casavecchia, P.; Minton, T. K., Oxidation and nitridation of vitreous carbon at high temperatures. *Carbon* **2020**, *167*, 388-402.
44. Poovathingal, S.; Schwartzentruber, T. E.; Murray, V. J.; Minton, T. K.; Candler, G. V., Finite-Rate Oxidation Model for Carbon Surfaces from Molecular Beam Experiments. *AIAA Journal* **2017**, *55*, 1644-1658.
45. Swaminathan-Gopalan, K.; Borner, A.; Murray, V. J.; Poovathingal, S.; Minton, T. K.; Mansour, N. N.; Stephani, K. A., Development and validation of a finite-rate model for carbon oxidation by atomic oxygen. *Carbon* **2018**, *137*, 313-332.

46. Prata, K. S.; Minton, T.; Schwartzentruber, T. E., *Air-Carbon Ablation Model for Hypersonic Flight from Molecular Beam Data*, 2020.
47. Poovathingal, S. J.; Qian, M.; Murray, V. J.; Minton, T. K., Reactive and Inelastic Scattering Dynamics of Hyperthermal O and O2 from a Carbon Fiber Network. 2021.
48. Marshall, T. D.; Pawelko, R. J.; Anderl, R. A.; Smolik, G. R.; Merrill, B. J.; Moore, R. L.; Petti, D. A., Oxygen reactivity of a carbon fiber composite. *Fusion Engineering and Design* **2003**, *69*, 663-667.
49. McKee, D. W., Oxidation behavior of matrix-inhibited carbon/carbon composites. *Carbon* **1988**, *26*, 659-664.
50. Bessire, B. K.; Borner, A. P.; Meurisse, J. B.; Monk, J. D., Progress Towards Modeling the Mars Science Laboratory PICA-NuSil Heatshield. **2019**.
51. Lee, Y. T.; McDonald, J. D.; LeBreton, P. R.; Herschbach, D. R., Molecular Beam Reactive Scattering Apparatus with Electron Bombardment Detector. *Review of Scientific Instruments* **1969**, *40*, 1402-1408.
52. Zhang, J.; Garton, D. J.; Minton, T. K., Reactive and inelastic scattering dynamics of hyperthermal oxygen atoms on a saturated hydrocarbon surface. *The Journal of Chemical Physics* **2002**, *117*, 6239-6251.
53. Zhang, J.; Upadhyaya, H. P.; Brunsvold, A. L.; Minton, T. K., Hyperthermal Reactions of O and O2 with a Hydrocarbon Surface: Direct C−C Bond Breakage by O and H-Atom Abstraction by O2. *The Journal of Physical Chemistry B* **2006**, *110*, 12500-12511.
54. Garton, D. J.; Brunsvold, A. L.; Minton, T. K.; Troya, D.; Maiti, B.; Schatz, G. C., Experimental and Theoretical Investigations of the Inelastic and Reactive Scattering Dynamics of O(3P) + D2 *The Journal of Physical Chemistry A* **2006**, *110*, 1327-1341.
55. Garton, D. J.; Minton, T. K.; Maiti, B.; Troya, D.; Schatz, G. C., A crossed molecular beams study of the O(3P)+H2 reaction: Comparison of excitation function with accurate quantum reactive scattering calculations. **2003**, *118*, 1585-1588.
56. Troya, D.; Schatz, G. C.; Garton, D. J.; Brunsvold, A. L.; Minton, T. K., Crossed beams and theoretical studies of the O(3P)+CH4→H+OCH3 reaction excitation function. *The Journal of Chemical Physics* **2004**, *120*, 731-739.
57. Buczala, D. M.; Brunsvold, A. L.; Minton, T. K., Erosion of Kapton H® by Hyperthermal Atomic Oxygen. *Journal of Spacecraft and Rockets* **2006**, *43*, 421-425.
58. Wright, J. S.; Jones, A.; Farmer, B.; Rodman, D. L.; Minton, T. K., POSS-enhanced colorless organic/inorganic nanocomposite (CORIN®) for atomic oxygen resistance in low earth orbit. *CEAS Space Journal* **2021**.
59. Brink, G. O., Electron Bombardment Molecular Beam Detector. *Review of Scientific Instruments* **1966**, *37*, 857-860.
60. Daly, N. R., Scintillation Type Mass Spectrometer Ion Detector. *Review of Scientific Instruments* **1960**, *31*, 264-267.
61. Minton, T. K.; Giapis, K. P.; Moore, T., Inelastic Scattering Dynamics of Hyperthermal Fluorine Atoms on a Fluorinated Silicon Surface. *The Journal of Physical Chemistry A* **1997**, *101*, 6549-6555.

62. Hurst, J. E.; Becker, C. A.; Cowin, J. P.; Janda, K. C.; Wharton, L.; Auerbach, D. J., Observation of Direct Inelastic Scattering in the Presence of Trapping-Desorption Scattering: Xe on Pt(111). *Physical Review Letters* **1979**, *43*, 1175-1177.
63. Michelsen, H. A.; Auerbach, D. J., A critical examination of data on the dissociative adsorption and associative desorption of hydrogen at copper surfaces. *The Journal of Chemical Physics* **1991**, *94*, 7502-7520.
64. Murray, V. J.; Smoll, E. J.; Minton, T. K., Dynamics of Graphite Oxidation at High Temperature. *The Journal of Physical Chemistry C* **2018**, *122*, 6602-6617.
65. Banks, B.; Miller, S.; de Groh, K., *Low Earth Orbital Atomic Oxygen Interactions With Materials*, 2004; Vol. 2.
66. Blum, Y. D.; Marschall, J.; Hui, D.; Young, S., Thick Protective UHTC Coatings for SiC-Based Structures: Process Establishment. *Journal of the American Ceramic Society* **2008**, *91*, 1453-1460.
67. Presser, V.; Nickel, K. G., Silica on Silicon Carbide. *Critical Reviews in Solid State and Materials Sciences* **2008**, *33*, 1-99.
68. Jacobson, N. S.; Myers, D. L. J. O. o. M., Active Oxidation of SiC. **2011**, *75*, 1-25.
69. de Heer, W. A.; Berger, C.; Ruan, M.; Sprinkle, M.; Li, X.; Hu, Y.; Zhang, B.; Hankinson, J.; Conrad, E., Large area and structured epitaxial graphene produced by confinement controlled sublimation of silicon carbide. *Proceedings of the National Academy of Sciences* **2011**, *108*, 16900-16905.
70. Drowart, J.; De Maria, G. In *Thermodynamic study of the binary system carbon-silicon using a mass spectrometer*, Proc. Conf. Silicon Carbide (1959, Boston), 1960; pp 16-23.
71. Guichelaar, P. J., Acheson process. In *Carbide, Nitride and Boride Materials Synthesis and Processing*, Springer: 1997; pp 115-129.
72. Mishra, N.; Boeckl, J.; Motta, N.; Iacopi, F., Graphene growth on silicon carbide: A review. *Phys. Status Solidi A* **2016**, *213*, 2277-2289.
73. Tromp, R. M.; Hannon, J. B., Thermodynamics and Kinetics of Graphene Growth on SiC(0001). *Physical Review Letters* **2009**, *102*, 106104.
74. Ciochoń, P.; Bodek, Ł.; Garb, M.; Zając, Ł.; Kołodziej, J. J., Si beam-assisted graphitization of SiC (0001). *Applied Physics A* **2018**, *124*, 727.
75. Enta, Y.; Nagai, T.; Yoshida, T.; Ujiie, N.; Nakazawa, H., Decomposition kinetics of silicon oxide layers on silicon substrates during annealing in vacuum. *Journal of Applied Physics* **2013**, *114*, 114104.
76. Gallet, J. J.; Silly, M. G.; Kazzi, M. E.; Bournel, F.; Sirotti, F.; Rochet, F., Chemical and kinetic insights into the Thermal Decomposition of an Oxide Layer on Si(111) from Millisecond Photoelectron Spectroscopy. *Scientific Reports* **2017**, *7*, 14257.
77. Liehr, M.; Lewis, J. E.; Rubloff, G. W., Kinetics of high ‐ temperature thermal decomposition of SiO2 on Si(100). *Journal of Vacuum Science & Technology A* **1987**, *5*, 1559-1562.
78. Tromp, R.; Rubloff, G.; Balk, P.; LeGoues, F.; Van Loenen, E., High-Temperature SiO2 Decomposition at the SiO2/Si Interface. *Physical Review Letters* **1985**, *55*, 2332.

79. Zhiqiang, F.; Chunhe, T.; Liang, T.; Jean-Charles, R., Oxidation of SiC and decomposition of SiO2 at low partial pressure of oxygen in He-O2 system. *Nuclear Engineering and Design* **2004**, *234*, 45-49.
80. Herdrich, G.; Fertig, M.; Löhle, S.; Pidan, S.; Auweter-Kurtz, M.; Laux, T., Oxidation Behavior of Siliconcarbide-Based Materials by Using New Probe Techniques. *Journal of Spacecraft and Rockets* **2005**, *42*, 817-824.
81. Luo, L.; Wang, Y.; Liu, L.; Duan, L.; Wang, G.; Lu, Y., Ablation behavior of C/SiC composites in plasma wind tunnel. *Carbon* **2016**, *103*, 73-83.
82. Wang, Y.; Chen, Z.; Yu, S., Ablation behavior and mechanism analysis of C/SiC composites. *Journal of Materials Research and Technology* **2016**, *5*, 170-182.
83. Sakraker, I.; Asma, C. O., Experimental investigation of passive/active oxidation behavior of SiC based ceramic thermal protection materials exposed to high enthalpy plasma. *Journal of the European Ceramic Society* **2013**, *33*, 351-359.
84. Tagawa, M.; Ema, T.; Kinoshita, H.; Ohmae, N.; Umeno, M.; Minton, T. K., Formation of Thin Oxide Films on Room-Temperature Silicon (100) by Exposure to a Neutral Beam of Hyperthermal Atomic and Molecular Oxygen. *Japanese Journal of Applied Physics* **1998**, *37*, L1455-L1457.
85. Harris, J., On vibrationally-assisted dissociation of H2 at metal surfaces. *Surface Science* **1989**, *221*, 335-345.
86. Hornetz, B.; Michel, H. J.; Halbritter, J., Oxidation and 6H‐SiC‐SiO2 interfaces. *Journal of Vacuum Science & Technology A* **1995**, *13*, 767-771.
87. Önneby, C.; Pantano, C. G., Silicon oxycarbide formation on SiC surfaces and at the SiC/SiO2 interface. *Journal of Vacuum Science & Technology A* **1997**, *15*, 1597-1602.
88. Hijikata, Y.; Yaguchi, H.; Yoshikawa, M.; Yoshida, S., Composition analysis of SiO2/SiC interfaces by electron spectroscopic measurements using slope-shaped oxide films. *Applied Surface Science* **2001**, *184*, 161-166.
89. Newsome, D. A.; Sengupta, D.; Foroutan, H.; Russo, M. F.; van Duin, A. C. T., Oxidation of Silicon Carbide by O2 and H2O: A ReaxFF Reactive Molecular Dynamics Study, Part I. *The Journal of Physical Chemistry C* **2012**, *116*, 16111-16121.
90. Zhu, Q.; Huang, L.; Li, W.; Li, S.; Wang, D., Chemical structure study of SiO2/4H-SiC (0001) interface transition region by angle-dependent x-ray photoelectron spectroscopy. *Applied Physics Letters* **2011**, *99*, 082102.
91. Soukiassian, P.; Amy, F., Silicon carbide surface oxidation and SiO2/SiC interface formation investigated by soft X-ray synchrotron radiation. *Journal of Electron Spectroscopy and Related Phenomena* **2005**, *144-147*, 783-788.
92. Brewer, L.; Edwards, R. K., The Stability of SiO Solid and Gas. *The Journal of Physical Chemistry* **1954**, *58*, 351-358.
93. Raider, S. I.; Herd, S. R.; Walkup, R. E., SiO2 film decomposition reaction initiated by carbon impurities located at a Si‐SiO2 interface. *Applied Physics Letters* **1991**, *59*, 2424-2426.
94. Raider, S. I., Carbon impurities at a Si-SiO2 interface. *Microelectronic Engineering* **1993**, *22*, 29-34.

95. Murray, V. J.; Pilinski, M. D.; Smoll, E. J.; Qian, M.; Minton, T. K.; Madzunkov, S. M.; Darrach, M. R., Gas–Surface Scattering Dynamics Applied to Concentration of Gases for Mass Spectrometry in Tenuous Atmospheres. *The Journal of Physical Chemistry C* **2017**, *121*, 7903-7922.
96. Murad, E., Spacecraft Interaction with Atmospheric Species in Low Earth Orbit. *Journal of Spacecraft and Rockets* **1996**, *33*, 131-136.
97. Flowers, O.; Stewart, D. A., *Catalytic surface effects on contaminated space shuttle tiles in a dissociated nitrogen stream*; National Aeronautics and Space Administration, Ames Research Center, 1985.
98. Magasinski, A.; Dixon, P.; Hertzberg, B.; Kvit, A.; Ayala, J.; Yushin, G., High-performance lithium-ion anodes using a hierarchical bottom-up approach. *Nature Materials* **2010**, *9*, 353-358.
99. Zhao, K.; Li, K.; Wang, Y., Rapid densification of C/SiC composite by incorporating SiC nanowires. *Composites Part B: Engineering* **2013**, *45*, 1583-1586.
100. Groh, K. K. d.; McCollum, T. A., Low Earth orbit durability of protected silicone for refractive photovoltaic concentrator arrays. *Journal of Spacecraft and Rockets* **1995**, *32*, 103-109.
101. Banks, B. A.; Rutledge, S. K.; Paulsen, P. E.; Steuber, T. J., Simulation of the low earth orbital atomic oxygen interaction with materials by means of an oxygen ion beam. *NASA Technical Memorandum* **1989**, *101971*.
102. Wang, H.; Minton, K. T.; Murray, J. V.; Dai, D.; Wu, B.; Yang, Y.; Che, L., Study on the Resistance of Thermal Control Coating of Phenyl Silicone Rubber to Hyperthermal Atomic Oxygen Attack. *Journal of Astronautics* **2017**, *38*, 662-668.
103. De Groh, K. K.; Dever, J. A.; Jaworske, D. A.; Miller, S. K.; Sechkar, E. A.; Panko, S. R., NASA Glenn research center's materials international space station experiments (MISSE 1-7). **2008**.
104. Shao, Y.; Brook, M. A., Structured metal films on silicone elastomers. *Journal of Materials Chemistry* **2010**, *20*, 8548-8556.
105. Grassie, N.; Macfarlane, I. G., The thermal degradation of polysiloxanes—I. Poly(dimethylsiloxane). *European Polymer Journal* **1978**, *14*, 875-884.
106. Camino, G.; Lomakin, S. M.; Lazzari, M., Polydimethylsiloxane thermal degradation Part 1. Kinetic aspects. *Polymer* **2001**, *42*, 2395-2402.
107. de Groh, H.; Miller, S.; Smith, I.; Daniels, C.; Steinetz, B. In *Adhesion of Silicone Elastomer Seals for NASA's Crew Exploration Vehicle*, 44th AIAA/ASME/SAE/ASEE Joint Propulsion Conference & Exhibit, 2008; p 4625.
108. Taylor, E. W. In *Overview of new and emerging radiation resistant materials for space environment applications*, 2011 Aerospace Conference, IEEE: 2011; pp 1-11.
109. Langston, S. L.; Lang, C. G.; Samareh, J. A. In *Parametric Study of an Ablative TPS and Hot Structure Heatshield for a Mars Entry Capsule Vehicle*, AIAA SPACE and Astronautics Forum and Exposition, 2017; p 5290.
110. Cooper, P.; Miserentino, R.; Sawyer, J.; Leatherwood, J. In *Assessment of the Shuttle Orbiter Thermal Protection System undensified tiles under mission dynamic loads*, 23rd Structures, Structural Dynamics and Materials Conference, 1982; p 790.

111. Schott, T.; Munk, M.; Herring, G.; Grinstead, J.; Prabhu, D. In *Fiber-based measurement of bow-shock spectra for reentry flight testing*, 48th AIAA Aerospace Sciences Meeting Including the New Horizons Forum and Aerospace Exposition, 2010; p 301.
112. Banks, B.; Rutledge, S.; Sechkar, E.; Stueber, T.; Snyder, A.; de Groh, K.; Haytas, C.; Brinker, D. In *Issues and effects of atomic oxygen interactions with silicone contamination on spacecraft in low earth orbit*, Materials in a Space Environment, Proceedings of the 8 th International Symposium, and Protection of Materials and Structures from the LEO Space Environment, Proceedings of the 5 th International Conference. ICPMSE, 2000.
113. Milos, F. S.; Scott, C. D.; Papa, S. V. D., Arcjet Testing and Thermal Model Development for Multilayer Felt Reusable Surface Insulation. *Journal of Spacecraft and Rockets* **2014**, *51*, 397-411.
114. Liu, C. K.; Glassford, A. P. M., Kinetics data for diffusion of outgassing species from RTV 560 silicone rubber. *Journal of Vacuum Science and Technology* **1978**, *15*, 1761-1768.
115. Rao, N.; Xie, X.; Wielizcka, D.; Zhu, D.-M., Quartz crystal microbalance sample stage for in situ characterization of thickness and surface morphology of spin coated polymer films. *Review of Scientific Instruments* **2006**, *77*, 116111.
116. Cooper, R.; Upadhyaya, H. P.; Minton, T. K.; Berman, M. R.; Du, X.; George, S. M., Protection of polymer from atomic-oxygen erosion using Al2O3 atomic layer deposition coatings. *Thin Solid Films* **2008**, *516*, 4036-4039.
117. Packirisamy, S.; Schwam, D.; Litt, M. H., Atomic oxygen resistant coatings for low earth orbit space structures. *Journal of Materials Science* **1995**, *30*, 308-320.
118. El-Kareh, B.; Hutter, L. N., *Fundamentals of semiconductor processing technology*; Springer Science & Business Media, 2012.
119. NuSil CV-1144-0 DataSheet. NuSil Technology: 2014.
120. Vandeparre, H.; Damman, P., Wrinkling of Stimuloresponsive Surfaces: Mechanical Instability Coupled to Diffusion. *Physical Review Letters* **2008**, *101*, 124301.
121. Yu, S.; Ni, Y.; He, L.; Ye, Q.-L., Tunable Formation of Ordered Wrinkles in Metal Films with Controlled Thickness Gradients Deposited on Soft Elastic Substrates. *ACS Applied Materials & Interfaces* **2015**, *7*, 5160-5167.
122. Bowden, N.; Brittain, S.; Evans, A. G.; Hutchinson, J. W.; Whitesides, G. M., Spontaneous formation of ordered structures in thin films of metals supported on an elastomeric polymer. *Nature* **1998**, *393*, 146-149.
123. Chan, E. P.; Crosby, A. J., Spontaneous formation of stable aligned wrinkling patterns. *Soft Matter* **2006**, *2*, 324-328.
124. Tanaka, T.; Sun, S.-T.; Hirokawa, Y.; Katayama, S.; Kucera, J.; Hirose, Y.; Amiya, T., Mechanical instability of gels at the phase transition. *Nature* **1987**, *325*, 796-798.
125. Sylgard 184 Silicone Elastomer Data Sheet. Dow Corning: 1998.
126. Okada, Y.; Tokumaru, Y., Precise determination of lattice parameter and thermal expansion coefficient of silicon between 300 and 1500 K. *Journal of Applied Physics* **1984**, *56*, 314-320.

127. RTV560 Technical Data Sheet. Momentive Performance Materials: 2012.
128. Townsend, J. A.; Park, G. In *A comparison of atomic oxygen degradation in low earth orbit and in a plasma etcher*, NASA: 1996; pp 295-304.
129. De Groh, K. K.; Banks, B. A.; Asmar, O. C.; Yi, G. T.; Mitchell, G. G.; Guo, A.; Sechkar, E. A., Erosion Results of the MISSE 8 Polymers Experiment After 2 Years of Space Exposure on the International Space Station. **2017**.
130. Fahy, W. P.; Chang, A.; Wu, H.; Koo, J. H., Recent Developments of Ablative Thermal Protection Systems for Atmospheric Entry. In *AIAA Scitech 2021 Forum*, 2021.
131. Edel, R.; Grabnic, T.; Wiggins, B.; Sibener, S. J., Atomically-Resolved Oxidative Erosion and Ablation of Basal Plane HOPG Graphite Using Supersonic Beams of O2 with Scanning Tunneling Microscopy Visualization. *The Journal of Physical Chemistry C* **2018**, *122*, 14706-14713.
132. Ferguson, J. C.; Panerai, F.; Lachaud, J.; Mansour, N. N., Theoretical study on the micro-scale oxidation of resin-infused carbon ablators. *Carbon* **2017**, *121*, 552-562.
133. Hariharan, S.; Majumder, M.; Edel, R.; Grabnic, T.; Sibener, S. J.; Hase, W. L., Exploratory Direct Dynamics Simulations of 3O2 Reaction with Graphene at High Temperatures. *The Journal of Physical Chemistry C* **2018**, *122*, 29368-29379.
134. Panerai, F.; Mansour, N. N.; Lachaud, J.; Martin, A., Numerical and experimental study of carbon fiber oxidation. In *52nd Aerospace Sciences Meeting*, 2014.
135. Tzeng, S.-S.; Chr, Y.-G., Evolution of microstructure and properties of phenolic resin-based carbon/carbon composites during pyrolysis. *Materials Chemistry and Physics* **2002**, *73*, 162-169.
136. Andreoli, S.; Eser, S., Relating reactivity to structure in cokes and carbon materials: Temperature-programmed oxidation and microscopy techniques. *Carbon* **2020**, *168*, 362-371.
137. Levendis, Y. A.; Flagan, R. C.; Gavalas, G. R., Oxidation kinetics of monodisperse spherical carbonaceous particles of variable properties. *Combustion and Flame* **1989**, *76*, 221-241.
138. Halbig, M. C.; McGuffin-Cawley, J. D.; Eckel, A. J.; Brewer, D. N., Oxidation Kinetics and Stress Effects for the Oxidation of Continuous Carbon Fibers within a Microcracked C/SiC Ceramic Matrix Composite. *Journal of the American Ceramic Society* **2008**, *91*, 519-526.
139. Hatta, H.; Aoki, T.; Kogo, Y.; Yarii, T., High-temperature oxidation behavior of SiC-coated carbon fiber-reinforced carbon matrix composites. *Composites Part A: Applied Science and Manufacturing* **1999**, *30*, 515-520.
140. Lamouroux, F.; Bertrand, S.; Pailler, R.; Naslain, R.; Cataldi, M., Oxidation-resistant carbon-fiber-reinforced ceramic-matrix composites. *Composites Science and Technology* **1999**, *59*, 1073-1085.
141. Lamouroux, F.; Camus, G.; Thébault, J., Kinetics and Mechanisms of Oxidation of 2D Woven C/SiC Composites: I, Experimental Approach. *Journal of the American Ceramic Society* **1994**, *77*, 2049-2057.
142. Liu, W.; Wei, Y.; Deng, J., Carbon-fiber-reinforced C-SiC binary matrix composites. *Carbon* **1995**, *33*, 441-447.

143. Murthy, T. S. R. C.; Reeman, L.; Zou, J.; Venkatachalam, V.; Baker, B.; Wang, M.; Binner, J., Role of rare earth oxide particles on the oxidation behaviour of silicon carbide coated 2.5D carbon fibre preforms. *Open Ceramics* **2020**, *2*, 100018.
144. Lachaud, J.; Mansour, N.; Ceballos, A.; Pejakovic, D.; Zhang, L.; Marschall, J., Validation of a volume-averaged fiber-scale model for the oxidation of a carbon-fiber preform. In *42nd AIAA Thermophysics Conference*, 2011.
145. Panerai, F.; Martin, A.; Mansour, N. N.; Sepka, S.; Lachaud, J., Flow-tube Oxidation Experiments on the Carbon Preform of PICA. In *44th AIAA Thermophysics Conference*, 2013.
146. Montemore, M. M.; van Spronsen, M. A.; Madix, R. J.; Friend, C. M., O2 Activation by Metal Surfaces: Implications for Bonding and Reactivity on Heterogeneous Catalysts. *Chemical Reviews* **2018**, *118*, 2816-2862.
147. Wallace, W. E., Mass Spectra. In *NIST Chemistry WebBook, NIST Standard Reference Database Number 69, Eds. P.J. Linstrom and W.G. Mallard*, National Institute of Standards and Technology, Gaithersburg MD, 20899.
148. Moldoveanu, S. C., Poly(siloxanes) and Other Silicon Containing Polymers. In *Analytical Pyrolysis of Synthetic Organic Polymers*, Elsevier: Amsterdam, 2005; Vol. 25, pp 657-666.
149. Sharma, S.; Shyam Kumar, C. N.; Korvink, J. G.; Kübel, C., Evolution of Glassy Carbon Microstructure: In Situ Transmission Electron Microscopy of the Pyrolysis Process. *Scientific Reports* **2018**, *8*, 16282.
150. Marchon, B.; Carrazza, J.; Heinemann, H.; Somorjai, G. A., TPD and XPS studies of O2, CO2, and H2O adsorption on clean polycrystalline graphite. *Carbon* **1988**, *26*, 507-514.
151. Laine, N. R.; Vastola, F. J.; Walker, P. L., THE IMPORTANCE OF ACTIVE SURFACE AREA IN THE CARBON-OXYGEN REACTION1,2. *The Journal of Physical Chemistry* **1963**, *67*, 2030-2034.
152. Chen, N.; Yang, R. T., Ab Initio Molecular Orbital Study of the Unified Mechanism and Pathways for Gas−Carbon Reactions. *The Journal of Physical Chemistry A* **1998**, *102*, 6348-6356.
153. E. Schrader, M., Chemisorption of oxygen to gold: AES study of catalytic effect of calcium. *Surface Science* **1978**, *78*, L227-L232.
154. He, Y.; Suliga, A.; Brinkmeyer, A.; Schenk, M.; Hamerton, I., Atomic oxygen degradation mechanisms of epoxy composites for space applications. *Polymer Degradation and Stability* **2019**, *166*, 108-120.
155. Boocock, G.; Cvetanović, R. J., REACTION OF OXYGEN ATOMS WITH BENZENE. *Canadian Journal of Chemistry* **1961**, *39*, 2436-2443.
156. Hong, C.; Han, J.; Zhang, X.; David, H.; Li, W.; Chen, Y.; Du, S., Novel phenolic impregnated 3-D Fine-woven pierced carbon fabric composites: Microstructure and ablation behavior. *Composites Part B: Engineering* **2012**, *43*, 2389-2394.
157. Lachaud, J.; Cozmuta, I.; Mansour, N. N., Multiscale Approach to Ablation Modeling of Phenolic Impregnated Carbon Ablators. *Journal of Spacecraft and Rockets* **2010**, *47*, 910-921.

158. Raether, F.; Meinhardt, J.; Kienzle, A., Oxidation behaviour of carbon short fibre reinforced C/SiC composites. *Journal of the European Ceramic Society* **2007**, *27*, 1217-1221.

APPENDIX A

SUPPORTING INFORMATION FOR CHAPTER FOUR

A.1. Additional Figures

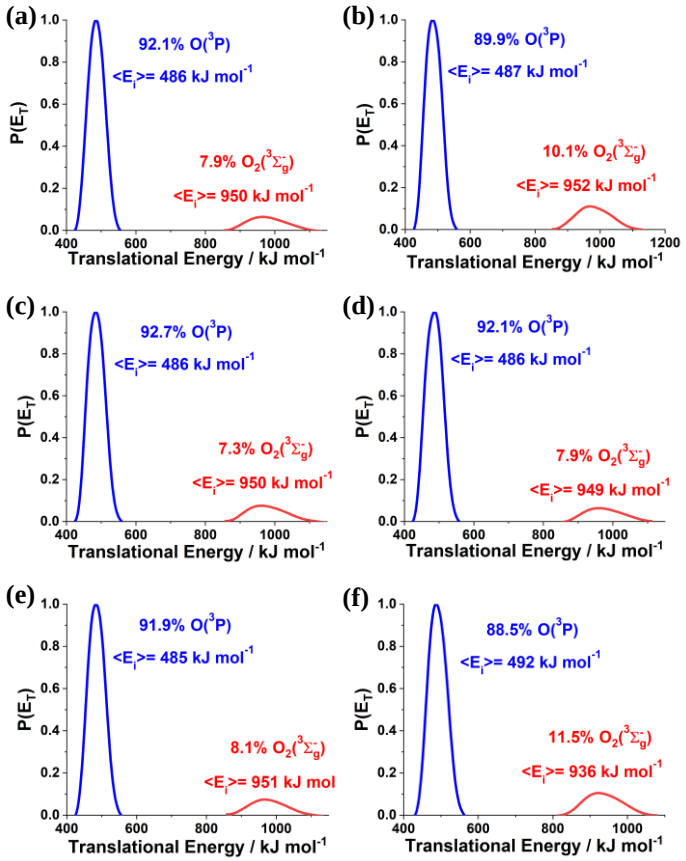

Fig. A-1. Translational energy distributions of the O/O_2 hyperthermal beams used for the different scattering experiments. For **(a)** uncoated FiberForm, **(b)** coated FiberForm_A, **(c)** coated FiberForm_B, **(d)** uncoated PICA, **(e)** coated PICA, **(f)** uncoated FiberForm for O_2 reactivity experiment.

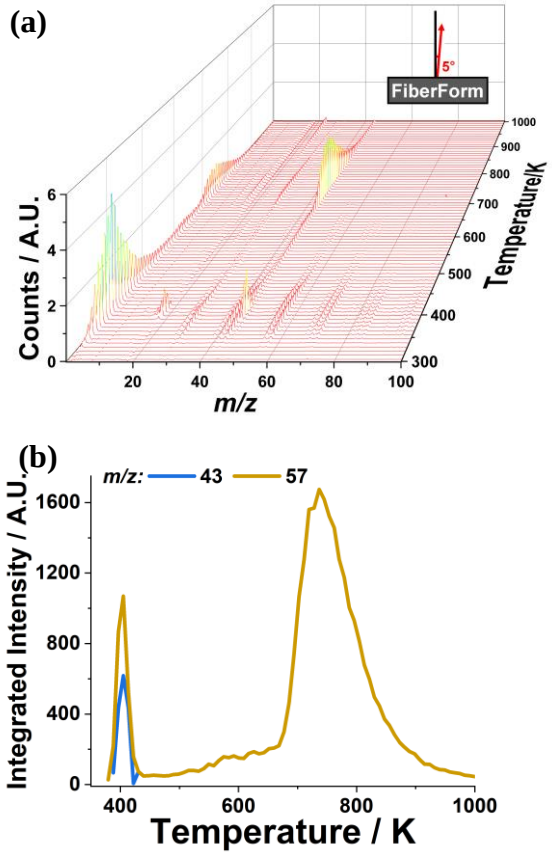

Fig. A-2. Mass spectral results from products released from pristine FiberForm as it was heated from room temperature to 1000 K, with a detector viewing angle of $\theta_f = 5°$ with respect to the normal of the macroscopic surface. **(a)** Mass spectra as a function of sample temperature. **(b)** Integrated intensities of peaks corresponding to specific *m/z* ratios as a function of sample temperature.

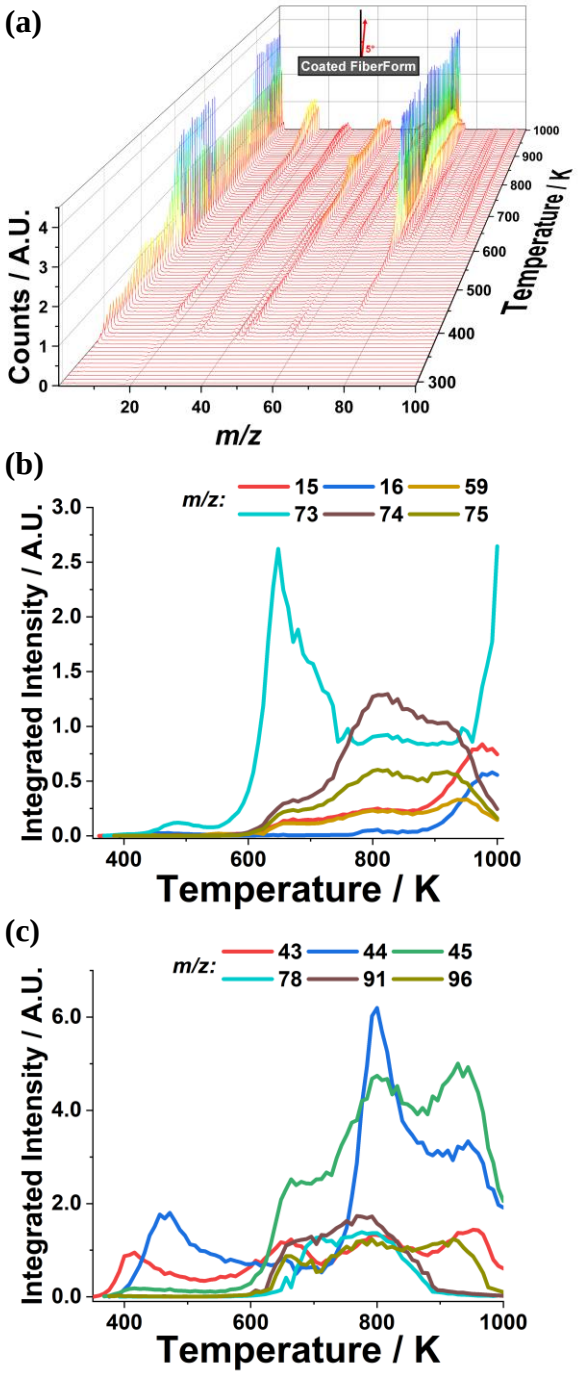

Fig. A-3. Mass spectral results from products released from coated FiberForm_A as it was heated from room temperature to 1000 K, with a detector viewing angle of $\theta_f = 5°$ with respect to the normal of the macroscopic surface. **(a)** Mass spectra as a function of sample temperature. **(b)** Selection of largest integrated intensities of peaks corresponding to specific *m/z* ratios as a function of sample temperature. **(c)** Selection of smaller integrated intensities of peaks corresponding to specific *m/z* ratios as a function of sample temperature.

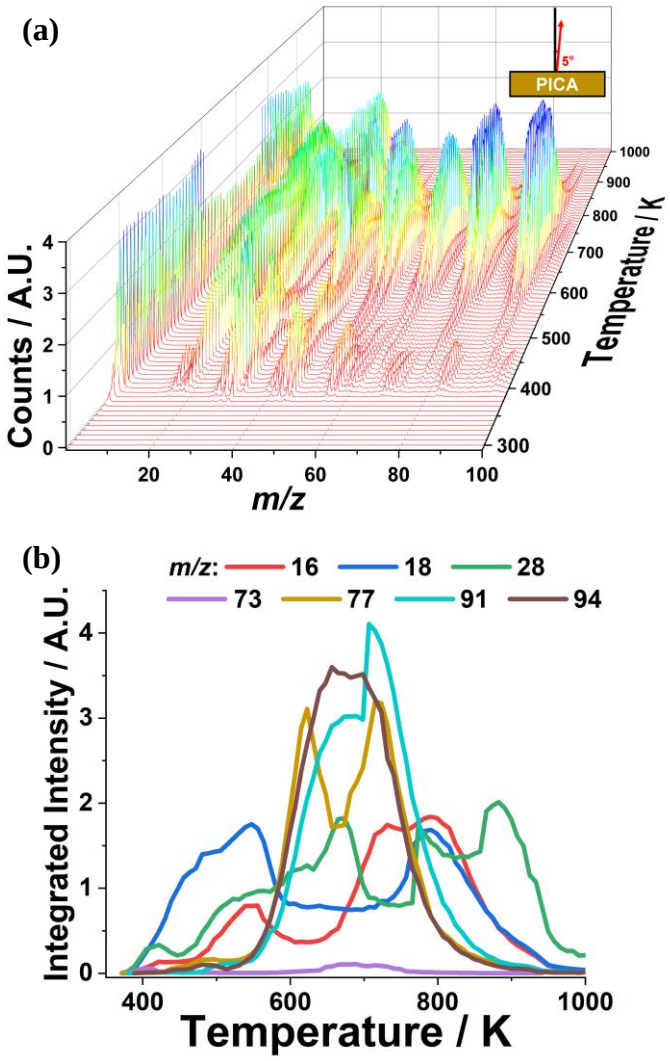

Fig. A-4. Mass spectral results from products released from uncoated PICA as it was heated from room temperature to 1000 K, with a detector viewing angle of $\theta_f = 5°$ with respect to the normal of the macroscopic surface. **(a)** Mass spectra as a function of sample temperature. **(b)** Selection of largest integrated intensities of peaks corresponding to specific *m/z* ratios as a function of sample temperature.

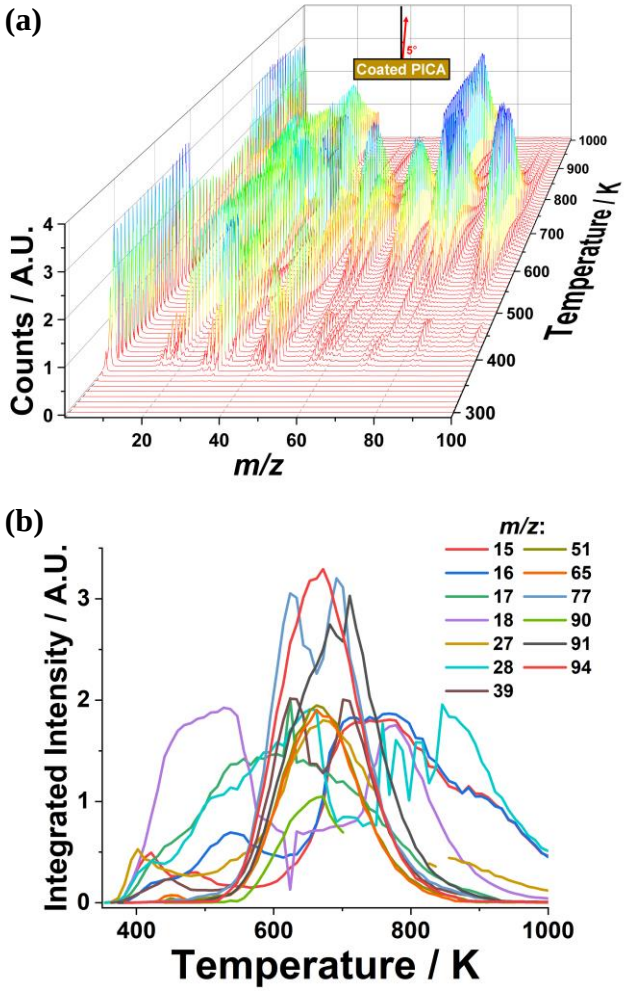

Fig. A-5. Mass spectral results from products released from coated PICA as it was heated from room temperature to 1000 K, with a detector viewing angle of $\theta_f = 5°$ with respect to the normal of the macroscopic surface. **(a)** Mass spectra as a function of sample temperature. **(b)** Selection of largest integrated intensities of peaks corresponding to specific *m/z* ratios as a function of sample temperature.

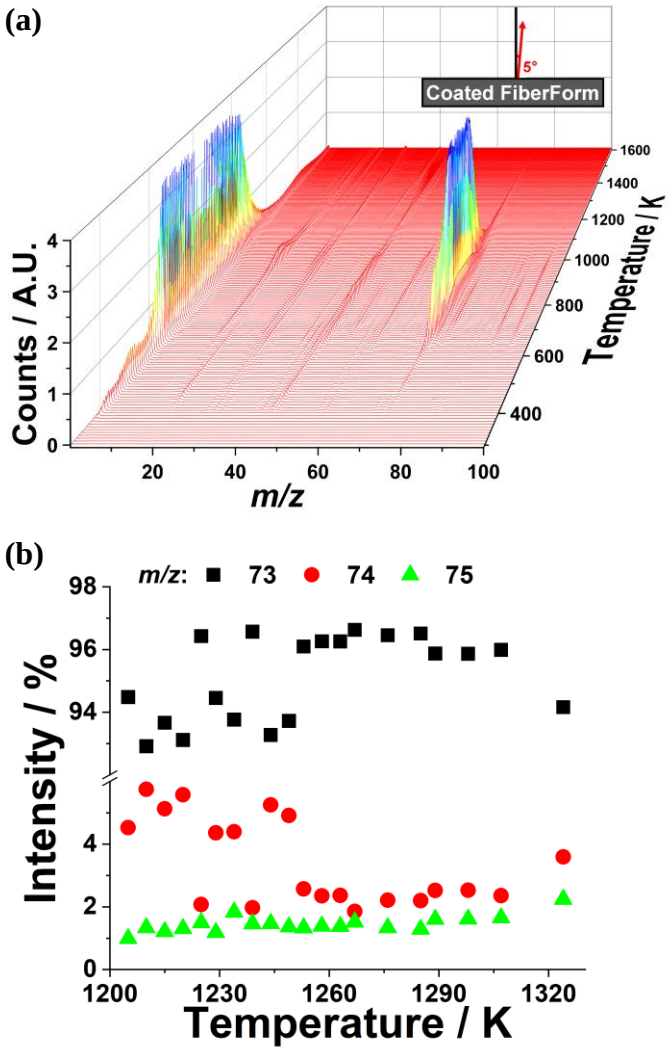

Fig. A-6. Mass spectral results from products released from coated FiberForm_B as it was heated from room temperature to 1600 K, with a detector viewing angle of $\theta_f = 5°$ with respect to the normal of the macroscopic surface. **(a)** Mass spectra as a function of sample temperature. **(b)** Intensities of signals detected at *m/z* = 73, 74, and 75 represented as percentages of the total signal at these three *m/z* ratios, as a function of sample temperature.

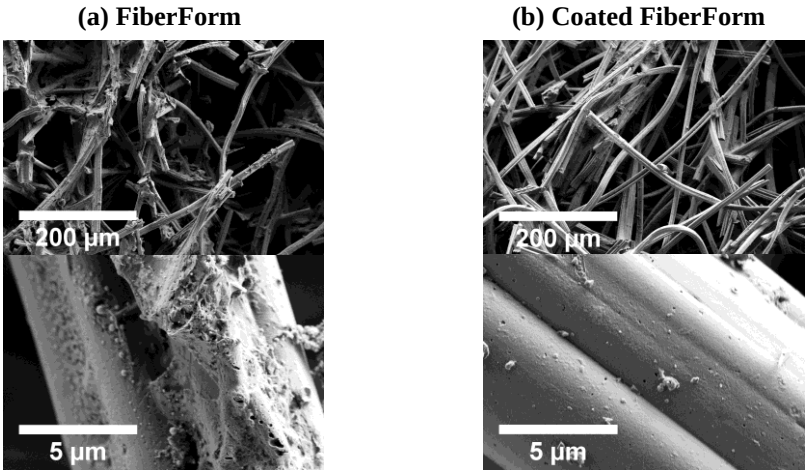

Fig. A-7. Additional SEM of **(a)** uncoated and **(b)** coated FiberForm annealed to 1800 K for 30 minutes without the O-atom beam.

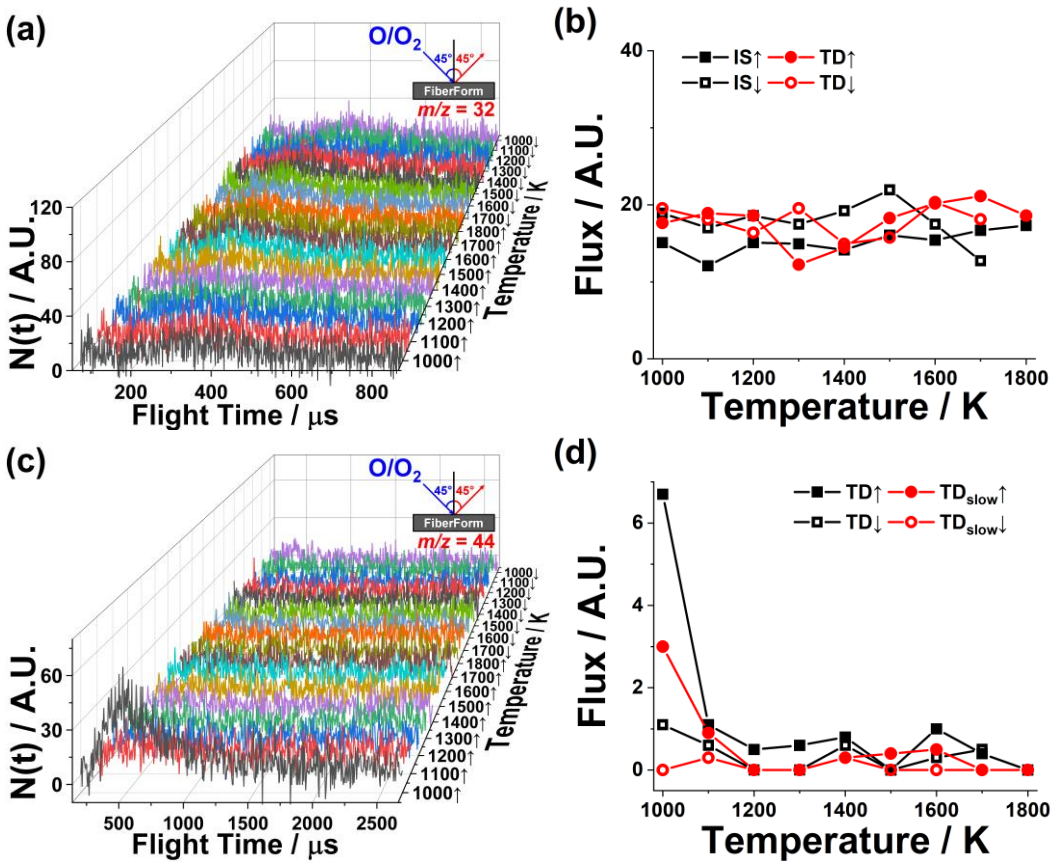

Fig. A-8. TOF product distributions and fluxes of O_2 and CO_2 from uncoated FiberForm. TOF distributions as a function of temperature increasing up to 1800 K, then decreasing to 1000 K, for **(a)** O_2 and **(c)** CO_2. Fluxes separated into their IS (O_2 only), TD, and TD_{slow} (CO_2 only) components shown in **(b)** and **(d)** for O_2 and CO_2, respectively. Arrows indicate signal at temperature point collected when temperature was either increasing or decreasing.

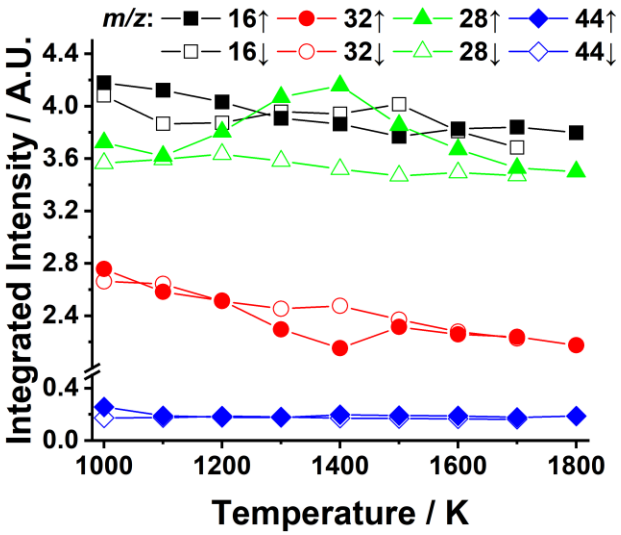

Fig. A-9. Integrated intensities of background TOF distributions for *m/z* = 16, 32, 28, and 44 products from uncoated FiberForm as a function of surface temperature from 1000 K to 1800 K. Arrows indicate signal at temperature point collected when temperature was either increasing or decreasing.

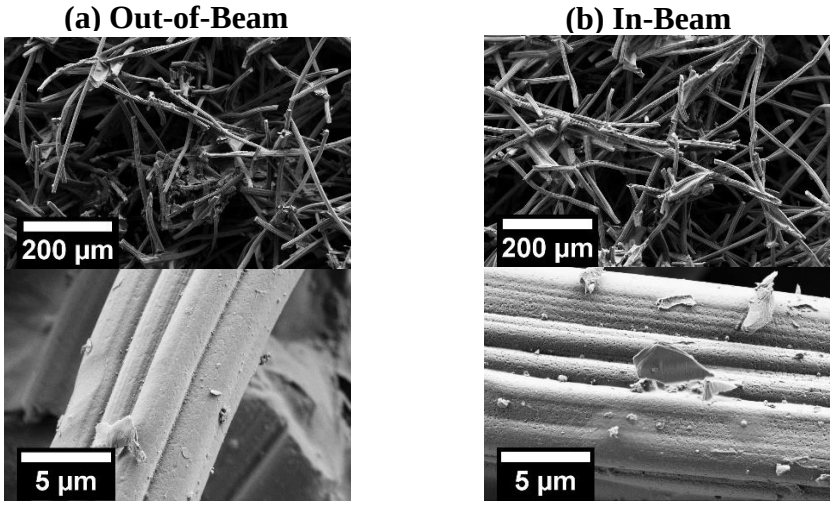

Fig. A-10. SEM of uncoated FiberForm in areas **(a)** out-of-beam, and **(b)** in-beam after experiments with hyperthermal O/O_2 beam.

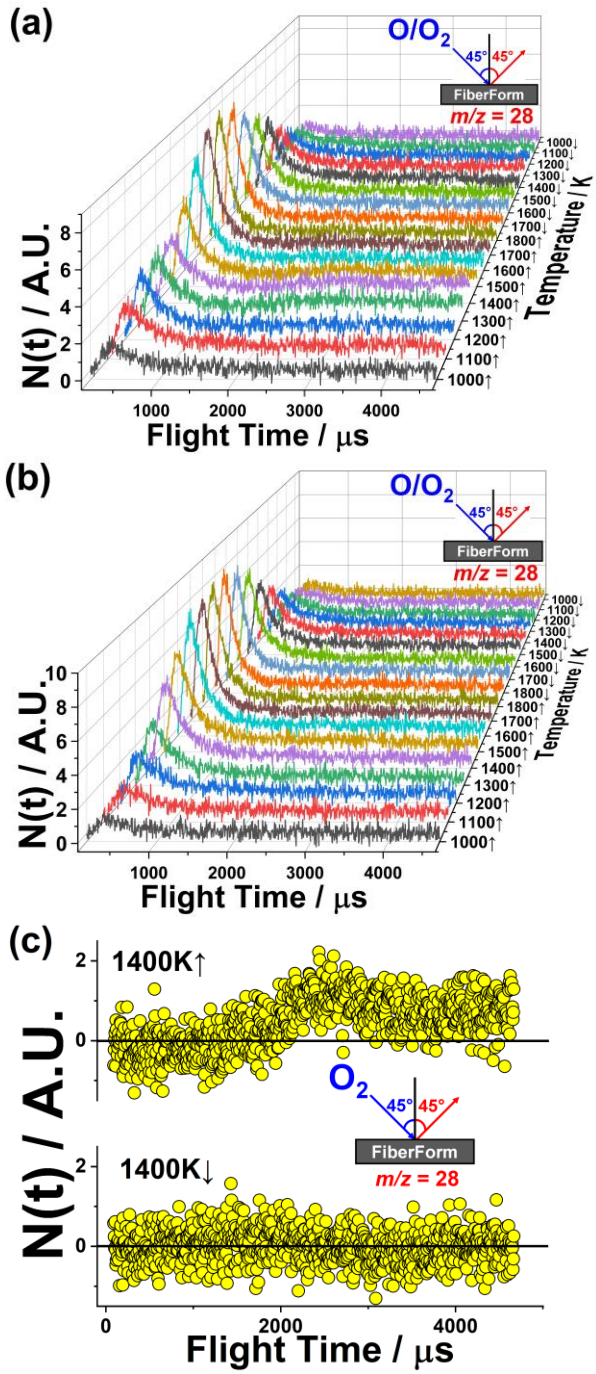

Fig. A-11. Additional results from O_2 reactivity experiment. TOF product distributions for CO product from uncoated FiberForm, scattered with O-atoms, as a function of temperature **(a)** before annealing once from 1000 K to 1800 K, and **(b)** after annealing. TOF distributions plotted out to 5,000 μs to reveal slow signal. **(c)** Individual TOF distributions for CO products from pristine FiberForm, scattered with O_2, at 1400 K↑ and 1400 K↓. Arrows indicate signal at temperature point collected when temperature was either increasing or decreasing.

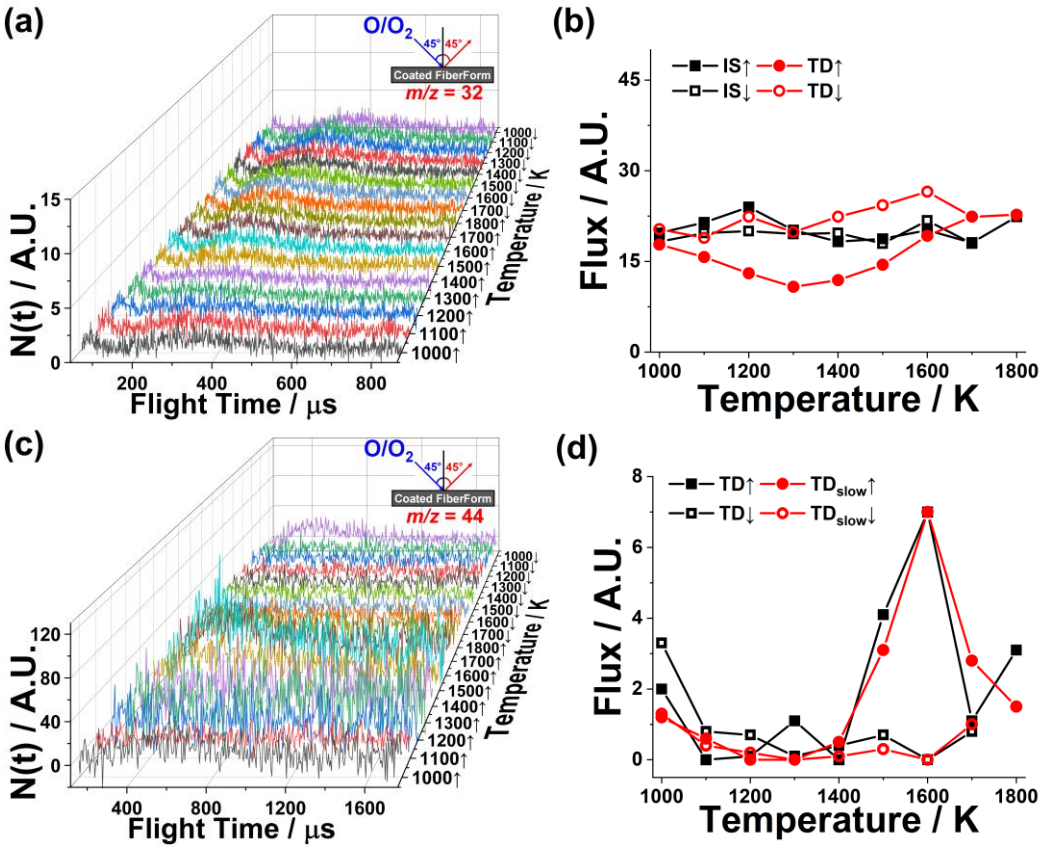

Fig. A-12. TOF product distributions and fluxes of O_2 and *m/z* = 44 from coated FiberForm_A. TOF distributions as a function of temperature increasing up to 1800 K, then decreasing to 1000 K, for **(a)** O_2 and **(c)** *m/z* = 44, corresponding either to CO_2 or SiO. Fluxes separated into their IS (O_2 only), TD, and TD_{slow} (*m/z* = 44 only) components shown in **(b)** and **(d)** for O_2 and *m/z* = 44, respectively. Arrows indicate signal at temperature point collected when temperature was either increasing or decreasing. For *m/z* = 44, fluxes at lower temperatures reflect CO_2 product, while fluxes at higher temperature likely reflect SiO.

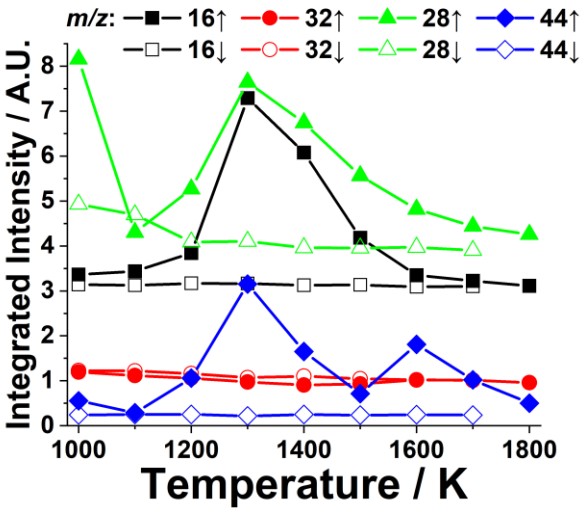

Fig. A-13. Integrated intensities of background TOF distributions for *m/z* = 16, 32, 28, and 44 products from coated FiberForm_A as a function of surface temperature from 1000 K to 1800 K. Arrows indicate signal at temperature point collected when temperature was either increasing or decreasing.

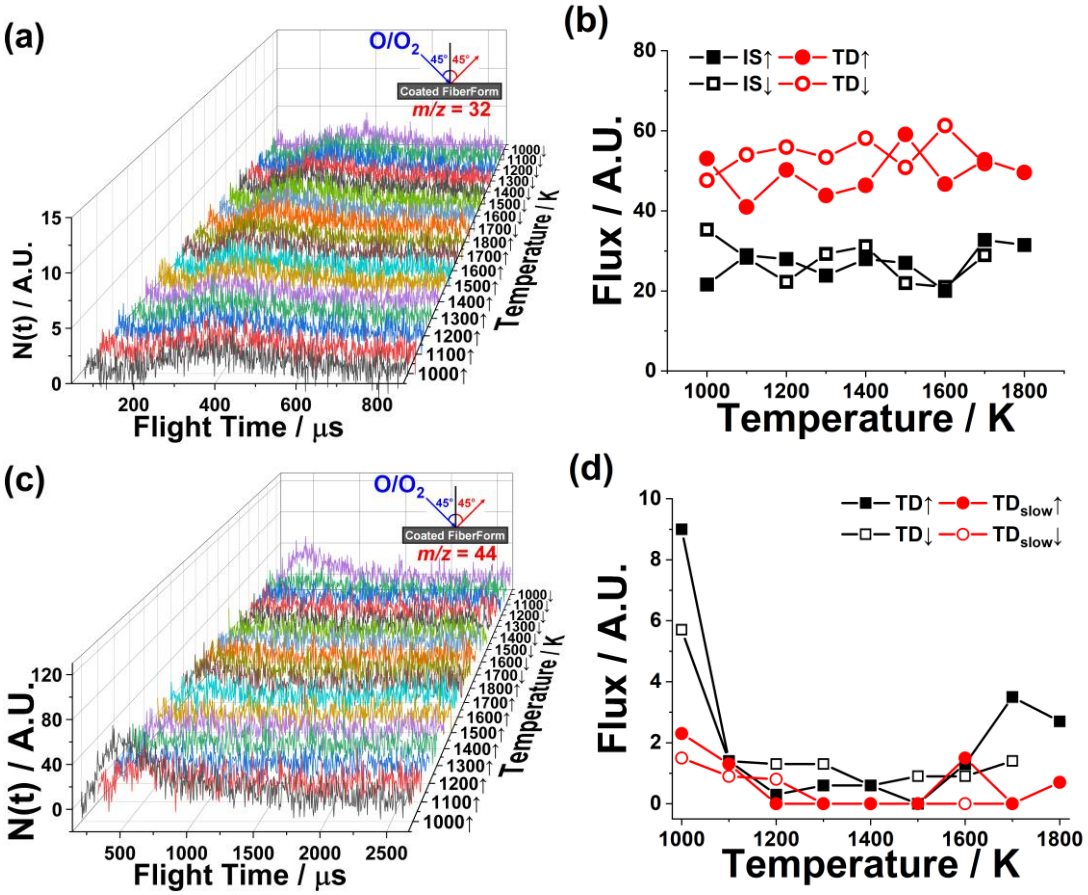

Fig. A-14. TOF product distributions and fluxes of O_2 and *m/z* = 44 from coated FiberForm_B. TOF distributions as a function of temperature increasing up to 1800 K, then decreasing to 1000 K, for **(a)** O_2 and **(c)** *m/z* = 44, corresponding either to CO_2 or SiO. Fluxes separated into their IS (O_2 only), TD, and TD_{slow} (*m/z* = 44 only) components shown in **(b)** and **(d)** for O_2 and *m/z* = 44, respectively. Arrows indicate signal at temperature point collected when temperature was either increasing or decreasing. For *m/z* = 44, fluxes at lower temperatures reflect CO_2 product, while fluxes at higher temperature likely reflect SiO.

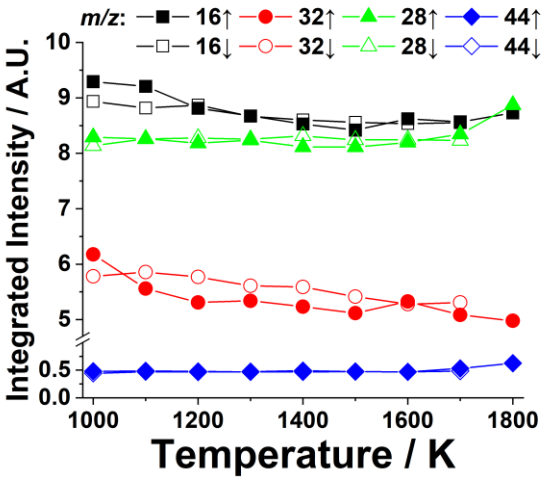

Fig. A-15. Integrated intensities of background TOF distributions for *m/z* = 16, 32, 28, and 44 products from coated FiberForm_B as a function of surface temperature from 1000 K to 1800 K. Arrows indicate signal at temperature point collected when temperature was either increasing or decreasing.

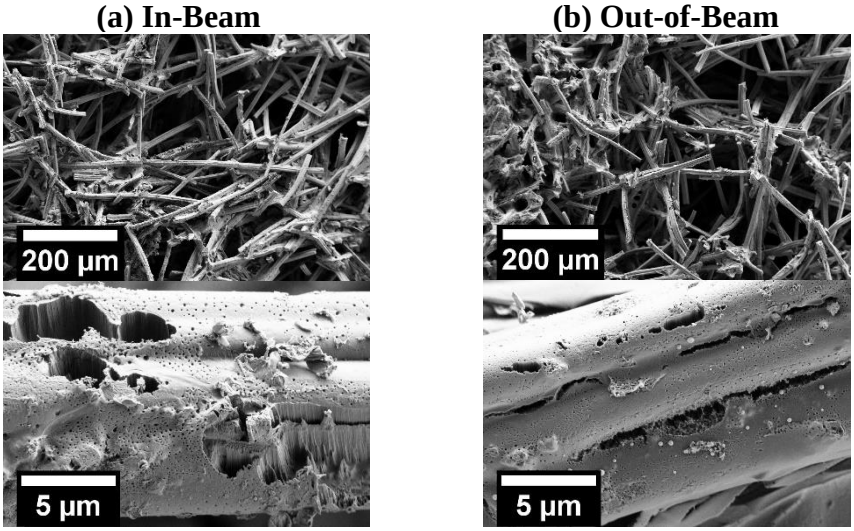

Fig. A-16. SEM of coated FiberForm after experiments with hyperthermal O/O_2 beam.

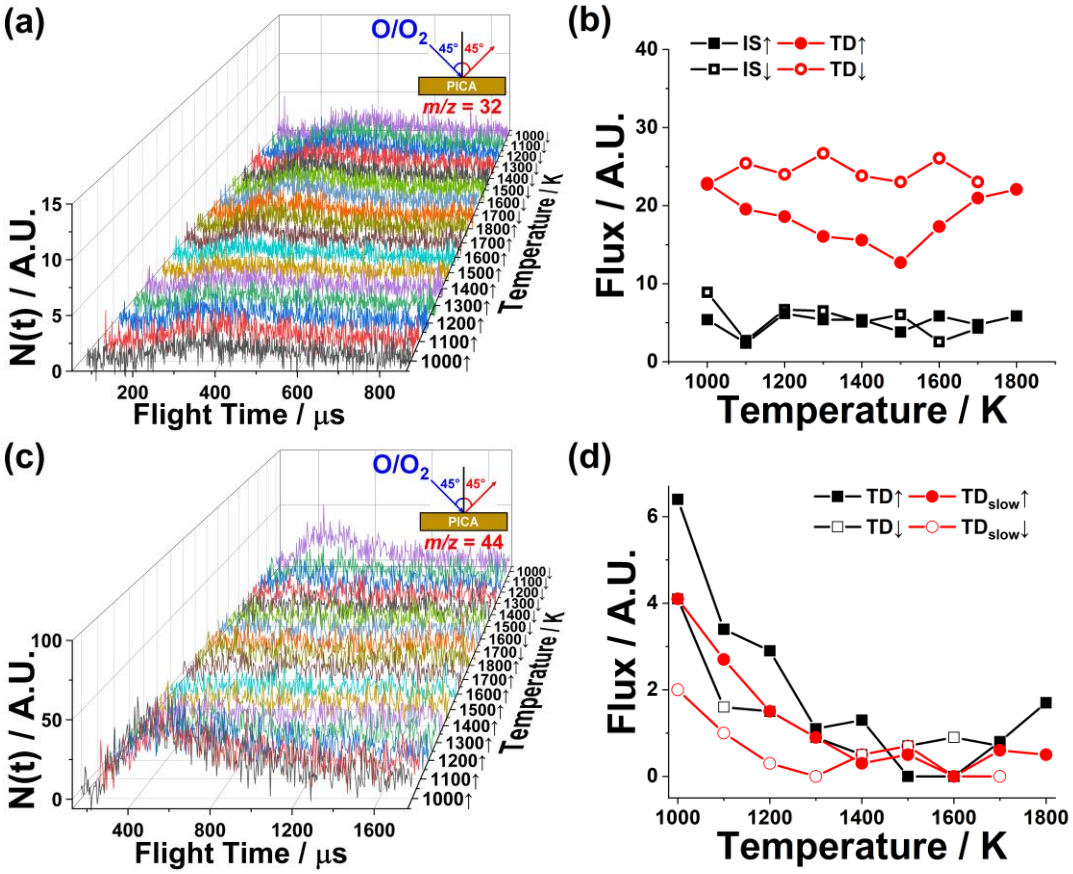

Fig. A-17. TOF product distributions and fluxes of O_2 and CO_2 from uncoated PICA. TOF distributions as a function of temperature increasing up to 1800 K, then decreasing to 1000 K, for **(a)** O_2 and **(c)** CO_2. Fluxes separated into their IS (O_2 only), TD, and TD_{slow} (CO_2 only) components shown in **(b)** and **(d)** for O_2 and CO_2, respectively. Arrows indicate signal at temperature point collected when temperature was either increasing or decreasing.

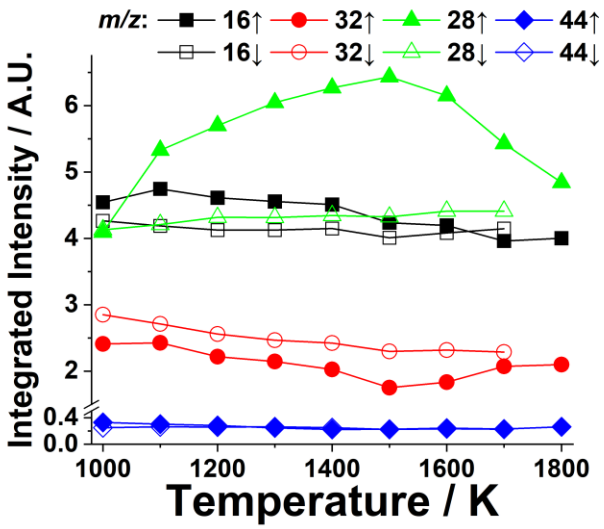

Fig. A-18. Integrated intensities of background TOF distributions for *m/z* = 16, 32, 28, and 44 products from uncoated PICA as a function of surface temperature from 1000 K to 1800 K. Arrows indicate signal at temperature point collected when temperature was either increasing or decreasing.

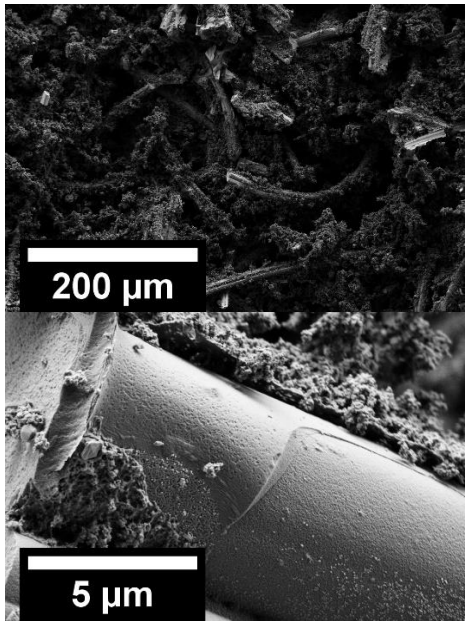

Fig. A-19. SEM of uncoated PICA after experiments with hyperthermal O/O_2 beam, within its out-of-beam area.

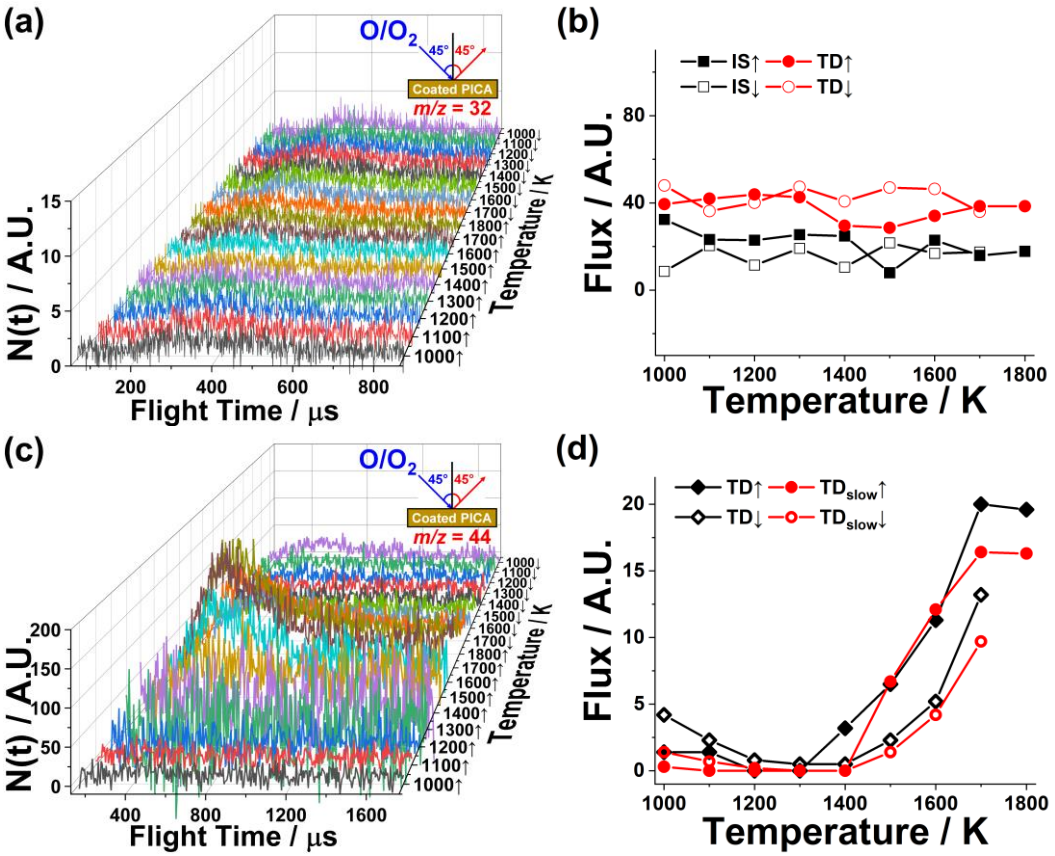

Fig. A-20. TOF product distributions and fluxes of O_2 and *m/z* = 44 from coated PICA. TOF distributions as a function of temperature increasing up to 1800 K, then decreasing to 1000 K, for **(a)** O_2 and **(c)** *m/z* = 44, corresponding either to CO_2 or SiO. Fluxes separated into their IS (O_2 only), TD, and TD_{slow} (*m/z* = 44 only) components shown in **(b)** and **(d)** for O_2 and *m/z* = 44, respectively. Arrows indicate signal at temperature point collected when temperature was either increasing or decreasing. For *m/z* = 44, fluxes at lower temperatures reflect CO_2 product, while fluxes at higher temperature likely reflect SiO.

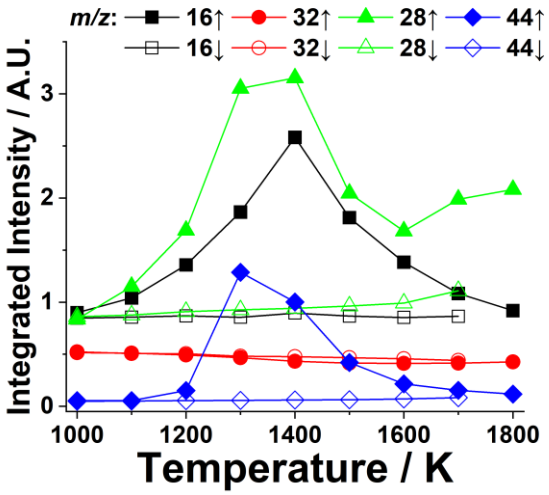

Fig. A-21. Integrated intensities of background TOF distributions for *m/z* = 16, 32, 28, and 44 products from coated PICA as a function of surface temperature from 1000 K to 1800 K. Arrows indicate signal at temperature point collected when temperature was either increasing or decreasing.

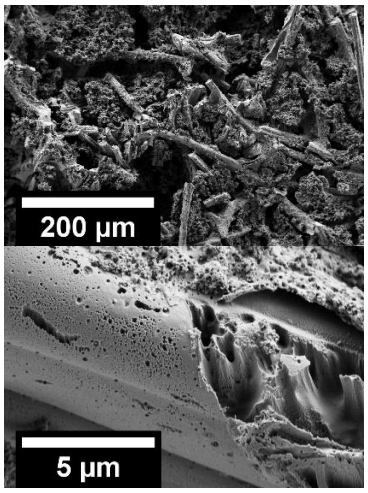

Fig. A-22. SEM of coated PICA after experiments with hyperthermal O/O_2 beam, within its out-of-beam area.